Executive Summary: Electromagnetic and Electromagnetic-circuit co-simulation in CoSMOS

EM and EM-circuit co-simulation Lead : Prof. Vikram Jandhyala
EM Team Members : Prof. Vikram Jandhyala, UW, Dr. Rob Sharpe, Dr. Dan White, Dr. Nathan Champagne, LLNL
EM-circuit co-simulation : Prof. Vikram Jandhyala, Prof. C.J. Richard Shi, Dr. Pavel Nikitin, UW

Students
(advisor Vikram Jandhyala) : Swagato Chakraborty (DARPA funded), Dipanjan Gope (NSF-SRC funded), Todd West (DARPA funded), Chuanyi Yang (NSF funded), Gong Ouyang (DARPA funded)
(advisors Jandhyala and Shi) : Yong Wang (NSF-SRC funded)

Internships and Placement: Yong Wang : ODT, Dipanjan Gope : interned at IBM Watson, Chuanyi Yang: interned at IBM Watson, S. Chakraborty : interned at CFDRC and Calypso Technologies, G. Ouyang: interned at INTEL Dupont

Overall achievement: Development of modern fast algorithms and coupling schemes for EM simulation in mixed-signal systems, resulting in the PILOT code suite, papers, and presentations. There are a large number of advances, discussed in the papers, and code suite documents included in this report. The state of the art of EM and circuit-EM for microelectronic and especially mixed-signal systems simulation was enhanced considerably beyond current industrial methods, and commercialization efforts are underway in a current phase of work. Advances were also made in two LLNL codes, i.e. EIGER and EMSOLVE, to enable these codes to tackle mixed-signal simulations.

Major achievements under NeoCAD funding

1. Coupled EM-circuit simulation enabling combined simulation of frequency domain circuits and electromagnetics without equivalent circuits or convolution
2. Fast full-wave and quasi-static solution with PILOT enabling 10-50x speedup and memory savings over commercial solvers (Sonnet, Ansoft, Zealand)
3. Fast frequency sweeps for coupled system enabling additional 10-50x speedups
4. Material models enabling accurate broadband skin effect characterization for the first time with surface formulations
5. Time domain stable EM-circuit nonlinear co-simulation for the first time
6. Incorporation of coupling schemes, material models, and fast frequency sweeps into the EIGER framework
7. Successful benchmarking of UW PILOT methods on structures from HRL, Rockwell, Intel, AFRL, Mayo
8. Further interest in commercialization from EDA vendors and microelectronics design industry
9. Semi-implicit and full-implicit time stepping algorithms developed in LLNL's EMSolve.

10. Development of EIGER and EMSolve interfaces to CFDRC's micromesh, with related mesher enhancements.

Papers related to EM and EM-circuit advances in NeoCAD (CoSMOS)

1. V. Jandhyala, Y. Wang, D. Gope, and C.J.R. Shi, "A surface-based integral equation formulation for coupled electromagnetic and circuit simulation," *Microwave Optical Technology Letters*, vol. 34, no. 2, pp. 103-106, July 20, 2002.
2. S. Chakraborty and V. Jandhyala, "Accurate computation of vector potentials in lossy media," *Microwave Optical Technology Letters*, vol. 36, no. 5, pp. 359-363, March 5, 2003.
3. D. Gope and V. Jandhyala, "PILOT: A Fast Algorithm for Enhanced 3D Parasitic Capacitance Extraction Efficiency", *Microwave Optical Technology Letters*, vol. 41, no. 3, pp. 169-173, May 5 2004.
4. Y. Wang, D. Gope, V. Jandhyala, and C.J.R. Shi, "Generalized Kirchoff's current and voltage law formulation for coupled circuit-electromagnetic simulation with surface integral equations," *IEEE Transactions on Microwave Theory and Techniques*, vol. 52, no. 7, pp. 1673-1682, July 2004.
5. D. Gope and V. Jandhyala, "Oct-tree based multilevel low-rank decomposition algorithm for rapid 3D parasitic extraction," accepted, manuscript #1303, to appear, *IEEE Transactions on Computer-Aided Design of Integrated Circuits and Systems*, November 2004.
6. Y. Wang, V. Jandhyala, and C.J.R. Shi, 'Efficient sensitivity analysis using coupled circuit-electromagnetic simulation," *Proceedings of the URSI Radio Science Meeting*, Monterey, CA, June 2004.
7. C. Yang and V. Jandhyala, "Prediction of package and chip substrate loss effects in microelectronic circuits using time-domain surface-integral equations," *Proceedings of the URSI National Radio Science Meeting*, Monterey, CA, June 2004.
8. D. Gope and V. Jandhyala, "An iteration-free fast multilevel solver for dense method of moment systems," *Proceedings IEEE Meeting on Electrical Performance of Electronic Packaging*, pp. 177-180, Boston, October 2001.
9. Y. Wang, V. Jandhyala, and C.J.R. Shi, "Coupled electromagnetic-circuit simulation of arbitrarily-shaped conducting structures," *Proceedings IEEE Meeting on Electrical Performance of Electronic Packaging*, pp. 233-236, Boston, October 2001.
10. V. Jandhyala, Y. Wang, D. Gope, and C.J.R. Shi, "Coupled electromagnetic-circuit simulation of arbitrarily-shaped conducting structures using triangular meshes," *Proceedings International Symposium on Quality Electronic Design*, pp. 38-42, San Jose, March 2002.
11. V. Jandhyala and C. Yang, "A time-domain surface-integral formulation for general coupled electromagnetic-circuit simulation," *Proceedings of the IEEE Antennas and Propagation Society International Symposium*, San Antonio, June 2002.

12. D. Gope, S. Chakraborty, Y. Wang, V. Jandhyala, and C.J.R. Shi, “A surface-based 3D coupled circuit-electromagnetic simulator with accurate lossy conductor modeling,” *Proceedings of the IEEE Antennas and Propagation Society International Symposium*, San Antonio, June 2002.
13. C. Yang and V. Jandhyala, “A time domain surface integral technique for mixed electromagnetic and circuit simulation,” *Proceedings IEEE Symposium on Electrical Performance of Electronic Packaging*, pp. 41-44, Monterey, CA, October 2002.
14. Y. Wang, D. Gope, V. Jandhyala, and C.J.R. Shi, “Integral equation-based coupled electromagnetic-circuit simulation in the frequency domain,” *Proceedings of the IEEE Antennas and Propagation Society International Symposium*, vol. 3, pp. 328-331, Columbus, OH, June 2003.
15. C. Yang and V. Jandhyala, “Coupled circuit-electromagnetic simulation with time domain integral equations,” *Proceedings of the IEEE Antennas and Propagation Society International Symposium*, vol. 3, pp. 316-319, Columbus, OH, June 2003.
16. S. Chakraborty and V. Jandhyala, “Evaluation of Green's function integrals in conducting media,” *Proceedings of the IEEE Antennas and Propagation Society International Symposium*, vol. 3, pp. 320-323, Columbus, OH, June 2003.
17. N.J. Champagne, J.D. Rockway, and V. Jandhyala, “Mixed Electromagnetic and Circuit Simulations using a Higher-Order Hybrid Formulation*,” Proceedings of the International Conference on Electromagnetics in Advanced Applications*, September 2003.
18. D. Gope and V. Jandhyala, **“**PILOT: a fast algorithm for enhanced 3D parasitic extraction,” *Proceedings IEEE Symposium Electrical Performance of Electronic Packaging*, pp. 337-340, Princeton, NJ, October 2003.
19. C. Yang, G. Ouyang, and V. Jandhyala, “Integral equation based time domain coupled EM-circuit simulation for packaged conductors,” *Proceedings IEEE Symposium Electrical Performance of Electronic Packaging*, pp. 371-374, Princeton, NJ, October 2003.
20. P. Nikitin, V. Jandhyala, D. White, N. Champagne, J. Rockway Jr., C.J.R. Shi, C. Yang, G. Ouyang, Y. Wang, R. Sharpe, and J. Rockway Sr., “Modeling and simulation of circuit-electromagnetic effects in electronic design flow,” *Proceedings IEEE International Symposium on Quality Electronic Design, San Jose, CA,* pp. 244-249, March 2004.
21. D. Gope, S. Chakraborty, and V. Jandhyala, “A fast parasitic extractor based on low-rank multilevel matrix compression for conductor and dielectric modeling in microelectronics and MEMS,” (163 papers out of 785 accepted), *Proceedings IEEE / ACM Design Automation Conference,* San Diego, June 2004.
22. J.T. West and V. Jandhyala, “A Padé via AWE fast frequency sweep for quasi-static coupled electromagnetic and circuit simulation,” *Proceedings of the IEEE Antennas and Propagation Symposium*, Monterey, CA, June 2004.
23. S. Chakraborty and V. Jandhyala, “Surface-based broadband electromagnetic-circuit simulation of lossy conducting structures in microelectronic circuits,” *Proceedings of the IEEE Antennas and Propagation Symposium*, Monterey, CA, June 2004.

24. V. Jandhyala, P. Nikitin, D. White, N. Champagne, J. Rockway Jr., C.J.R. Shi, R. Sharpe, D. Allstot, and J. Rockway Sr., “Electromagnetic modeling and electromagnetic-circuit co-simulation of mixed-signal systems-on-chip,” (invited, special session on EM for CAD of mixed-signal circuits and high-speed packages) *Proceedings of the IEEE Antennas and Propagation Symposium*, Monterey, CA, June 2004.
25. S. Chakraborty and V. Jandhyala, “A Surface Equivalence-Based Method to Enable Rapid Design and Layout Iterations of Coupled Electromagnetic Components in Integrated Packages,” *Proceedings of the IEEE Symposium Electrical Performance of Electronic Packaging*, October 2004.
26. B. Fasenfest, J. D. Rockway, N. Champagne, R. M. Sharpe, “A Generalized Fast Frequency Sweep Algorithm for Coupled Circuit-EM Simulations,” *Proceedings of the IEEE Antennas and Propagation Symposium*, Monterey, CA, June 2004.
27. D. Gope and V. Jandhyala, “Fast Iterative and Direct, QR-based Solvers for Large Scale, Massively Coupled Parasitic Extraction Problems,” *Semiconductor Research Corporation TECHCON*, June 2003.

to the feeding lines network. Moreover, this transition can be used in the Butler matrix to avoid the unavailable cross lines.

REFERENCES

1. O. Lafond, Conception et technologies d'antennes imprimées multicouches à 60 GHz, Thèse de doctorat de l'Université de Rennes 1, 2000.
2. O. Lafond, M. Himdi, and J.P. Daniel, Thick slot coupled printed antennas arrays for a 60 GHz indoor communication system, Microwave Opt Technol Lett 25 (2001), 105-108.
3. M. El Haj Sleimen, M. Himdi, J.P. Daniel, N. Haese, and P.A. Rolland, Technologie de réseaux d'antennes actifs et passifs en millimétrique, JINA 98, Session II-9, pp. 322-325.
4. M. El Haj Sleimen, Etude de réseaux d'antennes imprimées en millimétrique, Thèse de doctorat de l'Université de Rennes 1, 1999.
5. AVI&PESCHARD, ZAC de la Goulgatière, 35000 Chteaubourg, France.
6. B. Schiek and J. Kohler, An improved microstrip to microslot transition, IEEE Trans Microwave Theory Tech, MTT-24 (1976), 231-233.
7. K.C. Gupta, R. Garg, and I.J. Bahl, Microstrip lines and slotlines. Artech House, Norwood, MA, 1996.
8. CST MICROWAVE STUDIO, V 3.2.
9. J. Butler et al., Beam-forming matrix simplifies design of electrically scanned antennas, Electron Des 9 (1961), 170–173.
10. T. Seki, K. Uehara, and K. Kagoshima, NTT Wireless Systems Laboratories, 30-GHz multibeam antenna using bi-layer Butler matrix circuits, Proceedings of ISAP '96, Chiba, Japan, pp. 165–168.

A SURFACE-BASED INTEGRAL-EQUATION FORMULATION FOR COUPLED ELECTROMAGNETIC AND CIRCUIT SIMULATION

Vikram Jandhyala, Yong Wang, Dipanjan Gope, and C. J. Richard Shi
Department of Electrical Engineering
University of Washington
Seattle, Washington 98195

Received 9 January 2002

ABSTRACT: *A surface-based integral-equation formulation for coupled electromagnetic and circuit simulation is presented. The approach is sufficiently general to model arbitrarily shaped structures and high-frequency skin effects. The formulation is implemented in both an equivalent circuit form for spice compatibility, and in a more general form as a coupled-matrix system outside spice. The overall approach can be interpreted as either a modified surface-only partial element equivalent circuit approach, or as a circuit-coupled version of the surface-based method of moments.* © 2002 Wiley Periodicals, Inc. Microwave Opt Technol Lett 34: 103–106, 2002; Published online in Wiley InterScience (www.interscience.wiley.com). DOI 10.1002/mop.10386

Key words: *PEEC; method of moments; coupled simulation; integral equations*

1. INTRODUCTION

The simulation of electromagnetic (EM) effects in high-speed chips, packages, and boards is essential for complete electrical characterization. However, it is impractical to analyze the entire structure under test as a large EM problem; this is especially true in iterative design practice. Moreover, the introduction of circuit elements makes the overall problem an inherently coupled and hierarchical one. The partial element equivalent circuit (PEEC) approach [1,2] has been developed as a successful means to interface circuit and EM formulations. In the classical PEEC approach, conductor cross sections are divided into volumetric filaments of rectangular cross section. Equivalent inductance, capacitance, and resistance matrices are computed for EM interactions between these filaments. These matrices are then imported into SPICE or similar circuit solvers, either directly or in the form of reduced-order models. The coupled system can then be solved in the time or frequency domain.

Owing to recent developments in systems-on-chip and in high-speed integrated circuits, there is a need to go beyond the classical filament-based PEEC for a variety of reasons. First, there is a need to model arbitrarily shaped structures including on-chip inductors, micro-electro-mechanical devices, on-chip antenna structures, et cetera. Second, at high frequencies, skin effect modeling is crucial. The classical filament-based approach addresses this by mimicking the behavior of the conduction current at these frequencies through appropriate lateral meshing of filaments. Unfortunately, such an approach is both heavily frequency dependent and potentially computationally intensive. An elegant approach to modeling skin impedance is presented by the use of surface impedance approximations in the surface-based method of moments (MoM).

The work presented in this Letter aims at using surface-only formulations utilizing surface meshes [5,7,8] in order to model more complex current distributions and their field effects arising from nonrectangular conducting structures. The surface-based version of PEEC is first presented, in a SPICE-compatible form. The circuit-solver-free equivalent coupled matrix formulation is then presented. Finally, it is shown that, by a reformulation of unknowns, the surface-based formulation can be reformulated as a modified method of moments (MoM) system.

2. SURFACE-BASED COUPLED EM-CIRCUIT SIMULATION

Conducting structures are analyzed with the use of the electric field integral equation formulation (EFIE), wherein the surface current **J** satisfies the equation

$$j\omega \frac{\mu}{4\pi} \int_s \frac{J(\mathbf{r}')}{|\mathbf{r}-\mathbf{r}'|} ds' + (\nabla\phi)(\mathbf{r}) = -ZJ(\mathbf{r}) \tag{1}$$

and the scalar potential ϕ and surface charge density ρ are related through the equation

$$\phi = \frac{1}{4\pi\varepsilon} \int_s \frac{\rho(\mathbf{r}')}{|\mathbf{r}-\mathbf{r}'|} ds'. \tag{2}$$

In Eq. (1) Z represents the surface impedance

$$Z = \sqrt{\frac{j\omega\mu}{2\sigma}} \tag{3}$$

in terms of the circular frequency ω, permeability μ, and conductivity σ. The surface impedance approximation is valid at frequencies where the skin depth is smaller than the cross section of conductors. At lower frequencies, a coupled interior EFIE utilizing lossy medium Green's functions is required. For surface current and charge modeling, the standard RWG functions $\boldsymbol{f}$ [3,4], defined over pairs of triangles are used in conjunction with a triangular tessellation of the conductor surfaces. Upon testing the EFIE, the following matrix equations are obtained:

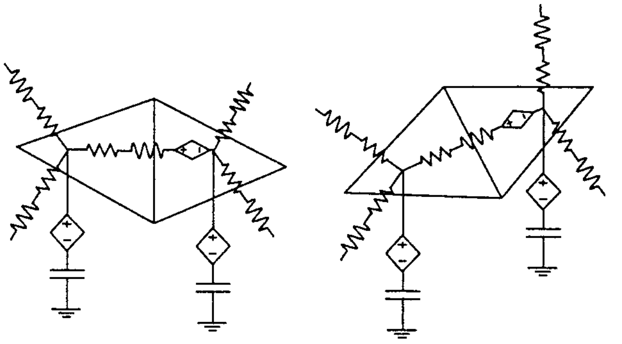

Figure 1 Equivalent circuit construction on a triangular mesh, showing inductances, resistances, capacitances, and dependent controlled sources

$$(j\omega\bar{\mathbf{L}} + \bar{\mathbf{Z}})\,\mathbf{J} = \mathbf{I} \tag{4}$$

$$\bar{\mathbf{P}}\mathbf{Q} = \mathbf{V}. \tag{5}$$

In these equations, the variables are the current, charge, and potential, and the excitation includes known terminal voltages v or current sources. The inductance, potential, and surface impedance matrices can be defined as

$$L_{ij} = \frac{\mu}{4\pi}\int_s\int_s \frac{\mathbf{f}_j(\mathbf{r}')}{|\mathbf{r}-\mathbf{r}'|}\,ds'\cdot\mathbf{f}_i(\mathbf{r}')\,ds, \qquad i,j = 1,\ldots,N_e, \tag{6}$$

$$P_{ij} = \frac{1}{4\pi\varepsilon}\int_s\int_s \frac{\nabla'\cdot\mathbf{f}_j(\mathbf{r}')}{|\mathbf{r}-\mathbf{r}'|}\,\nabla\cdot\mathbf{f}_i(r)\,ds\,ds', \qquad i,j = 1,\ldots,N_p, \tag{7}$$

$$Z_{ij} = Z\int \mathbf{f}_i(\mathbf{r})\cdot\mathbf{f}_j(\mathbf{r})\,ds, \qquad i,j = 1,\ldots,N_e, \tag{8}$$

where the indices traverse the total number of edges or patches, and the surface impedance matrix is nonzero for only those entries where RWG bases i and j share a common triangle. The matrix $\bar{\mathbf{A}}$ is a sparse, rectangular adjacency matrix that couples edges to triangular patches. Each row has two nonzero entries.

Such an approach can be used to incorporate EM effects, within the limitations of SPICE solvers and reduced-order models, through element stamps and controlled sources for mutual coupling terms. The distributed equivalent circuit based on triangular surface meshes is depicted in Figure 1, and Figure 2 shows the PEEC-like equivalent circuit for two neighboring triangular elements.

As discussed in the previous section, an alternative desirable approach is to remove the dependency on SPICE-like solvers, and to formulate the equations as a coupled system amenable to fast iterative or direct solution.

3. Coupled Method-of Moments-Formulation

The EFIE described in the previous section can be explicitly written in a coupled form outside SPICE in the following manner

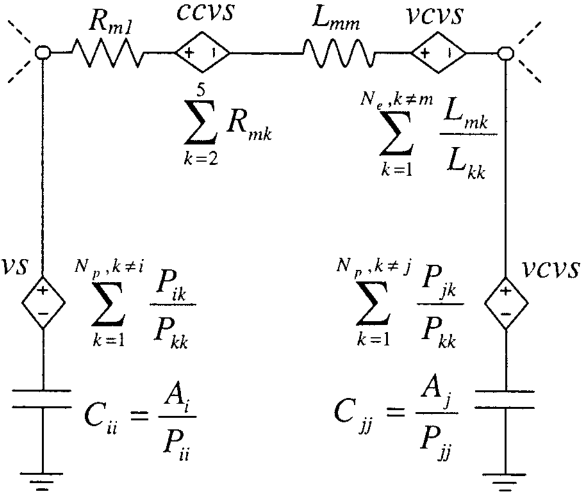

Figure 2 Equivalent PEEC-like circuit for two adjacent triangular mesh elements

$$\begin{pmatrix} j\omega\bar{\mathbf{L}} + \bar{\mathbf{Z}} & \bar{\mathbf{A}} & \bar{\mathbf{0}} & \bar{\mathbf{X}} \\ \bar{\mathbf{0}} & \bar{\mathbf{I}} & \bar{\mathbf{P}} & \bar{\mathbf{0}} \\ -\bar{\mathbf{A}}^T & \bar{\mathbf{0}} & j\omega\bar{\mathbf{D}} & \bar{\mathbf{0}} \\ \bar{\mathbf{X}}^T & \bar{\mathbf{0}} & \bar{\mathbf{0}} & \overline{\mathbf{MNA}} \end{pmatrix} \begin{pmatrix} \mathbf{J} \\ \mathbf{V} \\ \mathbf{Q} \\ \mathbf{ckt} \end{pmatrix} = \begin{pmatrix} \mathbf{0} \\ \mathbf{0} \\ \mathbf{0} \\ \mathbf{ckt\_ex} \end{pmatrix}. \tag{9}$$

In this formulation, the sparse matrix $\bar{\mathbf{X}}$ is used to enforce KVL, KCL, and field continuity. The sparse block $\overline{\mathbf{MNA}}$ represents the modified nodal analysis conductance matrix corresponding to circuit unknowns (**ckt**). The excitation includes voltage and current sources within the excitation vector **ckt_ex**. The matrix $\bar{\mathbf{D}}$ is a diagonal matrix used to enforce the current and charge continuity equation. The unknowns in this formulation include the surface current, potential, charge, and MNA circuit unknowns. Electric field excitation can also be included in this formulation, in the first block of the right-hand side. The above formulation is analogous to the filament-based PEEC method, but for a surface-only formulation. It is interesting to note that these equations can be reorganized and eliminated to obtain a simpler set of equations:

$$\begin{pmatrix} j\omega\bar{\mathbf{L}} + (j\omega)^{-1}\bar{\mathbf{A}}\bar{\mathbf{P}}\bar{\mathbf{D}}^{-1}\bar{\mathbf{A}}^T & \bar{\mathbf{X}} \\ \bar{\mathbf{X}}^T & \overline{\mathbf{MNA}} \end{pmatrix} \begin{pmatrix} \mathbf{J} \\ \mathbf{ckt} \end{pmatrix} = \begin{pmatrix} \mathbf{0} \\ \mathbf{ckt\_eq} \end{pmatrix}. \tag{10}$$

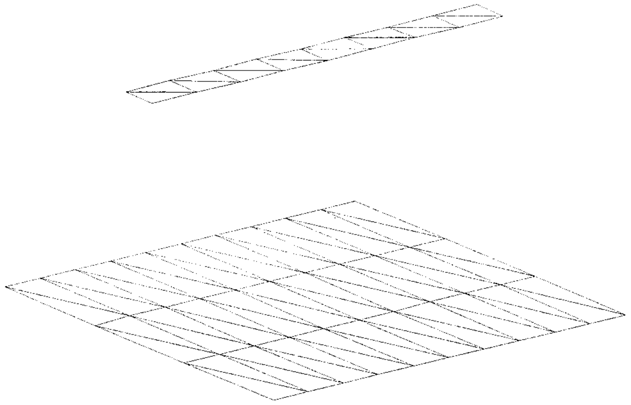

Figure 3 Interconnect over ground plane. The ground plane is 2 cm long and 1 cm wide, the interconnect is 2 cm long and 1 mm wide, and is 0.5 mm above the ground plane

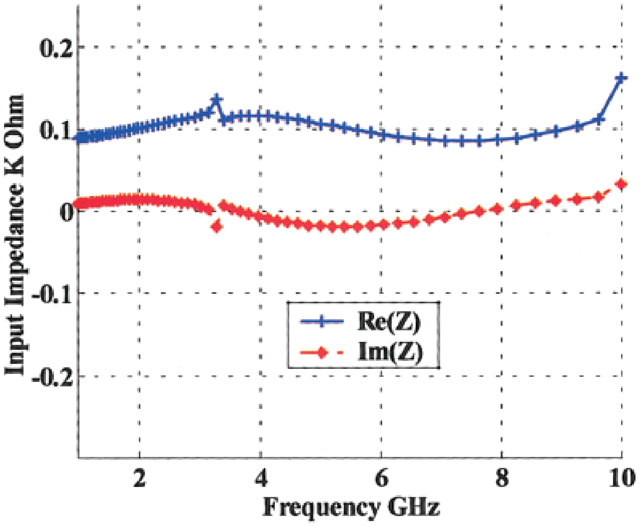

Figure 4 Input impedance of the interconnect over a ground plane as a function of frequency [Color figure can be viewed in the online issue, which is available at www.interscience.wiley.com.]

The first block of equations above is nothing but a statement of the MoM, with appropriate interfaces (voltages and currents) to ckt unknowns. The second block is the self-consistent set of circuit equations and independent excitations. Thus the surface-based coupled formulation can be reinterpreted as a classical MoM with appropriate excitation and circuit boundary conditions.

4. SIMULATION EXAMPLES

The first example (Figure 3) is that of an interconnect over a ground plane, as in [6]. The frequency dependence of the input impedance is shown in Figure 4. It is interesting to note that the transmission-line resonance behavior of this structure is also captured. The finite-sized impedance peaks are due to coarse frequency sampling at resonance.

The next example demonstrates the ability to model time-domain cross talk. Figure 5 shows two sets of traces over a ground plane, one set running parallel, and the other set with one trace having two right-angled discontinuities and with a larger average distance between the traces. One of the traces is excited with a 600-ps duration trapezoidal pulse. The far-end cross-talk waveforms on the unexcited traces are shown in Figure 6. As expected, the closer-in trace shows a large noise waveform. Also, the separation between the two large pulses, signifying the initiation and

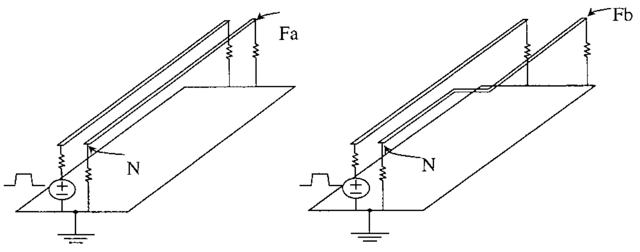

Figure 5 Pair of traces over a ground plane: straight, parallel traces (left), and bent traces (right). The ground plane is 2 cm long and 1 cm wide, the traces are 2 cm long 1 mm wide, and are 0.5 mm above the ground plane. In the left figure the traces are 1 mm apart; in the right figure the traces are 1 mm apart at the near end and 2 mm apart at the far end

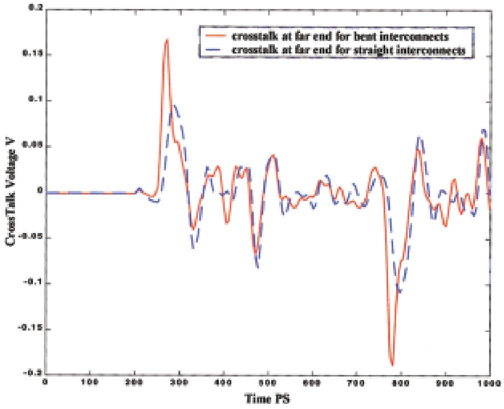

Figure 6 Far-end cross-talk voltage waveforms for the straight and bent pair of interconnects [Color figure can be viewed in the online issue, which is available at www.interscience.wiley.com.]

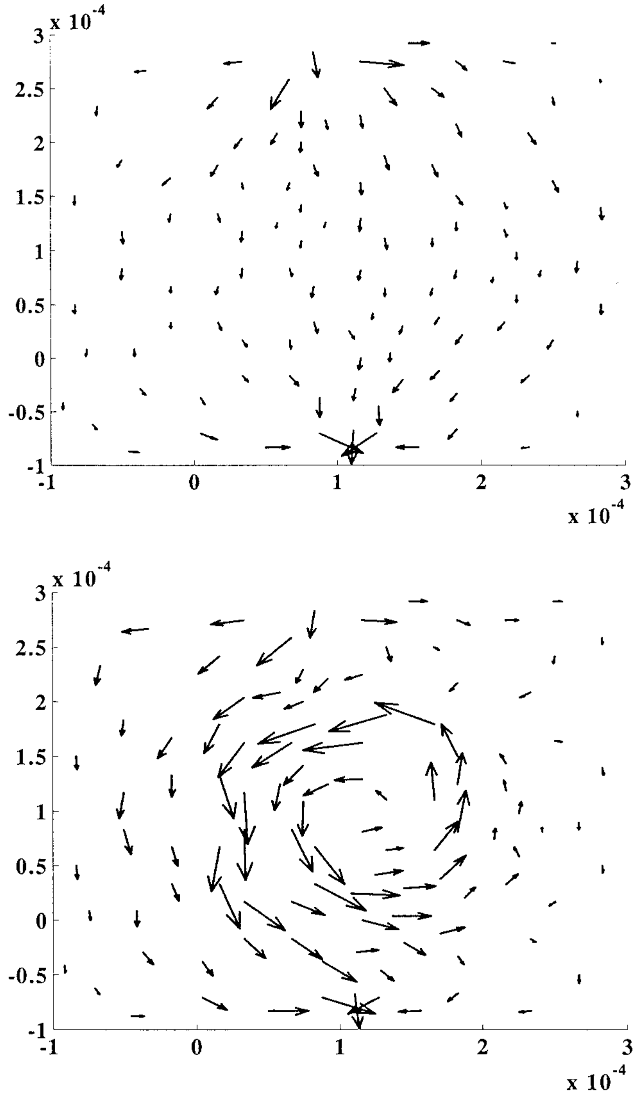

Figure 7 Induced ground plane current under spiral inductor, obtained with the use of equivalent surface-PEEC elements in SPICE, at 1 kHz (top) and 1 GHz (bottom). Spiral inductor is 200 μm × 200 μm and 30 μm above the ground plane, and the ground plane is 400 μm × 400 μm

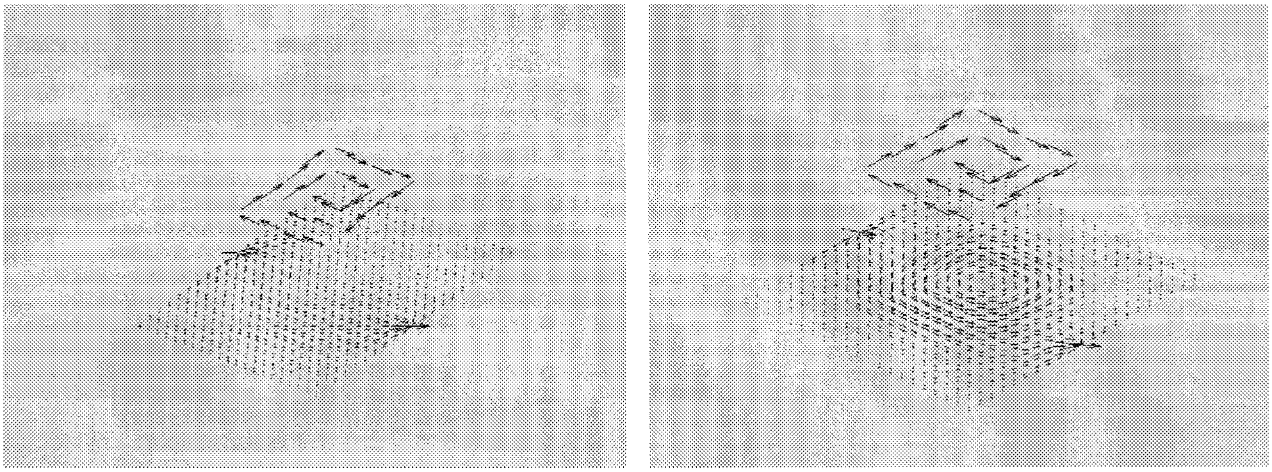

Figure 8 Induced current on ground plane under inductor, obtained with the use of the coupled-matrix solution, at 100 kHz (left) and 1 GHz (right). Also shown is the inductor current

conclusion of the trapezoidal pulse influence (through its derivative), is 600 ps.

The third example illustrates the ability of the coupled method to predict induced current behavior. A planar, spiral inductor over a ground plane is excited with a voltage source connected to the ground, and terminated with a resistance to an oppositely located point on the ground plane. At a frequency of 1 KHz, the current on the ground plane (Figure 7) is well spread out and travels along low-impedance paths from the terminal back to the source. However, at a higher frequency of 1 GHz, the inductance minimization phenomenon is observed. The current tries to flow in loops of small area in order to minimize inductive impedance at this high frequency. Although this is captured reasonably well by the SPICE-linked version of the surface-PEEC algorithm presented here, the example also highlights the strengths of the coupled matrix method. The presence of a dense matrix in SPICE makes the SPICE solution time large. However, with a dedicated dense iterative solver and coupled-matrix system outside SPICE, the overall solution is rendered far more efficient. Consequently, more resolved surface meshes can be used, and a smoother current distribution is obtained, as in Figure 8. Both high- and low-frequency behavior of the current below the inductor is exhibited in this figure.

5. CONCLUSIONS

A new surface-based coupled EM-circuit formulation is described for arbitrarily shaped three-dimensional conducting structures. The formulation is expressed first as a modified surface-based PEEC and is solved by introducing equivalent circuits in SPICE. Next it is shown that a coupled matrix system can be generated outside SPICE, which can be reduced to a modified MoM system, and can be solved efficiently with the use of an iterative solver. The method is general enough to be applicable to a wide variety of high-frequency and high-speed integrated circuit and packaging applications.

Continuing work is aimed at incorporating a fast multilevel iterative solver, multilayered and finite dielectrics, and specialized quadrature rules for very low frequency characterization of the interior lossy medium problem. A fast direct solution based on a multilevel low-rank decomposition algorithm is also being implemented.

ACKNOWLEDGMENTS

The authors would like to thank Dr. John W. Rockway of SSC San Diego for several stimulating discussions related to this research.

REFERENCES

1. A.E. Ruehli, Equivalent circuit models for three-dimensional multiconductor systems, IEEE Trans Microwave Theory Tech MTT-22 (1974), 216–221.
2. A.E. Ruehli and A.C. Cangellaris, Progress in the methodologies for the electrical modeling of interconnects and electronic packages, Proc IEEE 89 (2001), 740–771.
3. A.F. Peterson, S.L. Ray, and R. Mittra, Computational methods for electromagnetics, IEEE Press, New York, 1997.
4. S.M. Rao, D.R. Wilton, and A.W. Glisson, Electromagnetic scattering by surfaces of arbitrary shape, IEEE Trans Antennas Propagat AP-30 (1982), 409–418.
5. G. Coen, N. Fache, D. de Zutter, and P. Lagasse, Automatic equivalent discrete distributed circuit generation for microstrip interconnection discontinuities, AP-S Digest 3 (1994), 1702–1705.
6. W. Pinello, A.C. Cangellaris, and A. Ruehli, Hybrid electromagnetic modeling of noise interactions in packaged electronics based on the partial-element equivalent-circuit formulation, IEEE Trans Microwave Theory Tech MTT-45, (1997), 1889–1896.
7. Y. Wang, V. Jandhyala, and R. Shi, Coupled electromagnetic-circuit simulation of arbitrarily-shaped conducting structures, Proc. IEEE Meeting on Electrical Performance of Electronic Packaging, Cambridge, MA, 2001, pp. 233–236.
8. S. Rong and A.C. Cangellaris, Generalized PEEC models for three-dimensional interconnect structures and integrated passives of arbitrary shapes, Proc. IEEE Meeting on Electrical Performance of Electronic Packaging, Cambridge, MA, 2001, pp. 225–228.

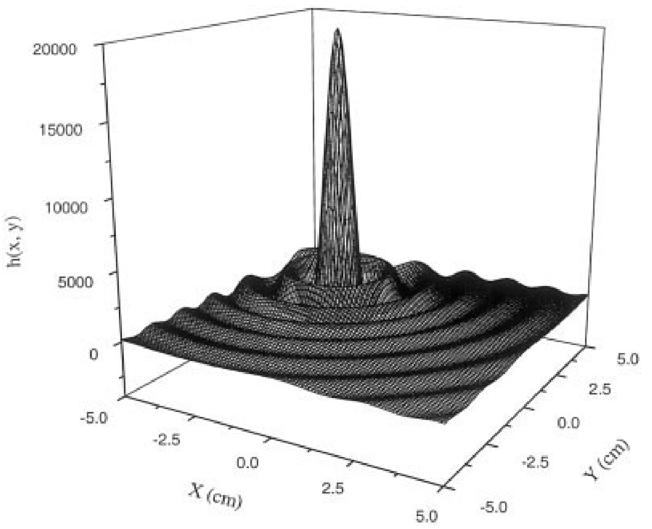

Figure 4 Point spread function (PSF) at point (−2.5 cm, 2.5 cm)

very high, at point (0, 0) and point (−2.5 cm, 2.5 cm), the resolutions are nearly the same. This implies that even when the imaging object is located far from the rotating center, it is possible to visually reconstruct the profile of the object. The numerical results show that the higher center frequency f_0 may yield better resolution if the sweep frequency range is fixed (for example, 10 GHz).

5. CONCLUSION

A novel theory about near-field microwave imaging has been proposed and a near-field microwave diversity imaging system has been constructed, which includes data acquirement, imaging process, and imaging display. This paper mainly focused on a theoretical investigation of the imaging process for the turntable mode. We derived the imaging function in both the space and spectrum domains. The imaging function is an integral of the backscattering of the object over a given window in the Fourier domain. The imaging resolution of this system, which depends on the sweep frequency and rotatory angle ranges (so-called frequency- and angle-diversity), was then studied. The theoretical results indicated that the PSF of the imaging system for the practical case could infinitely approach that of the ideal case when $B \rightarrow \infty$, namely, the Dirac-δ function. Further investigation is in progress and relevant developments will be reported soon.

REFERENCES

1. M.R. Tofighi and A.S. Daryoush, Near field microwave brain imaging, Electron Lett 37 (2001), 807–808.
2. I.T. Rekanos, M.S. Efraimidou, and T.D. Tsibouki, Microwave imaging: inversion of scattered near-field measurements, IEEE Trans Magnetics Mag 37 (2001), 3294–3297.
3. J. Ma and H. Wu, Spherical back-projection method imaging for perfectly conducting objects, Acta Electronica Sinica 24 (1995), 26–29.
4. J. Ma, Y. Jiao, and N. Mao, A new technique for image reconstruction from near-field backscattering, IEEE AP-S Dig (1998), 689–701.
5. T.H. Chu and D.B. Lin, Microwave diversity imaging of perfectly conducting objects in the near-field region, IEEE Trans Microwave Theory Tech MTT 39 (1991), 480–487.
6. H.J. Li and F.L. Lin, Near-field imaging for conducting objects, IEEE Trans Antennas Propagat AP 39 (1991), 600–605.

ACCURATE COMPUTATION OF VECTOR POTENTIALS IN LOSSY MEDIA

Swagato Chakraborty and Vikram Jandhyala
Department of Electrical Engineering
University of Washington
Seattle, WA 98195

Received 13 August 2003

ABSTRACT: *This paper presents an accurate formulation and integration scheme for computing vector potential interactions due to linear basis functions in lossy conducting media over wide frequency ranges. The emphasis is on an approach that is broadband and works both at high-frequency surface impedance limits and at low-frequency volumetric current flow limits. The method can be interpreted as a step towards a surface-only formulation for an integral-equation-based broadband characterization.* © 2003 Wiley Periodicals, Inc. Microwave Opt Technol Lett 36: 359–363, 2003; Published online in Wiley InterScience (www.interscience.wiley.com). DOI 10.1002/mop.10764

Key words: *vector potentials; method of moments; conducting media; skin effects; surface formulation*

1. INTRODUCTION

Modeling the interior problem associated with a lossy conductor is of particular importance in the ultra-wideband frequency-domain modeling of structures such as interconnects and packages. This is specifically of interest at frequencies where the cross sections of conductors are smaller than their skin depths. In such cases, surface impedance approximations break down, and recourse is normally taken to explicit volumetric formulations.

This paper presents a step towards surface-only wideband modeling of interconnects and packages through an exact formulation and accurate numerical integration scheme for efficiently computing highly damped vector potentials in lossy conductors. The presented method is general in terms of geometries, frequencies, material parameters, and relative separation and orientation of source and observer regions. The motivation behind the presented approach is that a coupled integral equation formulation, linking an exterior homogeneous medium problem to an interior lossy medium problem, is required in order to correctly predict electromagnetic behavior of conductors in specific frequency bands. As line widths and heights of interconnects become smaller, and as progressively smaller devices and structures are integrated at the package and chip levels, the underlying complex analyses cannot be handled by an *ad hoc* mixing of surface and volume formulations, and seamless wideband formulations become imperative.

2. VECTOR POTENTIALS IN LOSSY CONDUCTING MEDIA

Computing the electric field in a lossy medium requires computation of scalar and vector potentials. The scalar potential computation has been studied previously in [1], and this paper deals with the computation of vector potentials for arbitrarily located sources and observation points. The vector potential **A** is given by

$$\mathbf{A}(\mathbf{r}) = \frac{\mu}{4\pi} \int_{S'} \frac{e^{-jk|\mathbf{r}-\mathbf{r}'|}}{|\mathbf{r} - \mathbf{r}'|} \mathbf{J}(\mathbf{r}') ds', \tag{2.1}$$

where **r** and **r′** are the position vectors of the observation point and of an arbitrary point in the source region, respectively, and S' denotes the conductor surface. The source current density is denoted by **J**, and k is the wave number in the lossy medium given by

$$k = \omega\sqrt{\mu_0\mu_r\varepsilon_0\left(\varepsilon_r + \frac{\sigma}{j\omega\varepsilon_0}\right)}, \tag{2.2}$$

where σ is the conductivity of the lossy medium, μ_0 and ε_0 represent the free-space permeability and permittivity, respectively, and $\omega = 2\pi f$, where f is the frequency of interest. Also, μ_r and ε_r represent the relative permeability and relative permittivity of the lossy medium, including magnetic and dielectric losses; typically, these are both equal to 1 for metallic conductors. The popular triangle-pair-based Rao–Wilton–Glisson (RWG) functions [2] are used to represent $\mathbf{J}(\mathbf{r}')$, wherein current is modeled by piecewise linear vector functions. The vector potential integral computation (2.1) is replaced by integrals of the form

$$\iint_T \frac{\boldsymbol{\rho} e^{-jk|\mathbf{R}|}}{|\mathbf{R}|}\, ds', \tag{2.3}$$

where $\mathbf{R} = \mathbf{r} - \mathbf{r}'$, and $\boldsymbol{\rho}$ denotes a vector from the node opposite the edge of interest in triangle T to $\mathbf{r}'$. The distinction from the corresponding integrals in the exterior equivalent problem is that the wave-vector is complex and may lead to strong exponential decays in the integrands, depending upon the frequency of interest.

3. PREVALENT METHODS FOR LOSSY CONDUCTING MEDIA

Existing techniques for lossy media computations involve the use of polar coordinate transformations. This has been accomplished for the evaluation of the scalar Green's function [1], and in the context of lossless media [3, 4]. The self-term for the vector potential integral has been computed using a polar coordinate transformation [5], and the method presented therein is extendable to observation points in the plane of the source triangle. This precludes the important case of observation at a near-singular point located above or below the source triangle, as often occurs in thin conductors. In this work, the restrictions on observer location are lifted and a general computation of vector potentials due to RWG functions in lossy conducting media is performed.

4. FREQUENCY DEPENDENCE OF VECTOR POTENTIALS IN CONDUCTING MEDIA

The sparsity of the method of moments (MoM) matrix corresponding to Green's function interactions in lossy conducting media is highly frequency-dependent. At sufficiently high frequencies, where conductor cross-sections are significantly larger than skin depth, the surface impedance approximation is very accurate. Consequently, the MoM matrix based on the RWG and testing functions is nearly diagonal, with only interactions between overlapping functions being non-zero. As the frequency is reduced, the exact exponential decay of the potentials is apparent, and there is a distance beyond which the interactions are numerically zero (for example, in double precision). Further lowering of frequency yields a full matrix, with an exponential decay with distance. Finally, at very low frequencies, where the conductor cross-sections are significantly smaller than the skin depth, the matrix is dense with a mild exponential decay. The formulation and integration scheme presented here is intended for wideband vector potential in lossy conducting media, that is, to compute the interactions over the entire frequency range as described above.

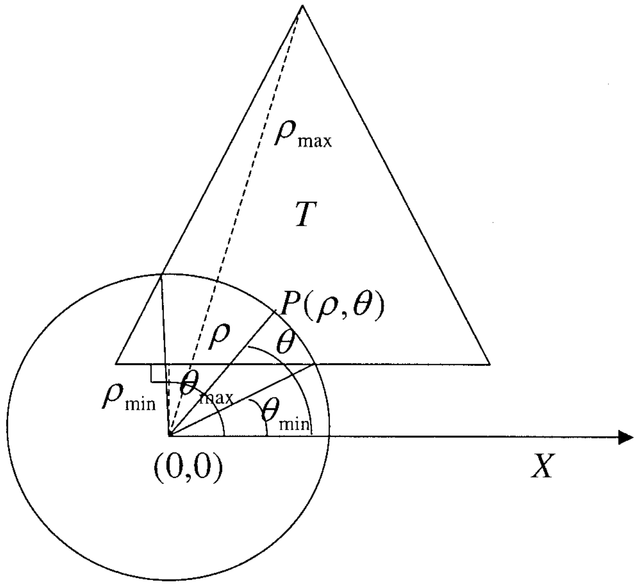

Figure 1 Triangle T in transformed coordinates, with the projection of the observation point as the origin

5. FORMULATION OF THE INTEGRALS AND NUMERICAL INTEGRATION SCHEME

The vector potential integral $\mathbf{G}_{Vect}$ due to RWG functions can be written in polar coordinates as

$$\mathbf{G}_{Vect}(\mathbf{r}) = \hat{\mathbf{x}} \int_T \frac{\rho e^{-jk\sqrt{\rho^2+d^2}}}{\sqrt{\rho^2+d^2}}\, \rho\cos(\theta)\, d\rho d\theta + \hat{\mathbf{y}} \int_T \frac{\rho e^{-jk\sqrt{\rho^2+d^2}}}{\sqrt{\rho^2+d^2}}\, \rho\sin(\theta)\, d\rho d\theta, \tag{5.1}$$

where it is assumed, for ease of discussion, and without loss of generality, that the triangle T (Fig. 1) lies in the x − y plane. In the above equation, the distance d is the height of the observation point from the plane of T, and the distance ρ is the separation of source points in T from the projection of the observation point onto the plane of T.

For the case when the observation point is in the plane of T, d equals zero and it is possible to carry out the integration as in [5] to yield

$$\mathbf{G}_{Vect}(\mathbf{r}) = \hat{\mathbf{x}} \int_T \rho e^{-jk\rho} d\rho \cos(\theta) d\theta + \hat{\mathbf{y}} \int_T \rho e^{-jk\rho} \sin(\theta) d\theta. \tag{5.2}$$

Existing work reported in the literature [5] focuses on the self-term computation, and the results can readily be extended to the in-plane observation case, but do not apply to the general case of arbitrarily located and oriented basis and testing functions at all frequencies. This is due to the lack of a closed-form expression for one-dimensional integration with respect to ρ in (5.1) for $d \neq 0$. In order to lift this restriction and to enable a one-dimensional analytic integration followed by a one-dimensional numerical integration for (5.1), the integration order needs to be reversed compared to existing work for scalar and in-plane cases; integra-

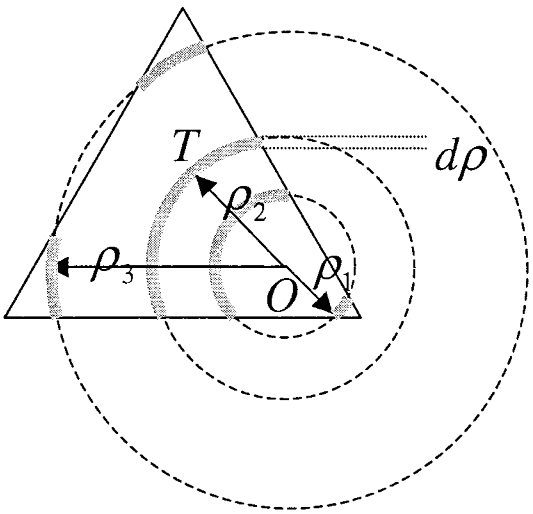

Figure 2 Region of integration for specific values of ρ for a triangle T. The origin for determining distances is the projection O of the observation point on the plane of T

tion over θ is performed analytically followed by a numerical integration over ρ:

$$\mathbf{G}_{vect}(\mathbf{r}) = \hat{\mathbf{x}} \int_{\rho_{\min}}^{\rho_{\max}} \frac{\rho^2 e^{-jk\sqrt{\rho^2+d^2}}}{\sqrt{\rho^2+d^2}} [\sin(\theta)]_{\theta_{\min}}^{\theta_{\max}} d\rho + \hat{\mathbf{y}} \int_{\rho_{\min}}^{\rho_{\max}} \frac{\rho^2 e^{-jk\sqrt{\rho^2+d^2}}}{\sqrt{\rho^2+d^2}} [-\cos(\theta)]_{\theta_{\min}}^{\theta_{\max}} d\rho. \quad (5.3)$$

In the above equation, $\left[\binom{-\cos\theta}{\sin\theta}\right]_{\theta_{\min}}^{\theta_{\max}}$ is required as a function of ρ. For a given ρ, when the integration points lie inside the triangle for all values of θ, the multiplying function becomes $\int_0^{2\pi} \binom{\cos\theta}{\sin\theta} d\theta$, which integrates to zero. Also, for $\forall(\rho, \theta) : P(\rho, \theta) \notin T$, the integral is zero, where $P(\rho, \theta)$ denotes a point having coordinate (ρ, θ). Hence, the limits are obtained for the piecewise boundaries, where $P(\rho, \theta) \in T$, as shown in Figure 2. To obtain the limits on θ as a function of ρ, the reference coordinate system in which T lies in the $x - y$ plane is translated so that the projection of the observation point onto the plane of T defines the origin (Fig. 1). The intersection of a circle of constant ρ with the sides of the triangle determines the limits of integration in θ. The expression $\left[\binom{-\cos\theta}{\sin\theta}\right]_{\theta_{\min}}^{\theta_{\max}}$ is evaluated for a given ρ to arrive at the final form of the one-dimensional integral

$$\mathbf{G}_{vect}(\mathbf{r}) = \hat{\mathbf{x}} \int_{\rho_{\min}}^{\rho_{\max}} \Psi_1(\rho) d\rho + \hat{\mathbf{y}} \int_{\rho_{\min}}^{\rho_{\max}} \Psi_2(\rho) d\rho, \quad (5.4a)$$

where

$$\Psi_1(\rho) = \frac{\rho^2 e^{-jk\sqrt{\rho^2+d^2}}}{\sqrt{\rho^2+d^2}} (\sin\theta_{\max}(\rho) - \sin\theta_{\min}(\rho)) \quad (5.4b)$$

and

$$\Psi_2(\rho) = \frac{\rho^2 e^{-jk\sqrt{\rho^2+d^2}}}{\sqrt{\rho^2+d^2}} (-\cos\theta_{\max}(\rho) + \cos\theta_{\min}(\rho)). \quad (5.4c)$$

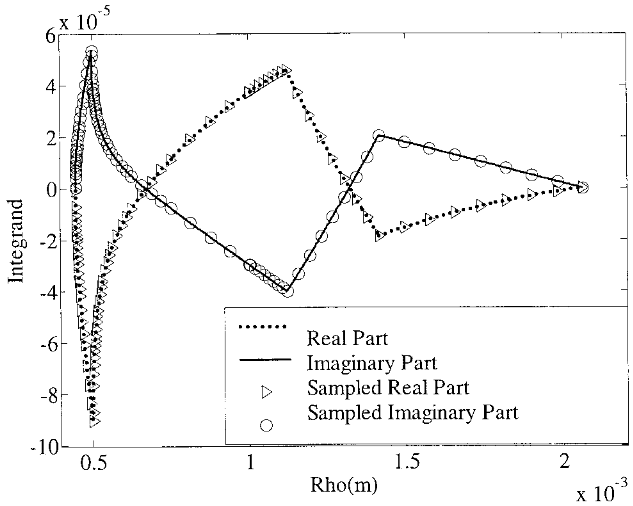

Figure 3 Behavior of $\psi_1(\rho)$ and adaptive sampling for the non-self-term integral, for a triangle with vertices $(\alpha, -\alpha, \alpha)$, $(\alpha, \alpha/2, \alpha)$, $(-2\alpha, \alpha/2, \alpha)$, and observation point located at $(0, 0, 2\alpha)$, where $\alpha = 0.001$ m, at a frequency of 1 KHz, with $\sigma = 5.8 \times 10^7$ S/m. The stopping threshold resulted in a relative integration error of 2.59×10^{-5}

The one-dimensional integrals arising above are evaluated using an adaptive integration technique. In general, the integrands appear as segmented piecewise functions, each of which has a smooth variation in its domain. Within each segment, a recursive adaptive integration is carried out. A binary segment split is performed, and the resultant integration value from a 5th-order Newton–Cotes formula (Bode's rule) [7] over the two sub-segments is compared to the integration value obtained with the same integration rule over the un-split segment. If the relative change in integration value is larger than a prespecified threshold, then the binary split continues recursively. In addition, a global threshold based on the contribution of a sub-segment to the total integral is used as a stopping criterion.

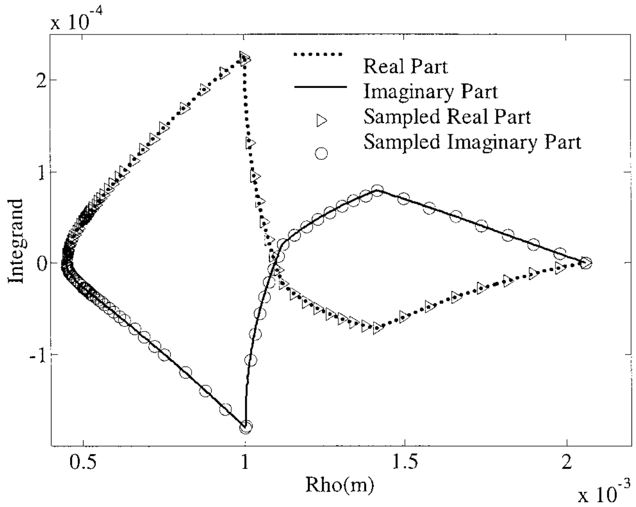

Figure 4 Behavior of $\psi_2(\rho)$ and adaptive sampling for the non-self-term integral, for a triangle with vertices $(\alpha, -\alpha, \alpha)$, $(\alpha, \alpha/2, \alpha)$, $(-2\alpha, \alpha/2, \alpha)$, and observation point located at $(0, 0, 2\alpha)$, where $\alpha = 0.001$ m, at a frequency of 1 KHz, with $\sigma = 5.8 \times 10^7$ S/m. The stopping threshold resulted in a relative integration error of 2.59×10^{-5}

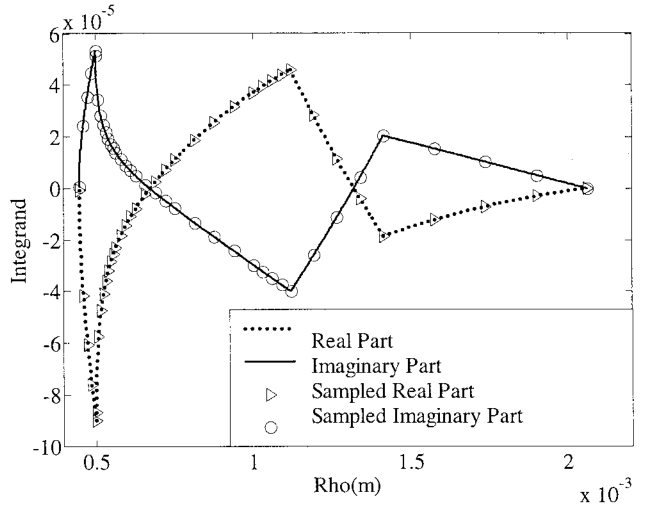

Figure 5 Behavior of $\psi_1(\rho)$ and adaptive sampling for the non-self-term integral, for a triangle with vertices (α, $-\alpha$, α), (α, $\alpha/2$, α), (-2α, $\alpha/2$, α), and observation point located at (0, 0, 2α), where $\alpha = 0.001$ m, at a frequency of 1 KHz, with $\sigma = 5.8 \times 10^7$ S/m. The stopping threshold resulted in a relative integration error of 2.23×10^{-3}

6. NUMERICAL SIMULATION AND VALIDATION

The real and imaginary parts of the two integrands $\psi_1(\rho)$ and $\psi_2(\rho)$ in Eq. (5.4) are shown in Figures 3 and 4 for a non-planar case. Also shown is the sampling based on the adaptive integration, within each segment of the integration, for $O(10^{-5})$ error in integration accuracy. The location of quadrature points can be intuited by the variation and curvature of the integrands, especially for lower accuracy cases; the sampling points are shown in Figures 5 and 6 for the same integrands for a higher error of $O(10^{-3})$ in integration accuracy.

The nature of the vector potential at both low frequencies and very high frequencies lends itself to simpler computation schemes, namely, singularity extraction [6] and Gaussian quadrature (typically 7 point) [7], and surface impedance forms, respectively. As a self-consistency check, the integration scheme constructed in this paper is compared against these standard methods. The results are shown in Figure 7, for a specific self-term case with $\sigma = 5.8 \times 10^7$ S/m. As can be seen, as the frequency increases, the relative error between the proposed integration method and surface impedance approximations drastically fall to very low values. Similarly, the proposed scheme shows very good agreement with standard Gaussian quadrature and singularity extraction at low frequencies. At the same time, the need for the accurate integration scheme is self-evident in the intermediate band of frequencies. The self-term was used in order to be able to compare against surface impedance. A similar comparison for the non-self-term case is shown in Figure 8 versus standard singularity extraction and Gaussian quadrature. In this case, the need for accurate integration is highlighted, since the standard singularity extraction and Gaussian quadrature starts performing poorly as the frequency is increased.

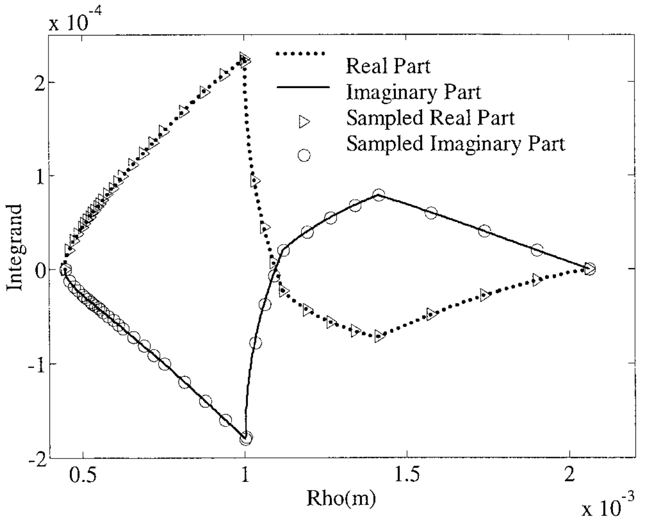

Figure 6 Behavior of $\psi_2(\rho)$ and adaptive sampling for the non-self-term integral, for a triangle with vertices (α, $-\alpha$, α), (α, $\alpha/2$, α), (-2α, $\alpha/2$, α), and observation point located at (0, 0, 2α), where $\alpha = 0.001$ m, at a frequency of 1 KHz, with $\sigma = 5.8 \times 10^7$ S/m. The stopping threshold resulted in a relative integration error of 2.23×10^{-3}

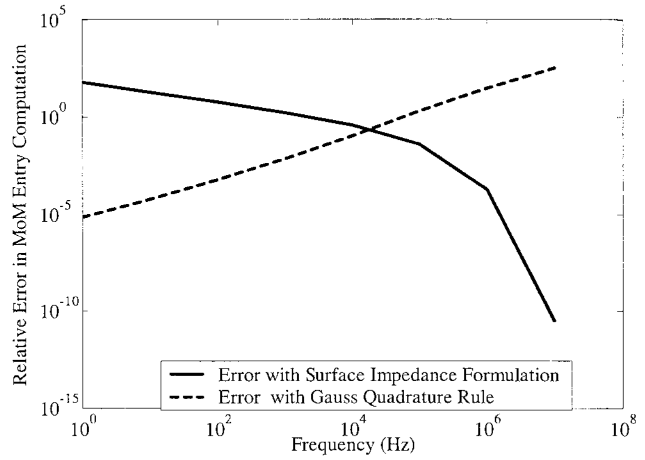

Figure 7 Validation and comparison of the proposed method with singularity extraction and a 7-point Gaussian quadrature rule for low frequencies and surface impedance for high frequencies. The compared value is the self-patch interaction for a triangle with vertices (0.1, −0.1, 0) cm, (0.1, 0.05, 0) cm, (−0.2, 0.05, 0) cm, with $\sigma = 5.8 \times 10^7$ S/m

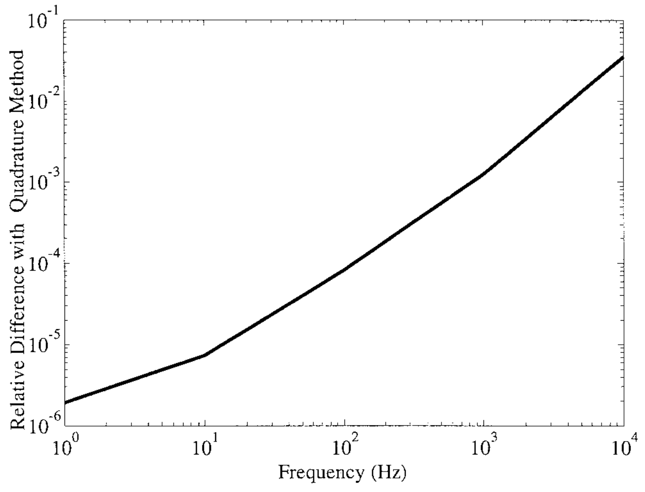

Figure 8 Comparison of the proposed method with singularity extraction and a 7-point Gaussian quadrature rule for a non-self-patch interaction, where the source triangle has vertices (0.1, −0.1, 0) cm, (0.1, 0.05, 0) cm, (−0.2, 0.05, 0) cm, and the observation point is at (0, 0, 0.1) cm, with $\sigma = 5.8 \times 10^7$ S/m

TABLE 1 Validation of the Proposed Method with the Existing Technique in [5] for In-Plane Observation Points

	$\mathbf{G}_{Vect}\cdot\hat{\mathbf{x}}$		$\mathbf{G}_{Vect}\cdot\hat{\mathbf{y}}$		
ρ-cm	Existing Method in [5]	Proposed Method	Existing Method in [5]	Proposed Method	Relative Error
0	$10^{-6} \times 0.126930 - 0.024078i$	$10^{-6} \times 0.126853 - 0.024049i$	$10^{-6} \times -0.000174 + 0.002200i$	$10^{-6} \times -0.000176 + 0.002192i$	6.41×10^{-4}
0.05	$10^{-6} \times -0.434146 + 0.261252i$	$10^{-6} \times -0.4341153 + 0.261176i$	$10^{-6} \times -0.107124 + 0.019400i$	$10^{-6} \times -0.107093 + 0.019376i$	1.73×10^{-4}
0.1	$10^{-6} \times 0.941456 + 0.494869i$	$10^{-6} \times 0.941245 + 0.494778i$	$10^{-6} \times -0.118088 + 0.027149i$	$10^{-6} \times -0.118055 + 0.027132i$	2.17×10^{-4}
0.15	$10^{-6} \times 0.796986 + 0.617191i$	$10^{-6} \times 0.796777 + 0.617102i$	$10^{-6} \times -0.073881 + 0.026486i$	$10^{-6} \times -0.073800 + 0.026438i$	2.42×10^{-4}

The source triangle has vertices (0.1, −0.1, 0) cm, (0.1, 0.05, 0) cm, (−0.2, 0.05, 0) cm, and the observation point is parameterized as (ρ, 0, 0). The frequency is 1 KHz, with $\sigma = 5.8 \times 10^7$ S/m.

Finally, the proposed scheme is compared for accuracy versus an existing method for the special case of in-plane observation. Table 1 shows the relative errors between the new method and the method in [5] for the components of the vector integral, for different source-observer distances. As can be seen, in all cases relative errors smaller than 10^{-3} are obtained.

7. CONCLUSION

A formulation and integration scheme to compute vector potentials in a lossy conducting medium was presented in this paper. This general method compares well in terms of accuracy with existing methods with restricted applicability, is error-controllable, and can be used for vector potential computations at all frequencies in conducting media, for arbitrarily located and oriented source and basis functions. Ongoing work focuses on similar formulation and integration rules for Green's function integrals arising in the modeling of lossy dielectric and lossy magnetic structures, extension of the method to polygonal regions, and a two-region surface integral equation formulation for wideband modeling of inductances and impedances of realistic interconnects and package structures.

ACKNOWLEDGMENTS

This work was supported in part by DARPA-MTO NeoCAD grant N66001-01-1-8920, NSF-CAREER grant ECS-0093102, NSF-SRC Mixed-Signal Initiative grant CCR-0120371, and by a grant from Ansoft Corporation. The authors would like to thank Dr. John Rockway, SSC San Diego, and Dr. J. Eric Bracken, Ansoft Corporation, Pittsburgh, for helpful discussions.

REFERENCES

1. Z. Zhu, J. Huang, B. Song, and J. White, Improving the robustness of a surface integral formulation for wideband impedance extraction of 3D structures, Proc Int Conf Computer Aided Design (2001), 592–597.
2. S.M. Rao, D.R. Wilton, and A.W. Glisson, Electromagnetic scattering by surfaces of arbitrary shape, IEEE Trans Antennas Propagat 30 (1982), 409–418.
3. M. Gimersky, S. Amari, and J. Bornemann, Numerical evaluation of the two-dimensional generalized exponential integral, IEEE Trans Antennas Propagat 44 (1996), 1422–1425.
4. J.K.H. Gamage, Efficient method of moments for compact large planar scatterers in homogeneous medium, Proc 11th Int Conf Antennas Propagat 480 (2001), 741–744.
5. L. Rossi and P.J. Cullen, On the fully numerical evaluation of the linear-shape function times the 3-D Green's function on a planar triangle, IEEE Trans Microwave Theory Techniques 47 (1999), 398–402.
6. R.D. Graglia, On the numerical integration of the linear shape function times the 3-D Green's function or its gradient on a planar triangle, IEEE Trans Antennas Propagat 41 (1993), 1448–1455.
7. M. Abramowitz and I. Stegun, Handbook of Mathematical Functions, Chapter 25, Dover, New York, 1970.

DESIGN OF STEERABLE NON-UNIFORM LINEAR ARRAY GEOMETRY FOR SIDE-LOBE REDUCTION

Ji-Hoon Bae,[1] Kyung-Tae Kim,[2] Joon-Ho Lee,[1] Hyo-Tae Kim,[3] and Jae-Ick Choi[1]
[1] Advanced Radio Department
Radio and Broadcasting Research Laboratory
Electronics and Telecommunication Research Institute
151 Gajeong-dong, Yuseong-gu
Daejeon, 305-350, Korea
[2] Dept. of Electrical Engineering and Computer Science
Yeungnam University
214-1 Dae-dong, Kyongsan
Kyungbuk, 712-749, Korea
[3] Electrical and Computer Engineering Division
Pohang University of Science and Technology
San 31 Hyoja-dong, Nam-gu, Pohang
Kyungbuk, 790-784, Korea

Received 12 August 2002

ABSTRACT: *In this paper, we present a pattern synthesis method of non-uniform linear array antennas for simultaneous reduction of the side-lobe level and pattern distortion during beam steering. To achieve these two requirements, the positions of linear array elements are adjusted using the Gauss–Newton method. It is shown that the proposed method can significantly reduce pattern distortion as well as the side-lobe level, although the beam direction is scanned.* Microwave Opt Technol Lett 36: 363–367, 2003;
DOI 10.1002/mop.10765

Key words: *antenna array pattern synthesis; non-uniform spacing; optimization technique; side-lobe reduction*

1. INTRODUCTION

In the field of antenna array pattern synthesis, the side-lobe level of an array radiation pattern can be reduced by appropriately changing inter-element spacing, namely, by applying a non-uniformly spaced array [1–4]. Of course, the desired low side-lobe level can be achieved by optimizing the amplitudes and phases of excited array elements with uniform spacing. However, this synthesis method degrades total radiation power efficiency due to amplitude tapering, which requires a complicated feed system. Therefore, it is preferable to use a non-uniformly spaced array to improve the side-lobe level, while maintaining total radiation power efficiency. The non-uniform linear array (NULA) can reduce inner side-lobes (nearby side-lobes from the main beam), whereas it may increase outer side-lobe levels [1]. Because of this phenomenon, its radiation pattern with scanning includes undesirable large side-lobes in the visible region, whose levels can be higher than the first side-lobe level. To overcome this problem, an optimization technique is adopted to reduce both the inner side-

PILOT: A FAST ALGORITHM FOR ENHANCED 3D PARASITIC EXTRACTION EFFICIENCY

Dipanjan Gope and **Vikram Jandhyala**
Department of Electrical Engineering, Box-352500 , University of Washington, Seattle, WA-98195, Telephone: 206-543-2186 Fax: 206-543-3842,{dip, *jandhyala}@ee.washington.edu*}

ABSTRACT

Integral equation methodologies applied to extract parasitics at the board, package, and on-chip levels involve solving a dense system of equations. In this paper, we present an improved oct-tree based multilevel QR compression technique for fast iterative solution. The regular tree and interaction structure of the fast multipole method, and the QR compression scheme applied to interaction sub-matrices as in IES^3 *are combined to achieve superior time and memory efficiency. As is demonstrated by numerical simulation results presented herein, the new algorithm is found to be faster than both existing QR based methods and FastCap.*

I. Introduction

Quasi-static parasitic extraction is an important problem in digital circuits and in mixed signal IC analysis. Due to the complexity of on-chip design structures, numerical techniques that utilize field solutions for parasitic extraction are preferred when high accuracy is necessitated. Among the existing approaches, a surface-based integral-equation methodology based on the Method of Moments (MoM) is ideally suited to address the problem. It leads to a well-conditioned system with reduced size compared to volumetric approaches, but the system of equations generated is inherently dense, thereby creating a time and memory bottleneck. Several fast iterative techniques have been developed to efficiently store and solve a MoM system. All these methods (e.g. QR-based methods, fast multipole methods (FMMs), FFT-based techniques etc.) rely on algorithms to accelerate matrix vector products and therefore expedite the iterative solution significantly to linear time and memory complexity.

The multilevel QR-based fast iterative solver (IES^3) [1] is particularly attractive for circuit problems. The approach is based on low-rank decomposition of MoM sub-matrices by Singular Value Decomposition (SVD) or the Modified Gram Schmidt (MGS) method [2]. It is independent of the Green's function kernel, and can be applied directly to multi-layered dielectrics without increasing the size of the problem unlike the other methods. Even in terms of free-space capacitance extraction IES^3 has been demonstrated as being more efficient in terms of memory and solve time. The method however, suffers from a higher setup time cost. For problems with large number of nets, that require solving for many right-hand-sides (RHS's), the higher setup cost is more than offset by faster matrix vector multiplies. However for well-conditioned systems with fewer nets and consequently fewer matrix vector products, the time efficiency of IES^3 could be inferior.

In this paper, we present a Predetermined Interaction List Oct Tree (PILOT) QR algorithm, that greatly reduces the setup time while maintaining the memory and solve time efficiency of the Rank-Map based Binary Tree QR (RMBT-QR), which is based on the same principles as IES^3. The PILOT-QR algorithm exploits the properties of a multilevel oct-tree implementation (common to FMM approaches), to create a predetermined set of interaction lists, thereby reducing the setup time considerably. In short the regular geometry structure of FMM and the compression efficiency of QR are combined together to yield an improved capacitance extraction algorithm. Though not discussed in this paper, the compression scheme is amenable to full-wave multi-layered dielectric kernel solutions and is stable for low frequency analysis without any modifications unlike some full-wave FMM techniques.

II. Integral Equation

Capacitance problems formulated using the MoM are solved via Poisson's Equation $\nabla^2\phi(\mathbf{r}) = -\rho(\mathbf{r})/\varepsilon$ relating potential ϕ and charge-density ρ. The discretization of the integral form of this equation results in a matrix system of the form $\bar{\mathbf{Z}}\mathbf{I} = \mathbf{V}$ where the $N \times N$ MoM matrix $\bar{\mathbf{Z}}$ is a dense Green's function matrix, $\mathbf{I}$ represent the unknown coefficients of known charge density basis functions, and $\mathbf{V}$ is the known potential excitation. Each element of the MoM matrix denotes the interaction between a testing and a basis function and is written as follows:

$$\bar{\mathbf{Z}}(\mathrm{j,i}) = \int_{S_j} ds\, t_j(\mathbf{r}) \int_{S_i} ds' g(\mathbf{r},\mathbf{r}')\, f_i(\mathbf{r}') \qquad (1)$$

where t_j is the testing function defined over S_j, f_i is the basis function defined over S_i and $g(\mathbf{r},\mathbf{r}')$ is the relevant Green's function. In the electrostatic case for P disconnected conductors, each column of the required $P \times P$ capacitance matrix is obtained by enforcing a voltage of 1V on the excited conductor, 0V on all other conductors, solving the above system, and integrating the charge density over each conductor. The $N \times N$ system of equations is therefore solved P times to obtain the capacitance matrix.

III. Existing Multilevel QR algorithm

The IES^3 fast iterative solver, based on the QR method reduces the cost of performing the matrix vector product $\overline{\mathbf{Z}}\mathbf{I}$ to $O(N \log N)$ from quadratic time. It exploits smoothness of the Green's function to decompose the numerically rank-deficient far-field sub-matrices of the MoM using QR decomposition; a sub-matrix $\overline{\mathbf{A}}$ of the MoM matrix $\overline{\mathbf{Z}}$ can be decomposed as $\overline{\mathbf{A}}_{mxn} = \overline{\mathbf{Q}}_{mxr}\overline{\mathbf{R}}_{rxn}$ where $\overline{\mathbf{R}}$ is upper triangular, $\overline{\mathbf{Q}}$ is unitary i.e. $\overline{\mathbf{Q}}^T\overline{\mathbf{Q}} = \overline{\mathbf{I}}$ and $r \ll (m, n)$. At the same time it is possible to construct the compressed representation without forming the entire sub-matrix from sampled rows and columns, thereby reducing the setup time to $O(N \log N)$.

In RMBT-QR, which is based on the same principles as IES^3, the algorithm has 3 main steps:

a) *Geometry subdivisions into cells*: Binary decompositions with density balancing and tight bounds technically known as tight-bound k-d trees [3] are employed, similar to that used in IES^3. As shown in figure 1 each cell is recursively decomposed along the largest side into 2 cells with equal number of entities.

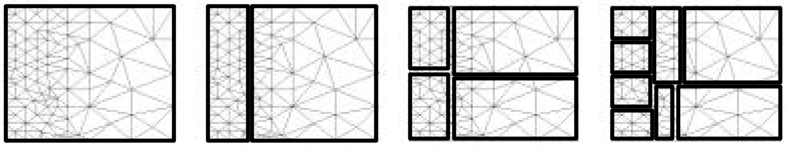

Figure 1: Multilevel tight bound k-d tree decomposition

It is interesting at this point to note that a tight-bound k-d tree may yield cells of any shape and size separated from each other by arbitrary distances depending on the geometry under consideration.

b) *Rank-Map predicted QR formations*: A rank-map is a statically-determined look up table that identifies low-ranked MoM sub-matrices on which QR formation from samples should be attempted. Large and low-ranked sub-matrices are the chief candidates to be identified by the rank-map so as to ensure maximum compression with minimum setup time. Each entry of the table outlines the expected rank of a cell-to-cell interaction, which is a function of various parameters pertaining to the source and observer cells:

$$r_E = f(l_s, b_s, h_s, l_o, b_o, h_o, d, g) \tag{2}$$

where r_E is the expected rank, l, b, h stands for the length, breadth and height of a cell, the subscripts s and o indicate source and observer cells respectively, d is the distance between the centers of the source and observer cells and g denotes the type of Green's function used e.g. free-space Green's function. The construction of this table is an expensive process considering all possible pairs of source and observer cells.

c) *Fine-tuning through splits and merges*: The rank-map only predicts the starting block structure for a MoM matrix. The rank estimation is often inaccurate and may result in underestimation of rank or missing larger low-rank blocks. These problems are addressed by splits and merges respectively [1].

The setup cost of the algorithm is largely controlled by the accuracy of rank map predictions. An accurate and exhaustive rank map would preclude the necessity for merges and unnecessary splits, and the optimum matrix block structure would be achieved without any backtracking or fine-tuning. However, a foolproof rank-map is difficult if not impossible to construct owing to the fact that the algorithm can lead to cells with any shape and size. This leads to a high constant being associated with the setup time cost of the algorithm.

IV. New Multilevel QR Algorithm

The proposed PILOT QR algorithm develops a predetermined multilevel matrix structure for the geometry under consideration, which guarantees maximum compression. The algorithm has 3 main steps:

a) *Oct-tree spatial decomposition in 3D*: Each cube is recursively decomposed by loosely bounded, spatially balanced splits along orthants leading to 8 child cubes in 3D. The cell data structure is in the form of an oct-tree, identical to that in multilevel FMMs [4].

b) *Basic multilevel interaction list*: The basic multilevel interaction list of FMM is used as the starting block in the process of building the optimal multilevel compressed matrix structure. In multilevel FMM every cube c_i has a nearest neighbor list and an interaction list. The nearest neighbor list is defined as: $K_{c_i} = \{c_j \mid c_j$ is in the same level as c_i and has at least 1 common vertex with $c_i\}$ and the interaction list is denoted by: $I_{c_i} = \{c_j \mid P_{c_j} \in K_{P_{c_i}}; c_j \notin K_{c_i}\}$, where P_{c_i} denotes parent of c_i. Direct Green's function computations are used only at the lowest level for interactions between cube c_i and K_{c_i}. Multipole expansions are used to construct $T(c_j, c_i)\ \forall j \mid c_j \in I_{c_i}$, where $T(c_j, c_i)$ denotes the interaction between testing functions of c_j^l and basis functions of c_i^l. Since PILOT does not explicitly require cubical regions but simply deals with interaction matrices, there is scope for further compression by combining cubes in I_{c_i} in an *a priori* manner into a new interaction list called the merged interaction list (MIL).

c) *Merged interaction list*: It is observed that the multilevel FMM interaction lists of siblings share many cubes in common as illustrated in figure 2. (2D version shown here for ease of illustration).

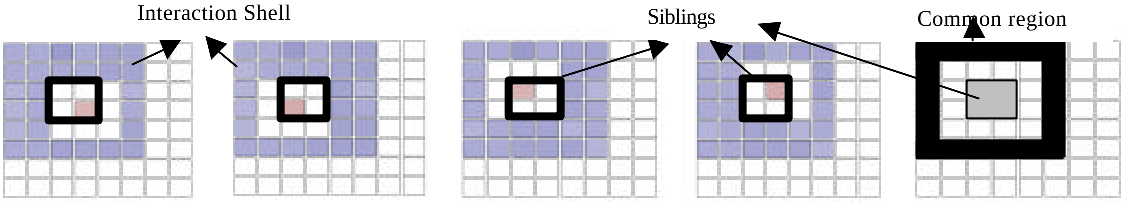

Figure 2: Common interaction shell of siblings in 2D

It is possible to group source and observer cubes of different interaction lists (merged interaction) in order to compress larger low-rank matrices and thereby gain in terms of overall compressibility. It must be noted that the entire common interaction list does not directly translate into a merged interaction because the rank of such an interaction sub-matrix will not be low. The common interaction list is carefully decomposed into disjointed parts such that the overall compression is optimized. Each such disjointed part is an interaction between grouped source cubes and observer cubes and forms an entry of the MIL denoted by m, which can be expressed as a combination of multilevel FMM cube-to-cube interactions: $m_k = \{T_p(c_j, c_i)\}\ \forall p \mid 1 \le p \le n_g$, where n_g is the number of FMM interactions grouped. Higher compression is achieved since a larger matrix is compressed to low rank:

$$\left(m_{m_k} + n_{m_k}\right) r_{m_k} < \sum_{i=1}^{n_g} \left(m_i + n_i\right) r_i \tag{3}$$

where *m*, *n* and *r* denote the number of rows, number of columns and the rank of a sub-matrix. The subscript *i* denotes a regular multilevel FMM interaction list entry that is now a constituent of the MIL. Figure 3 demonstrates the decomposition of the common interaction list of figure 2 into merged interactions.

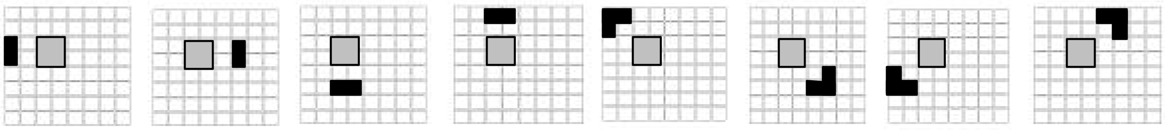

Figure 3: Merged interaction list entries corresponding to the common interaction list

The merged interactions shown in figure 3 are only a subset of all MIL entries. In PILOT there are in total 16 MIL entries in 2D and 40 in 3D. The same MIL pattern is valid for all sibling pairs across levels. The MIL can thus be visualized as an accurate replacement for rank-map used in RMBT-QR and leads to a predetermined matrix block structure. MoM sub-matrices pertaining to interactions of the MIL are compressed by forming QRs from samples. At the lowest level, dense blocks are retained for interactions of the smallest cube with its neighbors.

V. Simulation Results

In this section, simulation results are presented to demonstrate the accuracy and time and memory efficiency of PILOT. For a comparative analysis, results obtained from RMBT-QR, which is based on IES^3 and FastCap, which is an open source code based on FMM are presented side-by-side. A QR decomposition tolerance of 1e-3 is used for both PILOT and RMBT-QR whereas for FastCap the adaptive algorithm with multipole order of 2 is employed. An absolute residual of 1e-3 is used for the Krylov sub-space iterative solution. All tests were run on a processor with 4GB RAM and 1.6GHz CPU speed.

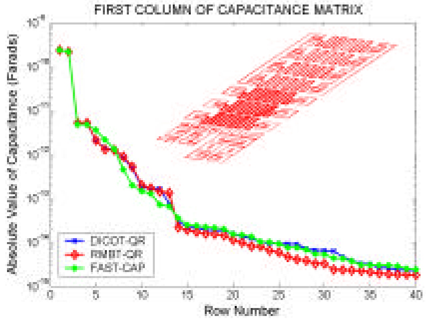

Figure 4: Absolute values of the first column of the capacitance matrix

In the first example the capacitance matrix of the multi-net structure (figure 4) is simulated. The surface of the structure is meshed with 0.113 million patches. The absolute values of the first column of the matrix as obtained from the 3 algorithms are plotted in figure 4, where it can be seen that even very small entries relative to the large ones match very well.

In the next example a 5-by-5 bus structure (figure 5) is considered. Each trace is 1 μm in length and 0.1μm X 0.1 μm in cross section. The distance between the layers of trace is 0.3 μm and the separation between traces on the same layer is 0.1 μm. The number of triangular patches is varied from 1000 to 0.7 million. The memory and time efficiency of PILOT is demonstrated first by comparison to regular direct and iterative solvers as in figure 5a and 5b and then to RMBT-QR and FastCap as in figure 5c and

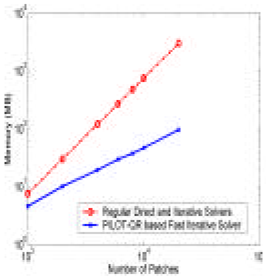

Figure 5a: Memory

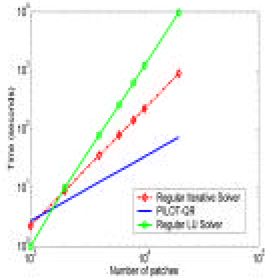

Figure 5b: Time

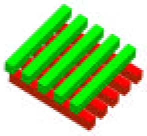

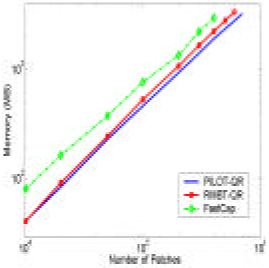

Figure 5c: Memory

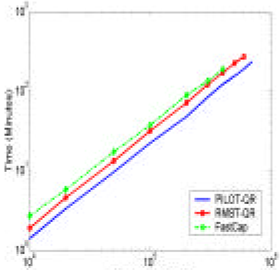

Figure 5d: Time

The next example demonstrates the relative advantage of QR methods as compared to FMM based algorithms for higher number of nets and consequently larger number of matrix vector products. A package structure with 14 leads as illustrated in figure 6a is considered. The surface is meshed with 0.101 million patches and then solved for increasing number of right hand sides (1 to14). The time requirements are plotted in figure 6b. The constant offset between the plots of PILOT and RMBT-QR is due to the superior one-time setup cost. The memory required for the process by PILOT is 441MB, by RMBT-QR is 445MB and FastCap 700MB. The largest problem solved using our method is an on-chip structure discretized with 0.913 million patches, similar to that in figure 4, with 30 times more traces in a 10 x 3 array. The problem took 3.3Gb and 48 minutes to setup and 90 minutes to solve for 3 specific excited nets. Both the other methods required more than the 4 Gb available.

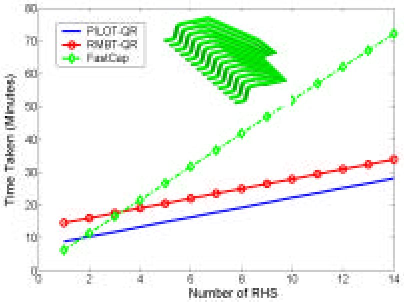

Figure 6) Setup and Solve Time

VI. Conclusions

A new oct-tree based QR technique for fast parasitic extraction, PILOT, was presented. The best features of FMM and IES^3 are exploited and merged, along with the generation of new merged interaction lists in order to yield superior run times and reduced memory consumption in PILOT. In the battle of reducing constants in the era of mature linear complexity algorithms, PILOT can potentially emerge as an optimal paradigm for parasitic extraction. While this paper is related to parasitic extraction, the PILOT paradigm can also be applied to full-wave applications in multi-layered microelectronic environments. *This work was partially supported by US DARPA/MTO NeoCAD program under Grant N66001-01-1-8920 and NSF Career Award grant ECS-0093102.*

References

[1] S.Kapur and D.E.Long, "IES^3: Efficient Electrostatic and Electromagnetic Solution" *IEEE Computer Sci. and Engg.* 5(4) pp. 60-67 Oct.-Dec 1998.
[2] G.H.Golub and C.F.Van Loan Matrix Computations 2nd Ed. The Johns Hopkins Univ. Press Baltimore 1989.
[3] R.J. Anderson,"Tree data-structures for N-body simulation", *SIAM J. Comp*,Vol. 28,No. 6, pp. 1923-1940, 1999.
[4] K. Nabors, S. Kim and J. White, "Fast capacitance extraction of general three-dimensional structures", *IEEE Trans. on Microwave Theory and Techniques*, vol. 40 issue7 pp. 1496-1506, July 1992.

Generalized Kirchoff's Current and Voltage Law Formulation for Coupled Circuit–Electromagnetic Simulation With Surface Integral Equations

Yong Wang, Dipanjan Gope, *Student Member, IEEE*, Vikram Jandhyala, *Senior Member, IEEE*, and
C.-J. Richard Shi, *Senior Member, IEEE*

***Abstract*—In this paper, a new formulation for coupled circuit–electromagnetic (EM) simulation is presented. The formulation employs full-wave integral equations to model the EM behavior of two- or three-dimensional structures while using modified nodal analysis to model circuit interactions. A coupling scheme based on charge and current continuity and potential matching, realized as a generalization of Kirchoff's voltage and current laws, ensures that the EM and circuit interactions can be formulated as a seamless system. While rigorous port models for EM structures can be obtained using the approach discussed herein, it is shown that the coupling paradigm can reveal additional details of the EM–circuit interactions and can provide a path to analysis-based design iteration.**

***Index Terms*—Coupled circuit–electromagnetic (EM) simulation, method of moments (MoM), signal integrity, surface integral equation.**

I. INTRODUCTION

WITH THE rapidly increasing interest in applications such as RF wireless communication and high-speed data processing, electronic systems are required to work at progressively higher frequencies [1]. As the operating frequencies enter gigahertz range, phenomena such as crosstalk, power and ground-plane voltage bounce, substrate losses, etc. can no longer be neglected. In order to design high-performance systems with fast time to market, it is essential to be able to analyze whole or part of the system at one fundamentally deeper level of physics: distributed electromagnetic (EM) field analysis needs to be rigorously and seamlessly included as an addition to traditional circuit simulation.

In the existing literature, several methods have been developed to model and simulate coupled circuit–EM problems. Those based on finite difference time domain (FDTD) [2]–[4] are effective for time-domain analysis. For broad-band simulation, the FDTD can be used to obtain frequency-domain results via a Fourier transform. However, it is not a direct frequency-domain method, and it also requires dispersive/frequency-dependent parameters to be represented in the time domain in order to model losses and frequency-dependent behavior, accomplished through recursive convolutions and similar methods. Furthermore, FDTD requires the discretization of the three-dimensional (3-D) space where the object under study resides, which can lead to substantially more system unknowns than in surface-based methods [5]. The finite-element method (FEM) has been applied to both time- and frequency-domain coupled circuit–EM simulation using schemes including port models [6] via paralleling each coupling circuit element to an FEM edge [7] or through a fully coupled approach [8], as has been the transmission-line method [9]. Analytical approaches [10] and simpler transmission lines are usually much faster than the numerical-based methods and can be easily coupled to circuit simulation. However, they are not general enough for analyzing irregular structures.

In recent years, methods based on integral equations have gained importance. Among them, the partial-element equivalent-circuit (PEEC) approach [11] has been widely used to study coupled circuit–EM problems. Very recently, nonorthogonal and generalized PEEC methods have been developed [12], [13]. By representing all the interactions using equivalent SPICE-compatible resistor–inductor–capacitor (RLC) elements and controlled sources, PEEC can solve the coupled circuit–EM problem using a traditional SPICE-like circuit simulator. However, due to the dense nature of the interactions and the fact that SPICE is tuned for solving sparse matrices, direct PEEC is limited to problems with a relatively small number of unknowns [14], although recently, fast methods in conjunction with PEEC are being developed [15], [16]. The PEEC method itself was inspired by EM integral equations. These equations, solved by the method of moments (MoM) [17] with appropriate basis functions, can be used for distributed effects simulation of arbitrarily shaped structures.

When nontrivial lumped circuits are simultaneously present, previous work can only solve the coupled problem based on port models through several steps: port parameters are calculated using an EM simulator first, curve-fitting or model order-reduction techniques are then used to generate an equivalent-circuit model, followed by circuit simulation to estimate complete electrical performance of the system. The port-model-based approach has several limitations: first, for complex multiport structures with frequency-dependent material properties, deriving the equivalent passive network within a

Manuscript received July 28, 2003; revised February 3, 2004. This work was supported in part by the Defense Advanced Research Projects Agency–Micro Technology Office under NeoCAD Grant N66001-01-1-8920, by the National Science Foundation (NSF) under CAREER Grant ECS-0093102, by the NSF–Semiconductor Research Cooperation under Mixed-Signal Initiative Grant CCR-0120371, and by the Ansoft Corporation under a grant.

The authors are with the Electrical Engineering Department, University of Washington, Seattle, WA 98195-2500 USA (e-mail: yongw@ee.washington.edu; dips@u.washington.edu; jandhyala@ee.washington.edu; shi@ee.washington.edu).

Digital Object Identifier 10.1109/TMTT.2004.830482

given accuracy is still an area of current research [18]. Second, after the EM structure is converted to a port model, information about the details of the EM-field distribution in the structure will be lost, such information could otherwise provide useful insights into the problem under study and be useful in design iterations. Third, the port-model approach, when used with a fast iterative solver, needs to solve the EM system repeatedly, i.e., for each port, which could be very expensive when both the number of ports and number of unknowns are large.

This paper presents a new and complementary approach to the formulation and solution of the coupled circuit–EM problem. EM conducting structures and lumped-element circuits are formulated jointly using one system matrix in a form amenable to existing fast iterative numerical solvers such as those based on the fast multipole method [19], fast Fourier transform (FFT) method [20], and low-rank decomposition [21], as well as emerging fast direct solvers [22]. Solving the EM and circuit simultaneously not only permits more detailed field information, but also obviates the necessity of generating port models and, thus, automates the design flow. The proposed method, originally presented by the authors as an idea at a recent conference [23], is detailed and advanced herein, and applied to several microelectronic problems. The technique is inherently hierarchical and provides seamless transitions between circuit and EM depending on the level of details required.

The EM formulation used in this paper is a full-wave MoM approach using surface triangular tessellations. Since Rao–Wilton–Glisson (RWG) basis functions [24] associated with triangular meshes do not make assumptions about current flow directions as the classical volumetric PEEC does, the adopted approach is suitable to model arbitrarily shaped structures often found in microwave and RF applications. The presented formulation employs a surface impedance approximation that is valid at high frequencies for thin and thick conductors. Although not presented here, for a complete broad-band solution, frequency-dependent effects can be modeled via employing lossy media's Green's functions in a two-region formulation without frequency-dependent meshing [25].

For the circuit subsystem, the standard modified nodal analysis (MNA) matrix is formulated. Kirchoff's current law (KCL) is enforced for each circuit node and Kirchoff's voltage law (KVL) is applied to branches containing voltage sources. Areas of EM structures where the circuit connections are made are defined as *contact* regions. Associated with each *contact* are coupling currents that are introduced as additional system unknowns. The coupling scheme is based on charge and current continuity equations and potential matching with the assumption that circuit voltage is equal to the EM scalar potential at a *contact* region.

The remainder of this paper is organized as following. Section II introduces the formulation of surface-based electric field integral equations (EFIEs) for EM structures, and MNA equations for lumped-element circuits. Implementation of the coupled method using RWG basis functions is presented in Section III. Section IV discusses port-model derivation and comparison between the port-model and coupled approaches. Numerical examples for a low-noise amplifier (LNA), power/ground-plane bounce modeling are given in Section V. Section VI discusses conclusions.

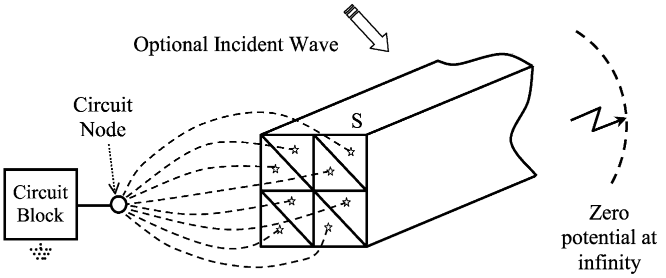

Fig. 1. Arbitrary lumped circuit connected through a contact to a 3-D geometric object.

II. COUPLED CIRCUIT–EM FORMULATION

This section presents a generalized KCL–KVL formulation for simulation of coupled circuit–EM problems. A typical high-speed microelectronic system layout consists of both lumped circuits and sections requiring distributed EM simulation. For modeling purposes, the circuit section is abstracted by a topology-based domain, wherein signals propagate along idealized conduction paths between lumped-circuit elements, while the EM section is represented by a geometry-based domain, wherein signals propagate in 3-D space and materials. The two domains couple to each other through contact interfaces where a circuit node is associated with an EM contact surface. As will be shown in this paper, this interface can be rigorously defined using a generalized version of Kirchoff's voltage and current laws.

Consider Fig. 1, which shows a 3-D geometric object connected through a *contact* to lumped circuits and, optionally, illuminated by incident fields.

The boundary condition for the electric field on the surface S of the object is

$$(\mathbf{E}^s(\mathbf{J}) + \mathbf{E}^i)_{\tan} = Z_s\mathbf{J} \tag{1}$$

where $\mathbf{E}^s$ is the scattered electric field produced by the induced equivalent-surface current $\mathbf{J}, \mathbf{E}^i$ is the incident electric field, subscript $_{\tan}$ denotes the tangential components on S, Z_s represents the surface impedance, and its value is

$$Z_s = \sqrt{j\omega\mu/\sigma} \tag{2}$$

where ω is angular frequency, and μ and σ are the permittivity and conductivity of the material, respectively. Note that surface impedance is a valid approximation to the behavior of fields internal to conductors only for frequencies where the skin depth is smaller than the dimension of the cross section of conductors. At lower frequencies, if a surface integral formulation is used, more accurate modeling of the lossy media Green's function within the conductor is required, as discussed in [26]. In terms of potentials, the electric field can be written as

$$\mathbf{E}^s(\mathbf{J}) = -j\omega\mathbf{A} - \nabla\Phi \tag{3}$$

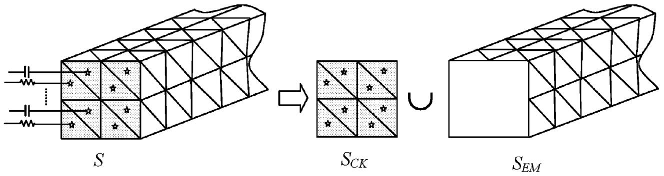

Fig. 2. Concept of surface contact.

where the vector potential $\mathbf{A}$ is defined as

$$\mathbf{A}(\mathbf{r}) = \frac{\mu}{4\pi}\int_S \frac{e^{-jk|\mathbf{r}-\mathbf{r}'|}\mathbf{J}(\mathbf{r}')}{|\mathbf{r}-\mathbf{r}'|}\,ds' \tag{4}$$

the scalar potential Φ is defined as

$$\Phi(\mathbf{r}) = \frac{1}{4\pi\varepsilon}\int_S \frac{e^{-jk|\mathbf{r}-\mathbf{r}'|}\rho(\mathbf{r}')}{|\mathbf{r}-\mathbf{r}'|}\,ds' \tag{5}$$

where $\mathbf{r}$ and $\mathbf{r}'$ are observation and source locations, respectively, $\mathbf{J}$ and ρ represent the equivalent surface current density and surface charge density, respectively, and μ, ε, k are the permeability, permittivity, and wavenumber, respectively, of the homogeneous medium enclosing the object.

The concept of a *contact* is introduced in Fig. 2, where surface S is divided into two subsurfaces, denoted by S_{CK} and S_{EM} such that

$$S_{\mathrm{EM}} \cup S_{\mathrm{CK}} = S \tag{6a}$$

and

$$S_{\mathrm{EM}} \cap S_{\mathrm{CK}} = \phi. \tag{6b}$$

On S_{EM}, the standard continuity equation relating the surface current density $\mathbf{J}$ and surface charge density ρ holds as follows:

$$\nabla_s \cdot \mathbf{J}(\mathbf{r}) + j\omega\rho(\mathbf{r}) = 0 \qquad \forall \mathbf{r} \in S_{\mathrm{EM}} \tag{7a}$$

or

$$\rho(\mathbf{r}) = -\nabla_s \cdot \mathbf{J}(\mathbf{r})/(j\omega) \qquad \forall \mathbf{r} \in S_{\mathrm{EM}} \tag{7b}$$

where ∇_s represents the surface divergence.

On S_{CK}, the continuity equation is altered due to the existence of injected circuit currents. This current introduces an additional source term in the continuity equation and, thus, affects the distribution of both surface currents and surface charges. Let S_{CK} be comprised of M disjoint surfaces $S_{\mathrm{CK}}^m, m = 1, \ldots, M$, each such unique subsurface S_{CK}^m is termed one of M *contacts*. On S_{CK}^m, the modified continuity equation has the following form:

$$\nabla_s \cdot \mathbf{J}(\mathbf{r}) + j\omega\rho(\mathbf{r}) = J_c^m(\mathbf{r}) \qquad \forall \mathbf{r} \in S_{\mathrm{CK}}^m \tag{8a}$$

or

$$\rho(\mathbf{r}) = \left(J_c^m(\mathbf{r}) - \nabla_s \cdot \mathbf{J}(\mathbf{r})\right)\Big/(j\omega), \qquad \forall \mathbf{r} \in S_{\mathrm{CK}}^m; \quad m = 1, \ldots, M \tag{8b}$$

where J_c^m represents the scalar volumetric current density produced on S_{CK}^m via a circuit interconnection, and ρ represents total surface charge density on S_{CK}.

Substitute (6a)–(8b) into (3)–(5), we have

$$\begin{aligned}\mathbf{E}^s(\mathbf{J}) = &-\frac{j\omega\mu}{4\pi}\int_S \frac{e^{-jk|\mathbf{r}-\mathbf{r}'|}\mathbf{J}(\mathbf{r}')}{|\mathbf{r}-\mathbf{r}'|}\,ds' \\ &-\nabla\frac{1}{4\pi\varepsilon j\omega}\int_S \frac{e^{-jk|\mathbf{r}-\mathbf{r}'|}\nabla'\cdot\mathbf{J}(\mathbf{r}')}{|\mathbf{r}-\mathbf{r}'|}\,ds' \\ &-\nabla\frac{1}{4\pi\varepsilon}\sum_{m=1}^{M}\int_{S_{\mathrm{CK}}^m} \frac{e^{-jk|\mathbf{r}-\mathbf{r}'|}J_c^m(\mathbf{r}')}{j\omega|\mathbf{r}-\mathbf{r}'|}\,ds'.\end{aligned} \tag{9}$$

The last two terms represent the contribution to the field produced by the gradient of the scalar potential, which, in turn, is produced by the equivalent surface charge density. The charge density itself is produced by $-\nabla_s \cdot \mathbf{J}/(j\omega)$ over S_{EM}, and by $(J_c^m - \nabla_s \cdot \mathbf{J})/(j\omega)$ over S_{CK}^m. Therefore, the current density introduced by the circuit interconnection produces an additional source or sink of charge that alters the scalar potential and the resulting electric field.

The current density J_c^m is a system unknown that is determined by the solution of the coupled circuit–EM system. An additional system equation can also be constructed, which is based on a generalized KVL that equates the scalar potential produced on electrically small contacts S_{CK}^m to the voltage of the circuit node associated with the interconnection at S_{CK}^m as follows:

$$\begin{aligned}Vn = \frac{-1}{4\pi\varepsilon j\omega}\Bigg(&\int_S \frac{e^{-jk|\mathbf{r}-\mathbf{r}'|}\nabla'\cdot\mathbf{J}(\mathbf{r}')}{|\mathbf{r}-\mathbf{r}'|}\,ds' \\ &-\sum_{m=1}^{M}\int_{S_{\mathrm{CK}}^m} \frac{e^{-jk|\mathbf{r}-\mathbf{r}'|}J_c^m(\mathbf{r}')}{j\omega|\mathbf{r}-\mathbf{r}'|}\,ds'\Bigg), \\ &\forall \mathbf{r} \in S_{\mathrm{CK}}^n; \quad n = 1, \ldots, M\end{aligned} \tag{10}$$

where Vn corresponds to the node voltage associated with a circuit node connected to *contact*.

The *contact*, as defined above, is inherently an electrically small surface, i.e., its dimensions are small compared to the wavelength of signals in a microelectronic system. Larger *contacts* can be defined by associating several circuit nodes with neighboring contact regions, thereby not enforcing erroneous constant potential over electrically large regions.

As can be seen from (10), the calculation of the scalar potential at the *contacts* assumes the potential at infinity is zero. Although the ground node can be chosen randomly in a pure circuit problem, in a coupled circuit–EM formulation, specifying a circuit node to be a ground node indicates this node has the same potential as the EM scalar potential at infinite distance. In the coupled formulation, there is no requirement to define a circuit ground and, in fact, every node has an associated KCL (which is not possible in a pure circuit problem since one of them will be redundant). Thus, there is one unambiguous ground (infinity) definition in the entire problem.

The final self-consistency condition, in addition to scalar potential matching, is a generalized KCL, which ensures that the coupling current will contribute one additional term I_c^n to the

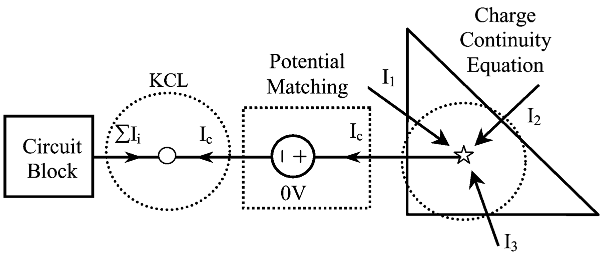

Fig. 3. Connection scheme for EM and circuit interface.

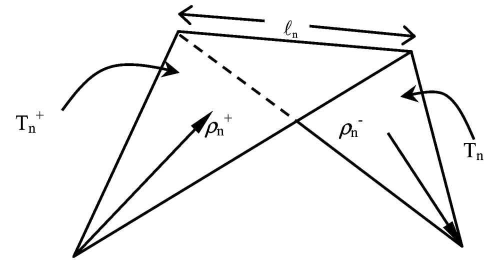

Fig. 4. Definition of RWG basis function.

KCL-based circuit equation associated with circuit node n as follows:

$$\sum_{i=1}^{B} Ii + I_c^n = 0 \tag{11}$$

where Ii is the current of the ith branch, and B is the total number of circuit branches connected to circuit node n. Fig. 3 shows the connection scheme for the EM–circuit interface.

We notice that whereas other approaches such as delta gap methods or wire basis functions [27] can be used to describe the coupling between the circuit and EM, they often need artificial parameters such as basis-function lengths, directions, and radii that are not consistent with topology-only circuit sections.

III. INTEGRAL EQUATION WITH RWG BASIS FUNCTIONS

The self-consistent coupled circuit–EM equations described in Section II are valid for arbitrary basis functions for modeling surface currents using surface integral formulations. Here, the method is expressed in more detail for the popular edge-based RWG spatial basis functions [24] that rely on a triangular tessellation of the surface S. An RWG function $\mathbf{f}_n(\mathbf{r})$, defined over two triangles with a common edge n, used to approximate the spatial distribution of current density has the well-known form

$$\mathbf{f}_n(\mathbf{r}) = \begin{cases} \dfrac{l_n}{2A_{n+}}\boldsymbol{\rho}_{n+}, & \mathbf{r} \in T_{n+} \\ \dfrac{l_n}{2A_{n-}}\boldsymbol{\rho}_{n-}, & \mathbf{r} \in T_{n-} \end{cases} \tag{12}$$

where l_n is the length of the nth edge, $A_{n\pm}$ is the area of triangle $T_{n\pm}$, and $\boldsymbol{\rho}_{n\pm}$ is the vector pointing to or from location $\mathbf{r}$ in triangle $T_{n\pm}$ with respect to the node opposite the edge. Fig. 4 illustrates the definition of RWG basis functions.

As a consequence of the above form, the charge density in each pair of triangles is modeled as a piecewise constant as follows:

$$\nabla \cdot \mathbf{f}_n(\mathbf{r}) = \begin{cases} \dfrac{l_n}{A_{n+}}, & \mathbf{r} \in T_{n+} \\ -\dfrac{l_n}{A_{n-}}, & \mathbf{r} \in T_{n-}. \end{cases} \tag{13}$$

The surface current density is expanded using RWG functions as

$$\mathbf{J}(\mathbf{r}) \cong \sum_{i=1}^{N_e} I_i \mathbf{f}_i(\mathbf{r}) \tag{14}$$

where I_i represents the coefficient of the ith RWG basis function, and N_e is the total number of nonboundary edges. For consistency with RWG basis functions, the charge associated with the coupling current is modeled using piecewise constant functions h (that have a value of unity on a given triangle and zero elsewhere) over each contact triangle

$$J_{c,n}^m(\mathbf{r}) \cong \sum_{m=1}^{M} \sum_{n=1}^{N_{p,\mathrm{CK}}^m} J_n^m h_n^m(\mathbf{r}). \tag{15}$$

Equation (9) is then expressed as

$$\begin{aligned} \mathbf{E}^s(\mathbf{r}) = &-j\omega\frac{\mu}{4\pi}\sum_{i=1}^{N_e} I_i \int\limits_{T_{i+}\cup T_{i-}} \frac{e^{-jk|\mathbf{r}-\mathbf{r}'|}\mathbf{f}_i(\mathbf{r}')}{|\mathbf{r}-\mathbf{r}'|}\,ds' \\ &+ \nabla\frac{1}{4\pi\varepsilon}\sum_{i=1}^{N_e} I_i \int\limits_{T_{i+}\cup T_{i-}} \frac{e^{-jk|\mathbf{r}-\mathbf{r}'|}\nabla_s\cdot\mathbf{f}_i(\mathbf{r}')}{j\omega|\mathbf{r}-\mathbf{r}'|}\,ds' \\ &- \nabla\frac{1}{4\pi\varepsilon}\sum_{m=1}^{M}\sum_{n=1}^{N_{p,\mathrm{CK}}^m} J_n^m \int\limits_{T_{n,\mathrm{CK}}^m} \frac{e^{-jk|\mathbf{r}-\mathbf{r}'|}h_n^m(\mathbf{r}')}{j\omega|\mathbf{r}-\mathbf{r}'|}\,ds' \end{aligned} \tag{16}$$

where N_e is the total number of nonboundary edges, $N_{p,\mathrm{CK}}^m$ is total number of triangles on *contact* m, and $T_{n,\mathrm{CK}}^m$ denotes the nth triangle on *contact* m that is used for circuit connection. Also, T_{i+} and T_{i-} are the positive and negative triangles associated with the ith RWG function. To solve for the unknown coefficients, the expression in (16) is substituted into (1) and tested with the RWG functions to yield

$$\begin{aligned} &j\omega\langle \mathbf{f}_n, \mathbf{A}(\mathbf{r})\rangle_{\tan} + \langle \mathbf{f}_n, \nabla\Phi(\mathbf{r})\rangle_{\tan} \\ &\quad = -\langle \mathbf{f}_n, Z_s\mathbf{J}\rangle_{\tan} + \langle \mathbf{f}_n, \mathbf{E}^i\rangle_{\tan}, \qquad n = 1, \ldots, N_e \end{aligned} \tag{17}$$

where $\langle\cdot,\cdot\rangle$ denotes a spatial dot product, and testing of the vector potential yields

$$\langle \mathbf{f}_n, \mathbf{A}(\mathbf{r})\rangle = \frac{\mu}{4\pi}\sum_{i=1}^{N_e} I_i \left\langle \mathbf{f}_n, \int\limits_{T_{i+}\cup T_{i-}} \frac{e^{-jk|\mathbf{r}-\mathbf{r}'|}\mathbf{f}_i(\mathbf{r}')}{|\mathbf{r}-\mathbf{r}'|}\,ds' \right\rangle. \tag{18}$$

The testing of the scalar potential is the result of the sum of two potential contributions, Φ_s from the EM surface current

$$\langle \mathbf{f}_n, \nabla\Phi_s(r)\rangle = \frac{-1}{4\pi\varepsilon}\sum_{i=1}^{N_e} I_i \times \left\langle \nabla\cdot\mathbf{f}_n, \int_{T_{i+}\cup T_{i-}} \frac{e^{-jk|\mathbf{r}-\mathbf{r}'|}\nabla_s\cdot\mathbf{f}_i(\mathbf{r}')}{j\omega|\mathbf{r}-\mathbf{r}'|}\right\rangle \tag{19}$$

and Φ_c from the coupling current

$$\langle \mathbf{f}_n, \nabla\Phi_c(r)\rangle = \frac{1}{4\pi\varepsilon}\sum_{m=1}^{M}\sum_{i=1}^{N_{p,\mathrm{CK}}^m} J_i^m \times \left\langle \nabla\cdot\mathbf{f}_n, \int_{T_{i,\mathrm{CK}}^m} \frac{e^{-jk|\mathbf{r}-\mathbf{r}'|}h_i^m(\mathbf{r}')}{j\omega|\mathbf{r}-\mathbf{r}'|}\right\rangle. \tag{20}$$

The surface impedance contribution is local and has nonzero values only for those combinations of basis and testing functions that share at least one triangle. Therefore, the contribution is a sparse matrix where each column has, at most, five nonzero entries as follows:

$$\langle \mathbf{f}_n, Z_s\mathbf{J}\rangle = Z_s\sum_{i=1}^{N_e} I_i\langle \mathbf{f}_n, \mathbf{f}_i\rangle, \qquad n, i \text{ share a common triangle.} \tag{21}$$

Finally, any incident electric field is tested as in the term $\langle \mathbf{f}_n, \mathbf{E}^i\rangle$.

The next set of equations is obtained by enforcing

$$V_n = \frac{-1}{4\pi\varepsilon j\omega} \times \left(\sum_{i=1}^{N_e} I_i \left\langle h_n^m, \int_{T_{i+}\cup T_{i-}} \frac{e^{-jk|\mathbf{r}-\mathbf{r}'|}\nabla_s\cdot\mathbf{f}_i(\mathbf{r}')}{|\mathbf{r}-\mathbf{r}'|}ds'\right\rangle + \sum_{m=1}^{M}\sum_{k=1}^{N_{p,\mathrm{CK}}^m} J_n^m \int_{S_{\mathrm{CK}}^m} \frac{e^{-jk|\mathbf{r}-\mathbf{r}'|}h_n^m(\mathbf{r}')}{|\mathbf{r}-\mathbf{r}'|}ds'\right)$$
$$\forall \mathbf{r}\in S_{\mathrm{CK}}^n; \quad n = 1,\ldots,M \tag{22}$$

and by enforcing (15). Substituting (19)–(22) in (18) leads to the matrix format of the coupled circuit–EM system

$$\begin{bmatrix} \mathbf{Z}_{11} & \mathbf{Z}_{12} & \mathbf{0} \\ \mathbf{Z_{21}} & \mathbf{Z_{22}} & \mathbf{C} \\ \mathbf{0} & \mathbf{C^T} & \mathbf{MNA}\end{bmatrix}\begin{bmatrix}\mathbf{i} \\ \mathbf{j_c} \\ \mathbf{ckt}\end{bmatrix} = \begin{bmatrix}\mathbf{v_{em}} \\ \mathbf{0} \\ \mathbf{v_{ckt}}\end{bmatrix} \tag{23}$$

where $\mathbf{Z_{11}}$ is the regular MoM matrix whose elements can be interpreted as equivalent partial impedances if a comparison with a surface-based PEEC is desired. The partial inductances, capacitances, and resistances are equivalent to the terms in (19)–(21). The remaining three dense EM matrices define the *contact*. Matrix $\mathbf{Z_{12}}$ represents the scalar potential contribution due to the coupling current at S_{EM}, and matrix $\mathbf{Z_{21}}$ denotes the potential contribution from the EM surface current at S_{CK}. Finally, matrix $\mathbf{Z_{22}}$ represents the scalar potential contribution to S_{CK} due to coupling currents. This two-by-two system is a self-consistent definition of the EM interactions with a circuit section. To complete the coupled formulation, a sparse rectangular matrix $\mathbf{C}$ is introduced as connection matrix to enforce generalized KCL and KVL. This matrix has one nonzero element per row to select the potential of the circuit node associated with a *contact* triangle. The transpose matrix $\mathbf{C}^{\mathrm{T}}$ selects the coupling current and adds it to the KCL equation of the circuit node at the *contact*. The **MNA** matrix represents circuit interactions for linear RLC elements and the linearized small-signal models of nonlinear elements such as diodes and transistors. The system unknowns $\mathbf{i}, \mathbf{j_c}$, and **ckt** relate to surface equivalent currents, coupling currents, and circuit voltages/currents, respectively. The right-hand-side excitation vector consists of the tested incident EM field $\mathbf{v_{em}}$, the strengths of independent voltage, and current sources $\mathbf{v_{ckt}}$ [28].

IV. PORT MODEL VERSUS COUPLED SOLUTION

The port model is a widely used approach for circuit designers to include EM effects. Here, we first show how the coupled solver can be used to generate port models, and then we give a comparison between the port-model and coupled approach to show that coupled solver has advantages in terms of simulation cost and automation.

In addition to being used as a fully coupled solver, the formulation discussed in Section III can also be used in a manner similar to port-model approaches. Equations (15) and (22) permit sufficient flexibility in solution in order to aid iterations in circuit design. When structures to be analyzed with EM analysis remain unchanged and circuit parameters and topologies vary during design iterations, an *EM contact model* is generated. By combining the first two equations and unknowns, (23) can be rewritten as

$$\begin{pmatrix}\mathbf{EM} & \mathbf{C}' \\ \mathbf{C}'^{\mathrm{T}} & \mathbf{MNA}\end{pmatrix}\begin{pmatrix}\mathbf{i}' \\ \mathbf{ckt}\end{pmatrix} = \begin{pmatrix}\mathbf{v_{em'}} \\ \mathbf{v_{ckt}}\end{pmatrix} \tag{24}$$

where **EM** contains $\mathbf{Z_{11}}, \mathbf{Z_{12}}, \mathbf{Z_{21}}$, and $\mathbf{Z_{22}}$ in (23), $\mathbf{C}', \mathbf{i}'$, and $\mathbf{v_{em'}}$ are extensions of their corresponding entry in (23). In (24), the EM surface current and coupling current unknowns $\mathbf{i}'$ can be eliminated from the first set of equations and the rest of the system can be written in the Schur complement form

$$\left(\mathbf{MNA} - \mathbf{C'^T}\mathbf{EM^{-1}}\mathbf{C}'\right)\mathbf{ckt} = \mathbf{v_{ckt}} - \mathbf{C'^T}\mathbf{EM^{-1}}\mathbf{v_{em'}}. \tag{25}$$

Therefore, the formal inversion of the matrix **EM** only needs to be done once as long as the EM structures do not change. For large-sized EM problems, the equivalent of the inversion is obtained by iteratively solving the EM system with each of the contacts excited independently. The *EM contact model* can, therefore, be obtained through exciting each contact and using an iterative solver, or through the formal inversion shown in (25).

The *EM contact model* ultimately permits the EM structure to be represented in an MNA-compatible element-stamping

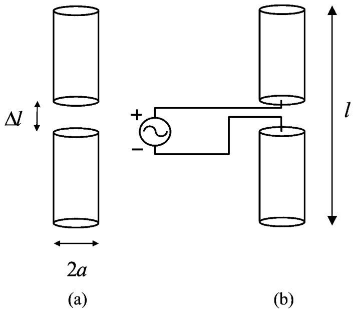

Fig. 5. Illustration of a short-wire antenna of length l and radius a ($l/2a = 74.2$). (a) Classic MoM solution. (b) Coupled circuit–EM solution.

format $\mathbf{C}'^{\mathbf{T}}\mathbf{E}\mathbf{M}^{-1}\mathbf{C}'$ and the incident EM wave in the equivalent-circuit excitation format $\mathbf{C}'^{\mathbf{T}}\mathbf{E}\mathbf{M}^{-1}\mathbf{v}_{\mathbf{em}'}$. The advantage of the above nodal contact model compared to the traditional port model is that it eliminates the intermediate step of constructing an equivalent circuit with its associated cost, accuracy limitations, and complexity in terms of ensuring passivity.

The advantages of coupled formulation over port-model methods lie in several areas. First, computation cost for port-model extraction, assuming a standard or fast iterative solver, increases linearly with the number of ports. Consider an N-port EM structure as an example, column i of its Y-parameter matrix needs to be calculated with port i connected to 1 V, while the rest of ports are grounded. Thus, an N-port structure will necessitate solving the system for N times. Since the coupled solver only needs to solve the system equations (23) once, the port-model approach will be computationally more expensive than the coupled method. Second, the coupled solver can reveal the distributed field information more easily. Distributed field information is important for layout-based circuit design. In the coupled formulation, since surface currents are formulated as system unknowns, field distribution will be just a simple post-processing after the system is solved. In the port-model approach, to derive distributed field information, one has to either solve the problem again with the derived port voltage and current or use complex bookkeeping and superposition to recalculate the field distribution. Coupled formulation also automates the process to consider EM effects during circuit design.

V. NUMERICAL RESULTS

A fully coupled circuit–EM simulator has been developed based on the above-described approach. The first example is a validation test against the classical MoM. As shown in Fig. 5, the input admittance of a center-fed antenna is simulated [17].

In Fig. 5, the short-wire antenna under consideration is of length l and radius a such that the ratio of the length and diameter is 74.2 and $\Delta l \ll l$. The input admittance is first simulated using our in-house MoM solver, employing a delta-gap excitation at its center, as shown in Fig. 5(a). The antenna is then excited at its center by a circuit voltage source and our coupled solver is used to solve for the input impedance, as shown in Fig. 5(b). The simulation results from both methods are illustrated in Fig. 6, which demonstrates a good match. These also match very well with the published results in [17].

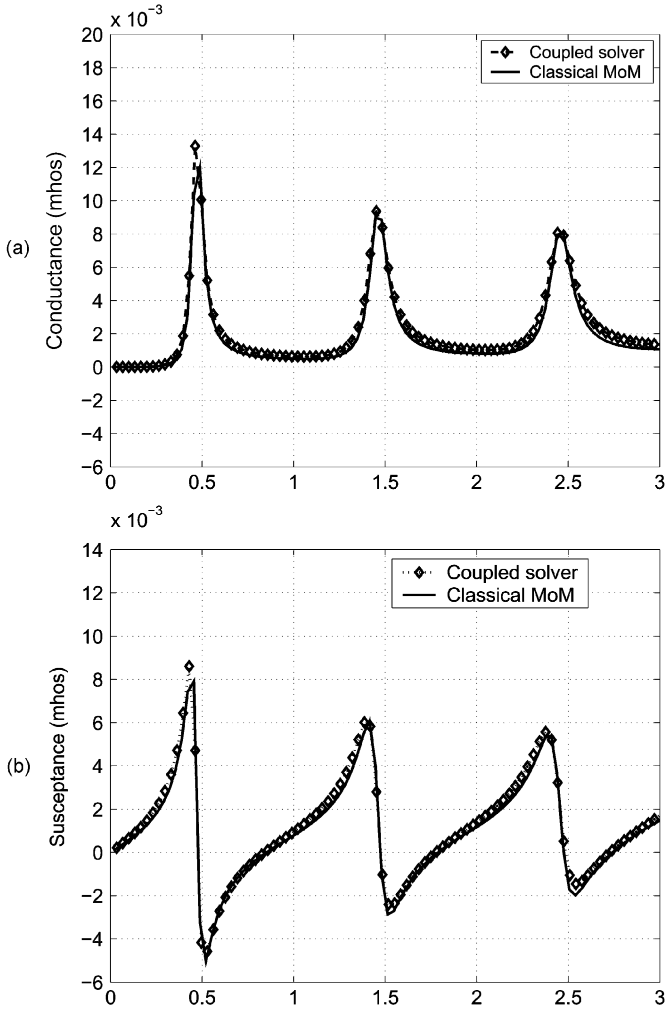

Fig. 6. Input conductance and susceptance versus l/λ. (a) Conductance. (b) Susceptance.

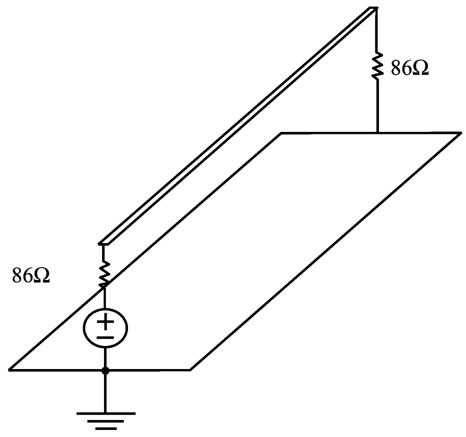

Fig. 7. Interconnect over a solid ground plane.

Another validation example, comparing the presented approach to the standard PEEC, is an interconnect over a ground plane, as in [29], and as shown in Fig. 7.

The ground plane is 2 cm long × 1 cm wide and the trace is 2 cm long × 1 mm wide and stays 0.5 mm above the ground plane. The frequency dependence of the input impedance is depicted in Fig. 8, and matches well. The small bump is very near

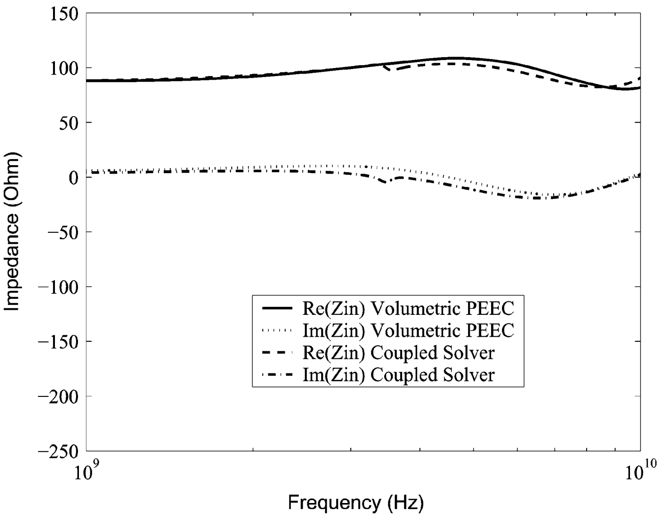

Fig. 8. Input impedance of an interconnect over a ground plane.

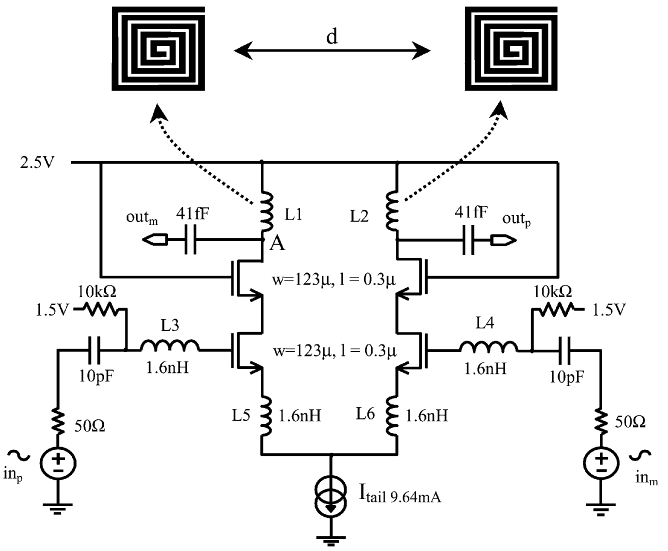

Fig. 9. Schematic of a 5.6-GHz LNA.

the first resonant frequency, and might be related to internal resonant effects in the EFIE system, but this is not clear.

One of the typical applications is circuit/layout co-simulation for RF electronics system design, where on-chip inductors are often employed. In RF circuit design, accurate characterization of the inductor is the most challenging task. Fig. 9 shows the topology of a 5.6-GHz differential-mode LNA, where several on-chip inductors are included either for the frequency-selection purpose such as $L1$ and $L2$ or for the impedance matching purpose such as $L3$–$L6$.

With 5.6-GHz central working frequency, performance of the LNA will be affected by both the distributed effect and the crosstalk of on-chip spiral inductors. The precision of two inductors $L1$ and $L2$ is most important since it affects the central frequency where the maximum gain can be derived. While the transistor sizes are fixed by the requirement of the optimum noise figure [30] to be 123 μm, the main design task is to adjust the turns and spacing of spiral inductors to tune the resonant frequency of the LC tank to the central frequency 5.6 GHz.

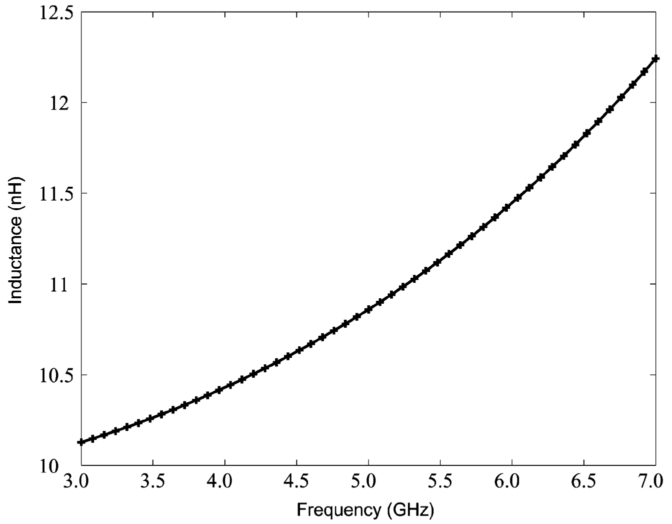

Fig. 10. Extracted equivalent inductance.

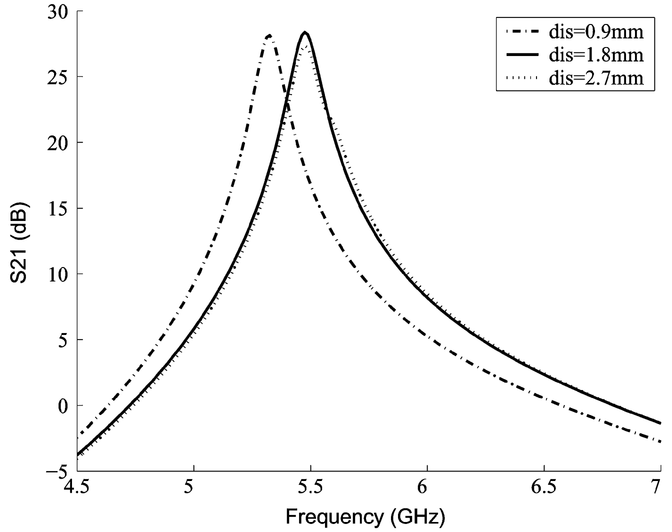

Fig. 11. S_{21} curve versus distance between inductors.

The spiral inductor $L1$ is first simulated using the coupled solver to decide the number of turns according to the extracted equivalent inductance. With a total parasitic capacitance to be 105 fF at node A, the inductor is designed to be five turns with an area of 500 μm × 500 μm. Fig. 10 shows the extracted equivalent inductance of such a single spiral inductor. The increase in inductance with frequency is due to approaching self-resonance frequency of the inductor.

Due to the radiation and inductive coupling effects, the two inductors will mutually couple, and lead to a shift in the central frequency. Fig. 11 shows a series of S_{21} curves versus different distances between the two inductors.

As the two inductors are moved closer, the coupling effect becomes prominent and leads to poorer performance. In actuality, the coupling effect could also be used to an advantage: due to the differential mode nature of the currents through the two inductors, a larger effective inductance can be realized by tight coupling between the two inductors. In other words, the same inductance value could be achieved using a lesser number

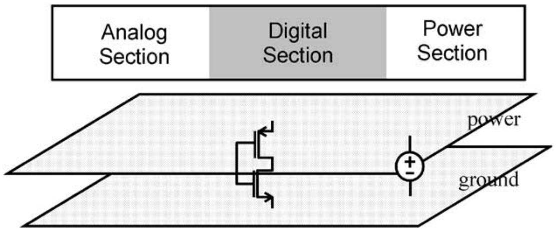

Fig. 12. Structure of a mixed-signal board with a noise source at the center.

of turns and, thus, less chip area. Some new multilevel inductor designs are based on this concept.

To simulate the coupled system in the frequency domain, an operating point analysis is first performed to linearize the nonlinear BSIM3 transistor model [31]. As an existing circuit simulation technique, the operating point is calculated via Newton–Raphson iterations. EM structures are not involved in those iterations directly; instead, these are represented by a resistance network calculated using a volumetric resistance extractor.

If large-signal analysis instead of the small-signal analysis presented above is required for the coupled system, the frequency domain can be facilitated through a harmonic-balance method [32] coupled to the EM simulation. However, this is beyond the scope of this paper.

A frequency sweep is then performed for the range of interest. The EM problem was meshed with 5120 RWG basis functions and it required 43 s to set up the problem and 88 s to solve using our in-house low-rank compression fast iterative solver on a 1.6-GHz Pentium processor. In contrast, extraction of the entire port model requires 42-s one-time setup time and 334-s solve time. Note that the solve time for port-model extraction is approximately four times as long as the solve time for the coupled solver, which is because the problem needs to be solved four times in order to extract the port model, each for one column of the Y matrix with a 1-V excitation on one port and 0-V excitation on the rest of ports.

The second example studies the power/ground-plane voltage bounce distribution due to a high-frequency noise source. Consider a typical mixed analog/digital print circuit board (PCB), as shown in Fig. 12.

Since digital circuits are usually associated with high-speed signal switching that contains numerous high-frequency components, the potential difference between power and ground planes will not be equal to ideal supply voltage everywhere. At high frequencies, the power and ground planes need to be considered as a distributed RLC network instead of ideal conduction planes. The voltage bounce could cause digital logic circuits to switch erroneously. In such a case, decoupling capacitors are needed to suppress the peak bounce voltage.

With traditional port-model-based EM–circuit simulation methods, it is difficult to acquire the voltage bounce distribution information all over the plane since the potentials can only be accessed via ports. Thus, deriving the spatial distribution of the potential requires ports everywhere on the plane and could make the problem cumbersome or too large to solve. On the other hand, since the coupled circuit–EM solver uses equivalent surface currents as system unknowns, the voltage/field distribution can then be easily derived by a post-processing operation once the coupled system is solved.

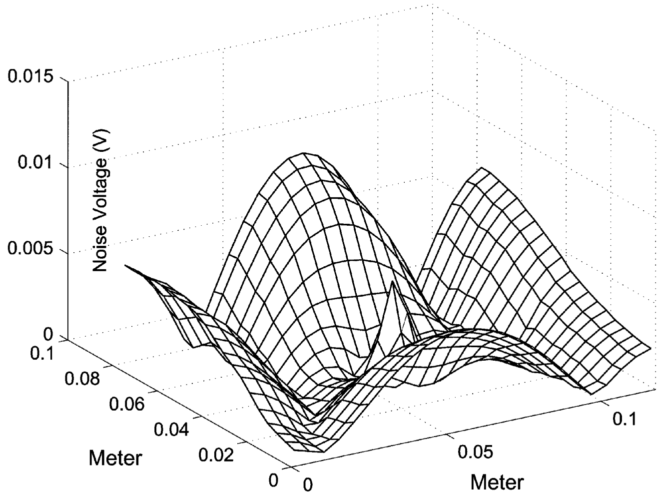

Fig. 13. Bounce-voltage distribution at 3 GHz.

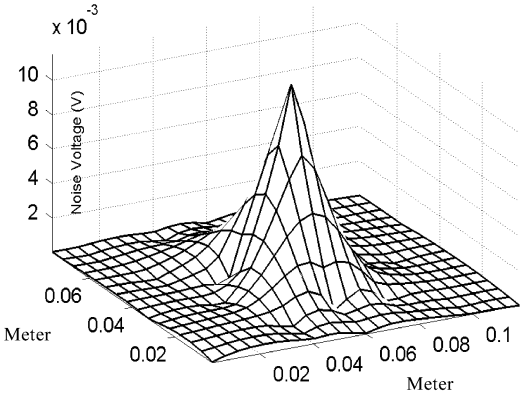

Fig. 14. Bounce-voltage distribution at 3 GHz after adding 20 decoupling capacitors.

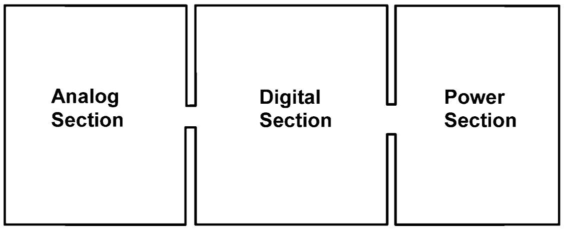

Fig. 15. Partially split power ground-plane design.

In Fig. 12, the size of the PCB board is 12 cm × 8 cm. At 3 GHz, 1-mA noise source at the board center can cause a bounce-voltage distribution, as shown in Fig. 13.

By continuously pinning down the peak bounce voltage using 10-nF decoupling capacitors, peaks of the noise voltage can be isolated in a local area of the noise source, as shown in Fig. 14, after adding approximately 20 decoupling capacitors.

Note that the EM part of the problem does not change as additional capacitors are added and, hence, the factorization and storage of the EM section can be done just once if required, using the *EM port model* of the coupled system.

An alternative design approach is to design the power/ground board, as shown in Fig. 15, with partially split planes.

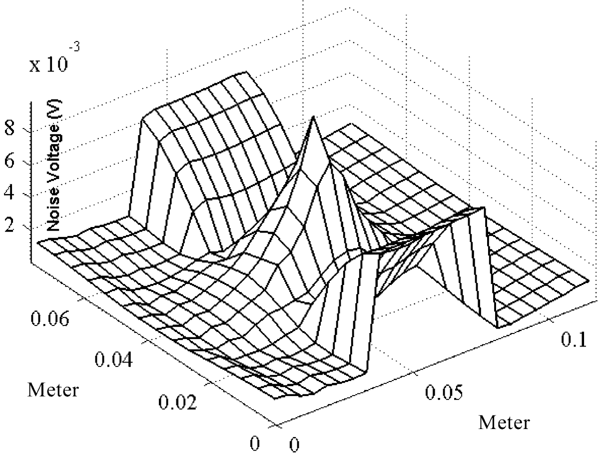

Fig. 16. Bounce-voltage distribution at 3 GHz for split power/ground plane.

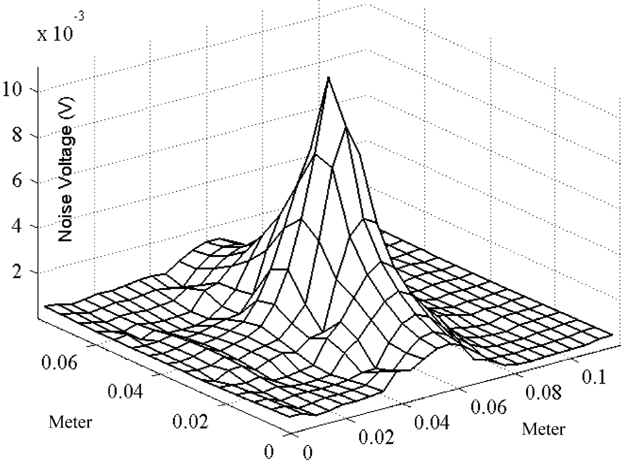

Fig. 17. Bounce-voltage distribution at 3 GHz for split power/ground plane with nine decoupling capacitor.

Simulation results reveal that the bounce-voltage localization effect was achieved even without adding decoupling capacitors, as shown in Fig. 16.

Further localization of bounce voltage will need a smaller number of decoupling capacitors compared to the previous example. Bounce localization shown in Fig. 17 was achieved by using nine decoupling capacitors.

VI. CONCLUSION

In this paper, a coupled circuit–EM formulation has been presented. The EM solution is based on full-wave surface integral equations (i.e., EFIEs), the circuit solution is based on KVL and KCL, and the coupling is ensured by charge and current continuity, as well as potential matching. The primary objective of the method is to ensure proper physics-based coupling between the circuit and the EM parts such that a coupled matrix can be formulated. While different kinds of EM and circuit port models can be derived, a fully coupled solution process will guarantee complete electrical transparency in the entire system, including all EM and circuit effects. Work in progress is aimed at extending the same approach to the time-domain simulation to include the effect of lossy conductors and to incorporate fast multilevel solvers and fast frequency-sweep methods for the coupled system.

REFERENCES

[1] K. Kundert, H. Chang, D. Jefferies, G. Lamant, E. Malavasi, and F. Sendig, "Design of mixed-signal systems-on-a-chip," *IEEE Trans. Computer-Aided Design* , vol. 19, pp. 1561–1571, Dec. 2000.

[2] I. Erdin and M. Nakhla, "Mixed circuit/electromagnetic analysis of field coupling to high speed interconnects in inhomogeneous medium," in *Int. IEEE Electromagnetic Compatibility Symp.*, vol. 1, Aug. 1999, pp. 446–449.

[3] W. Sui, D. A. Christensen, and C. H. Durney, "Extending the two-dimensional FDTD method to hybrid electromagnetic systems with active and passive lumped elements," *IEEE Trans. Microwave Theory Tech.*, vol. 40, pp. 724–730, Apr. 1992.

[4] R. Khazaka and M. Nakhla, "Analysis of high-speed interconnects in the presence of electromagnetic interference," *IEEE Trans. Microwave Theory Tech.*, vol. 46, pp. 940–947, July 1998.

[5] M. N. Abdulla and M. B. Steer, "Extraction of network parameters in the electromagnetic analysis of planar structures using the method of moments," *IEEE Trans. Microwave Theory Tech.*, vol. 49, pp. 94–103, Jan. 2001.

[6] A. Canova, M. Ottella, and D. Rodger, "A coupled field-circuit approach to 3D FEM analysis of electromechanical devices," in *IEEE 9th Int. Electrical Machines and Drive Conf.*, Sept. 1999, pp. 71–75.

[7] M. Feliziani and F. Maradei, "Circuit-oriented FEM: Solution of circuit-field coupled problems by circuit equations," *IEEE Trans. Magn.*, vol. 38, pp. 965–968, Mar. 2002.

[8] M. C. Costa, S. I. Nabeta, and J. R. Cardoso, "Modified nodal analysis applied to electric circuits coupled with FEM in the simulation of a universal motor," *IEEE Trans. Magn.*, vol. 36, pp. 1431–1434, July 2000.

[9] P. P. M. So and W. J. R. Hoefer, "A general framework for SPICE-TLM interconnection," in *IEEE MTT-S Int. Microwave Symposium Dig.*, vol. 2, June 2002, pp. 1123–1126.

[10] S. Chun, M. Swaminathan, L. D. Smith, J. Srinivasan, Z. Jin, and M. K. Iyer, "Modeling of simultaneous switching noise in high speed systems," *IEEE Trans. Adv. Packag.*, vol. 24, pp. 132–142, May 2001.

[11] A. E. Ruehli, "Equivalent circuit models for three-dimensional multiconductor systems," *IEEE Trans. Microwave Theory Tech.*, vol. MTT-22, pp. 216–221, Mar. 1974.

[12] A. E. Ruehli, G. Antonini, J. Esch, J. Ekman, A. Mayo, and A. Orlandi, "Nonorthogonal PEEC formulation for time-and frequency-domain EM and circuit modeling," *IEEE Trans. Electromagn. Compat.*, vol. 45, pp. 167–176, May 2003.

[13] A. Rong and A. C. Cangellaris, "Generalized PEEC models for three-dimensional interconnect structures and integrated passives of arbitrary shapes," in *Proc. Electrical Performance of Electronic Packaging Conf.*, vol. 10, Boston, MA, Oct. 2001, pp. 225–228.

[14] Y. Wang, V. Jandhyala, and C. J. Shi, "Coupled electromagnetic-circuit simulation of arbitrarily-shaped conducting structures," in *Proc. Electrical Performance of Electronic Packaging Conf.*, vol. 10, Boston, MA, Oct. 2001, pp. 233–236.

[15] M. Kamon, M. J. Ttsuk, and J. K. White, "FASTHENRY: A multipole-accelerated 3-D inductance extraction program," *IEEE Trans. Microwave Theory Tech.*, vol. 42, pp. 1750–1758, Sept. 1994.

[16] G. Antonini, A. Orlandi, and A. E. Ruehli, "Harten's scheme for PEEC method," in *IEEE Int. Electromagnetic Compatibility Symp.*, vol. 1, Aug. 2001, pp. 340–344.

[17] R. F. Harrington, *Field Computation by Moment Methods*. Malabar, FL: Krieger, 1982, pp. 71–72.

[18] A. Odabasioglu, M. Celik, and L. T. Pileggi, "PRIMA: Passive reduced-order interconnect macromodeling algorithm," in *IEEE/ACM Int. Computer-Aided Design Conf. Tech. Dig.*, Nov. 1997, pp. 58–65.

[19] K. Nabors and J. K. White, "FastCap: A multipole accelerated 3-D capacitance extraction program," *IEEE Trans. Computer-Aided Design*, vol. 10, pp. 1447–1459, Nov. 1991.

[20] J. R. Phillips and J. K. White, "Efficient capacitance extraction of 3D structures using generalized pre-corrected FFT methods," in *3rd Electrical Performance of Electronic Packaging Topical Meeting*, Nov. 1994, pp. 253–256.

[21] S. Kapur and D. E. Long, "IES^3: A fast integral equation solver for efficient 3-dimensional extraction," in *IEEE/ACM Int. Computer-Aided Design Conf. Dig.*, Nov. 1997, pp. 448–455.

[22] D. Gope and V. Jandhyala, "An iteration-free fast multilevel solver for dense method of moment systems," in *Proc. Electrical Performance Electronic Packaging Conf.*, vol. 10, Boston, MA, Oct. 2001, pp. 177–180.

[23] Y. Wang, D. Gope, V. Jandhyala, and R. Shi, "Integral equation based coupled electromagnetic-circuit simulation in the frequency domain," in *Proc. IEEE AP-S URSI Symp.*, vol. 3, Columbus, OH, June 2003, pp. 328–331.

[24] S. M. Rao, D. R. Wilton, and A. W. Glisson, "Electromagnetic scattering by surfaces of arbitrary shape," *IEEE Trans. Antennas Propagat.*, vol. AP-30, pp. 409–418, May 1982.

[25] S. Chakraborty and V. Jandhyala, "Evaluation of Green's function integrals in conducting media," in *Proc. IEEE AP-S Symp. Dig.*, vol. 3, Columbus, OH, June 2003, pp. 320–323.

[26] ——, "Accurate computation of vector potentials in lossy media," *Microwave Opt. Technol. Lett.*, vol. 36, no. 5, pp. 359–363, Mar. 2003.

[27] N. J. Champagne II, J. T. Williams, and D. R. Wilton, "The use of curved segments for numerically modeling thin wire antennas and scatterers," *IEEE Trans. Antennas Propagat.*, vol. 40, pp. 682–689, June 1992.

[28] J. Vlach and K. Singhal, *Computer Methods for Circuit Analysis and Design*. New York: Van Nostrand, 1983.

[29] W. Pinello, A. C. Cangellaris, and A. Ruehli, "Hybrid electromagnetic modeling of noise interactions in packaged electronics based on the partial-element equivalent-circuit formulation," *IEEE Trans. Microwave Theory Tech.*, vol. 45, pp. 1889–1896, Oct. 1997.

[30] B. Razavi, *RF Microelectronics*. Englewood Cliffs, NJ: Prentice-Hall, 1997, ch. 6.

[31] Y. Cheng and C. M. Hu, *MOSFET Modeling and BSIM3 User's Guide*. New York: Kluwer, 1999.

[32] V. Rizzoli, A. Lipparini, A. Costanzo, F. Mastri, C. Cecchetti, A. Neri, and D. Masotti, "State-of-the-art harmonic-balance simulation of forced nonlinear microwave circuits by the piecewise technique," *IEEE Trans. Microwave Theory Tech.*, vol. 40, pp. 12–28, Jan. 1992.

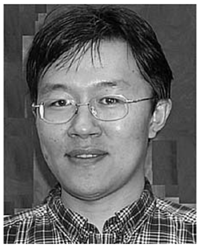

Yong Wang received the B.S. and M.S. degrees in electronics from Tsinghua University, Beijing, China, in 1994 and 1998 respectively, and is currently working toward the Ph.D. degree in electrical engineering at the University of Washington, Seattle.

From 1994 to 1996, he was a Research Assistant with the Circuit and System Laboratory, Tsinghua University, where he was involved with circuit simulation and macromodeling. From 1998 to 2000, he was with Analogy Inc., where he was involved with modeling engineering. His research interests include analog/mixed-signal circuit simulation, EM simulation, and analog design automation.

Dipanjan Gope (S'00) received the B.Tech. degree in electronics and electrical communication engineering from Indian Institute of Technology (IIT), Kharagpur, India, in 2000, the M.S. degree in electrical engineering from the University of Washington, Seattle, in 2003, and is currently working toward the Ph.D. degree in computational electromagnetics at the University of Washington.

He is currently a Graduate Research Assistant wit the University of Washington. His research interests include combined circuit–EM simulations, signal integrity in high-speed circuits and devices, and fast solution algorithms.

Vikram Jandhyala (M'00–SM'03) received the B.Tech. degree in electrical engineering from the Indian Institute of Technology (IIT), Delhi, India, in 1993, and the M.S. and Ph.D. degrees from the University of Illinois at Urbana-Champaign, in 1995 and 1998, respectively.

As part of his graduate work, he co-developed the steepest descent fast-multipole method for rapid simulation of a large class of EM problems. From 1998 to 2000, he was a Research and Development Engineer with the Ansoft Corporation, Pittsburgh, PA. He was involved in the acceleration of Ansoft's integral-equation solvers, and co-developed a fast multipole-based extraction tool in Ansoft's SPICElink versions released in 1999 and 2000. Since 2000, he has been an Assistant Professor with the Electrical Engineering Department, University of Washington, Seattle. He directs the Applied Computational Electromagnetics Laboratory, with research interests and projects in several areas of computational electromagnetics, including fast solvers and integral-equation formulations in the frequency and time domains, high-speed circuits and devices, coupled multiphysics simulation, novel materials, and propagation. He has visiting research status with the Lawrence Livermore National Laboratories. He has authored or coauthored over 70 journal and conference papers.

Dr. Jandhyala is a full elected member of the International Scientific Radio Union (URSI) Commission B. He has served as a reviewer for several IEEE journals and conferences and national and international proposal panels. He is on the Technical Program Committee of the IEEE Design Automation Conference and the IEEE Antennas and Propagation Society (IEEE AP-S) Symposium. He was a recipient of the 2001 National Science Foundation (NSF) CAREER grant, a 1998 Outstanding Graduate Research Award presented by the University of Illinois, and a 1996–1997 IEEE Microwave Graduate Fellowship.

C.-J. Richard Shi (M'91–SM'99) is currently an Associate Professor of electrical engineering with the University of Washington, Seattle. He is a key contributor to IEEE Standard 1076.1-1999 (VHDL-AMS) for the description and simulation of mixed-signal circuits and systems. His research interests include several aspects of the computer-aided design and test of integrated circuits and systems, with particular emphasis on analog/mixed-signal and deep-submicrometer circuit modeling, simulation, and design automation.

Dr. Shi founded the IEEE International Workshop on Behavioral Modeling and Simulation (BMAS) in 1997. He has served on the Technical Program Committees of several international conferences. He has been an associate editor, as well as a guest editor, for the IEEE Transactions on Circuits and Systems—II, Analog and Digital Signal Processing. He is currently an associate editor of the IEEE Transactions on Computer-Aided Design of Integrated Circuits and Systems. He was the recipient of a Best Paper Award presented by the IEEE/Association for Computing Machinery (ACM) Design Automation Conference, a Best Paper Award presented by the IEEE Very Large Scale Integration (VLSI) Test Symposium, a National Science Foundation CAREER Award, and a Doctoral Prize presented by the Natural Science and Engineering Research Council of Canada.

Short Papers

Oct-Tree-Based Multilevel Low-Rank Decomposition Algorithm for Rapid 3-D Parasitic Extraction

Dipanjan Gope and Vikram Jandhyala

***Abstract*—Fast parasitic extraction is an integral part of high-speed microelectronic simulation at the package and on-chip level. Integral equation methods and related fast solvers for the iterative solution of the resulting dense matrix systems have enabled linear time complexity and memory usage. However, these methods tend to have large disparities between setup and matrix-vector product times that affect their efficiency when applied to multiple excitation problems, i.e., problems with a large number of nets. For example, FastCap, which is based on the fast multipole method, has a significantly faster setup time than the multilevel QR decomposition-based IES^3, but relatively slow matrix-vector products. In this paper, we present a novel oct-tree-based QR compression technique for fast iterative solution. The regular cube structure of the fast multipole method and the QR compression scheme for interaction submatrices as in IES^3 are combined to achieve a predetermined compressible matrix-block structure and, consequently, superior memory, setup, and solve time efficiencies.**

***Index Terms*—Low-rank-decomposition, oct-tree multilevel hierarchy, parasitic extraction.**

I. Introduction

In deep submicron technology, as the trace width decreases, the height-to-width ratio is increased to maintain low wire resistance. The larger trace aspect ratio along with the reduction in trace spacing leads to increasing parasitic capacitances [1]–[3], such that the connectivity delay becomes the dominant delay [4]. At the same time, the rise in clock frequencies render the estimation of interconnect delay and, hence, the associated parasitic quantities extremely crucial for modern day circuit design [5], [6]. Due to the complexity of on-chip design structures, numerical techniques that utilize field solutions for parasitic extraction are preferred, to achieve maximum accuracy [7].

Among the existing numerical tools, a surface-based integral equation methodology such as the method of moments (MoM) [8] is ideally suited to address the problem. It leads to a well-conditioned system with reduced size, compared to volumetric methods [9], but the system of equations generated is inherently dense, thereby creating a time and memory bottleneck [10]–[14]. Several fast iterative techniques have been developed to efficiently store and solve an MoM system. All these methods, including QR-based approaches [10]–[12], fast multipole methods (FMMs) [13], and fast Fourier transform (FFT)-based techniques [14] accelerate matrix-vector products and, therefore, expedite the Krylov-subspace iterative solution [15]. The memory requirement and the setup time is reduced from $O(N^2)$ to $O(N)$ or $O(N \log N)$ and the solve time is reduced from $O(N^3)$ as in Gaussian elimination or $O(N^2) \times p \times r$ as in a regular iterative solver to $O(N) \times p \times r$ or $O(N \log N) \times p \times r$, where N is the number of degrees of freedom, and p is the number of iterations for convergence per right-hand side (RHS), and r is the number of RHS vectors.

The QR-based fast iterative solver (IES^3) is particularly attractive for circuit problems. The approach is based on the utilization of the low-rank property of MoM submatrices under a user-specified tolerance. The rank of a submatrix obtained by such a tolerance-based decomposition process is referred to as the epsilon-rank. This low-epsilon-rank decomposition is achieved by singular-value decomposition (SVD) or the modified gram schmidt method [16]. Unlike fast multipole methods, it is independent of the kernel (Green's function), and can be applied directly to multilayered dielectric cases [17] without increasing the size of the problem [10]. Even in terms of free-space capacitance extraction, IES^3 has been demonstrated as being more efficient in terms of memory and solve time. However, in absolute terms, the setup cost has a high value, owing to complexities in the underlying binary tree decomposition in IES^3.

In this paper, we present a predetermined interaction list supported oct tree (PILOT)-based QR algorithm that greatly reduces the setup time while maintaining the memory and solve time efficiency of rank-map binary tree QR (RMBT-QR), which is a prototype implementation based on the same principles as IES^3. PILOT exploits the properties of a multilevel oct-tree implementation used in FMMs to create a predetermined set of interaction lists, thereby reducing the setup time considerably. In short, the regular oct-tree structure of FMM and the compression efficiency of QR are combined together to yield an enhanced efficiency capacitance extraction algorithm. Though not discussed in this paper, the compression scheme is amenable to full-wave multi-layered dielectric kernel solutions for electrically-small structures and is also stable for these problems unlike traditional full-wave FMM techniques.

The paper is organized as follows. Section II introduces the integral equation formulation for an MoM-based parasitic capacitance extraction problem. In Section III, the algorithm of PILOT-QR with its associated components is discussed in detail. Performance comparisons of PILOT, RMBT-QR and FastCap [13] are presented in Section IV. Section V concludes the paper.

II. Integral Equation

Capacitance problems formulated using MoM are solved using the integral form of the Poisson's equation as follows:

$$\nabla^2 \phi(\mathbf{r}) = -\frac{\rho(\mathbf{r})}{\varepsilon} \tag{1}$$

relating potential ϕ and charge density ρ. The discretization of the geometry into N basis functions results in a matrix system of the form

$$\overline{\mathbf{Z}}\mathbf{I} = \mathbf{B} \tag{2}$$

where the $N \times N$ MoM matrix $\overline{\mathbf{Z}}$ is a dense Green's function matrix, $\mathbf{I}$ represents the unknown coefficients of known basis functions for charge density, and $\mathbf{B}$ represents the known potential excitations on each basis function. Each element of the MoM matrix denotes the

Manuscript received July 17, 2003; revised December 15, 2003. This work was supported in part by the DARPA/MTO NeoCAD program under Grant N66001-01-1-8920, in part by a National Science Foundation Career Award under Grant ECS-0093102, in part by the National Science Foundation/Semiconductor Research Corporation Joint Initiative on Mixed-Signal Electronic Technologies, and in part by the Ansoft Corporation. This paper was recommended by Associate Editor S. Saxena.

The authors are with the Electrical Engineering Department, University of Washington, Seattle, WA 98195 USA (e-mail: dips@u.washington.edu; jandhyala@ee.washington.edu).

Digital Object Identifier 10.1109/TCAD.2004.836723

interaction between a testing and a basis function and is written as follows:

$$\overline{\mathbf{Z}}(\mathrm{j},\mathrm{i}) = \int\limits_{S_j} ds\, t_j(\mathbf{r}) \int\limits_{S_i} ds' g(\mathbf{r},\mathbf{r}') f_i(\mathbf{r}') \tag{3}$$

where t and f are the testing and basis functions, respectively, S denotes function domain, and $\mathrm{g}(\mathbf{r},\mathbf{r}')$ is the relevant Green's function.

In the electrostatic case for P disconnected conductors, the charge-voltage relation is given by

$$\overline{\mathbf{C}}\mathbf{V} = \mathbf{Q} \tag{4}$$

where $\overline{\mathbf{C}}$ is the $P \times P$ capacitance matrix, $\mathbf{V}$ denotes the potential on each conductor and $\mathbf{Q}$ is the resultant charge on the conductors. The jth column of $\overline{\mathbf{C}}$ is obtained by enforcing a voltage of 1 V on the jth conductor, 0 V on all other conductors in (2)

$$\begin{aligned} \mathbf{B}_i &= 1, \quad i \in \text{Conductor}_j \\ &= 0, \quad \text{otherwise.} \end{aligned} \tag{5}$$

Then, the above system is solved, and charge density over each conductor is integrated

$$C_{ij} = \sum \mathbf{I}_k \quad k \in \text{Conductor}_i \tag{6}$$

The $N \times N$ system of (2) is, therefore, solved P times to obtain the entire capacitance matrix.

III. Oct-Tree-Based QR-Compression Algorithm

The presented PILOT QR algorithm develops a predetermined matrix structure for arbitrary 3D geometries that ensures efficient compression. The algorithm has 4 main constituents:

A. *Oct-Tree Spatial Decomposition in Three-Dimensions (3-D)*

The algorithm is based on maintaining a regular geometric pattern of cells. The best combination, which yields a regular cell pattern, is *loosely bounded*, *spatially balanced* decomposition into *orthants* [18]. Note that, as in FMM, empty cells are ignored.

The starting cell c_0^0 is the smallest cube that encloses the entire geometry. The superscript indicates the level of decomposition to which the cube belongs to and the subscript denotes the cube number in that level. Each cell is then recursively decomposed into a maximum of eight cubes in 3-D, depending on the distribution of basis functions. Thus, each cube c_i^l, which is the ith cube at level l is decomposed by spatially balanced splits along each coordinate, x, y, and z

$$\begin{aligned} \text{split}_x &= \frac{x_{\max} + x_{\min}}{2} \\ \text{split}_y &= \frac{y_{\max} + y_{\min}}{2} \\ \text{split}_z &= \frac{z_{\max} + z_{\min}}{2} \end{aligned} \tag{7}$$

where split_x, split_y, and split_z are the split positions in the three orthogonal directions and $x_{\max}$, $x_{\min}$, $y_{\max}$, $y_{\min}$, $z_{\max}$, and $z_{\min}$ are the bounding coordinates of the cube. Each cube c_j^{l+1} resulting from this decomposition is called a child of c_i^l and the latter is denoted as the parent of c_j^{l+1}

$$P_{c_j^{l+1}} = c_i^l. \tag{8}$$

All the child cubes of c_i^l are siblings of each other, where a sibling set is defined as follows:

$$S_{c_j^{l+1}} = \left\{ c_k^{l+1}\ \forall k | P_{c_k^{l+1}} = P_{c_j^{l+1}} \right\}. \tag{9}$$

At each level, the generated cells are identical cubes and the pattern repeats across levels. For 3-D arbitrarily shaped geometries, the cell data structure is in the form of an oct tree. The geometric decomposition is, hence, exactly similar to that of multilevel FMM [13] and, hence, its interaction scheme can be leveraged in the presented algorithm.

B. *Basic Multilevel Interaction List*

Every cube $c_i^l \forall i,\ l | 0 \le l \le l_c;\ 0 \le i < n_c^l$, where l_c is the total number of levels and N_c^l is the total number of cubes at level l, has a nearest neighbor list $K_{c_i^l}$ and an interaction list $I_{c_i^l}$. The nearest neighbor list, is defined as

$$K_{c_i^l} = \left\{ c_j^l | c_j^l \text{ is in the same level as } c_i^l \text{ and has at least one contact point with } c_i^l \right\}. \tag{10}$$

Consequently, the interaction list is defined as

$$I_{c_i^l} = \left\{ c_j^l | P_{c_j^{l+1}} \in k_{p_{c_i^l}};\, c_j^l \notin K_{c_i^l} \right\}. \tag{11}$$

In multilevel FMM, interactions between the testing functions of cube c_i^l with basis functions of cubes belonging to $I_{c_i^l}$ are constructed using multipole expansion. In other words, multipoles are used to construct $T(c_j^l, c_i^l) \forall j | c_j^l \in I_{c_i^l}$ where $T(c_j^l, c_i^l)$ denotes the interaction between testing functions of c_j^l and basis functions of c_i^l. Furthermore, multipole expansions are formed only once for c_i^l and used for all its interactions with other cubes. Direct Green's function computations are used only at the finest level to construct $T(c_j^{l_c}, c_i^{l_c}) \forall j | c_j^{l_c} \in K_{c_i^{l_c}}$. Since PILOT does not explicitly require cubical regions but simply deals with interaction matrices, there is scope for further compression by combining cubes in $I_{c_i^l}$ in an a priori manner into a new interaction list called the merged interaction list (MIL).

C. *MIL*

It is observed that the interaction lists of siblings share many common cubes

$$I_S = \bigcap I_{c_i^l} \neq 0 \quad \forall i | c_i^l \in S_{c_j^l}. \tag{12}$$

The common cubes in the interaction lists of the siblings are denoted by I_s. For visualization purposes, the two-dimensional (2-D) common interaction shell is illustrated in Fig. 1, though our algorithm is designed for 3-D geometries.

It is, therefore, possible to group source cubes and observer cubes of different interaction lists in order to compress larger matrices to low epsilon-ranks and thereby gain in terms of overall compressibility. It must be noted that the common interaction list does not directly translate into a merged interaction because the epsilon-rank of such an interaction submatrix will not in general be low. The common interaction list is decomposed into disjointed parts such that the overall compression is optimized. Each such disjointed part is an interaction between grouped source cubes and observer cubes and forms an entry of the MIL denoted as μ. A μ can be expressed as a combination of multilevel FMM cube-to-cube interactions

$$\mu_k = \left\{ T_p\left(c_j^l, c_i^l\right) \right\} \qquad \forall p | 1 \le p \le n_g \tag{13}$$

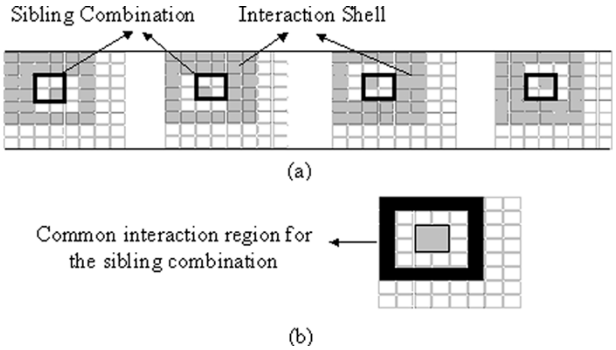

Fig. 1. (a) Individual interaction shells of each cube belonging to the sibling combination. (b) Common interaction shell for the sibling combination formed by the intersection of individual interaction regions of cubes belonging to the sibling combination. For visualization purpose 2-D shells are illustrated. Similar common-interaction regions exist for 3-D geometries.

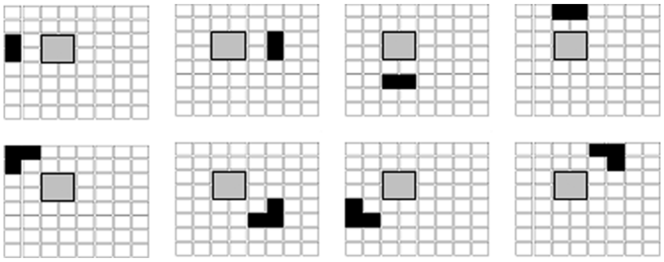

Fig. 2. Merged interaction-list entries corresponding to the common interaction region of Fig. 6(b). Each such entry gives rise to a low epsilon-ranked matrix block.

where n_g is the number of FMM interactions grouped. Higher compression is achieved since a larger matrix is compressed to a low epsilon-rank under the same tolerance

$$(m_{\mu_k} + n_{\mu_k})\, r_{\mu_k} < \sum_{i=1}^{n_g} (m_i + n_i) r_i \tag{14}$$

where m, n, and r denote the number of rows, number of columns, and the epsilon-rank of a submatrix. The subscript i denotes a regular multilevel interaction list entry that is now a constituent of the MIL. Fig. 2 demonstrates the decomposition of the common interaction list of Fig. 1(b) into merged interactions. Further compression is possible considering common interaction lists for pairs of siblings. Thus, the regular interaction list is replaced by the merged interaction list, which has fewer interactions to consider and larger low epsilon-ranked matrices to compress with the same tolerance.

PILOT supports MIL for both 3-D and 2-D geometries. However, for visualization purposes, the 2-D MIL construction is illustrated in detail. For 2-D geometries, each cube has a maximum of 27 cubes in its interaction list and this pattern repeats for all cubes across levels. In PILOT, the interaction lists of four siblings are replaced by 16 merged interaction entries as demonstrated in Table I. The MIL entries, along with the expected ranks, are setup as a one-time process for a given kernel. The expected epsilon-rank is the maximum rank observed for sources and observers randomly placed in an MIL setup. The expected epsilon-ranks supplied in Table I apply for the free space Green's Function kernel. The cube numbering used in the process is illustrated in Fig. 3.

Though there are 16 entries in the MIL, there are only three different types of interactions to be evaluated and the rest could be derived from symmetry considerations. The same MIL pattern is valid for sibling pairs across all levels. The MIL is thus an accurate replacement of the rank-map used in RMBT-QR and leads to a predetermined tree structure. The 2-D MIL shell structure is invariant for multilayered dielectric Green's functions, for structures parallel to the layers and only the expected epsilon-ranks change. A similar MIL has been derived for 3-D geometries with 40 entries, with only five unique entries owing to symmetry.

TABLE I
MIL Entries With Expected Epsilon-Ranks

MIL No.	Observer Cubes	Source Cubes	Expected Eps-Rank
1	1,2,3,4	5, 6, 8	6
2	1,2,3,4	13, 14, 15	6
3	1,2,3,4	25, 27, 28	6
4	1,2,3,4	34, 35, 36	6
5	1,2,3,4	9, 10	6
6	1,2,3,4	17, 20	6
7	1,2,3,4	22, 23	6
8	1,2,3,4	31, 32	6
9	1,2	26, 29, 30	7
10	3,4	11, 12, 16	7
11	2,3	7,18,19	7
12	1,4	21, 24, 33	7
13	1	16	5
14	2	33	5
15	3	26	5
16	4	7	5

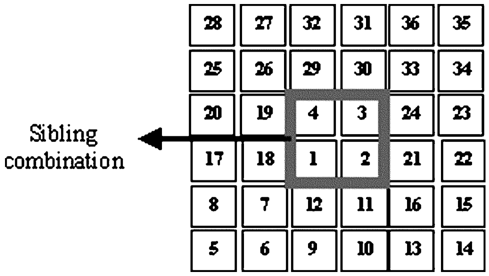

Fig. 3. Siblings, and cubes belonging to their interaction shells are numbered. The MIL entry table (Table I) follows the numbering scheme demonstrated in this figure.

The construction of the MIL is a one-time process for a given multilayered dielectric environment and due to the regular pattern of the cube structure, only a few interactions need to be considered for epsilon-rank evaluation. The MIL determines the final tree structure for any geometry under consideration.

D. QR Compression of MIL Entries

MoM submatrices pertaining to interactions of the MIL are compressed by forming QRs from samples. Consider n source basis functions f_i defined over domain S_i for $i = 1, 2, \ldots, n$, such that $S_i \in R_{\mathrm{src}}$, where R_{src} is the region of space inside an MIL entry source group. Similarly, consider m testing functions whose domains belong to region R_{obs}, which is delimited by the MIL entry observer group. Let the sub-matrix $\overline{\mathbf{Z}}^{\mathrm{sub}}_{m\times n}$ of the full MoM matrix $\overline{\mathbf{Z}}$ represent the interactions between the basis and the testing functions through the designated Green's function $g(\mathbf{r}, \mathbf{r}')$. Green's functions encountered in capacitance extraction problems including those for multilayered dielectrics vary smoothly with distance [10]. Therefore, the column of $\overline{\mathbf{Z}}^{\mathrm{sub}}$ pertaining to the interaction of f_i with all testing functions is closely related to other columns that capture similar interactions for $f_j\ \forall j | S_j$ is in the neighborhood of S_i.

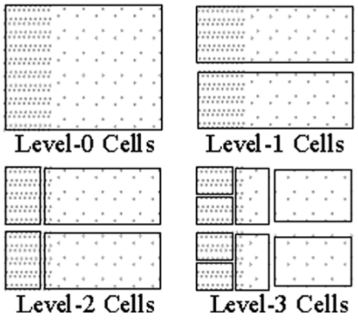

Fig. 4. Levels of tight bound k-d tree decomposition. As can be seen, rectangular (parallelepipeds in 3-D) cells obtained from subdivision can have arbitrary dimensions depending on the distribution of basis functions.

Using the MGS process and a user-specified tolerance ε, $\overline{\mathbf{Z}}^{\text{sub}}$ can be decomposed into a unitary matrix $\overline{\mathbf{Q}}_{m\times r}$ and an upper triangular matrix $\overline{\mathbf{R}}_{r\times n}$ such that

$$\frac{\|\overline{\mathbf{Z}}^{\text{sub}} - \overline{\mathbf{Q}}\,\overline{\mathbf{R}}\|}{\|\overline{\mathbf{Z}}^{\text{sub}}\|} < \varepsilon \tag{15}$$

where

$$\overline{\mathbf{Q}}^{H}\overline{\mathbf{Q}} = \overline{\mathbf{I}} \tag{16}$$

and the matrix norm $\|\overline{\mathbf{X}}\|$ is defined as the maximum singular value of the matrix $\overline{\mathbf{X}}$.

The QR decomposition of $\overline{\mathbf{Z}}^{\text{sub}}$, as shown above, requires the construction of the entire submatrix. With such a scheme the setup time for an $N \times N$ MoM matrix will be $O(N^2)$. However it is possible to obtain the compressed form of the MoM matrix in subquadratic time [11].

IV. ADVANTAGES OVER EXISTING QR ALGORITHM

The absolute setup time for RMBT-QR is large owing to the following reasons. The setup cost of the algorithm [11] is largely controlled by the accuracy of rank map predictions. An accurate and exhaustive rank map would preclude the necessity for unnecessary merges and splits and the optimum tree structure would be achieved without any backtracking or refinement within the tree structure. However, a foolproof rank-map is difficult if not impossible to construct owing to the fact that the algorithm can lead to cells with any shape and size as can be seen in Fig. 4. It is unfeasible to cover the infinite combinations of parameters, thus introducing a scope of error in the rank map. A conservative rank map will require more merges, whereas a liberal rank map will induce wastage of time by constructing unacceptable QRs, which are then discarded. Thus, the setup time is largely increased by the variability of the tree structure and the resulting backtracking and refinement.

In our work, we significantly reduce the setup time without compromising on memory or solve-time compression. The new algorithm exploits the regularity of cell size, shape, and location of a spatially balanced oct tree as in a multilevel FMM algorithm. By recourse to the FMM interaction list and by adding a few additional features to maximize compression, a regular and compressed interaction pattern is generated. The number of different interactions to be evaluated is finite and small and, therefore, an exhaustive and accurate *a priori* epsilon-rank estimation is possible. PILOT therefore incorporates the best features of the regular cube structure of multilevel FMM and the kernel-independent low-epsilon-rank compression of IES^3.

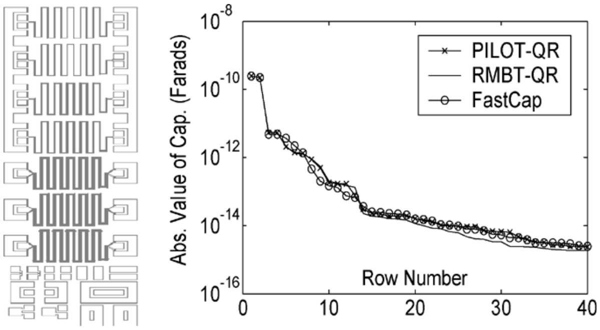

(a) (b)

Fig. 5. (a) Structure under simulation with meander lines, coplanar waveguides, pads, etc. (b) The absolute values of the first column of the capacitance matrix for the structure in Fig. 5(a) are plotted for all three algorithms. Even for relatively small off-diagonal terms the results agree remarkably well.

TABLE II
ACCURACY, MEMORY, AND TIME

Algorithm	$\overline{C}_{11}$	$\overline{C}_{1T}$	Memory	Time
PILOT	2.413e-10	-5.259e-12	365MB	19min
RMBT-QR	2.413e-10	-5.261e-12	380MB	27min
FastCap	2.412e-10	-5.257e-12	500MB	30min

V. SIMULATION RESULTS

In this section, simulation results are presented to demonstrate the accuracy and time and memory efficiency of the PILOT algorithm. For a comparative analysis, results obtained from RMBT-QR, which is based on IES^3, and FastCap are presented side-by-side. Analytic integration scheme [20] is used for near-field integrals and discretization scheme is collocation. A QR decomposition tolerance of 1e-3 is used for both PILOT and RMBT-QR, whereas for FastCap the adaptive algorithm with multipole order of two is employed. An absolute residual of 1e-3 is used for the Krylov subspace iterative solution. Diagonal preconditioners are used and the number of iterations required is observed to be the same for the same problem with all the iterative algorithms. All tests were run on a processor with 4-GB RAM and 1.6-GHz CPU speed.

In the first example, the capacitance matrix of a structure consisting of meander lines, coplanar waveguides and pads as in Fig. 5(a) is simulated. The surface of the structure is then meshed into triangular patches. Piecewise constant basis functions are defined on each triangular patch. The total number of patches for this particular problem is 0.113 million and the number of nets involved is 40. The absolute values of the 40 entries of the first column as obtained from all the three algorithms are plotted in Fig. 5(b). The elements are found to closely match the ones obtained by solving the system with RMBT-QR or FastCap even for relatively small off-diagonal terms. In Table II, selected values of the capacitance matrix as obtained with all three algorithms are presented as well as the comparative time and memory required for the process. The total time includes the entire setup and iteration time for six excitations.

The next example is that of a three-layer interconnect structure embedded in a 10 × 4 × 1-μm space. Each interconnect is 0.1 ×0.1 μm in cross section. The separations between the layers are 0.4 μm and the minimum separation between traces on the same layer is 0.15 μm. The number of triangular patches is varied from 2000 to 0.6 million and the problem is solved with ten of the interconnects as active nets and the rest as floating conductors. The time and memory requirements

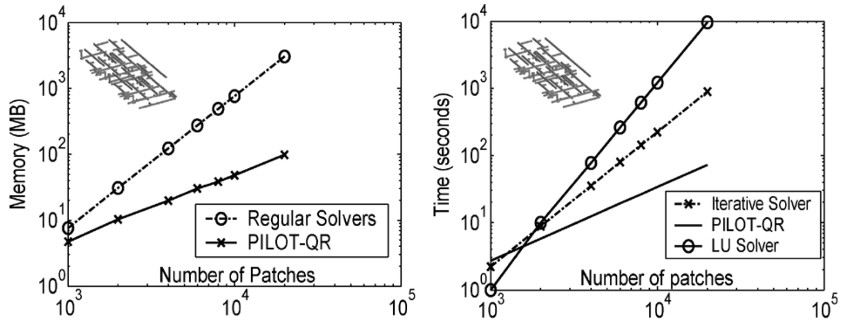

(a) (b)

Fig. 6. Performance comparison of PILOT with regular direct and iterative solvers for an interconnect bus structure. (a) Memory requirement in MB and (b) Time requirement in minutes for setup and 10 RHS solutions.

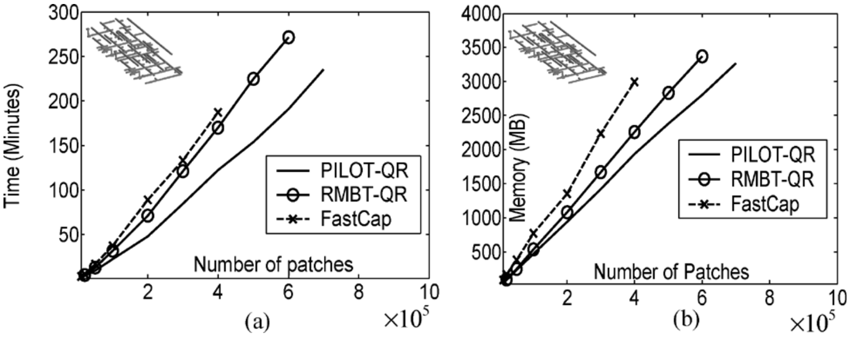

Fig. 7. Performance comparison of PILOT with existing fast solvers for an interconnect bus structure. (a) Memory requirement in MB and (b) time requirement in minutes for setup and 10 RHS solutions.

of PILOT are first compared to those of regular direct and iterative solvers in Fig. 6. It is observed that performance of PILOT is orders of magnitude superior for large number of patches. The efficiency of the algorithm is then compared to those of RMBT-QR and FastCap in Fig. 7. Due to limitations of RAM space, FastCap results are available for up to 0.3 million patches. As expected the time required by PILOT is least among the algorithms: it beats FastCap in faster matrix vector products and RMBT-QR in faster setup. Memory-wise PILOT is superior to FastCap due to greater compression. Also it is observed that PILOT, on occasions, requires less memory compared to RMBT-QR. This is because of the fact that the latter, inspite of multiple splits and merges often fails to attain the optimal tree structure compared to the physics-based interaction list in PILOT, leading to less compression than expected.

The third example demonstrates the relative advantage of QR methods as compared to FMM-based algorithms for higher number of nets and consequently larger number of matrix vector products. A package structure with 14 leads as illustrated in Fig. 8(a) is considered. The surface is meshed with 0.101 million patches and then solved for increasing number of right hand sides (1–14). The time requirements are plotted in Fig. 8(b). The constant offset between the plots of PILOT and RMBT-QR is due to the superior one-time setup cost. The memory required for the process by PILOT is 441 MB, by RMBT-QR is 445 MB and by FastCap is 700 MB.

The last example demonstrates the computing efficiency of the PILOT algorithm for very large-scale problems. The structure of example 1 is repeated in a 10 × 3 array, and shown in Fig. 9. The entire structure is meshed with 0.913 million patches. The problem is setup and solved for three different excitations. In the 4 GB of memory available, only PILOT was able to fit and run this example, and required 3.3 GB, 48 min for setup, and 90 min for solution with three RHS.

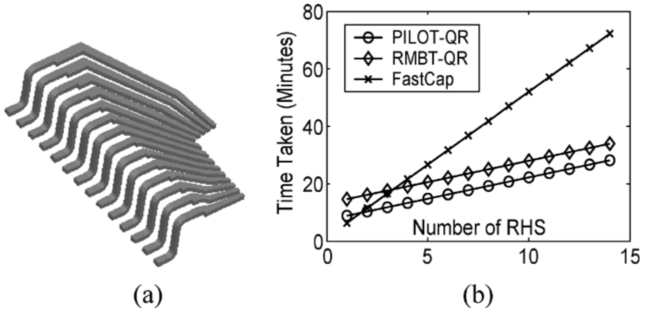

Fig. 8. Performance comparison showing efficiency of QR-based algorithms for increasing number of RHS (a) multipin structure considered for simulation consisting of 14 pins (b) setup and solve time for increasing number of RHS.

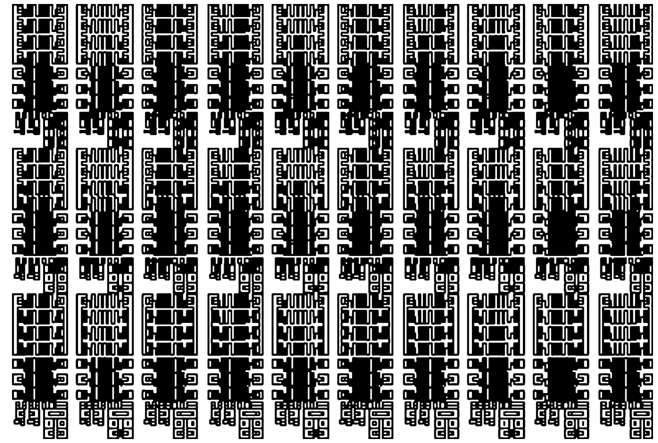

Fig. 9. Illustrated structure is generated by placing the geometry of Fig. 5(a) in a 10 × 3 array. The surface is meshed with 0.913 triangular patches.

VI. CONCLUSION

In this paper, we presented PILOT, an improved algorithm for QR-compression-based fast iterative solver and apply it to parasitic capacitance extraction problems modeled on surface-based method of moments. The regular geometry decomposition scheme of FMM and improved compression capability of IES^3 are combined together to yield an algorithm with superior efficiency. From the IES^3 perspective, the concept of rank-map and fine-tuning through merges and splits is replaced by the *a priori* merged interaction list, enabled through exploitation of the regular oct-tree structure in FMM. As a result, accurate prediction of predetermined low epsilon-rank blocks is possible and this, in turn, reduces the setup time of the process. Compared to the FMM interaction list, greater compression is achieved through merging source sibling cubes and observer cubes in their interaction list to form the merged interaction list. The resultant blocks in the list are then QR-compressed. The merged interaction list, like the rank-map of IES^3 is created only once for a given Green's function. However, due to the regular pattern of cubes, far fewer epsilon-rank evaluations are required to construct the list compared to the original binary-tree rank map.

The simulation results presented demonstrate the relative efficiency of the PILOT algorithm compared to existing QR methods and FastCap, in terms of setup time, memory, and matrix-vector products for large number of excitations. While we have discussed PILOT only in the context to parasitic capacitance extraction, continuing work focuses on its application to full-wave kernels in multilayered media for electrically small structures where classical FMM techniques break down.

ACKNOWLEDGMENT

The authors thank Prof. M. Gu, Department of Mathematics, University of California, Berkeley, for stimulating discussions on this topic, and the reviewers for their suggestions for improvement.

REFERENCES

[1] G. Servel and D. Deschacht, "On-chip crosstalk evaluation between adjacent interconnections," in *Proc. 7th IEEE Int. Conf. Electron., Circuits, Syst.*, vol. 2, 2000, pp. 827–834.

[2] Y. Im and K. Roy, "A novel high-performance predictable circuit architecture for the deep submicron era," in *Proc. IEEE Custom Integrated Circuits Conf.*, 2000, pp. 503–506.

[3] M. Kuhlmann, S. S. Sapatnekar, and K. K. Parhi, "Efficient crosstalk estimation," in *Proc. Int. Conf. Comput. Design*, 1999, pp. 266–272.

[4] E. A. Dengi and R. A. Rohrer, "On-chip interconnect modeling technologies," in *Proc. IEEE 6th Topical Meeting Elect. Perform. Electron. Packag.*, 1997, p. 41.

[5] K. Kundert, H. Chang, D. Jefferies, G. Lamant, E. Malavasi, and F. Sendig, "Design of mixed-signal systems-on-a-chip," *IEEE Trans. Computer-Aided Design*, vol. 19, pp. 1561–1571, Dec. 2000.

[6] N. K. Verghese, T. J. Schmerbech, and D. J. Allstot, *Simulation Techniques and Solutions for Mixed-Signal Coupling in Integrated Circuits*. Norwell, MA: Kluwer, 1995, p. 160.

[7] A. Husain, "Models for interconnect capacitance extraction," in *Proc. Int. Symp. Quality Electron. Design*, 2001, pp. 167–172.

[8] R. F. Harrington, *Field Computation by Moment Methods*. New York: IEEE Press, 1991.

[9] T.-Y. Chou and Z. J. Cendes, "Capacitance calculation of IC packages using the finite element method and planes of symmetry," *IEEE Trans. Computer-Aided Design*, vol. 13, pp. 1159–1166, Sept. 1994.

[10] S. Kapur and D. E. Long, "IES^3: efficient electrostatic and electromagnetic solution," *IEEE Comput. Sci. Eng.*, vol. 5, pp. 60–67, Oct./Dec. 1998.

[11] S. Kapur and D. Long, "IES^3: A fast integral equation solver for efficient 3-dimensional extraction," in *Proc. IEEE/ACM Int. Conf. Computer-Aided Design*, Nov. 1997, pp. 448–455.

[12] S. Kapur, D. Long, and J. Zhao, "Efficient fullwave simulation in layered lossy medium," in *Proc. IEEE Custom Integrated Circuits Conf.*, May 1998, pp. 211–214.

[13] K. Nabors and J. White, "FastCap: A multipole accelerated 3-D capacitance extraction program," *IEEE Trans. Computer-Aided Design*, vol. 10, pp. 1447–1459, Nov. 1991.

[14] J. R. Phillips and J. White, "A precorrected-FFT method for electrostatic analysis of complicated 3-D structures," *IEEE Trans. Computer-Aided Design*, vol. 16, pp. 1059–1072, Oct. 1997.

[15] H. A. van der Vorst, "Krylov subspace iteration," *Comput. Sci. Eng.*, vol. 2, no. 1, pp. 32–37, 2000.

[16] G. H. Golub and C. F. Van Loan, *Matrix Computations*, 2nd ed. Baltimore, MD: Johns Hopkins Univ. Press, 1989.

[17] A. Cangellaris and Y. Ling, "Rapid calculation of electrostatic green's functions in layered dielectrics," *IEEE Trans. Magn.*, vol. 37, pp. 3133–3136, Sept. 2001.

[18] R. J. Anderson, "Tree data-structures for N-body simulation," *SIAM J. Comput.*, vol. 28, no. 6, pp. 1923–1940.

[19] A. E. Ruehli and P. A. Brennan, "Efficient capacitance calculations for three-dimensional multiconductor systems," *IEEE Trans. Microwave Theory Tech.*, vol. 29, pp. 76–82, Feb. 1973.

[20] D. Wilton, S. Rao, A. Glisson, D. Schaubert, O. Al-Bundak, and C. Butler, "Potential integrals for uniform and linear source distributions on polygonal and polyhedral domains," *IEEE Trans. Antennas Propagat.*, vol. 32, pp. 276–281, Mar. 1984.

Accurate and Efficient Modeling of SOI MOSFET With Technology Independent Neural Networks

S. Hatami, M. Y. Azizi, H. R. Bahrami, D. Motavalizadeh, and
A. Afzali-Kusha

***Abstract*—This paper presents neural network (NN) approaches for modeling the I–V characteristics of silicon-on-insulator MOSFETs. The modeling approach is technology independent, fast, and accurate, which makes it suitable for circuit simulators. In the model, two different NN architectures, namely, multilayer perceptron and generalized radial basis function, are used and compared. To increase the training efficiency of the NN, both modular and region partitioning methods have been proposed and utilized. In addition, two approaches for obtaining the transconductance and output conductance of the device are discussed. The first approach makes use of an NN for the conductances, while the second uses the numerical differentiation of the I-V results. To confirm the accuracy of the model, the drain-current characteristics as well as conductances obtained by the model are compared to the simulation data for the points where the NNs are not trained. The comparison shows excellent agreements with relative errors of around 1% over a wide range of drain and gate voltages as well as channel lengths and widths.**

***Index Terms*—Circuit simulation, fully depleted (FD), I-V characteristic, neural network (NN) modeling, partially depleted (PD), silicon-on-insulator (SOI) modeling, technology independent modeling, unified modeling.**

I. INTRODUCTION

MOSFET devices in silicon-on-insulator (SOI) technology have many advantages over bulk counterparts, such as lower parasitic capacitance and radiation hardness. The silicon layer on the oxide

---

Manuscript received March 18, 2003; revised December 19, 2003. This paper was recommended by Associate Editor C.-J. R. Shi.

The authors are with the Department of Electrical and Computer Engineering, Faculty of Engineering, University of Tehran, Tehran, Iran (e-mail: hatami_safar@yahoo.com; y.azizi@ece.ut.ac.ir; hrbahrami@yahoo.com; motavalizadeh@yahoo.com; afzali5@gmail.com).

Digital Object Identifier 10.1109/TCAD.2004.836725

Efficient Sensitivity Analysis using Coupled Circuit-Electromagnetic Simulation

Yong Wang*, Vikram Jandhyala and C.J. Richard Shi
Dept. of Electrical Engineering, University of Washington
Box 352500, Seattle WA 98195, Ph: 206-543-2186, Fax: 206-543-2186
Email: jandhyala@ee.washington.edu

With the rapidly increasing interest in applications such as radio frequency wireless communication and high-speed data processing, electronic systems are required to work at progressively higher frequencies. As the operating frequencies enter the high GHz range, phenomena such as cross talk, parasitic-induced delay, and substrate losses etc. can no longer be neglected. In order to design high-performance systems with short time-to-market, it is essential to perform EM simulation to include these layout related effects at design stages prior to fabrication. In particular, sensitivity of EM-related behavior, i.e. the analysis of variation of results with parametric changes in design, layout and material distribution is very important.

Traditional sensitivity computation employs a finite difference approach, for example, the sensitivity of a system performance P using the forward finite-difference approximation can be written as $\frac{\partial P(x_i)}{\partial x_i} \approx \frac{P(x_i + \Delta x_i) - P(x_i)}{\Delta x_i}$, where x_i is a design variable. In such methods, the system needs to be solved twice for each design variable thus making the method computationally expensive. Moreover, the accuracy of this method depends on the step size Δx_i; while a large value of Δx_i will lead to inaccurate sensitivity, a small value could also introduce numerical error due to solver precision. Recent approaches (Georgieva *et. al*., IEEE Trans. MTT, 50, 2751-2758, 2002) using the *adjoint variable method* greatly reduce the computation cost by employing the fact that the inverse of the system matrix can be derived with little cost once the problem is solved, and prove to be an effective way for calculating sensitivity.

The simulation approach used in this work is based on a coupled circuit-electromagnetic formulation. In this approach the system unknowns consist of both EM parts (typically surface currents related to the method of moments) and circuit parts (node voltages and branch currents). The system performance is itself typically related to a sub-set of the circuit unknowns, which are system unknowns in the coupled formulation. This leads to the sensitivity calculation being more convenient than with the adjoint method. Therefore there is no requirement to introduce additional adjoint variables, and the only extra computation needed for the proposed method is the calculation of the spatial derivative of the overall coupled system matrix versus design variable x_i, in addition to a few simple matrix-vector multiplications and additions. The spatial derivatives of the basis functions used in the system matrix are derived by analytical spatial differentiation of near- and far-field expressions of the method of moments matrix elements.

Efficient EM sensitivity computation as discussed above can help high frequency circuit design in two ways. First, it enables identification of EM structures that are extremely sensitive to small variations of geometric or material parameters; such structures could cause the system performances to be very different and unacceptable due to process and layout variation. Second, efficient and accurate sensitivity calculation enables gradient-based optimization of EM structures, which is useful to automate high-frequency circuit design.

Prediction of Package and Chip Substrate Loss Effects in Microelectronic Circuits Using Time-Domain Surface-Integral Equations

Chuanyi Yang* and Vikram Jandhyala
Dept. of Electrical Engineering, University of Washington
Box 352500, Seattle WA 98195, Ph: 206-543-2186, Fax: 206-543-2186
Email : {cyang1,jandhyala}@ee.washington.edu

With the modern microelectronic industry entering a new era featured by progressively higher speed and higher integration mixed-signal systems on chip, accurate modeling of distributed electromagnetic behavior of sections which may includes signal traces, power planes, substrates etc, is crucial during the design flow. Driven by broadband and non-linear circuit design, time domain coupled electromagnetic and circuit simulation has been gaining popularity. In particular, integral equation methods have proven to be useful since radiation conditions are built in and only surface meshing and modeling is needed. In this work, the time-domain integral equation (TDIE) method is enhanced to model realistic loss behavior in substrates, which is a crucial component for quality factor prediction of integrated passives, as well as for thermal pattern prediction.

The EM simulation environment in present and future 3D integrated circuits is characterized by multiple piecewise homogeneous regions. Each region is comprised of lossy materials, which may or not have a strong impact on the overall performance. In general, for higher speed and higher sensitivity systems such as RF and analog methods, the loss is a crucial factor in determining system specifications and performance. The TDIE approach has been shown to work with lossy material (M. J. Blunk and S. P. Walker, Antennas and Propa, 49, 875-879, 2001) wherein the Green's functions, besides possessing delta functions in time, also include a broadly exponentially decaying "wake". This leads to the implementation issue that the spatial integrals at retarded times have to be replaced by temporal convolutions. This convolution brings not only coding complexity but also increases the computational cost dramatically.

In the presented work, the multi-region substrate geometry is addressed with a TDIE solver. An equivalent surface approach for each region is used along with the following method to tackle the lossy medium Green's function. To circumvent the difficulty caused by the convolution in time, the decaying "wake" in the Green function is approximated by a sum of decaying exponentials via Prony's method. It is shown that for circuit dimensions and realistic losses, the decaying "wake" changes slowly with the variation of the distance between the source and observation point. This allows the building of an exponential fitting table for discrete distances. The use of the exponential models permit the convolutions in time to be computed recursively. This then achieves the purpose of reducing computational complexity, with an added constant, to be the same as that of a TDIE solver for lossless media.

AN ITERATION-FREE FAST MULTILEVEL SOLVER FOR DENSE METHOD OF MOMENT SYSTEMS

Dipanjan Gope (*dips@u.washington.edu*) and
Vikram Jandhyala (*jandhyala@ee.washington.edu*)
Department of Electrical Engineering, Box-352500,
The University of Washington, Seattle, WA-98195.
Telephone: 206-543-2186 Fax: 206-543-3842

ABSTRACT

A fast multilevel direct solver for the Method of Moments - based analysis of electrically small structures is presented. The approach is based on a combination of low-rank decompositions and fill-in control. It is particularly advantageous for multiple right-hand-side problems such as those encountered in digital circuit and IC analyses, as is demonstrated by numerical simulation results presented here.

I. Introduction

Quasi-static parasitic extraction is an important problem in digital circuits and in mixed signal IC analysis. While several fast integral equation-based techniques have been proposed and developed to address this problem, practically all these methods including Fast Multipole Methods, FFT methods, QR-based methods, rely on fast algorithms to accelerate the iterative solution of the Method of Moments (MoM) system. These approaches primarily solve one right hand side (RHS) at a time, and therefore become considerably slower when a problem involves a large number of RHS vectors such as substrate coupling, or parasitic extraction in the presence of a large number of nets. Moreover, in certain formulations, such as the Partial Equivalent Electric Circuit (PEEC) method, or in coupled electromagnetic circuit simulation, it is advantageous to rapidly obtain the explicit inverse or LU factors of the MoM system.

While fast iterative solvers reduce the cost of $N \times N$ MoM matrix-vector products to O(N) or O(N log$N$) from O(N^2), the overall solution cost is also proportional to the number of RHSs and the number of iterations per RHS. The overall cost for large RHS problems can be very large depending on the number of iterations or the conditioning of the system. A regular direct solver such as LU decomposition, on the other hand, has no iterative steps, and the single initial O(N^3) decomposition step is performed only once. Subsequent solutions are obtained through an O(N^2) forward and backward substitution. While the relative advantage of the LU method increases with the number of RHSs (more so if the problem is inherently poorly conditioned), the large costs of the initial step and subsequent solution steps relative to fast iterative methods is a large bottleneck. Moreover, regular direct solvers consume O(N^2) memory for matrix storage compared to the O(N) or O($N \log N$) memory requirements of fast iterative solvers.

The multilevel schemes developed for fast matrix-vector products do not inherently lend themselves to obtain fast methods for direct decomposition or inversion; however Canning and Rogovin [1] suggested sparse-LU and Sherman-Morrison-Woodbury schemes based on a multilevel sparse representation of the full-wave MoM matrix. In their work, an *a priori* low-rank structure, or class of structures, is assumed for the MoM matrix. In this work the QR-based low-rank representation and the sparse-LU computation are integrated in order to alleviate the computational overhead associated with fill-ins for an arbitrary block structure and thus make feasible the fast analysis of any 3D structures. Here a fast iteration free scheme to rapidly setup the inverse of the MoM matrix is proposed. The inverse so generated can also be applied to each RHS in quick time. This approach thus bypasses the need for an iterative solver, associated pre-conditioning and the uncertainty and time of convergence in an iterative scheme. The method is general enough in nature to be relevant to both quasi-static and full-wave analyses (electrically small structures), in free-space and in multi-layered media.

II. Approach

Capacitance problems formulated using MoM are solved by transforming the electrostatic equation $\nabla^2\phi(\mathbf{r}) = -\rho(\mathbf{r})/\varepsilon$ relating potential ϕ and charge-density ρ to a related integral equation. The discretization of the equation results in a matrix system of the form $\bar{\mathbf{Z}}\mathbf{I} = \mathbf{V}$ where the $N \times N$ MoM matrix $\bar{\mathbf{Z}}$ is a dense Green's function matrix, **I** represent the unknown coefficients of known basis functions for charge density, and **V** represents the known potential excitation. Each element of the MoM matrix denotes the interaction between 2 basis functions and is written as follows:

$$\bar{\mathbf{Z}}(\mathrm{j,i}) = \int_{S_j} ds\, t_j(\mathbf{r}) \int_{S_i} ds' g(\mathbf{r},\mathbf{r}')\, f_i(\mathbf{r}')$$

where t_j is the testing function defined over S_j, f_i is the basis function defined over S_i and $\mathrm{g}(\mathbf{r},\mathbf{r}')$ is the relevant greens function. In the electrostatic case for P disconnected conductors, each column of the required $P \times P$ capacitance matrix is obtained by enforcing a voltage of 1V on the excited conductor, 0V on all other conductors, solving the above system, and integrating the charge density over each conductor. The $N \times N$ system of equations is therefore solved P times to obtain the capacitance matrix.

The state-of-the-art fast iterative solver based on the QR method reduces the cost of doing the matrix vector product $\bar{\mathbf{Z}}\mathbf{I}$ to O(*NlogN*). It takes advantage of the smoothness of the Green's function in decomposing the rank deficient far field sub-matrix of the MoM using QR decomposition. In QR decomposition a sub-matrix $\bar{\mathbf{A}}$ of the MoM matrix $\bar{\mathbf{Z}}$ can be decomposed as $\bar{\mathbf{A}}_{\mathrm{mxn}} = \bar{\mathbf{Q}}_{\mathrm{mxr}}\bar{\mathbf{R}}_{\mathrm{rxn}}$ where $\bar{\mathbf{R}}$ is upper triangular and Q is orthogonal i.e. $\bar{\mathbf{Q}}^{\mathrm{T}}\bar{\mathbf{Q}} = \bar{\mathbf{I}}$. However the cost of this scheme is proportional to the number of iterations and the number of RHS and therefore becomes quite expensive for large number of RHS, as is the case in IC parasitic analysis.

The presented method relies on a combination of a fast compression scheme for reduced representation of the MoM matrix using the modified Gram-Schmidt method, followed by a fast method to LU-decompose the resultant compressed matrix. The compression scheme is based on the separation of the MoM matrix into dominant (near field) and low rank (far-field) portion based on a cost estimating algorithm. Subsequently the sparse LU scheme is applied to this multilevel sparse structure of the MoM matrix.

Developing the sparse LU structure:

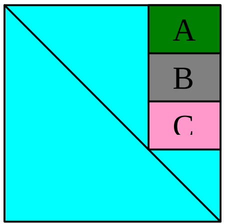

Consider the low ranked sub matrix $\bar{\mathbf{A}}$ and also assume its rank is 1 so that $\bar{\mathbf{A}}_{\mathrm{mxn}} = \bar{\mathbf{Q}}_{\mathrm{A\,mx1}}\bar{\mathbf{R}}_{\mathrm{A1xn}}$. The first row of this block will remain the same in its LU form. Consider the second row of the block. Notice that all the elements of this row may be changed to its LU form by changing the second element of $\bar{\mathbf{Q}}_{\mathrm{A}}$ as follows $\bar{\mathbf{Q}}_{\mathrm{A}}^{\mathrm{lu}}(2) = \bar{\mathbf{Q}}_{\mathrm{A}}(2) - \bar{\mathbf{Q}}_{\mathrm{A}}(1) * \mathrm{L}(1)$ where L(1) is the proper multiplying coefficient from the lower triangular part. Thus the sparse LU form of block A becomes $\bar{\mathbf{Q}}_{\mathrm{A}}^{\mathrm{lu}}\bar{\mathbf{R}}_{\mathrm{A}}$. For block B we not only need to modify the $\bar{\mathbf{Q}}_{\mathrm{B}}$ but also need contributions from block A in the form of fill-ins. The sparse LU representation for block B will thus be in the form of $\bar{\mathbf{Q}}_{\mathrm{B}}^{\mathrm{lu}}\bar{\mathbf{R}}_{\mathrm{B}} - \bar{\mathbf{F}}_{\mathrm{AB}}\bar{\mathbf{R}}_{\mathrm{A}}$. For block C similarly we need to modify the $\bar{\mathbf{Q}}_{\mathrm{C}}$ as well as obtain fill-ins from blocks A and B. The sparse representation of block C thus looks like $\bar{\mathbf{Q}}_{\mathrm{C}}^{\mathrm{lu}}\bar{\mathbf{R}}_{\mathrm{C}} - \bar{\mathbf{F}}_{\mathrm{AC}}\bar{\mathbf{R}}_{\mathrm{A}} - \bar{\mathbf{F}}_{\mathrm{BC}}\bar{\mathbf{R}}_{\mathrm{B}}$ However it should be noted here that when we are working on block C, block B has been modified to its LU form. Therefore when we manipulate $\bar{\mathbf{F}}_{\mathrm{BC}}$ we need to update $\bar{\mathbf{F}}_{\mathrm{AC}}$ to counter for $\bar{\mathbf{F}}_{\mathrm{AB}}$. Thus we see that $\bar{\mathbf{F}}_{\mathrm{AC}}$ needs to be modified twice, once for the direct contribution of block A to block C and second indirectly through the contribution of block B to block C. Therefore the number of computations required to generate the fill-ins is greater than the storage required by them due to these indirect effects. In the solving step during forward and backward substitution also we can reduce the number of computations by using the developed LU sparse representation.

Summarizing the process:

In the L part *Q is unaltered R is altered and F s (fill-ins) acting as substitute R s of left blocks are created.* In the U part *Q is altered R is unaltered and F s acting as substitute Q s of upper blocks are created.*

Figure 1: The top 3 QR blocks of the U part of LU

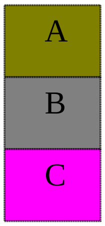

$$\overline{\mathbf{Q}}^{lu}_{A\,m_A x r_A} * \overline{\mathbf{R}}_{A\,r_A x n_A}$$

We compute $\overline{\mathbf{Q}}^{lu}_{A}(i,r)=\overline{\mathbf{Q}}_{A}(i,r)-\sum_{n=1}^{i-1}\overline{\mathbf{Q}}^{lu}_{A}(n,r)*L(n)$

$$\overline{\mathbf{Q}}^{lu}_{B\,m_B x r_B} * \overline{\mathbf{R}}_{B\,r_B x n_B} - \overline{\mathbf{F}}_{AB\,m_B x r_A} * \overline{\mathbf{R}}_{A\,r_A x n_A}$$

We compute $\overline{\mathbf{F}}_{AB}(i,r)=\sum_{n=1}^{m_A}\overline{\mathbf{Q}}^{lu}_{A}(n,r)*L(n)$

$$\overline{\mathbf{Q}}^{lu}_{C\,m_C x r_C} * \overline{\mathbf{R}}_{B\,r_C x n_C} - \overline{\mathbf{F}}_{AC\,m_C x r_A} * \overline{\mathbf{R}}_{A\,r_A x n_A} - \overline{\mathbf{F}}_{BC\,m_c x r_B} * \overline{\mathbf{R}}_{B\,r_B x n_B}$$

We compute $\overline{\mathbf{F}}_{AC}(i,r)=\sum_{n=1}^{m_A}\overline{\mathbf{Q}}^{lu}_{A}(n,r)*L(n)+\sum_{n=1}^{m_B}\overline{\mathbf{F}}_{AB}(n,r)*L(n)$

Developing the optimized sparse QR structure: The fill-ins require extra memory and cost along with the Q s and the R s. So the algorithm that optimizes the rank based memory of the Qs Rs, applicable to the QR based iterative solver is obviously not suitable for this particular purpose. The 2 main operations are the split and the merge.

Outline of the split Algorithm: (The merge algorithm is exactly similar)

1. Find entry from the list.
2. Split dense block into 2 diagonal dense blocks and 2 non-diagonal QR blocks or QR block into 4 QR blocks (Ensures that the final block structure has a dense block diagonal part + all non-diagonal parts are expressed as QR)
3. Calculate the new cost of sparse LU setup from the knowledge of number of rows and columns of the then block structure i.e. the one obtained after the recent split.
4. If (new cost > previous cost) retain the split form of the block.
   Else retain the non-split form of the block.

III. Quasi-static Simulation Results:

We considered a number of real life 3D structures like 5 by 5 bus, comb drive, multiple pin packages, multi-layered contacts (substrate coupling problem). Some of the results are shown here while others are tabulated below. In the plots, SLU denotes our sparse LU method.

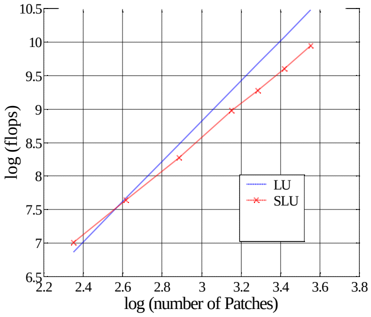

Figure 2: LU setup cost

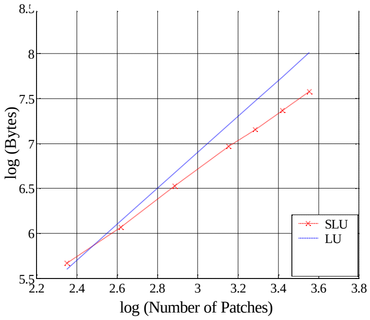

Figure 3: LU memory cost

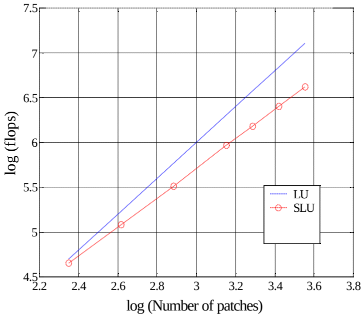

Figure 4: Solve cost per RHS

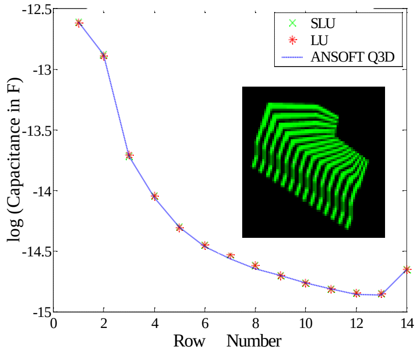

Figure 5: First Column of capacitance matrix

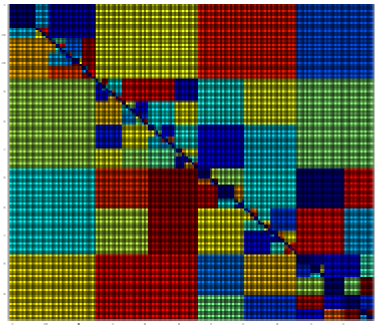

Figure 6: QR block structure obtained by the algorithm

Table 1: The order and constants observed

Type of problem	Slope of setup	Slope of solve per RHS	Slope of Memory
Thin strip	2.29	1.29	1.29
Refined Plate	2.43	1.65	1.65
5 by 5 bus	2.41	1.667	1.65
Comb drive	2.31	1.68	1.61
Multi pin package	2.51	1.667	1.61

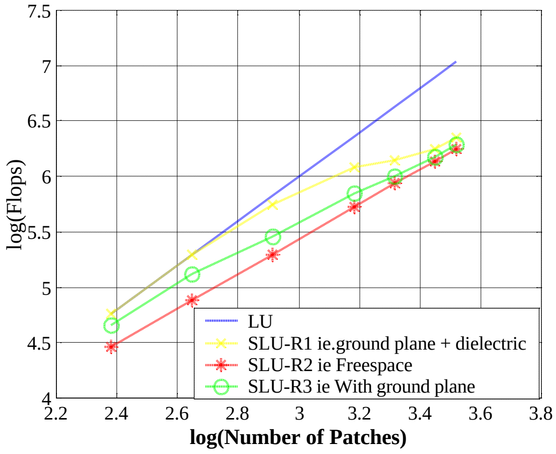

Figure 7: Solve time for multi-layered case

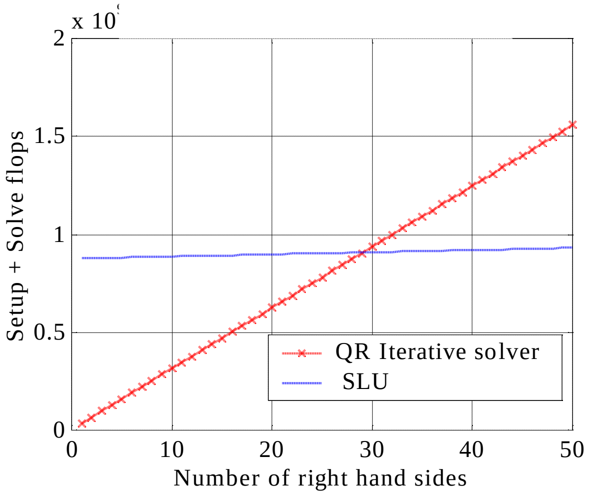

Figure 8: Solution time for multiple RHS

IV. Conclusions:

This new method exploits the QR structure with no a priori assumptions. It has been shown that this fast direct solver is suitable for multiple right hand sides' problem and that it can be used for multi-layered media. The QR decomposition concept is known to work well with full-wave MoM for electrically small structures. Thus this method needs very slight changes to be made adaptable to complex full-wave analysis for small electrical structures. Also since the above schemes are based on simple linear algebraic methods the possibility of coupled fast EM-circuit matrix solutions can be seen. The limitation of the schemes discussed however lies in the fact that it will break down for high frequencies and will cost wise not be useful for less number of RHS.

A similar approach using the Sherman-Morrison-Woodbury formula (SMW) is also analyzed. The direct inverse setup time is found to be more expensive than the sparse LU method. Also since the MoM inverse cannot be represented in a sparse form the solution step for every RHS remains $O(N^2)$. This makes the generated inverse unfavorable for use in the solve step. However in the PEEC approach, where each unknown is treated as a separate entity, the generated inverse would directly give the "detailed" capacitance matrix. Thus SMW eliminates the cost of solving for N right hand sides and becomes a better option. Further work is being carried on in this topic.

Acknowledgements: This work was partially supported by Ansoft Corporation, Pittsburgh, The Royalty Research Fund, University of Washington and by NSF CAREER grant ECS-0093102.

References:

[1] Francis X. Canning and Kevin Rogovin, "Fast Direct Solution of Standard Moment-Method Matrices" *IEEE Antennas and Propagation Magazine* Vol. 40 No. 3 pp. 15 – 26, June 1998.
[2] S.Kapur and D.E.Long, "IES^3: Efficient Electrostatic and Electromagnetic Solution" *IEEE Computer Sci. and Engg.* 5(4) pp. 60-67 Oct.-Dec 1998.
[3] G.H.Golub and C.F.Van Loan Matrix Computations 2nd Ed. The Johns Hopkins University Press Baltimore 1989

Coupled Electromagnetic-Circuit Simulation of Arbitrarily-Shaped Conducting Structures

Yong Wang, Vikram Jandhyala, and C.-J. Richard Shi
Dept. of Electrical Engineering, University of Washington, Seattle, WA 98195
Phone: (206)-221-5720 Fax: (206)-543-3842 Email: {yongw, jandhyala, cjshi}@ee.washington.edu

Abstract–This paper presents a triangular surface mesh-based formulation of the Partial Element Equivalent Circuit (PEEC) approach. Rao-Wilton-Glisson (RWG) basis functions defined on triangular tessellations are used to model arbitrarily-shaped conducting structures via SPICE compatible netlists. This approach is potentially useful for modeling on-chip electromagnetic interactions.

I. INTRODUCTION

The PEEC method [1] is a particularly effective approach for modeling the electromagnetic effects of a multi-wire or multi-conductor structure using SPICE compatible elements. The classical PEEC method relies on a longitudinal filament discretization of all structures. This paradigm, which assumes a direction of current flow along the length of the filament, is well-suited for thin and long interconnect structures. A System-on-Chip (SoC) scenario [2], however, involves some arbitrarily shaped structures, including inductors, regular and split ground planes wherein the filament approach is inherently not well suited, because of the arbitrary directions of current flow in such structures.

In this paper, we utilize Rao-Wilton-Glisson (RWG) basis functions [3,4], which are linear basis functions defined over triangles, to model conductors using surface triangular meshes [5]. Interactions between RWG basis functions are then represented as circuit elements, in a manner analogous to that used in the classic filament-based PEEC approach. This surface-only formulation includes a surface-impedance term to represent high-frequency skin effects and should prove to be valuable for modeling conducting structures in SoC scenarios.

II. TRIANGULAR MESHES AND PARTIAL ELEMENT EQUIVALENT CIRCUIT EXTRACTION

A typical electromagnetic problem involving three-dimensional multi-wire or multi-conductor structures can be described using the Electric Field Integral Equation (EFIE) [3]. In the EFIE formulation, the unknowns are scalar potential φ, surface charge density ρ and current density $\overline{J}$. Note the explicit use of potential as an unknown for low-frequency stability and compatibility with circuit-level voltages. The resulting EFIE is

$$j\omega \frac{\mu}{4\pi}\int_S \frac{\overline{\mathbf{J}}(\mathbf{r}')}{|\mathbf{r}-\mathbf{r}'|}ds' + (\nabla\varphi)(\mathbf{r}) = -R\,\overline{\mathbf{J}}(\mathbf{r}) \tag{1}$$

$$\varphi = \frac{1}{4\pi\varepsilon}\int_S \frac{\rho(\mathbf{r}')}{|\mathbf{r}-\mathbf{r}'|}ds' \tag{2}$$

where R is the surface resistance for non-ideal conductors and is given by $\mathrm{R} = \mathrm{Re}\left(\sqrt{\frac{j\omega\mu}{2\sigma}}\right)$ and σ is the volume conductivity.

Assuming a triangular tessellation of the conductor surfaces with N_e non-boundary edges and N_p patches, Eqns. (1) and (2) can be recast as

$$j\omega\overline{\mathbf{L}}\mathbf{I} + \overline{\mathbf{A}}\varphi = \overline{\mathbf{R}}\mathbf{I} \tag{3}$$

$$\overline{\mathbf{P}}\,\mathbf{Q} = \mathbf{V} \tag{4}$$

where $L_{ij} = \frac{\mu}{4\pi}\int_S\int_S \frac{\mathbf{f}_j(\mathbf{r}')}{|\mathbf{r}-\mathbf{r}'|}ds'\cdot\mathbf{f}_i(\mathbf{r}')\,ds \quad i,j = 1,..,N_e$, with **f** denoting an RWG basis function, $\overline{\mathbf{A}}$ is a sparse coefficient matrix with two non-zero elements at each row, $P_{ij} = \frac{1}{4\pi\varepsilon}\int_S\int_S \frac{\nabla'\cdot\mathbf{f}_j(\mathbf{r}')}{|\mathbf{r}-\mathbf{r}'|}\nabla\cdot\mathbf{f}_i(r)\,ds\,ds' \quad i,j = 1,\ldots,N_p$, and $\overline{R}$ is a sparse, nearly diagonal matrix, with $R_{ij} = R\int \mathbf{f}_i(\mathbf{r})\cdot\mathbf{f}_j(\mathbf{r})\,ds$ if edge *i* and edge *j* share a common triangle, and 0 otherwise.

As in the classic filament-based PEEC method, mutual capacitances and inductances can be obtained through Voltage Controlled Voltage Sources (VCVSs) available in SPICE. For example, using the relation $j\omega L_{ij}I_j = L_{ij}(j\omega I_j) = L_{ij}\frac{\varphi_{jj}}{L_{jj}}$, mutual inductance can be represented by a VCVS. Off-diagonal R_{ij} entries are represented by Current Controlled Voltage Sources. The triangular mesh-based circuit topology is shown in Fig. 1, and a typical PEEC cell is shown in Fig. 2.

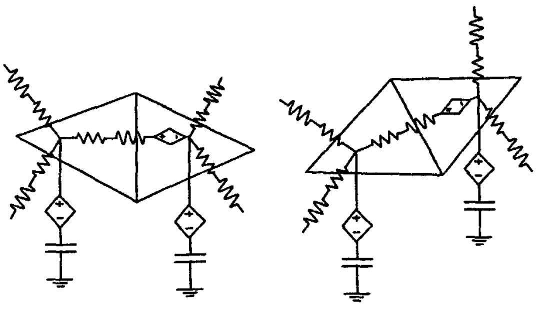

Figure 1. PEEC elements defined on triangular meshes.

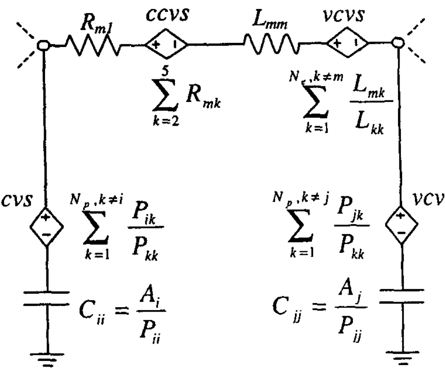

Figure 2. A typical PEEC cell.

III. NUMERICAL RESULTS

The first example, depicted in Fig. 3, is an interconnect over a ground plane, and is used to validate the triangular approach against the previously published filament PEEC solution [6]. The interconnect is driven by a voltage source and is terminated by 86 Ohm resistors at both ends. The ground plane is 2.0cm long by 1.0cm wide. The interconnect is 2.0cm long, 1mm wide and 0.5mm above the ground plane. The input impedance shown in Fig. 3 (b) matches very well with the published filament PEEC result [6].

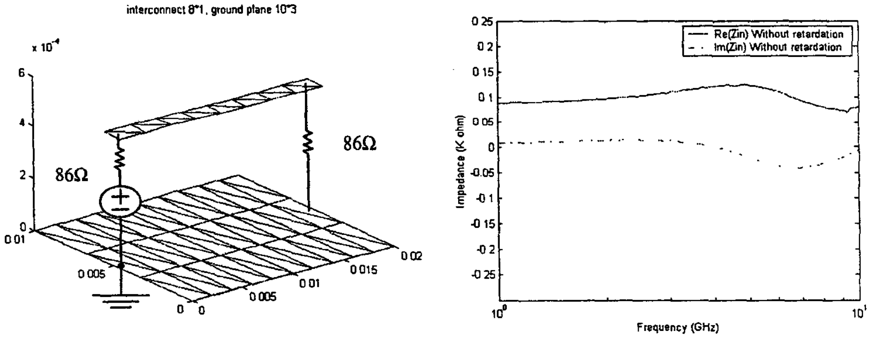

(a) (b)

Figure 3. (a) Triangular discretization of the strip and the ground plane. (b) Input impedance of active line.

The second example illustrates the use of the triangle-based PEEC for time-domain cross-talk analysis. We consider two scenarios as shown in Fig. 4; in one scenario two strips are 0.5mm above the ground plane and 1mm apart, and in the other the two strips are also 0.5mm above the ground plane and 1mm apart at the near end, but 3mm apart at the far end. When a pulse input is added at one strip, the cross-talk voltages can be observed via a triangle-based PEEC time-domain simulation, as shown in Fig. 5. The simulation results show that the wider separation results in a smaller cross talk voltage.

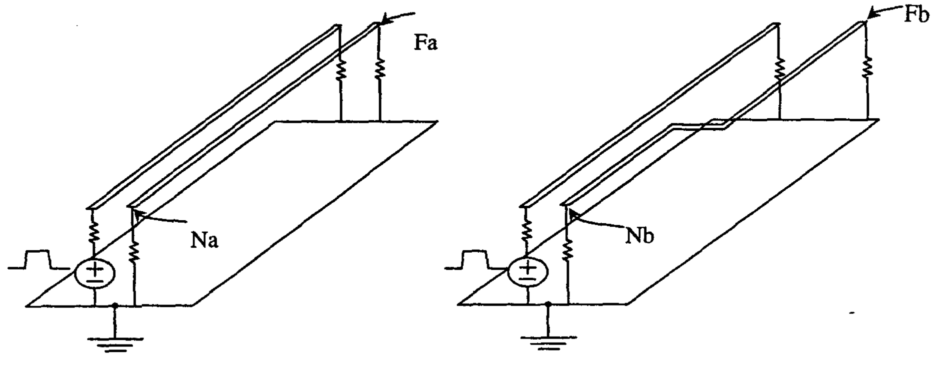

(a) (b)

Figure 4. (a) Two parallel strips. (b) Two strips, with larger distance at the far end.

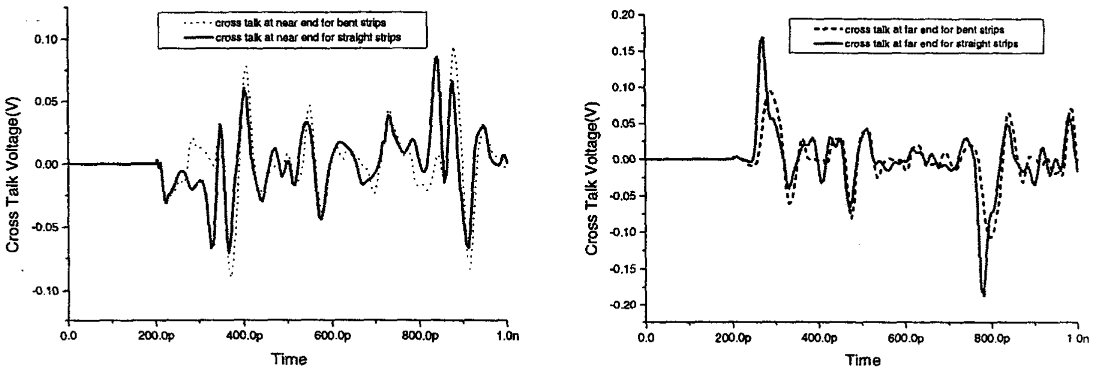

(a) (b)

Figure 5. (a) Cross talk at the near end. (b) Cross talk at the far end.

The third example is a spiral inductor, of dimensions 200μm×200μm and 30μm above the ground plane, as illustrated in Fig. 6. The line width and the gap width of the inductor are both 20μm.

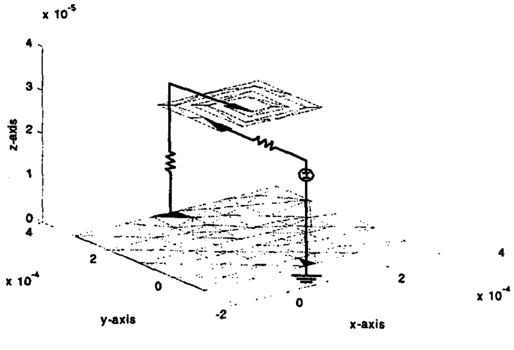

Figure 6. Spiral inductor above a ground plane.

The triangular PEEC approach is used to model the induced current distribution on the ground plane at both low and high frequencies, 1KHz and 1GHz respectively. The results of triangle PEEC simulation are given in Figs. 7(a) and 7(b). The physically correct behavior associated with low- and high- frequency induced currents is reproduced: while the currents are spread out over the ground plane at lower frequencies, the increased inductive component of impedance at higher frequencies dictates that the induced current crowd under the inductor. This phenomenon is modeled very accurately with the triangular discretization. It is expected that this ability to model true current distributions will make the triangular PEEC method particularly suited for SoC applications.

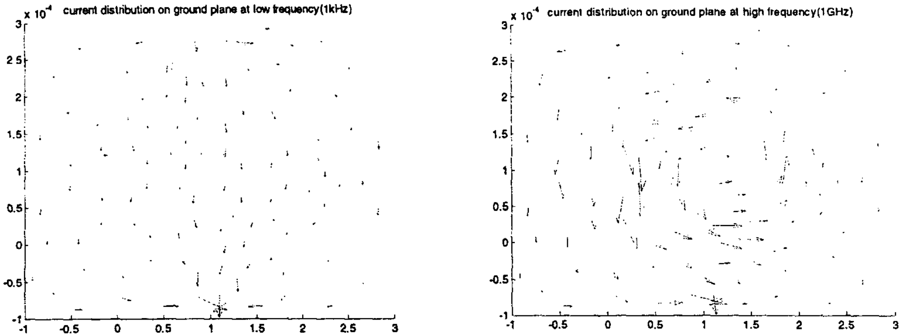

(a) (b)

Figure 7. (a) Low frequency ground plane current distribution (1KHz). (b) High frequency ground plane current distribution (1GHz).

IV. CONCLUSIONS

A modified PEEC approach based on triangular tessellations on surface meshes was presented. The resulting partial capacitance, inductance, and surface resistance terms were used to obtain an equivalent SPICE model. Numerical results were presented to validate the approach and demonstrate its advantages in modeling induced and return current densities. The approach also has the advantage of modeling thin structures with a two-dimensional formulation. It is expected that a hybrid approach, with filaments to model current flow on longitudinal interconnects, and triangles to model arbitrarily-shaped structures and ground planes will yield the best results in terms of accuracy and efficiency. Future work will aim at enhancements to the triangle-based formulation including a full-wave time domain implementation, a fast matrix-vector multiply scheme, and reduced-order modeling.

This work was supported in part by the Defense Advanced Research Projects Agency under the NeoCAD initiative, in part by the National Science Foundation and the Semiconductor Research Corporation under a joint initiative on Mixed-Signal Electronic Technologies, and in part by by NSF CAREER grant ECS-0093102.

REFERENCES

[1] A. E. Ruehli, "Equivalent circuit models for three-dimensional multiconductor systems," *IEEE Trans. on Microwave. Theory and Techniques.*, vol. MTT22 (3), pp. 216-221, March 1974.

[2] K. Kundert, H. Chang, D. Jefferies, G. Lamant, E. Malavasi, and F. Sendig, "Design of mixed-signal systems-on-a-chip," *IEEE Trans. on Computer-Aided Design of Integrated Circuits and Systems,* vol. 19 no.12, pp. 1561–1571, Dec. 2000.

[3] Andrew F. Peterson, Scott L. Ray, Raj Mittra, *Computational Methods for Electromagnetics*, IEEE PRESS, 1997.

[4] S. M. Rao, D. R. Wilton, and A. W. Glisson, "Electromagnetic scattering by surfaces of arbitrary shape," *IEEE Trans. Antennas Propagation,* vol. AP-30, pp. 409-418, May 1982.

[5] Coen, G., Fache, N., de Zutter, D., Lagasse, P. "Automatic equivalent discrete distributed circuit generation for microstrip interconnection discontinuities," *Proc. Antennas and Propagation Society International Symposium,* 1994. AP-S. Digest , Volume: 3, pp1702 –1705, 1994.

[6] W. Pinello, A. C. Cangellaris, and A. Ruehli, "Hybrid electromagnetic modeling of noise interactions in packaged electronics based on the partial-element equivalent-circuit formulation," *IEEE Trans. on Microwave Theory and Techniques,* vol. 45, no.10 part 2, pp. 1889–1896, Oct. 1997.

Coupled Electromagnetic-Circuit Simulation of Arbitrarily-Shaped Conducting Structures using Triangular Meshes

Vikram Jandhyala, Yong Wang, Dipanjan Gope, and Richard Shi

Department of Electrical Engineering, University of Washington, Seattle, WA 98195

Ph: 206-543-2186 Fax: 206-543-3842, email {jandhyala, cjshi}@ee.washington.edu

Abstract

The Partial-Element-Equivalent-Circuit (PEEC) approach is an effective method to convert three-dimensional on-chip multi-conductor structures to circuit-level descriptions. In this paper, a triangular-mesh-based PEEC approach is described, wherein the surfaces of arbitrarily-shaped conducting structures are represented by triangular mesh tesselations. A coupled EM-circuit formulation is obtained through the separation of the scalar, vector, and ohmic potential interactions between pairs of triangular edges-based basis functions. The overall approach can be interpreted as a SPICE-free, surface-only version of PEEC method and is especially useful for on-chip signal integrity analysis of systems-on-chip layout where components with irregular shapes are common.

I. INTRODUCTION

Recently, Systems-on-Chip (SoCs) have become one of the focus areas in VLSI. Through the integration of analog and digital parts into a single chip, the resulting system under design achieves more reliability and shorter manufacture to market cycle than solutions based on individual digital and analog integrated circuits. Meanwhile, new problems have emerged in SoC design [1], e.g., the fast-switching current in the digital part of a chip can electromagnetically couple to the analog part which is noise sensitive. This is especially true when the system is functioning at the GHz range or beyond.

In order to analyze crosstalk due to EM coupling, electromagnetic simulation is needed for the layout of the SoC chip. The PEEC method [2] is a particularly effective approach to model the electromagnetic effects of a multi-wire or multi-conductor structure using SPICE compatible elements.

The interaction of a multi-wire or multi-conductor structure can be described using the Electric Field Integral Equation (EFIE) [3]. In classical electromagnetics (EM), the EFIE is usually formulated using a Method of Moments (MoM) approach [4]. Instead of filling the Method of Moments (MoM) matrix and solving the resultant set of linear equations, the PEEC method extracts partial elements including resistance, self/mutual capacitance and self/mutual inductance from the EFIE formulation, by identifying these elements with ohmic, scalar, and vector potential interactions, respectively. A SPICE compatible netlist can then be generated using these extracted partial elements. Through this extraction, the original EM problem is converted to a circuit problem, and a circuit simulator can then predict the performance of a layout while automatically considering the electromagnetic effects due to geometry and structure [2].

The classical PEEC method, originally formulated for modeling crosstalk between digital traces, relies on a longitudinal filament discretization of all structures. This discretization, which assumes a direction of current flow along the length of the filament, is very well-suited for thin and long interconnect structures. However, an SoC scenario leads to several arbitrarily shaped structures, including spiral inductors, and regular and split ground planes wherein the filament approach is inherently not well suited, because of the arbitrary directions of current flow in such structures. Moreover, it is not intuitive to represent current flow on non-longitudinal structures in terms of scalar longitudinal filaments.

In this paper, Rao-Wilton-Glisson (RWG) basis functions [4,5] that are linear basis functions defined over triangles are used to model conductors using surface-only triangular meshes. Interactions between RWG basis functions are then extracted and were used to form a coupled matrix which also includes MNA formulation of circuits. The aim of developing a coupled formulation outside SPICE is to reduce reliance on sparse-matrix solvers, since sections of the coupled matrix system are inherently dense.

The rest of the paper is organized as follows. Section II briefly outlines the classical filamental PEEC method, and introduces the RWG triangle-basis functions. Section III presents the triangular mesh approach and the coupled EM-circuit formulation. Numerical simulation results are given in Section IV and Second V summarizes the paper.

II. MESH GENERATION: FILAMENTS VERSUS TRIANGLE MESHES

The PEEC method, originally developed to model digital interconnects, inherently assumes that filaments, i.e. thin and long structures, can be used to model sections of the structure under analysis, as well as the current flow (along the filament length). As shown in Fig. 1, filamental PEEC divides the object into filaments. Each filament, represented as a volume cell, represents a longitudinal current, and related surface cells represent surface charge.

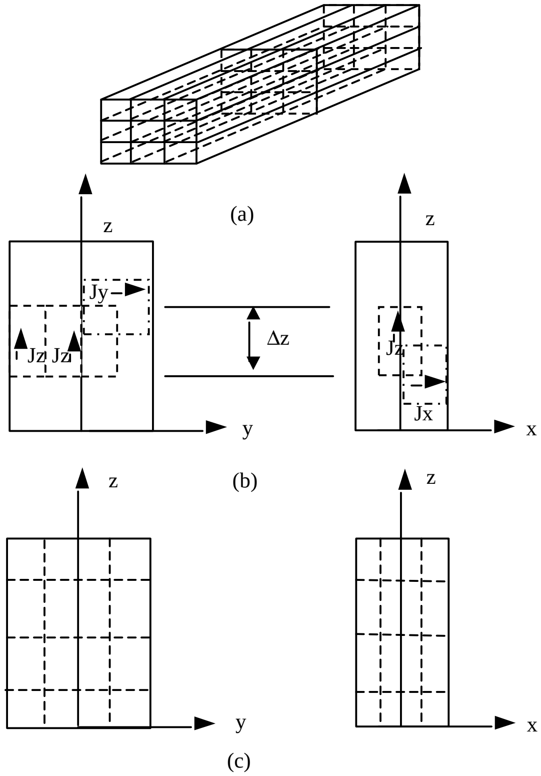

Figure 1. (a) rectangular conductor divided into filaments (b) Volume cells for currents (c) Surface cells for capacitive

For structures where 2D (e.g. a thin ground plane) or 3D (e.g. a thick ground plane) current distribution is necessitated, independent discretizations in terms of filaments in each direction are required, and the efficiency of the filamental PEEC method rapidly degrades. Also inherent in filamental approach is an eventual staircase approximation to the current distribution. In general, filamental PEEC is ideal for long rectangular structures under the assumption that the currents flow only along the longitudinal direction.

In this paper, triangular meshes are used to represent arbitrarily-shaped surfaces. Common edges between triangles are used to define RWG basis functions that define current flow and charge distribution. Fig. 2 shows the triangle pair on which the current density and charge density is defined. An RWG basis function, defined with respect to the common edge, defines current flows from one triangle (+) across the common edge to the other (-) triangle.

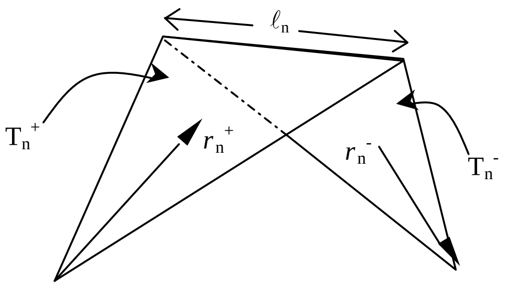

Figure 2. Definition of triangle basis function

III. COUPLED EM-CIRCUIT SYSTEM FORMULATION

In the MoM, conducting structures are analyzed using the electric field integral equation formulation (EFIE), wherein the surface current density $\boldsymbol{J}$ satisfies the equation:

$$jw\,\frac{m}{4p}\int_S \frac{\boldsymbol{J}(\mathbf{r}')}{|\mathbf{r}-\mathbf{r}'|}ds' + (\nabla f)(\mathbf{r}) = -Z_s \boldsymbol{J}(\mathbf{r}) \qquad (3.1)$$

Scalar potential ϕ and surface charge density ? are related through the equation:

$$f = \frac{1}{4pe}\int_S \frac{?(\mathbf{r}')}{|\mathbf{r}-\mathbf{r}'|}ds' \qquad (3.2)$$

In the above equation Z_s represents surface impedance

$$Z_s = (1+j)\sqrt{\frac{wm}{2s_v}} \qquad (3.3)$$

which is a valid approximation at frequencies where the skin depth is smaller than the cross section of conductors. At lower frequencies, a second (interior) problem and accurate modeling of the lossy medium Green function within the conductor is required.

Upon testing the EFIE, the following matrix equation can be derived, entries of the matrix can then be extracted from the interaction of basis function.

$$jw\,\overline{\mathbf{L}}\,\mathbf{J} + \overline{\mathbf{A}}\,\mathbf{V} = -\overline{\mathbf{Z}}\,\mathbf{J} \qquad (3.4)$$

$$\overline{\mathbf{P}}\,\mathbf{Q} = \mathbf{V} \qquad (3.5)$$

After dividing the surface of the object into triangular meshes, the unknowns of interest are: distribution of scalar potential ϕ, surface charge density q, and surface current density $\boldsymbol{J}$. These quantities are expanded using basis functions defined over triangles:

ϕ: piecewise constant basis function $\phi = \sum_{n=1}^{Np} \mathrm{V}_n \mathrm{C}_n$

Np is the number of total patches, C_n is a piecewise constant basis function, which is 1 on triangle *n*, and 0 elsewhere.

q: piecewise constant basis function $q = \sum_{n=1}^{Np} \mathrm{Q}_n \mathrm{C}_n$

$\boldsymbol{J}$: RWG basis function $\boldsymbol{J} = \sum_{n=1}^{Ne} \mathrm{J}_n\, \mathbf{f}_n(\mathbf{r})$

Ne is the number of total non-boundary edges, $\mathbf{f}_n$ is RWG basis function that is defined as:

$$\mathbf{f}_n(\mathbf{r}) = \begin{cases} \dfrac{l_n}{2A_n^+}\mathrm{r}_n^+ & \text{when } \mathbf{r} \text{ is in } T_n^+ \\ \dfrac{l_n}{2A_n^-}\mathrm{r}_n^- & \text{when } \mathbf{r} \text{ is in } T_n^- \\ 0 & \text{elsewhere} \end{cases} \qquad (3.6)$$

In the above expression, l_n is the length of the common edge, A_n^+ and A_n^- is the area of triangle T_n^+ and T_n^- respectively.

With the above three basis functions, the entries of the L, P, and Z matrices can be defined as:

$$L_{ij} = \frac{m}{4p} \int_S \int_S \frac{\mathbf{f}_j(\mathbf{r}')}{|\mathbf{r}-\mathbf{r}'|} ds' \cdot \mathbf{f}_i(\mathbf{r}')\, ds \tag{3.7}$$

$$P_{ij} = \frac{1}{4\pi\varepsilon} \int_S \int_S \frac{C_j(\mathbf{r}')}{|\mathbf{r}-\mathbf{r}'|} ds' C_i(\mathbf{r})\, ds \tag{3.8}$$

$$Z_{ij} = Z_s \int_S \int_S \mathbf{f}_j(\mathbf{r}') \cdot \mathbf{f}_i(\mathbf{r}')\, ds' ds \quad i, j = 1,.., N_e \tag{3.9}$$

where Z_{ij} is non-zero only if edges *i* and edge *j* share a common triangle.

The matrix formulation for the EM part will be:

$$\begin{pmatrix} j\omega\bar{\mathbf{L}}+\bar{\mathbf{Z}} & \bar{\mathbf{A}} & \bar{\mathbf{0}} \\ \bar{\mathbf{0}} & \bar{\mathbf{I}} & \bar{\mathbf{P}} \\ -\bar{\mathbf{A}}^{T} & \bar{\mathbf{0}} & \bar{\mathbf{D}} \end{pmatrix} \begin{pmatrix} \mathbf{J} \\ \mathbf{V} \\ \mathbf{Q} \end{pmatrix} = \begin{pmatrix} \mathbf{0} \\ \mathbf{0} \\ \mathbf{0} \end{pmatrix} \tag{3.10}$$

$\bar{\mathbf{A}}$ is a sparse matrix which describes the adjacency of edges and patches, each row has two non-zero terms which correspond to patches associated with a particular edge. $\bar{\mathbf{D}}$ is a diagonal matrix used to enforce the current and charge continuity equation. The unknowns are the coefficients associated with the current, potential, and charge basis functions.

When coupled with circuits, the formulated EM matrix needs to be extended to include both the circuit part and the EM-circuit connection part, as in equation 3.11.

$$\begin{pmatrix} \mathbf{j?}\,\bar{\mathbf{L}}+\bar{\mathbf{Z}} & \bar{\mathbf{A}} & \bar{\mathbf{0}} & \bar{\mathbf{X}} \\ \bar{\mathbf{0}} & \bar{\mathbf{I}} & \bar{\mathbf{P}} & \bar{\mathbf{0}} \\ -\bar{\mathbf{A}}^{T} & \bar{\mathbf{0}} & \bar{\mathbf{D}} & \bar{\mathbf{0}} \\ \bar{\mathbf{X}}^{T} & \bar{\mathbf{0}} & \bar{\mathbf{0}} & \overline{\mathbf{MNA}} \end{pmatrix} \begin{pmatrix} \mathbf{J} \\ \mathbf{V} \\ \mathbf{Q} \\ \mathbf{ckt} \end{pmatrix} = \begin{pmatrix} \mathbf{0} \\ \mathbf{0} \\ \mathbf{0} \\ \mathbf{ckt\_ex} \end{pmatrix} \tag{3.11}$$

$\overline{\mathbf{MNA}}$ is the Modified Nodal Analysis matrix of the circuit part, $\bar{\mathbf{X}}$ is a connection matrix which guarantees the current and field continuity at the node where EM structures and circuits are connected. The excitation includes regular voltage and current sources.

IV NUMERICAL RESULTS

The first example is an interconnect over a ground plane, as in [6]. The geometry is drawn again in Fig.3:

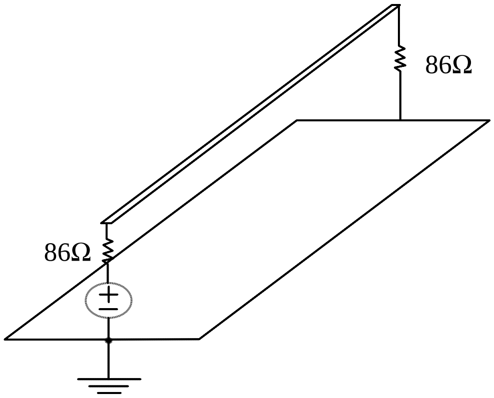

Figure 3. Interconnect above a solid ground plane

The interconnect is driven by a voltage source and is terminated by 86 Ohm resistors at both ends. The interconnect is 2.0cm long, 1mm wide and 0.5mm above the ground plane. In this example, the current flow on both the interconnect and ground plane is considered to be two dimensional. The discretized structure and the input impedance are shown in Fig. 4.

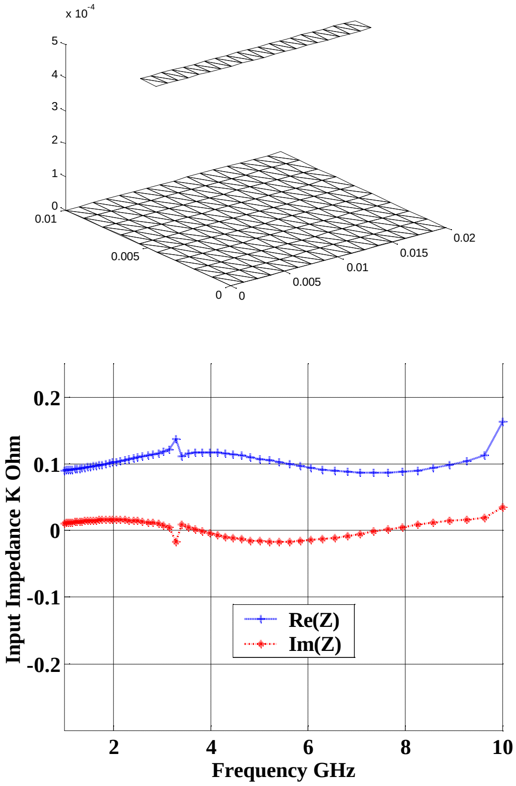

Figure 4. Triangular meshing of the structure (top)
Input impedance of interconnect over a ground plane(bottom)

It is interesting to note that the transmission line resonance behavior of this structure is also captured. The finite-sized impedance peaks is due to coarse frequency sampling at resonance.

The second example illustrates that the coupled method can be used for cross talk analysis. Two scenarios are studied here: in one scenario two traces are 0.5mm above the ground plane and 1mm apart, in the other scenario the two traces are 1mm apart at the near end and 2mm apart at the far end. One trace is excited with a 600 ps symmetrical trapezoidal pulse with a 10 ps rise time.

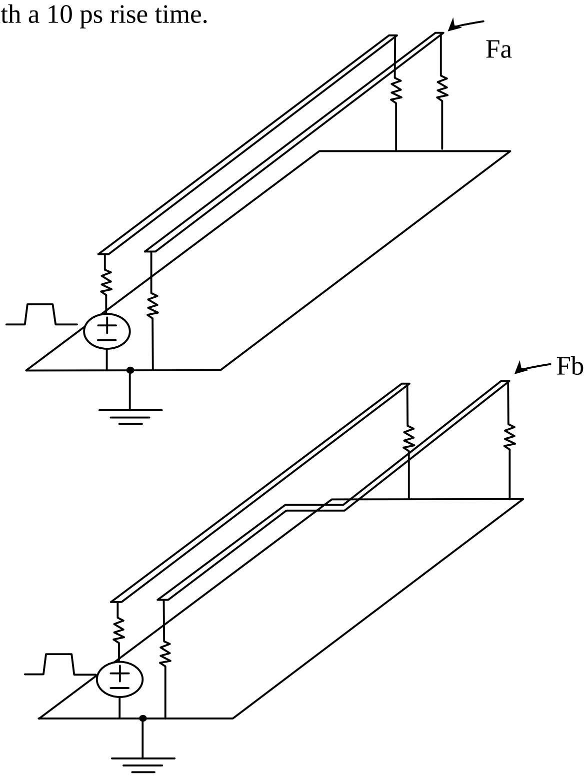

Figure 5. Two parallel traces(top), two traces with larger distance at far end(bottom)

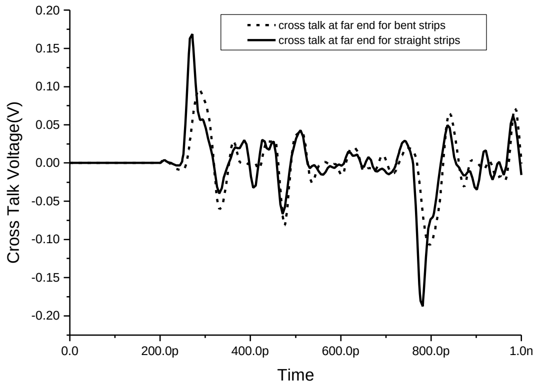

Figure 6. Cross talk at far end

As can be seen from Fig. 6, the far end cross talk voltage waveform is weaker for the second case. Also, the time lag between the two crosstalk peaks is the same as the length of the input pulse.

The third example is a spiral inductor of dimensions 200μm×200μm, placed 30μm above the ground plane, as shown in Fig. 7. The observation of interest is the current distribution on the ground plane. The inductor has two turns, and both the line width and the gap width are 20μm.

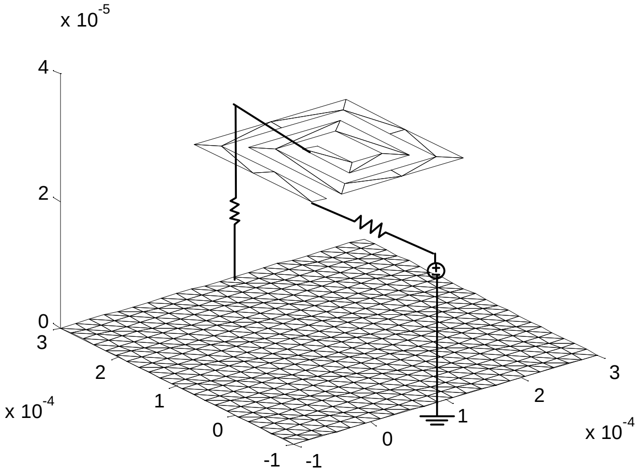

Figure 7. Spiral inductor above a ground plane

The coupled EM-circuit simulation gives ground current distribution as in Fig. 8. At 1 GHz the current concentrates below the inductor in order to minimize the inductive impedance of the loop including return current.

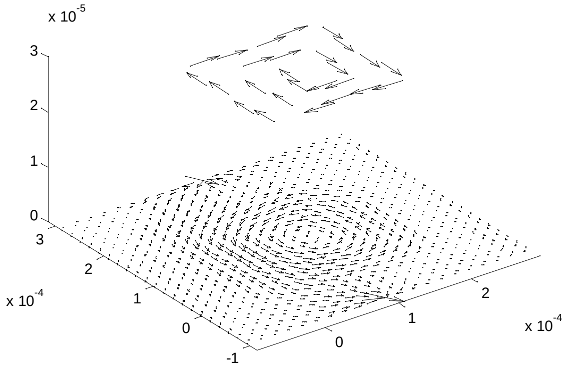

Figure 8. Current distribution of inductor and ground plane at 1GHz

V. CONCLUSION

In this paper, a generalized PEEC approach based on triangular meshes and well-known RWG basis functions was presented. Also, a SPICE-free coupled EM-circuit formulation was developed in order to solve the dense coupled system outside SPICE. Numerical results were presented to validate the approach and demonstrate its advantages in modeling induced and return current density due to arbitrarily-shaped structures. Furthermore, since the approach is surface-based, it can be used to reduce the numerical computation overhead of circuit-EM analysis by representing very thin structures by a two-dimensional representation.

ACKNOWLEDGEMENT

The work presented here is partially supported by the DARPA NeoCAD program, a University of Washington Royalty Research Fund grant, an NSF Career Award grant, and a joint contract from NSF-Semiconductor Research Corporation.

REFERENCE

[1] K. Kundert, H. Chang, D. Jefferies, G. Lamant, E. Malavasi, and F. Sendig, “Design of mixed-signal systems-on-a-chip,” *IEEE Trans. on Computer-Aided Design of Integrated Circuits and Systems*, vol. 19 no.12, pp. 1561–1571, Dec. 2000

[2] A. E. Ruehli. Equivalent circuit models for three dimensional multiconductor systems. IEEE Trans. On Microw. Theory and Techn., MTT22 (3) pp. 216-221, March 1974

[3] Andrew F. Peterson, Scott L. Ray, Raj Mittra, *Computational Methods for Electromagnetics*, IEEE PRESS, 1997.

[4] S. M. Rao, D. R. Wilton, and A. W. Glisson, "Electromagnetic scattering by surfaces of arbitrary shape," IEEE Trans. Antennas Propagat., vol. AP-30, pp. 409-418, May 1982.

[5] D. R. Wilton, S. M. Rao, A. W. Glisson, D. H. Schaubert, O. Al-Bundak, and C. M. Butler, "Potential integrals for uniform and linear source distributions on polygonal and polyhedral domains," IEEE Trans. Antennas Propagation, vol. AP-32, pp. 276-281, March 1984.

[6] W. Pinello, A. C. Cangellaris, and A. Ruehli, “Hybrid electromagnetic modeling of noise interactions in packaged electronics based on the partial-element equivalent-circuit formulation,” *IEEE Trans. on Microwave Theory and Techniques*, vol. 45, no.10 part 2, pp. 1889–1896, Oct. 1997

A Time-Domain Surface-Integral Formulation for General Coupled Electromagnetic-Circuit Simulation

Vikram Jandhyala* and Chuanyi Yang
Dept. of Electrical Engineering, University of Washington
Box 352500, Seattle WA 98195, Ph: 206-543-2186, Fax: 206-543-2186
Email : {jandhyala,cyang1}@ee.washington.edu

The Partial Element **[1]**Electric Circuit (PEEC) approach is a popular method for coupled electromagnetic-circuit simulation in both frequency and time domains. In the classical PEEC approach, volumetric filament structures are used to model directional conduction current flow within a conductor. For curved, non-orthogonal structures such as those found on systems-on-chip, including inductors and RF components, a more natural description is based on using surface-equivalent currents and a surface-integral formulation, as has been accomplished with great success for scattering problems in both the time and frequency domains.

The coupling of surface-integral equation **[2]**approaches is normally carried out through S-parameter models, or semi-infinite ports. The PEEC approach, on the other hand, uses a very intuitive and direct connection to circuit nodes owing to the fact that all electromagnetic interactions are represented in terms of equivalent circuits which can directly be linked to circuit nodes. Time or phase-delays are accounted for by controlled sources placed between two circuit nodes.

In this work, we apply the equivalent-circuit-based coupling idea of the classical PEEC formulation for time-domain surface-integral equations. In a coupled time-domain system, the electromagnetic interactions are represented in terms of equivalent circuits, and connections to circuit equations are facilitated through modified nodal analysis. This coupled system is then reduced back to a form where it can be represented as a time-domain surface electric field integral equation coupled to modified nodal analysis in the time domain through sparse coupling matrices obtained from the connections of underlying equivalent circuits. Thus equivalent circuits are used to formulate the connections between the electromagnetic and circuit problems only.

The resulting coupled matrix system can be interpreted as both a generalized time-domain PEEC approach, as well as a coupled time-domain surface integral equation and circuit solver. The coupling mechanisms includes an inductor-based equivalent model for planar connections to a two-dimensional structure, and a continuity equation-based model for a planar facial terminal on a three-dimensional structure. The advantage of this approach is that it can be incorporated into a SPICE-like solver without altering the modified nodal analysis submatrix. Furthermore, the sparse coupling mechanism enables a variety of direct and iterative solution methods, fast matrix-vector schemes, as well as design iteration on sub-sections of the circuit schematic. Numerical examples and application include transient simulations, impedance computations, and time-domain crosstalk simulation.

A Surface-Based 3D Coupled Circuit-Electromagnetic Simulator with Accurate Lossy Conductor Modeling

Dipanjan Gope, Swagato Chakraborty, Yong Wang, Vikram Jandhyala*, and Richard Shi
Department of Electrical Engineering
University of Washington, Seattle WA 98195.
Email {jandhyala,cjshi}@ee.Washington.edu

With the increase in working frequencies for mixed signal ICs to GHz range, the accurate modeling of the on-chip and package-level electromagnetic (EM) effects becomes imperative for successful single-pass chip design. The Partial Element Equivalent Circuit (PEEC) method addresses the problem of coupled EM circuit simulation by deriving equivalent circuit elements like capacitors, inductors and resistors from the EM interactions. The equivalent circuit can then be fed into a SPICE-like simulator to obtain the performance of the circuit including EM effects.

Classical PEEC uses a filament discretization, which is not necessarily efficient for accurate modeling of skin effects in arbitrarily-shaped structures. This is because at high frequencies the current tends to flow on the surface of the conductor, with the magnitude of current reducing exponentially away from the surface. Hence volumetric modeling of the current needs a finer discretization near the surface. In order to accurately model the decaying current an appropriate filament meshing is required near the surface. However the skin depth, which determines the rate of decay of the current, is frequency dependent, which in turn necessitates frequency-adaptive meshing. Such dynamic meshing is computationally expensive for frequency domain analysis. Previous surface-based attempts to solve this problem employ the surface impedance formulation (Y. Wang et. al. Proc. *IEEE Meeting on Elec. Perf. of Electron. Packaging,* pp. 233-236, Sept. 2001). However this method is accurate only at high frequencies, where cross sections are larger than twice the skin depth. Thus at relatively lower frequencies, when the current flows through the entire cross section of the conductor, surface impedance is a poor approximation to the interior lossy problem.

In this work we propose a surface based formulation for coupled circuit EM analysis with simultaneous solution of interior and exterior problems. The skin depth is modeled accurately by solving the interior problem based on the frequency-domain lossy medium Green's Function. Since this discretization is surface based, the need for dynamic volumetric meshing for different frequencies is avoided. The solution of the interior problem with the lossy medium Green's function accurately models the skin depth at all frequencies, and reduces to the surface impedance at sufficiently high frequencies.

For 3D problems, the EM structure is coupled to the circuit by enforcing electrical field integral equations for the EM part, KVL and KCL for the circuit unknowns and electrical field continuity for circuit EM coupling. The unknowns in this formulation include the surface equivalent current, and circuit quantities like voltage and current. Both circuit and electric field excitations can be modeled by proper formulation of the right hand side. The interior problem is solved using the lossy medium Green's function. For the lossy medium, the wave number is complex and thus the Green's function falls exponentially away from the excitation region. Hence instead of the normal singularity extraction procedure, which is applied for the integration of free space Green's function, an analytical singularity cancellation method is implemented for accurate modeling. Results presented at the conference will include applications of the simulator in real design problems, comparison with surface impedance formulation and impedance frequency response of lossy conductors.

A Time Domain Surface Integral Technique for Mixed Electromagnetic and Circuit Simulation

Chuanyi Yang and Vikram Jandhyala
Department of Electrical Engineering
University of Washington, Seattle, WA 98195 USA
Tel. (206) 543-2186, Fax (206) 543-3842
{ cyang1, jandhyala }@ee.washington.edu

Abstract

A full-wave time domain surface integral approach to coupled electromagnetic and circuit simulation is presented in this paper. In particular, non-linear circuit elements and effect of interference and crosstalk can be modeled in the time domain. The coupling of lumped elements to a surface integral formulation is detailed. Losses are modeled with an efficient recursive convolution.

1 Introduction

Time domain electromagnetic-circuit simulation is of interest to digital and analog-RF designers, and is essential in the case of non-linear elements and broadband coupling. In this work we propose a time-domain surface-only form that models losses using a recursive formulation of surface impedance. Using an implicit method ensures stability of the scheme. Furthermore, lumped linear and non-linear elements can be directly incorporated into this formulation through a rigorous coupling scheme for both open and closed conducting structures. The approach may be interpreted as a time-domain version of the partial element electric circuit (PEEC) [1,2] method, with the significant distinctions that the solution uses well-established method of moment (MoM) forms, is surface-only (no volumetric discretization required), makes no a priori assumptions on current flow directions. Examples include validation against time-domain PEEC, as well as a demonstration of coupling and non-linear effects.

2 Integral Equation Formulation

For a lossy conductor, the following time domain integral equation (TDIE) holds under a surface impedance approximation

$$\left[\frac{\partial \mathbf{A}(\mathbf{r},t)}{\partial t}+\nabla\Psi(\mathbf{r},t)\right]_{\tan} = \left[-Z_s(t)*\left(\frac{\partial\, \mathbf{J}(\mathbf{r},t)}{\partial t}\right)\right]_{\tan} + \mathbf{E}^i(\mathbf{r},t)\Big|_{\tan} \qquad (1)$$

where $\mathbf{A}(\mathbf{r},t)$ is the vector potential, $\Psi(\mathbf{r},t)$ is the scalar potential, Z_s is the time-domain surface impedance, $\mathbf{J}$ is the equivalent surface current density, and $\mathbf{E}^i(\mathbf{r},t)$ is incident electric field or its equivalent due to a circuit excitation. For a homogeneous medium the potentials are given by

$$\mathbf{A}(\mathbf{r},t) = \mu\int_s \frac{\mathbf{J}(\mathbf{r}',t-R/c)}{4\pi R}ds',\ \Psi(\mathbf{r},t) = \frac{1}{\varepsilon}\int_s \frac{q_s(\mathbf{r}',t-R/c)}{4\pi R}ds' \qquad (2)$$

where the domain S is the surface of the conductor, and the surface impedance is given by $Z_s(t) = \sqrt{\mu/\pi\sigma t}$ where μ, ε, and σ are the material parameters. The surface charge density q_s is related to $\mathbf{J}$ through the continuity equation $q_s(t) = -\int_{\tau=0}^{t}\nabla\cdot\mathbf{J}d\tau$. In this work the TDIE (1) is formulated and solved in the method of moments (MoM) form using the surface-triangle-pair based Rao-Wilton-Glisson (RWG) basis functions [3,4].

3 Efficient Loss Modeling in the Time Domain

The surface impedance model leads to a convolution for each time step, which can become prohibitively expensive. To circumvent this, we adopt the following fast recursive formulation, presented in [5]. The convolution involving the surface impedance is

$$Z_s(t)*\left(\frac{\partial J(\mathbf{r},t)}{\partial t}\right) = \int_0^t \sqrt{\frac{\mu}{\pi\sigma\tau}}\,\frac{\partial \mathbf{J}(\mathbf{r},t-\tau)}{\partial(t-\tau)}\,d\tau = \sqrt{\frac{\mu}{\pi\sigma}}\int_0^t \frac{1}{\sqrt{\tau}}\,\frac{\partial \mathbf{J}(\mathbf{r},t-\tau)}{\partial(t-\tau)}\,d\tau \tag{3}$$

After applying finite difference in time and some algebraic manipulation, (3) can be rewritten as

$$\sqrt{\frac{\mu}{\pi\Delta t\sigma}}\sum_{m=0}^{n-1} Z_0(m)\left[\mathbf{J}(\mathbf{r},(n-m)) - \mathbf{J}(\mathbf{r},(n-m-1))\right] \quad ; \quad Z_0(m) = \int_m^{(m+1)} \frac{d\alpha}{\sqrt{\alpha}} \tag{4}$$

where the indices *m* and *n* specify present and cumulative time steps. Finally, the function in (4) can be accurately represented as a sum of complex exponentials as $Z_0(m) = \int_m^{m+1} \frac{1}{\sqrt{\alpha}} d\alpha \cong \sum_{i=1}^{N} a_i e^{m\beta_i}$ where the coefficients and exponential weights are determined by Prony's method. It is shown in [5] that N=10 suffices to produce very high accuracy approximations for the given function. This enables (4) to be rewritten as

$$\sqrt{\frac{\mu}{\pi\sigma\Delta t}}\sum_{i=1}^{N}\sum_{m=0}^{n-1} a_i e^{m\beta_i}\left[\mathbf{J}(\mathbf{r},(n-m)) - \mathbf{J}(\mathbf{r},(n-m-1)\right] = \sqrt{\frac{\mu}{\pi\sigma\Delta t}}\sum_{i}^{N} \mathbf{\Phi}_i^n \tag{5}$$

Finally, a recursive relationship can be obtained between $\mathbf{\Phi}_i^n$ and $\mathbf{\Phi}_i^{n-1}$

$$\mathbf{\Phi}_i^n = a_i\left[\mathbf{J}(\mathbf{r},n) - \mathbf{J}(\mathbf{r},(n-1))\right] + e^{\beta_i}\mathbf{\Phi}_i^{n-1} \tag{6}$$

This permits a single computation at each time step instead of a convolution, thus enabling rapid loss computation along with the regular TDIE time stepping.

4 Coupling Circuit and Electromagnetic Equations

A critical part of the use of TDIE for circuit problems is the proper form of excitation, based on circuit sources. Moreover, compatibility and interference modeling also requires field excitation that standard in electromagnetic integral equation forms. For the circuit excitation, we follow the approach proposed in [6] and [7] in the frequency domain, and extend it to the time domain here. To summarize the approach, two distinct coupling schemes are proposed (Fig. 1). The first is for open or zero thickness structures wherein circuit current feeds into edges of the triangular mesh. In this instance, current continuity, along with the use of half-RWG bases is sufficient; in physical terms half-RWG bases are equivalent to inductors projecting out from each terminal edge, which are then connected equi-potentially to a circuit node. In the second case, a circuit current is introduced to a closed equivalent surface. One or more triangles may be considered to be part of the terminal. In this case, the continuity equation needs to be modified to include the current due to the circuit I$_c$: $\nabla \cdot \vec{J} + \frac{\partial q_s}{\partial t} = \frac{I_c}{A_p}$ where the denominator denotes the area of the terminal, which may contain one or more triangles. This new source creates a new scalar potential through modification of the total charge and divergence of current. The potentials of terminal triangles are tied to the circuit node potential.

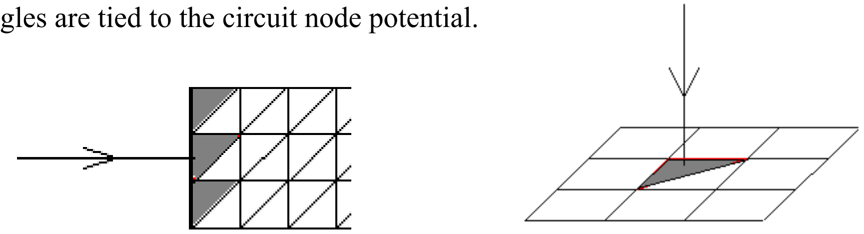

Figure 1. Circuit-EM mesh interconnections for open (left) and closed (right) structures

Based on the above coupling mechanism a coupled matrix system is established as following.

$$\begin{bmatrix} \overline{\mathbf{EM}} & \overline{\mathbf{EC}} \\ \overline{\mathbf{EC}^{\mathrm{T}}} & \overline{\mathbf{MNA}} \end{bmatrix}\begin{bmatrix} \mathbf{J} \\ \mathbf{CIR} \end{bmatrix} = \begin{bmatrix} \mathbf{HISTORY} + \mathbf{E\_FIELD} \\ \mathbf{SOURCE} \end{bmatrix} \tag{7}$$

The **EM** block in the coupled matrix represents the MoM section. The sparse **EC** block is the connectivity between the EM and the circuit part. The **MNA** block represents the modified nodal analysis conductance matrix corresponding to the circuit unknowns (**CIR**). The **J** vector represents the surface unknowns on the conductors. he **HISTORY** represents influence from past times, and the **E_FIELD** vector is the electrical field incident to the circuit. The **SOURCE** vector contains voltage or current sources applied to the circuit.

5 Numerical Results

In the first example, common mode current is computed for the structure In Fig. 2. A wire is placed between two ground strips, where L1 and L2 are 2cm and 0.4cm long respectively. The gap between the wire and the ground strip is 0.5mm. The wire and the two ground strips have the same width of 1mm. Trapezoidal voltage pulses with 1V amplitude, and rising, roof and falling time of 100ps are applied as shown. A 10Ω resistor is placed between the source and the ground. Because of the different length of the two ground strips, there is a common mode component in the ground currents, which is evident in Fig. 3. This result matches well with the published result for the same structures in [8].

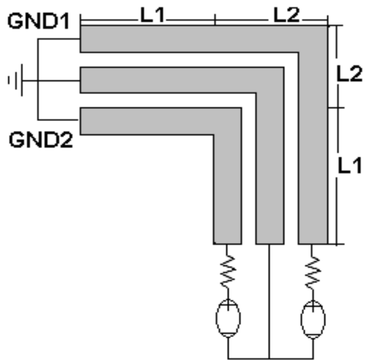

Figure 2. Wire between two ground strips

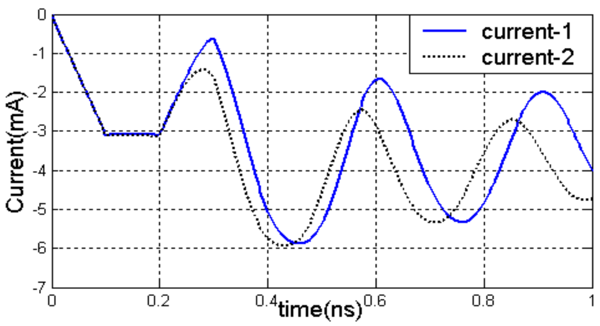

Figure 3. Current through GND1 and GND2

The second example deals with interference on a two-level multiple crossover circuit (Fig. 4) comprised of lossy interconnects with conductivity 5.8e+6 S/m, with non-linear circuit elements. Interconnects on the upper level are $40\mu m$ wide, 0.75mm long, with a $40\mu m$ separation between them. Interconnects on the lower level are $50\mu m$ wide, 0.68mm, with a $50\mu m$ separation between them. The distance between the two levels of interconnect is $50\mu m$. Each port at the upper level, except ports 2 and 4, is terminated by a 10pF capacitor. Ports 2 and 4 are terminated by diodes with characteristics Is=5.e-9A and VT=25.e-3V. Each port at the lower level is terminated by a 200Ω resistor. A 1V sinusoidal voltage source $V(t) = \sin(\omega t)$, where $\omega = 2\pi f$, $f = 10\,GHz$ is applied to port 1. A plane wave with $\mathbf{k} = +\hat{\mathbf{z}}$, $\mathbf{E}(t) = -1000\sin(\omega_0 t)(V/m)\hat{\mathbf{y}}$, where $\omega_0 = 2\pi f_{0,} f_0 = 5GHz$, is incident to the nonlinear circuit. The output with no interfering plane wave, at port 2, as well as crosstalk at port 4, is shown in Fig. 5. Once the interference is introduced, the output distorts as shown in Fig. 6, and the crosstalk also changes. What is interesting is the non-linear effect of harmonic coupling, where the harmonic of the plane wave at 10GHz couples into the circuit, causing distortions at the circuit frequency of 5GHz. This is observed in Figs. 7 and 8, where the FFT's of the uncoupled and distorted signals are depicted.

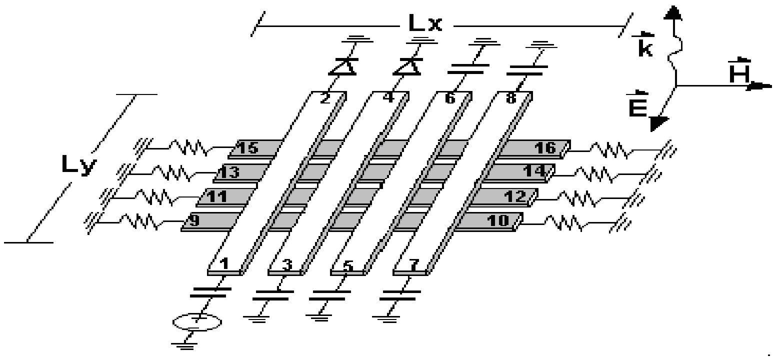

Figure 4. Incident field coupling to nonlinear circuit

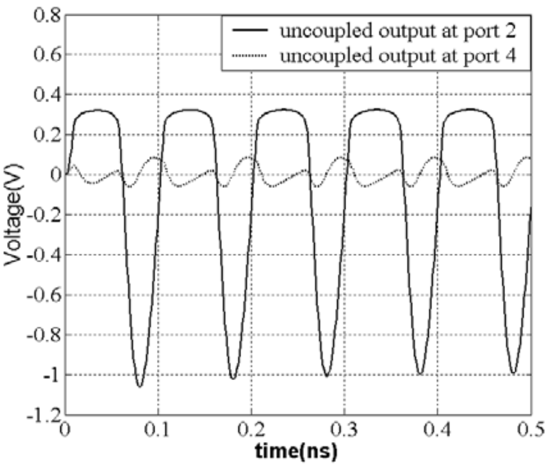

Figure 5. Uncoupled output at port 2

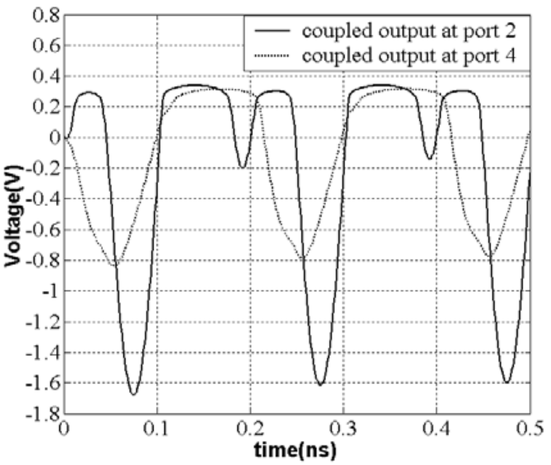

Figure 6. Coupled output at port 4

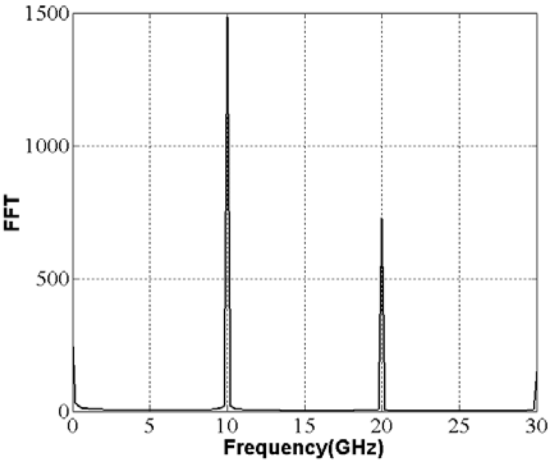

Figure 7. FFT magnitude of uncoupled output at port 2

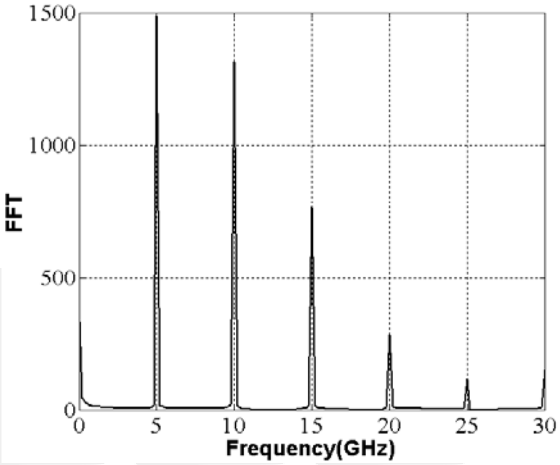

Figure 8. FFT magnitude of coupled output at port 2

6 Conclusions

A time domain, surface based, full-wave coupled-EM and circuit matrix system was developed. Loss was modeled with a recursive convolution. Coupling schemes were discussed and examples were shown that included common mode currents, non-linear circuits, and coupling to interference. Current and future work includes adaptive time stepping, mesh refinement, and fast solvers.

This work is partially supported by the DARPA NeoCAD program, by NSF-SRC Mixed Signal Initiative Grant CCR-0120371, and by NSF CAREER Grant ECS-0093102.

References

[1] A. E. Ruehli, “Equivalent circuit models for three dimensional multiconductor systems,” *IEEE Trans. Microwave Theory Tech.*, vol. 22, pp. 216–221, Mar. 1974.
[2]P.J. Restle, A.E. Ruehli, S.G. Walker, and G. Papadopoulos, “Full-wave PEEC time-domain method for the modeling of on-chip interconnects,” *IEEE Trans. Comp.-Aided Des. of Integ. Circuits Systems*, vol. 20, no. 7, pp. 877-886, July 2001.
[3] S. M. Rao and D. R.Wilton, “Transient scattering by conducting surfaces of arbitrary shape,” *IEEE Trans. Antennas Propagat.*, vol. 39, pp. 56–61, Jan. 1991.
[4] S. M. Rao, *Time Domain Electromagnetics*, Academic Press, San Diego, CA, 1999.
[5] K.S. Kunz and R.J. Luebbers, *The Finite Difference Time Domain Method in Electromagnetics*, CRC Press, Boca Raton, FL, 1993.
[6] Y. Wang, V. Jandhyala, and R. Shi, “Coupled electromagnetic-circuit simulation of arbitrarily-shaped conducting structures,” *Proceedings of Electrical Performance of Electronic Packaging*, pp. 233-236, 2001.
[7] V. Jandhyala, Y. Wang, D. Gope, and R. Shi, “A surface-based integral equation formulation for coupled circuit-electromagnetic simulation,” *Microwave Optical Technology Letters*, July 20, 2002.
[8] W. Pinello, A. Ruehli, A. Cangellaris, “Analysis of interconnect and package structures using PEEC models with radiated emissions,” *Proc. IEEE Int. Symp. Electromagnetic Compatibility*, pp. 353-358, 1997.

Integral Equation-Based Coupled Electromagnetic-Circuit Simulation in the Frequency Domain

Yong Wang, Dipanjan Gope*, Vikram Jandhyala, and C.J. Richard Shi

Dept of Electrical Engineering, University of Washington, Seattle WA 98195
Email: jandhyala@ee.washington.edu, Ph: 206-543-2186, Fax: 206-543-3842

In this paper, an approach to couple electromagnetic surface integral equations and circuit simulation is presented. Terminals are defined that connect lumped circuit models to objects modeled with distributed electromagnetic simulation. A modified form of the charge-current continuity equation is proposed for connectivity at terminals. The resulting scheme enables simultaneous solution of electromagnetic integral equations for arbitrarily-shaped objects and SPICE-like modeling for lumped circuits, and permits design iterations and visualization of the interaction between the two domains.

1. INTRODUCTION

There are several existing methodologies aimed at incorporating EM effects in circuit simulations. One such approach, the partial element equivalent circuit (PEEC) method [1,2] has been developed as a successful means to discretize objects and to directly represent the coupling between the discretized elements using SPICE compatible RLC elements and dependent sources. Due to the dense nature of the interactions and the fact that SPICE is tuned for solving sparse matrices, the direct PEEC method is size limited. To obviate this limit, ongoing work has focused on reduced order models and fast solvers.

Another approach is to directly use a regular Method of Moments (MoM) solver to derive the port parameters. Thereafter, equivalent circuits are generated in conjunction with model reduction methods in order to obtain characteristics at the ports that approximate the frequency-dependent EM simulation results. This approach can become unattractive for a variety of reasons, including ill-defined ports at chip and package level, complexity of modeling for multi-port parameters, and loss of information about the electromagnetic problem once the port model is obtained.

In this paper a new approach to formulating and simulating the coupled EM-circuit problem is presented. The distributed EM effects and the lumped circuit models are formulated in conjunction in one system matrix amenable to fast direct and iterative solutions. Although standard port and terminal models for EM structures can also be generated using the approach discussed herein, it is shown that solving the EM-circuit system simultaneously provides more detailed field information and also obviates the equivalent circuit generation step, thus automating the design flow. In addition, the coupled formulation not only handles circuit excitations, but also the effects of incident electric field radiations on the EM-circuit system. The methodology is inherently hierarchical, with seamless transitions possible between circuit and EM representations depending on the level of detail required.

2. FORMULATION

Consider a conducting object with surface S to be modeled with distributed electromagnetic simulation, connected to arbitrary circuits, excited through voltage and current sources within the circuit, and optionally illuminated by one or more electromagnetic wave excitations. The surface S is divided into two sub-surfaces, denoted by S_{CK} and S_{EM}, where S_{CK} denotes *terminals*, the regions where lumped circuits are connected to S. On the entire surface S the boundary condition for the electric field is:

$$\left[\mathbf{E}^{s}(\mathbf{J})+\mathbf{E}^{i}\right]_{\tan}=Z_{s}\,\mathbf{J} \tag{2.1}$$

where $\mathbf{E}^{s}$ is the scattered electric field produced by the induced equivalent surface current $\mathbf{J}$, $\mathbf{E}^{i}$ is the incident electric field, subscript tan denotes the tangential components on the surface *S*, $Z_{s}=\sqrt{j\omega\mu/2\sigma}$ represents surface impedance. On S_{EM} the standard continuity equation relating the surface current $\mathbf{J}$ and surface charge ρ holds:

$$\nabla_{s}\cdot\mathbf{J}(\mathbf{r})+j\omega\rho(\mathbf{r})=0 \quad \forall\mathbf{r}\in S_{EM} \tag{2.2}$$

where ∇_{s} represents surface divergence, with standard notation used for material parameters and frequency above. On S_{CK}, the following condition is proposed. The current flowing out of the circuit node associated with a terminal flows into the patches on S_{CK}. This coupling current introduces an additional source term that alters the surface current and surface charge on S through a modified continuity equation valid for S_{CK}. The modified continuity equation has the following form:

$$\nabla_{s}\cdot\mathbf{J}(\mathbf{r})+j\omega\rho(\mathbf{r})=J_{c}^{m}(\mathbf{r}) \quad \forall\mathbf{r}\in S_{CK} \tag{2.3}$$

where J_{c}^{m} represents the scalar current density into the terminal *m*. Therefore the scattered electric field can be expressed in a modified form as:

$$\begin{aligned}\mathbf{E}^{s}(\mathbf{J})=&-j\omega\frac{\mu}{4\pi}\int_{S}\frac{e^{-jk|\mathbf{r}\text{-}\mathbf{r}'|}\mathbf{J}(\mathbf{r}')}{|\mathbf{r}-\mathbf{r}'|}ds'-\nabla\frac{1}{j\omega4\pi\varepsilon}\int_{S}\frac{e^{-jk|\mathbf{r}\text{-}\mathbf{r}'|}[-\nabla_{s}.\mathbf{J}(\mathbf{r}')]}{|\mathbf{r}-\mathbf{r}'|}ds'\\&-\nabla\frac{1}{4\pi\varepsilon}\sum_{m=1}^{M}\int_{S_{CK}^{m}}\frac{e^{-jk|\mathbf{r}\text{-}\mathbf{r}'|}J_{c}^{m}(\mathbf{r}')}{j\omega|\mathbf{r}-\mathbf{r}'|}ds'\end{aligned} \tag{2.4}$$

While other approaches such as delta gap methods or wire basis functions can also be used to describe the coupling, they are either not general enough for connection with arbitrary circuits or need artificial parameters such as basis lengths, directions and radii.

Based on the assumption that the scalar potential produced on electrically small terminals S_{CK}^{m} is equal to the voltage of the circuit node associated, an additional set of equations can be setup:

$$V_{n}=\frac{1}{4\pi\varepsilon}\left(\int_{S}\frac{e^{-jk|\mathbf{r}\text{-}\mathbf{r}'|}\rho(\mathbf{r}')}{|\mathbf{r}-\mathbf{r}'|}ds'+\sum_{m=1}^{M}\int_{S_{CK}^{m}}\frac{e^{-jk|\mathbf{r}\text{-}\mathbf{r}'|}J_{c}^{m}(\mathbf{r}')}{j\omega|\mathbf{r}-\mathbf{r}'|}ds'\right),\ \forall\mathbf{r}\in S_{CK}^{n},\ n=1,\ldots,M \tag{2.5}$$

In addition, the regular Kirchoff's Current Law (KCL) is enforced at each terminal circuit node n, which involves all circuit currents entering or leaving the node in addition to the coupling currents.

With the above coupling schemes, and using Rao-Wilton-Glisson basis functions, the coupled problem can be formulated as:

$$\begin{pmatrix}\overline{\mathbf{Z}}_{11} & \overline{\mathbf{Z}}_{12} & \overline{\mathbf{0}}\\ \overline{\mathbf{Z}}_{21} & \overline{\mathbf{Z}}_{22} & \overline{\mathbf{C}}\\ \overline{\mathbf{0}} & \overline{\mathbf{C}}^{\mathrm{T}} & \overline{\mathbf{MNA}}\end{pmatrix}\begin{pmatrix}\mathbf{J}\\ \mathbf{I_{c}}\\ \mathbf{ckt}\end{pmatrix}=\begin{pmatrix}\mathbf{ex_{EM}}\\ \mathbf{0}\\ \mathbf{ex_{ckt}}\end{pmatrix} \tag{2.6}$$

$\overline{\mathbf{Z}}_{11}$ and $\overline{\mathbf{Z}}_{12}$ represent the tested electric field produced by the scalar and vector potentials due to EM currents, and by the scalar potential due to coupling currents, respectively. Similarly $\overline{\mathbf{Z}}_{21}$ and $\overline{\mathbf{Z}}_{22}$ represent the tested scalar potential at the terminal patches produced by the charge associated with the RWG currents and the coupling currents, respectively. $\overline{\mathbf{C}}$ is the EM-circuit connectivity matrix with one non-zero entry per row. $\overline{\mathbf{MNA}}$ represents the Modified Nodal Analysis for the lumped circuit elements. $\mathbf{I}$ and $\mathbf{I}_c$ are the strengths of RWG currents and the coupling currents respectively while $\mathbf{ckt}$ represents the circuit voltage and current unknowns. The excitations on the RHS include $\mathbf{ex}_{EM}$, the tested incident electric fields and $\mathbf{ex}_{ckt}$, the current and voltage sources.

3. NUMERICAL RESULTS

One typical application is circuit/layout co-simulation for RF electronics systems where on-chip inductors are often employed. Figure 2a shows the topology of a 5.6GHz differential mode Low Noise Amplifier (LNA) where several on-chips inductors are included either for frequency selection purpose (L1 L2) or for impedance matching purpose (L3, L4, L5, L6).

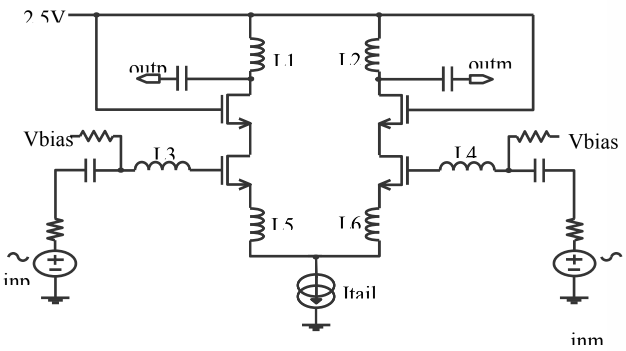

Fig 1a: A 5.6GHz Low Noise Amplifier

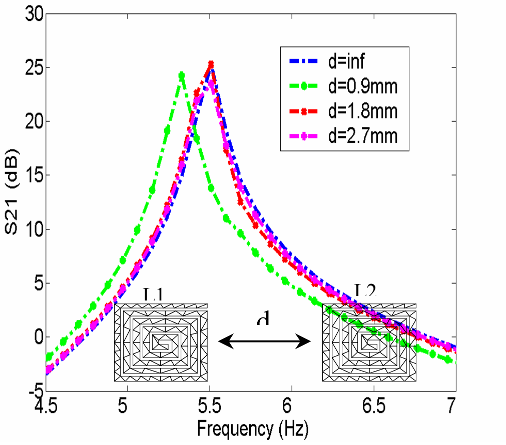

Fig 1b: S21 curve versus distance between inductors

Shown in Figure 1b are a series of S21 curves plotted by varying the distances between two inductors L1 and L2, and the resultant shift in center frequency due to changing mutual coupling effects; d=inf corresponds to ignoring mutual coupling. In the above design example, the coupled circuit-EM solver avoids the port model generation/curve fitting steps, which are necessary for traditional design methods.

The second example is to study the power/ground plane voltage bounce distribution due to a high-speed noise source. Consider a typical mixed analog/digital PCB board as shown in Figure 2.

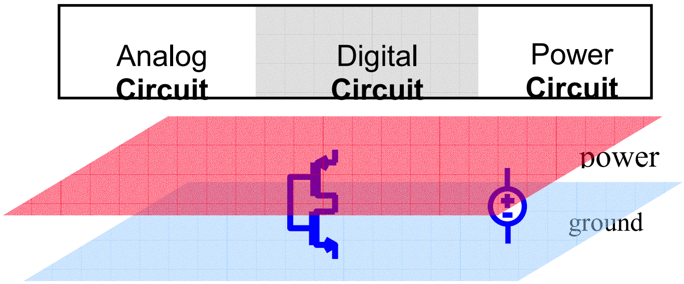

Fig 2: Mixed Signal PCB

With traditional port model based EM-circuit simulation methods, it is difficult to know the bounce voltage distribution all over the plane since voltage/field spatial distribution information is lost in a port model. If all the spatial points on the plane are treated as ports, then the scale of the problem will be extremely large. On the other hand, since the coupled circuit-EM solver uses equivalent surface current as system unknowns, the voltage/field distribution can then be easily derived by a single post processing once the coupled system is solved. Figure 3a shows the ground bounce voltage distribution for a PCB board of dimensions 12cm X 8cm, at 3GHz, with a 1mA noise source.

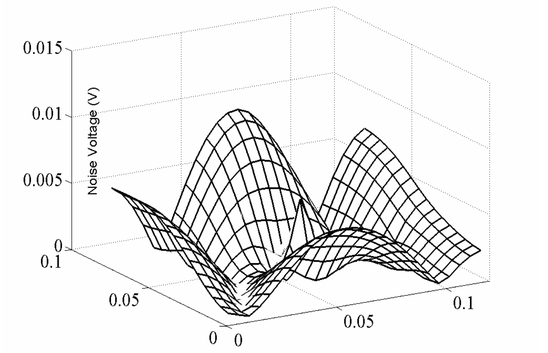

Fig 3a: Bounce voltage distribution at 3GHz

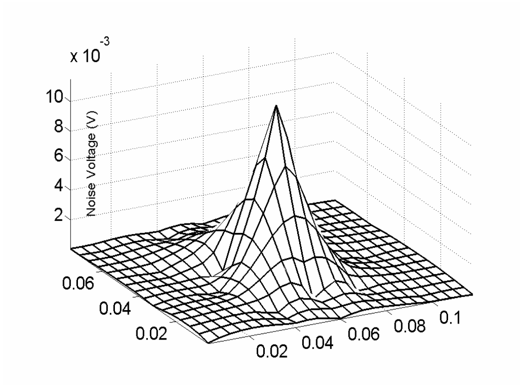

Fig 3b: Bounce voltage distribution at 3GHz after 20 decoupling capacitors

By continuously pinning down the peak bounce voltage using 10nF decoupling capacitors, the distribution of noise voltage was controlled as in Figure 3b after adding approximately twenty capacitors. The coupled nature of the proposed approach enabled field-based placement of decoupling capacitors, which would be difficult with port-based methods.

4. CONCLUSIONS

This paper presents a coupled EM-circuit approach that enables seamless transition between the two domains. Although the proposed method can be used to generate frequency-dependent port models, it also permits fully-coupled simulation, thereby automating design flow, and retaining EM information which can provide design insight.

ACKNOWLEDGEMENTS

This work was partially supported by DARPA-MTO NeoCAD grant N66001-01-1-8920, NSF-CAREER grant ECS-0093102, NSF-SRC Mixed-Signal Initiative grant CCR-0120371, and by a grant from Ansoft Corporation.

REFERENCES

[1] S. M. Rao, D. R. Wilton, and A. W. Glisson, "Electromagnetic scattering by surfaces of arbitrary shape," *IEEE Trans. Antennas Propagation,* vol. AP-30, pp. 409-418, May 1982.

[2] A. E. Ruehli, "Equivalent circuit models for three-dimensional multiconductor systems," *IEEE Trans. on Microwave. Theory and Techniques.,* vol. MTT22 (3), pp. 216-221, March 1974.

[3] K. Kundert, H. Chang, D. Jefferies, G. Lamant, E. Malavasi, and F. Sendig, "Design of mixed-signal systems-on-a-chip," *IEEE Trans. on Computer-Aided Design of Integrated Circuits and Systems,* vol. 19 no.12, pp. 1561–1571, Dec. 2000.

[4] W. Pinello, A. C. Cangellaris, and A. Ruehli, "Hybrid electromagnetic modeling of noise interactions in packaged electronics based on the partial-element equivalent-circuit formulation," *IEEE Trans. on Microwave Theory and Techniques,* vol. 45, no.10 part 2, pp. 1889–1896, Oct. 1997.

Coupled Circuit-Electromagnetic Simulation with Time Domain Integral Equations

Chuanyi Yang* and Vikram Jandhyala

Department of Electrical Engineering, University of Washington, Seattle WA 98195
Phone: 206-543-2186, Fax: 206-543-3842, Email: jandhyala@ee.washington.edu

1.Introduction

Time domain electromagnetic solvers are useful for simulating coupled circuit-electromagnetic (EM) problems involving integrated circuit packages and systems-on-chip, wherein effects of nonlinearities of circuit elements can be modeled accurately [1]. The surface-based time domain integral equation (TDIE) approach has been gaining in popularity owing to its flexibility in modeling arbitrarily-shaped structures and its enhanced computational performance due to advances in fast solution methods.

Existing methods to couple TDIE formulations to circuits have been based on port models, convolution methods, and the partial element equivalent circuit (PEEC) approach [2,3]. However, a seamless approach to integrate circuit and EM interactions without converting to circuits has not been developed within the scope of TDIEs.

In this work, a generalized rigorous coupling scheme, to simultaneously simulate circuits with SPICE-like time-domain simulation, and EM interactions with a TDIE method, is presented. This approach enables direct solution of circuit-EM equations without the need for generating port models. The method permits both circuit and EM excitations and thereby has potential as a signal integrity and as an EMI/EMC modeling tool.

2. Formulation

Consider a conducting object to be modeled with distributed EM simulation, with surface *S*, connected to arbitrary circuits, through terminals to be defined later, excited through voltage and current sources within the circuit, and optionally illuminated by one or more EM wave excitations. Assuming a surface impedance approximation for modeling finite connectivity, the boundary condition for the electric field on the surface of the object is

$$\left[\mathbf{E}^{s}(\mathbf{J})+\mathbf{E}^{inc}\right]_{\tan}=\left[Z_{s}*\frac{\partial \mathbf{J}}{\partial t}\right]_{\tan} \tag{1}$$

where $\mathbf{E}^{s}$ is the scattered electric field produced by the induced equivalent surface current $\mathbf{J}$, $\mathbf{E}^{inc}$ is the incident electric field, tan denotes the tangential components on the *S*, * denotes temporal convolution, and $Z_{s}(t)=\sqrt{\mu/\pi\sigma t}$ is the time domain representation of surface impedance. The surface *S* comprises of two disjoint surfaces, S_{EM} and S_{CK} such that on S_{EM} the standard continuity equation relating the surface current and charge holds

$$\nabla_{s}\cdot\mathbf{J}(\mathbf{r},t)+\frac{\partial\rho(\mathbf{r},t)}{\partial t}=0 \quad \forall\mathbf{r}\in S_{EM} \tag{2}$$

where ∇_{s} represents surface divergence. On S_{CK}, the *terminal* surfaces, the circuit current flowing onto S_{CK} from a corresponding circuit node introduces an additional source term that alters the surface current and charge on S. This permits connection of two disparate domains, the topology-based (connectivity only) circuit domain, and the geometry-based EM domain.

0-7803-7846-6/03/$17.00 ©2003 IEEE

Let S_{CK} itself be comprised of M disjoint surfaces $S_{CK}^m \quad m = 1,\ldots,M$. Each such unique sub-surface S_{CK}^m is termed one of M *terminals.* On S_{CK}^m the modified continuity equation has the following form

$$\nabla_s \cdot \mathbf{J}(\mathbf{r},t) + \frac{\partial \rho(\mathbf{r},t)}{\partial t} = J_c^m(\mathbf{r},t) \quad \forall\, \mathbf{r} \in S_{CK}^m \quad m = 1,..,M \tag{3}$$

where J_c^m represents the scalar volumetric current density produced on S_{CK}^m via a circuit interconnection. The current density introduced by the circuit interconnection produces an additional source or sink of charge that alters the time-dependent scalar potential and the resulting electric field.

When triangle-pair-based RWG spatial basis functions are used [4,5], the scattered field is written as

$$\begin{aligned}\mathbf{E}^s(\mathbf{r},t) = &-\frac{\partial}{\partial t}\frac{\mu}{4\pi}\sum_{i=1}^{N_e}\int_{T_{i+}\cup T_{i-}} \frac{\mathbf{J}(\mathbf{r}',t-|\mathbf{r}-\mathbf{r}'|/c)}{|\mathbf{r}-\mathbf{r}'|}ds' + \nabla\frac{1}{4\pi\varepsilon}\sum_{i=1}^{N_e}\int_{T_{i+}\cup T_{i-}}\int_0^{t-|\mathbf{r}-\mathbf{r}'|/c}\frac{\nabla_s\cdot\mathbf{J}(\mathbf{r}',\tau)}{|\mathbf{r}-\mathbf{r}'|}d\tau\, ds' \\ &-\nabla\frac{1}{4\pi\varepsilon}\sum_{m=1}^{M}\sum_{k=1}^{N_{p,CK}^m}\int_{T_{k,CK}^m}\int_0^{t-|\mathbf{r}-\mathbf{r}'|/c}\frac{J_{c,k}^m(\mathbf{r}',\tau)}{|\mathbf{r}-\mathbf{r}'|}d\tau\, ds'\end{aligned} \tag{4}$$

where N_e is the total number of triangular patches, $N_{p,CK}$ is the total number of triangular patches on all terminals, $T_{k,CK}^m$ denotes the kth triangular patch on terminal m, and T_{i+} and T_{i-} are the two patches associated with the ith edge. The standard procedure of testing [4,5] the above equation in space and time leads to a matrix equation of the form

$$\sum_{i=1}^{N_c} Z_{mi}^a(t_l) + \Delta t\sum_{i=1}^{N_c} Z_{mi}^b(t_l) + \Delta t\sum_{n=1}^{M}\sum_{k=1}^{N_{p,CK}^n} Q_{mnk}^a(t_l) = \Delta t\, F_m(t_l) + \sum_{i=1}^{N_e} Z_{mi}^a(t_{l-1}) + Z_m^c(t_l) \tag{5}$$

where the first matrix on the left relates to field from vector potential, the second matrix relates to field from scalar potential, and the third relates to field from scalar potential due to coupling currents. The first term on the right is the incident field, the second term is the history of vector potential and the third term is surface impedance contributions in a recursive convolution form. In addition to the scattered field, two more conditions are required for the circuit interconnection; electrically small terminals are assumed to be equipotential, leading to

$$\sum_{i=1}^{N_e} Z_{nk,i}^d(t_l) + \sum_{n'=1}^{M}\sum_{k'=1}^{N_{p,CK}^{n'}} Q_{nk,n'k'}^b(t_l) = V_m(t_l) \tag{6}$$

for $n = 1,\ldots,M; k = 1,..,N_{p,CK}^n$ where V_m is the circuit potential at the circuit node connected to terminal m, the first matrix represents scalar potential from surface current, and the second term is due to scalar potential from coupling currents. The final set of self-consistency equations relates to the application of Kirchoff's Current Law at the M nodes connected to the terminals :

$$\sum_{j=1}^{adj(n)} i_j^n(t_l) = \int_{S_{CK}^n} J_c^n(t_l)\,ds \tag{7}$$

for $n = 1,\ldots,M$ where $adj(n)$ denotes the number of nodes adjacent (neighboring) to the circuit node associated with terminal n, i_j^n is the circuit current entering node n from its j-th immediate neighbor, and J_c^n is the volume conduction current density at terminal n.

The systems of Equations (5-7) can be combined to yield the time-domain circuit-EM coupled system. The linear and non-linear circuits connected to the terminals are modeled by

Modified Nodal Analysis (MNA). The details for the linear and non-linear stamps in the MNA matrices and related solution methods are not discussed here. The combined system has the form

$$\begin{bmatrix} \overline{\mathbf{Z}_0^{ab}} & \overline{\mathbf{Q}_0^{a}} & \bar{\mathbf{0}} \\ \overline{\mathbf{Z}_0^{c}} & \overline{\mathbf{Q}_0^{b}} & \bar{\mathbf{C}} \\ \bar{\mathbf{0}} & \mathbf{C}^{\mathrm{T}} & \overline{\mathbf{MNA}_0} \end{bmatrix} \begin{bmatrix} \mathbf{I}(t_j) \\ \mathbf{J}_c(t_j) \\ \mathbf{ckt}(t_j) \end{bmatrix} = \sum_{i=1}^{j} \begin{bmatrix} \overline{\mathbf{Z}_i^{ab}} & \overline{\mathbf{Q}_i^{a}} & \bar{\mathbf{0}} \\ \overline{\mathbf{Z}_i^{c}} & \overline{\mathbf{Q}_i^{b}} & \bar{\mathbf{0}} \\ \bar{\mathbf{0}} & \bar{\mathbf{0}} & \overline{\mathbf{MNA}_i} \end{bmatrix} \begin{bmatrix} \mathbf{I}(t_{j-i}) \\ \mathbf{J}_c(t_{j-i}) \\ \mathbf{ckt}(t_{j-i}) \end{bmatrix} + \begin{bmatrix} \mathbf{src}_{EM}(t_j) \\ \mathbf{0} \\ \mathbf{src}_{CK}(t_j) \end{bmatrix} \quad (8)$$

where the unknown vector at time t_j relates to the strengths of surface currents, coupling currents, and circuit quantities. The sub-matrix subscripts refer to the type of matrices generated earlier. The vector $\mathbf{src}_{EM}(t_j)$ represents the tested incident field, and the vector $\mathbf{src}_{CK}(t_j)$ denotes the values of circuit sources. The matrix $\bar{\mathbf{C}}$ is a sparse bipolar adjacency matrix that is used for enforcing Kirchoff's Voltage and Current Laws at the circuit nodes connected to the terminals. This approach enables both linear and non-linear (through local Newton-Raphson on the MNA sub-matrix) circuit simulation in conjunction with EM simulation.

3. Numerical Results

In the first example, the coupled noise between an active signal pin and a passive signal pin located in the center of the structure is computed, and the impact of ground pins on the crosstalk between the two signal pins is analyzed (Fig. 1). Either end of the active pin is connected to its corresponding ground through a 52 Ω resistor, with a ramp voltage source in series with the resistor at top end. The passive pin is connected to the grounds through two similar resistors only. The voltage drop across the top and bottom end resistors of the passive pin are plotted. As more ground pins are added, the crosstalk dramatically decreases due to shorter return paths.

In the second example, incident field coupling to a nonlinear circuit through distributed bends is simulated (Fig. 2). A trapezoidal voltage source is applied to the nonlinear circuit, and a Gaussian pulse excitation is used to model the incident field. The simulation result shown is the output voltage at the inverter without and with the disruption of the incident field. The field causes switching times to change and also introduces an extra noise pulse, which can cause spurious switching.

4. Conclusions

A coupling scheme to simultaneously time-step MNA and TDIE equations was developed in this paper in order to model complex circuits with different levels of hierarchy. The method enables nonlinear simulation as well as EMI/EMC modeling.

5. Acknowledgements

This work was partially supported by DARPA-MTO NeoCAD grant N66001-01-1-8920, NSF-CAREER grant ECS-0093102, NSF-SRC Mixed-Signal Initiative grant CCR-0120371, and by a grant from Ansoft Corporation.

References

[1] I. Erdin, M. S. Nakhla, R. Achar, "Circuit Analysis of electromagnetic radiation and field coupling effects for networks with embedded full-wave modules," *IEEE Trans. Electromagnetic Compatibility*, vol. 42, pp. 449-460, Nov. 2000.

[2] W. Pinello, A. C. Cangellaris, A. Ruehli, "Hybrid electromagtic modeling of noise interactions in packaged electronics based on the partial-element equivalent-circuit formulation, " *IEEE Trans. Microwave Theory and Techniques*, vol. 45, pp. 1889-1896, Oct. 1997.

[3] P. J. Restle, A. E. Ruehli, S. G. Walker, G. Papadopoulos, “Full-wave PEEC time-domain method for the modeling of on-chip interconnects,” *Computer-Aided Design of Integrated Circuits and Systems, IEEE Trans.*vol. 20. pp. 877-866, Jul 2001.
[4]S. M. Rao, D. R. Wilton, “Transient scattering by conducting surfaces of arbitrary shape,” *IEEE Trans. Antennas Propagat.* vol. 39, pp. 56-61, Jan. 1991.
[5]S.M. Rao, *Time Domain Electromagnetics*, Academic Press, San Diego, CA, 1999.

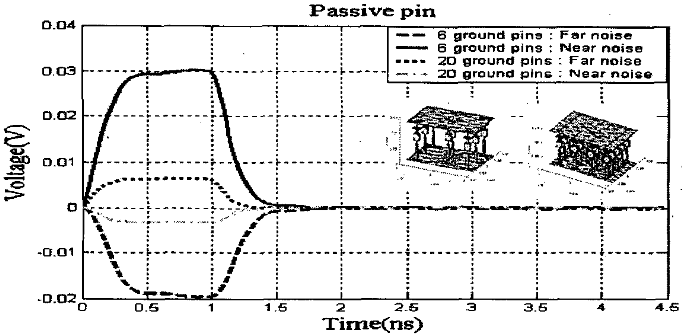

Figure 1: Near and Far end Noise voltage across a victim via due to an active via in the presence of grounding pins. Inset: Structures with 6 and 20 grounding pins

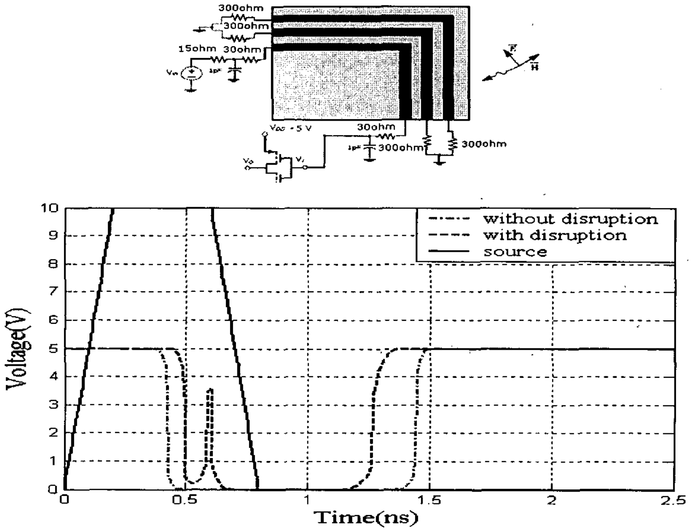

Figure 2: Output voltage (bottom) at inverter with and without a Gaussian pulse disruption of 10 KV/m. The input is a trapezoidal pulse to a three-conductor bend structure with ground on two conductors (top).

Evaluation of Green's Function Integrals in Conducting Media

Swagato Chakraborty and Vikram Jandhyala, *Member IEEE*

Abstract—**This paper presents an accurate integration method for computing Green's function operators related to lossy conducting media. The presented approach is ultra-wideband i.e. the integration schemes cover the entire range of frequency behavior, from high frequencies where skin current is prevalent to low frequencies where volume current flow dominates. The scheme is a step towards permitting exact ultra-wideband frequency domain surface-only-based integral-equation simulation of arbitrarily-shaped 3D conductors, and towards obviating the need for volume-based explicit frequency-dependent skin effect modeling. This work deals specifically with the computation of Green's functions and not with the unrelated but important low-frequency conditioning issue associated with the standard electric field integral equation.**

Index Terms— **Boundary Element methods, Conducting bodies, Electromagnetic Scattering, Integral Equations, Skin Effect.**

I. INTRODUCTION

SURFACE and volumetric integral equation techniques are powerful paradigms for modeling electromagnetic (EM) interactions in integrated circuit (IC) and packaging problems. While coupled electromagnetic and circuit analyses have been successfully realized through the popular volumetric partial element equivalent circuit (PEEC) approach [1],[2] the search for more general approaches, especially for modeling frequency-dependent skin effects and for arbitrarily-shaped structures, has led to circuit-coupled surface-based electric field integral equation (EFIE) formulations [3],[4]. In these and other works [5]-[12] it has been shown that surface integral equations and method of moments (MoM) formulations can be interpreted and applied as generalizations of volumetric EFIE - based PEEC. At high frequencies, surface impedance approximations are sufficiently accurate to model losses and inductive behavior caused by skin effects. However, at lower frequencies, standard surface impedance approximations are invalid. Therefore, for broadband simulation as necessitated in digital or ultra-wideband systems, a volumetric formulation is typically required at low frequencies. However in a volumetric formulation, the skin effect needs to be modeled explicitly through a volume meshing. It is noted that some recent efforts have been aimed at obtaining new surface impedance approximations.

Handling a mix of full-wave and skin-like effects with a surface-only formulation is desirable since frequency-dependent effects can be tracked without changing geometric discretization and without taking recourse to a special volume formulation at low frequencies. This is particularly true for small microelectronic structures where geometry detail and not wavelength is the guiding factor in mesh discretization. To accomplish a surface-only formulation valid for realistic conductors over a broad range of frequencies, the interior lossy medium EM problem must be addressed and coupled to the external medium model [10], and such a formulation requires explicit computation of the Green's function integrals in the interior lossy medium, in contrary to the volumetric formulation, where the Green's function integrals are always computed in the background medium.

This paper presents an exact formulation and accurate numerical quadrature scheme to efficiently compute highly damped Green's functions in lossy conductors. The presented method is general in terms of geometries, frequencies, material parameters, and relative separation and orientation of source and observer regions, and potentially forms an important step towards the realization of a surface-only ultra-wideband integral equation formulation.

It should be noted that the low frequency-dependence and modeling issue being addressed here is distinct from the classical low frequency ill-conditioning of an EFIE formulation. In fact, depending on the conductance involved, the issue discussed here can arise at much larger frequencies than those where the EFIE is inherently ill-conditioned. The treatment here is complementary to advances in improving EFIE conditioning [9] at low frequencies.

The presented quadrature scheme, discussing computation of the relevant Green's function integrals in lossy media using RWG functions in a PMCHW formulation, is initially facilitated by transforming the Green's function computation associated with RWG functions into polar coordinates. Subsequently, the proper order of integration results in one analytic integration along one coordinate. Finally, the remaining one-dimensional integral is computed as a summation of several superposed integrals over different bands in the integration coordinate.

Manuscript received October 28, 2002. This work was supported in part by DARPA-MTO NeoCAD grant N66001-01-1-8920, NSF-CAREER grant ECS-0093102, NSF-SRC Mixed-Signal Initiative grant CCR-0120371, and by a grant from Ansoft Corporation.

The authors are with the Department of Electrical Engineering, University of Washington, Seattle, WA 98195 USA. (phone : 206-543-2186; fax: 206-543-3482; e-mail: jandhyala@ee.washington.edu).

Section II of this paper presents the two-region formulation that utilizes the integrals that are the subject of this paper. Existing quadrature schemes are discussed in Section III. The specific frequency dependence of the integrals under study is outlined in Section IV. Section V presents the polar-coordinate-based integration schemes. Numerical results, self-consistency checks and comparisons with other techniques are detailed in Section VI, and Section VII presents conclusions and continuing work.

II. FORMULATION AND RESULTANT INTEGRALS

In a two-region surface equivalent problem [10], with the two regions being a homogeneous lossless background medium, typically free space or a lossless dielectric, and the interior of a realistic conductor, the exterior equivalent problem utilizes the background medium Green's function, while the lossy medium Green's function is required for the interior equivalent problem. For the electric field integral equation (EFIE), scalar and vector potential integrals will be necessitated, while for the magnetic field integral equation (MFIE), an integrand that represents the curl of the vector potential is required. In general, for PMCHW [10] and combined field integral equation (CFIE) formulations, all three types of integrands need to be computed.

Typically for a region characterized with material properties given by the permeability μ and permittivity ε, the electric and magnetic field $\mathbf{E}$ and $\mathbf{H}$ can be represented by the equations

$$\mathbf{E} = \mathbf{E}^{inc} - j\omega\mathbf{A} - \nabla\phi - \frac{1}{\varepsilon}\nabla\times\mathbf{F} \tag{1a}$$

$$\mathbf{H} = \mathbf{H}^{inc} - j\omega\mathbf{F} - \nabla\psi + \frac{1}{\mu}\nabla\times\mathbf{A} \tag{1b}$$

where $\mathbf{E}^{inc}$ and $\mathbf{H}^{inc}$ are the incident electric and magnetic fields in the region, $\mathbf{A}$ and $\mathbf{F}$ are the magnetic and electric vector potentials, ϕ and ψ represent the electric and magnetic scalar potentials, $\omega = 2\pi f$ where f is the frequency of operation.

The scalar and vector potentials can be written in terms of the Green's function G and the electric and magnetic current density, $\mathbf{J}$ and $\mathbf{M}$ as:

$$\mathbf{A}(\mathbf{r}) = \frac{\mu}{4\pi}\int_{S'} G(\mathbf{r},\mathbf{r}')\,\mathbf{J}(\mathbf{r}')\,ds' \tag{2a}$$

$$\mathbf{F}(\mathbf{r}) = \frac{\varepsilon}{4\pi}\int_{S'} G(\mathbf{r},\mathbf{r}')\,\mathbf{M}(\mathbf{r}')\,ds' \tag{2b}$$

$$\phi(\mathbf{r}) = \frac{j}{4\pi\varepsilon\omega}\int_{S'} G(\mathbf{r},\mathbf{r}')\nabla\cdot\mathbf{J}(\mathbf{r}')\,ds' \tag{2c}$$

$$\psi(\mathbf{r}) = \frac{j}{4\pi\mu\omega}\int_{S'} G(\mathbf{r},\mathbf{r}')\nabla\cdot\mathbf{M}(\mathbf{r}')\,ds' \tag{2d}$$

where the Green's functions $G(\mathbf{r},\mathbf{r}')$ for a source point $\mathbf{r}'$ located in the source region S', and an observation point $\mathbf{r}$ is

$$G(\mathbf{r},\mathbf{r}') = \frac{e^{-jk|\mathbf{r}-\mathbf{r}'|}}{|\mathbf{r}-\mathbf{r}'|} \tag{3}$$

k is the wave number at an angular frequency ω for a material with $\sigma, \mu_r, \varepsilon_r$ as the conductivity, relative permeability and permittivity respectively, and is given by

$$k = \omega\sqrt{\mu_0\mu_r\varepsilon_0(\varepsilon_r + \frac{\sigma}{j\omega\varepsilon_0})} \tag{4}$$

Two auxiliary potentials $\mathbf{\Pi}$, and Γ are introduced to represent the four potentials in (2) as, $\mathbf{A} = \mu\mathbf{\Pi}$, $\mathbf{F} = \varepsilon\mathbf{\Pi}$; $\phi = \frac{\Gamma}{\varepsilon}, \psi = \frac{\Gamma}{\mu}$, where

$$\mathbf{\Pi}(\mathbf{r}) = \frac{1}{4\pi}\int_{S'} G(\mathbf{r},\mathbf{r}')\,\mathbf{X}(\mathbf{r}')\,ds' \tag{5a}$$

$$\Gamma(\mathbf{r}) = \frac{j}{4\pi\omega}\int_{S'} G(\mathbf{r},\mathbf{r}')\nabla\cdot\mathbf{X}(\mathbf{r}')\,ds' \tag{5 b}$$

Additionally, the curl operators in (1) are represented as

$$\nabla\times\mathbf{\Pi}(\mathbf{r}) = -\frac{1}{4\pi}\int_{S'} \nabla' G(\mathbf{r},\mathbf{r}')\times\mathbf{X}(\mathbf{r}')\,ds' \tag{5c}$$

where $\mathbf{X}$ represents the electric or magnetic current density. The popular triangle-pair-based Rao-Wilton-Glisson (RWG) functions [7] are used to represent $\mathbf{X}(\mathbf{r}')$, wherein current is modeled by edge-based piecewise linear vector functions, and the divergence of current is represented by piecewise constant scalar functions as $\mathbf{X}(\mathbf{r}) = \frac{\boldsymbol{\rho}'^{\pm} l}{2A^{\pm}}$, and $\nabla\cdot\mathbf{X}(\mathbf{r}) = \frac{l}{A^{\pm}}$ [7] where $\boldsymbol{\rho}'^{\pm}$ represents the vector joining the node opposite to the edge in question to (from) the source point $\mathbf{r}'$ in the positive (negative) triangle, $A^{\pm}$ denotes the area of the positive(negative) triangle, and l is the length of the edge.

The generalized potential integrals (5) can be written for RWG sources as

$$\mathbf{\Pi}(\mathbf{r}) = \frac{l}{8\pi A}(\mathbf{M}_{vect} + \boldsymbol{\rho}^c M_{scal}) \tag{6a}$$

$$\Gamma(\mathbf{r}) = \frac{jl}{4\pi\omega A}M_{scal} \tag{6b}$$

$$\nabla\times\mathbf{\Pi}(\mathbf{r}) = \frac{l}{8\pi A}[\mathbf{R}^i\times(\mathbf{N}_{vect} + \boldsymbol{\rho}^c N_{scal})] \tag{6c}$$

where

$$\mathbf{M}_{vect} = \iint_T \boldsymbol{\rho}\frac{e^{-jkR}}{R}\,ds' \tag{7a}$$

$$M_{scal} = \iint_T \frac{e^{-jkR}}{R}\,ds' \tag{7b}$$

$$\mathbf{N}_{vect} = \iint_T \boldsymbol{\rho}\frac{e^{-jkR}(1+jkR)}{R^3}\,ds' \tag{7c}$$

$$N_{scal} = \iint_{T} \frac{e^{-jkR}(1+jkR)}{R^3}\, ds' \tag{7d}$$

and $\mathbf{R}^i$ represents the vector joining the vertex of the source triangular region *T* (Fig. 1) opposite to the edge in question to the observation point, $\boldsymbol{\rho}^c$ is the vector from the same vertex to the projection of the observation point onto the plane of *T*, and $\boldsymbol{\rho}$ is the vector from the projection of the observation point $\mathbf{r}$ on the plane of *T* to a source point $\mathbf{r}'$ on *T*. $R = |\mathbf{r} - \mathbf{r}'|$, is the radial distance between the source and the observation point.

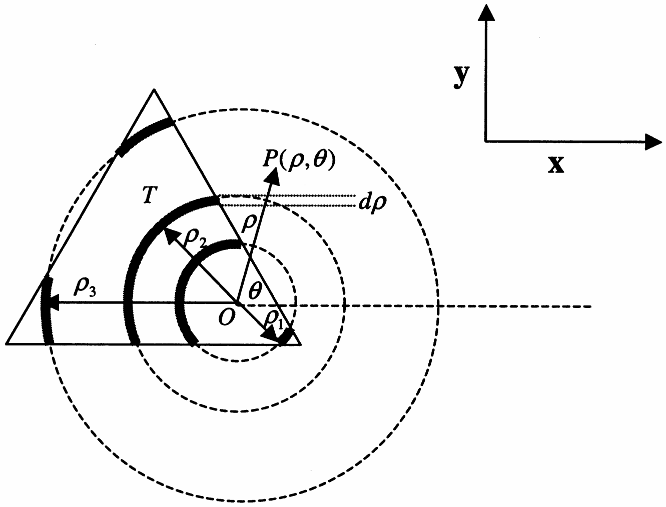

Figure 1: Region of integration is shown for ($\rho = \rho_1, \rho_2, \rho_3$), for a triangular region T, for the projection of the observation point on the plane of triangle O. Gray sections denote intervals of θ where the source point $P(\rho,\theta)$ lies within the triangle.

III. EXISTING ANALYTICAL AND NUMERICAL QUADRATURE SCHEME FOR EVALUATING GREEN'S FUNCTIONS

In the extant literature, evaluation of the potential integral (5) in free-space and low-loss media has been done by a variety of numerical schemes. For near-field terms, singularity extraction of the kernels in (5a, 5b) is performed analytically [11],[12] to leave a function that can be integrated numerically with a low-order quadrature rule [13]. Recently, methods based on the Duffy transform have emerged, wherein the triangular integration region is transformed to a rectangle with a subsequent cancellation of the singularity. The integral in (5c) has been evaluated in free space [14], and in lossless dielectrics [10].

When the medium is conducting, even the singularity-extracted part may exhibit a rapid spatial decay, i.e. the extracted integral appears nearly singular when the observation point is sufficiently close to the source triangle. Hence, standard singularity extraction [11] fails to evaluate the integral accurately.

A suitable approach to Green's function computation in lossy media is polar coordinate integration, which can render the non-essential singularity cancelled through the Jacobian of transformation. Such methods are discussed previously in [15], [16] for lossless media and in [17] for lossy media, for the restricted case of the scalar Green's function in (7b). However these methods are not sufficiently general for the integrals in (7a, 7c, 7d) that are related to the vector potential or its curl. Another polar coordinate approach is proposed in [18] to evaluate the vector integral for the specific case of self-term integration. The method is extendable to the case when the observation point is located anywhere in the plane of the source triangle itself. This precludes the important case of observation at a near-singular point located above or below the source triangle, as occurs in thin conductors.

In Section V we propose a general method for evaluating scalar, vector, and gradient Green's functions in lossy media with RWG basis functions. The presented technique works for all frequencies and for all relative positions between source triangles and observation points. The next section discusses the frequency-dependent behavior of the generalized potential integrals in conducting media that necessitates the specialized quadrature presented in later sections.

IV. FREQUENCY DEPENDENCE OF GREEN'S FUNCTIONS IN CONDUCTING MEDIA

The behavior of the Green's functions in (7) for conducting media is highly dependent on frequency. Consider a Method of Moments (MoM) [7] matrix created for interactions between RWG functions for the interior medium equivalent, which uses the conducting medium Green's functions. At high frequencies, the MoM matrix is nearly diagonal because of a very rapid exponential spatial decay of the conducting medium Green's function owing to the large imaginary part of the wave-number in (4).

At lower frequencies, the interactions between non-overlapping RWG functions are not negligible; and the MoM matrix becomes progressively less sparse but has sections which are numerically sparse (e.g. in double precision arithmetic) due to large exponential decays. As the frequency is further lowered the MoM matrix is completely full while showing a weak exponential decay with distance. Eventually, the MoM matrix is full and the exponential decay is very weak or absent.

To summarize, at intermediate frequencies, between sharp fall-off and no fall-off regimes, special numerical treatment is required; the integrands presented by the lossy medium Green's function have sharp radial decay, and non-self interactions are also prominent. Depending on the frequency, the entire MoM matrix might be numerically significant. Fixed-order 2D Gaussian quadrature rules in [13], that are popular in RWG-based MoM implementations will not provide accurate answers at such frequencies, owing to rapid decays of the Green's functions over finite distances.

V. COMPUTATION OF GENERALIZED POTENTIAL INTEGRALS IN CONDUCTING MEDIUM

The generalized potential integrals in (6) for RWG sources are constituted by the four terms in (7), which can be transformed into polar coordinates as,

$$\mathbf{M}_{vect} = \hat{\mathbf{x}}\iint_T \frac{\rho^2 e^{-jk\sqrt{\rho^2+d^2}}}{\sqrt{\rho^2+d^2}}\cos\theta\, d\rho\, d\theta + \hat{\mathbf{y}}\iint_T \frac{\rho^2 e^{-jk\sqrt{\rho^2+d^2}}}{\sqrt{\rho^2+d^2}}\sin\theta\, d\rho\, d\theta \qquad (8a)$$

$$M_{scal} = \iint_T \frac{\rho\; e^{-jk\sqrt{\rho^2+d^2}}}{\sqrt{\rho^2+d^2}} d\rho\, d\theta \qquad (8b)$$

$$\mathbf{N}_{vect} = \hat{\mathbf{x}}\iint_T \frac{\rho^2(1+jk\sqrt{\rho^2+d^2})\, e^{-jk\sqrt{\rho^2+d^2}}}{(\sqrt{\rho^2+d^2})^3}\cos\theta\, d\rho\, d\theta + \hat{\mathbf{y}}\iint_T \frac{\rho^2(1+jk\sqrt{\rho^2+d^2})\, e^{-jk\sqrt{\rho^2+d^2}}}{(\sqrt{\rho^2+d^2})^3}\sin\theta\, d\rho\, d\theta \qquad (8c)$$

$$N_{scal} = \iint_T \frac{\rho\;\, (1+jk\sqrt{\rho^2+d^2})\, e^{-\,jk\sqrt{\rho^2+d^2}}}{(\sqrt{\rho^2+d^2})^3} d\rho\, d\theta \qquad (8d)$$

In the above equations, the $\hat{\mathbf{x}}$ and $\hat{\mathbf{y}}$ coordinates are local to the source triangle *T* (Fig. 1) and define the plane in which *T* lies. Also, *d* is the perpendicular distance of the observation point from the plane of *T*, and (ρ, θ) is the polar coordinate of a source point in *T*, with the projection of the observation point onto the plane of *T* as the origin. The scalar integrals in (8b, 8d) and the scalar components of the vector integrals in (8a, 8c) can be written in a generalized form, as

$$I_{\varphi\chi} = \int_{\rho}\int_{\theta}\varphi(\rho)\chi(\theta)d\rho d\theta \qquad (9)$$

where φ is one of $\varphi_{M,vect}$, $\varphi_{M,scal}$, $\varphi_{N,vect}$, $\varphi_{N,scal}$ defined below as

$$\varphi_{M,vect}(\rho) = \frac{\rho^2 e^{-jk\sqrt{\rho^2+d^2}}}{\sqrt{\rho^2+d^2}} \qquad (10a)$$

$$\varphi_{M,scal}(\rho) = \frac{\rho\, e^{-jk\sqrt{\rho^2+d^2}}}{\sqrt{\rho^2+d^2}} \qquad (10b)$$

$$\varphi_{N,vect}(\rho) = \frac{\rho^2(1+jk\sqrt{\rho^2+d^2})e^{-jk\sqrt{\rho^2+d^2}}}{(\sqrt{\rho^2+d^2})^3} \qquad (10c)$$

$$\varphi_{N,scal}(\rho) = \frac{\rho(1+jk\sqrt{\rho^2+d^2})e^{-jk\sqrt{\rho^2+d^2}}}{(\sqrt{\rho^2+d^2})^3} \qquad (10d)$$

Also χ is one of χ_c, χ_s, χ_0 defined below as

$$\chi_c(\theta) = \cos\theta \qquad (11a)$$

$$\chi_s(\theta) = \sin\theta \qquad (11b)$$

$$\chi_0(\theta) = 1 \qquad (11c)$$

Owing to the simple closed form expressions for the integral of $\chi(\theta)$, the integral $I_{\varphi\chi}$ can be recast as a function of ρ as

$$I_{\varphi\chi} = \iint_T \varphi(\rho)\chi(\theta)d\rho d\theta = \int_{\rho_{\min}}^{\rho_{\max}}\varphi(\rho)\xi(\rho)d\rho \qquad (12)$$

where $\rho_{\min}$ and $\rho_{\max}$ are the extremal ρ for which $\Im\theta \ni P(\rho,\theta) \in T$, $P(\rho,\theta)$ denotes a point having coordinate (ρ,θ) (Fig. 1), and ξ is one of ξ_c, ξ_s, ξ_0 with

$$\begin{pmatrix}\xi_c(\rho)\\ \xi_s(\rho)\\ \xi_0(\rho)\end{pmatrix} = \sum_{i=1}^{K(\rho)}\begin{pmatrix}\xi_c^i(\rho)\\ \xi_s^i(\rho)\\ \xi_0^i(\rho)\end{pmatrix} = \sum_{i=1}^{K(\rho)}\int_{\theta_{\min}^i(\rho)}^{\theta_{\max}^i(\rho)}\begin{pmatrix}\cos\theta\\ \sin\theta\\ 1\end{pmatrix}d\theta$$

$$= \sum_{i=1}^{K(\rho)}\begin{bmatrix}\sin\theta\\ -\cos\theta\\ \theta\end{bmatrix}_{\theta_{\min}^i(\rho)}^{\theta_{\max}^i(\rho)} = \sum_{i=1}^{K(\rho)}\begin{bmatrix}\sin\theta_{\max}^i\;\;(\rho) - \sin\theta_{\min}^i(\rho)\\ -\cos\theta_{\max}^i(\rho) + \cos\theta_{\min}^i(\rho)\\ \theta_{\max}^i(\rho) - \theta_{\min}^i(\rho)\end{bmatrix} \qquad (13)$$

Also, $K(\rho)$ is the number of intervals (Fig. 1) in $\theta, 0 \le \theta < 2\pi$, for which $P(\rho,\theta)$ lies in *T*, and $\theta_{\max}^i$ and $\theta_{\min}^i$ are the limits on θ for the i^{th} interval. The values of $\theta_{\max}^i(\rho)$ and $\theta_{\min}^i(\rho)$ for each section are computed by obtaining the intersection of *T* and the circle of radius ρ centered at the projection of the observation point onto the plane of *T*. If the circle with radius ρ lies entirely in *T*, $K(\rho) = 1, \theta_{\max}^1 = 2\pi$, and $\theta_{\min}^1 = 0$. Hence

$$\begin{pmatrix}\xi_c(\rho)\\ \xi_s(\rho)\\ \xi_0(\rho)\end{pmatrix} = \begin{pmatrix}0\\ 0\\ 2\pi\end{pmatrix} \qquad (14)$$

Alternatively, if for a given ρ, if the circle is completely outside *T* then the integral contributions are all zero. Consequently, the constituents of the generalized potential integrals (8) can be computed using (10-13) as

$$\mathbf{M}_{vect} = \hat{\mathbf{x}}\int_{\rho_{\min}}^{\rho_{\max}}\varphi_{M,vect}(\rho)\xi_c(\rho)d\rho + \hat{\mathbf{y}}\int_{\rho_{\min}}^{\rho_{\max}}\varphi_{M,vect}(\rho)\xi_s(\rho)d\rho \qquad (15a)$$

$$M_{scal} = \int_{\rho_{\min}}^{\rho_{\max}}\varphi_{M,scal}(\rho)\xi_0(\rho)d\rho \qquad (15b)$$

$$\mathbf{N}_{vect} = \hat{\mathbf{x}} \int_{\rho_{\min}}^{\rho_{\max}} \varphi_{N,vect}(\rho)\xi_c(\rho)d\rho + \hat{\mathbf{y}} \int_{\rho_{\min}}^{\rho_{\max}} \varphi_{N,vect}(\rho)\xi_s(\rho)d\rho \tag{15c}$$

$$N_{scal} = \int_{\rho_{\min}}^{\rho_{\max}} \varphi_{N,scal}(\rho)\xi_0(\rho)d\rho \tag{15d}$$

It is important to note that the kernels $\varphi_{N,vect}(\rho), \varphi_{N,scal}(\rho)$ of the integrals in (15c,d) are singular for $\rho \to 0, d = 0$ in evaluating the self-term. However, for such case in (6c), $\mathbf{R}^i$, $\mathbf{N}_{vect}$, and $\boldsymbol{\rho}^c$, lie in the plane of the source triangle. Hence $\nabla \times \mathbf{\Pi}(\mathbf{r})$ in (6c) is perpendicular to the plane of the source triangle, which is also the observation triangle for the self-term evaluation. Thus when tested with a testing function tangential to the observation triangle (e.g. Galerkin testing, etc.), the resulting contribution always vanishes. Hence special treatment to take care of the non-removable singularity in the integrals in (15c,d) is not required for the special case of planar discretization discussed in the paper.

VI. NUMERICAL RESULTS

In this section, the proposed integration schemes are used to compute integrals for all the cases in (15). Comparisons with 2D Gaussian quadrature are presented along with the results obtained by incorporating the presented technique in a two-region circuit coupled field solver.

For purposes of illustration, and without loss of generality, the source triangle T^{source} for the presented results has nodes located at $(1,-1,0)$, $(1,0.5,0)$, $(-2,0.5,0)$, and the observation point P^{obs} lies outside the plane of T^{source}, at $(0,0,1)$, with all distances measured in mm. The conductivity of the medium is that of copper 5.8×10^7 Sm^{-1}.

A relative accuracy comparison between the proposed scheme and fixed order 2D Gaussian quadrature with singularity extraction is demonstrated in Fig. 2 and Fig. 3. At low frequencies, the Green's functions in lossy media exhibit slow decay over distance and hence, for example, a 7-point 2D Gaussian quadrature scheme [13] works adequately, and the relative difference between the two methods is small. As the frequency is increased, the details of the decay in the Green's functions due to the increased imaginary part of the wave-number (2.4) are not captured by the low-order 2D Gaussian rule and the proposed methodology of this paper is required. The fact that the discrepancy between the results from the proposed method and from low-order 2D Gaussian quadrature is due to the Gaussian quadrature becoming inaccurate is further evident from comparisons with a higher-order 2D Gaussian quadrature rule using 25 points on a triangle. In this case the frequency at which the 25-point quadrature breaks down increases compared to the 7-point quadrature. In general, for any order of 2D Gaussian quadrature, there is a frequency point beyond which the fixed order 2D quadrature will be inaccurate due to insufficient sampling of the details in the decay of the Green's function. The presented method accurately models the decay through an analytic integration and is therefore accurate at any frequency. This is seen in both the vector integrals (15a,c) (Fig. 2a) and the scalar integrals (15 b,d) (Fig. 2b), where the observation point does not lie on the plane of the source triangle. Similar plots for vector (15a) (Fig. 3a) and scalar (15b) (Fig. 3b) are provided for the self-term integration. While the main aim of this work is the formulation and development of the quadrature rules themselves, one example of the behavior of the rules when included in a complete two-region PMCHW formulation is shown next.

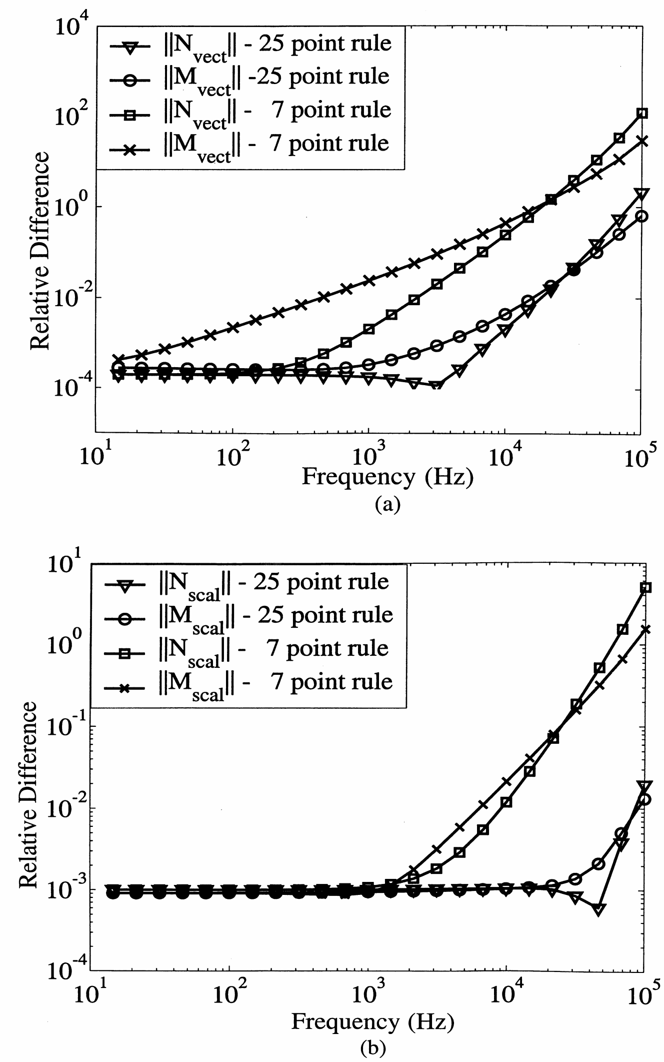

Figure 2: Comparison between 2D Gaussian rules with singularity extraction and proposed method for evaluation of the integral $\mathbf{N}_{vect}$, $\mathbf{M}_{vect}$ in (7c,7a) (a), and N_{scal} and M_{scal} in (7d,7b) (b) for the non-self-term integral, for a triangle with vertices ($\alpha, -\alpha, 0$),($\alpha, \alpha/2, 0$),($-2\alpha, \alpha/2, 0$), and observation point located at $(0, 0, \alpha)$,where $\alpha = 1$ mm , with $\sigma = 5.8 \times 10^7$ Sm^{-1}.

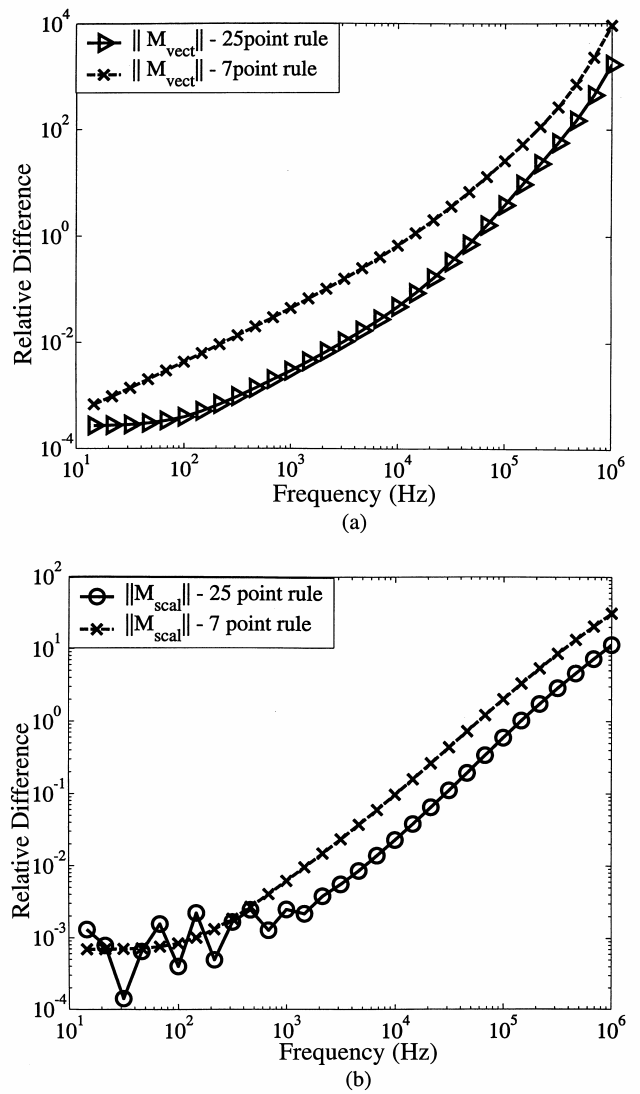

(a)

(b)

Figure 3: Comparison between 2D Gaussian rules with singularity extraction and proposed method for evaluation of the integral $\mathbf{M}_{vect}$ in (7a) (a) and M_{scal} in (7b) (b) for the self-term integral, for a triangle with vertices $(\alpha,-\alpha,0)$,$(\alpha,\alpha/2,0)$,$(-2\alpha,\alpha/2,0)$, and observation point located at $(0,0,0)$,where $\alpha = 1$ mm , with $\sigma = 5.8\times10^7$ Sm^{-1}.

Figure 4 demonstrates the comparison between analytic and extracted resistances using the presented quadrature in both quasi-static and full-wave codes.

As expected, the two codes give same results as analytic computations at low frequencies; eventually, at high frequencies, the full-wave code also predicts additional radiation resistance.

Figure 5a compares the extracted resistance using a coupled circuit-EM formulation [3] and the quadrature scheme presented in this paper, versus standard 2D Gaussian quadrature rules in the same formulation, as well as versus an (approximate) impedance boundary formulation where interior quadrature is not required [19].

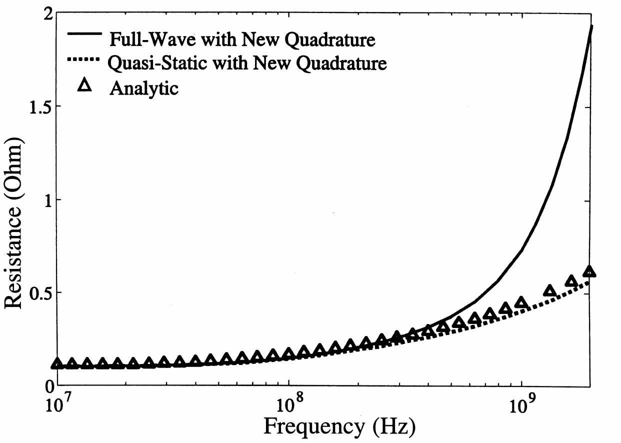

Figure 4: Extracted resistance of a cylinder with radius 0.5mm and length 5 mm, using PMCHW formulation with the proposed quadrature scheme, for a full-wave and a quasi-static formulation, and the analytic value of resistance using skin effect approximation.

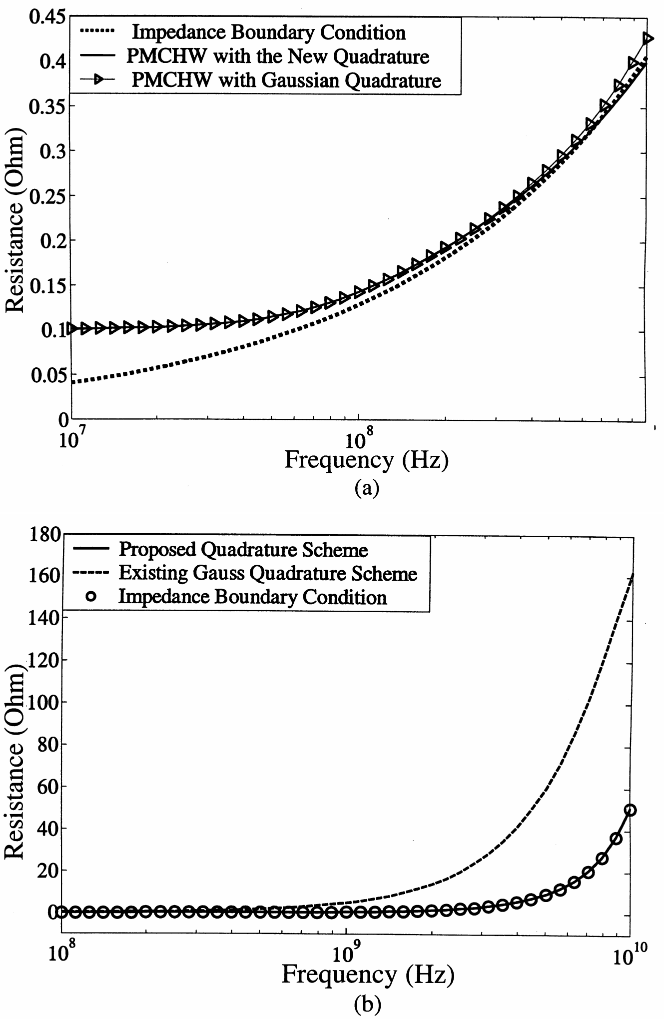

(a)

(b)

Figure 5: Extracted resistance of a cylinder with radius 0.5mm and length 5 mm, using PMCHW formulation with the proposed quadrature scheme, Gaussian quadrature, and impedance boundary condition for low frequencies (a), and high frequencies (b).

At low frequency, the expected match between the two quadrature-rules is validated (owing to small decay in the Green's function). At high frequencies, (Fig. 5b) the new quadrature also matches with the impedance boundary formulation [19] results; the impedance boundary condition is inaccurate at low frequencies (Fig. 5a) relative to skin depth, and fails to capture the leveling off of the resistance at low frequency. Conversely, the 2D Gauss quadrature scheme becomes inaccurate at high frequencies, which is demonstrated in Fig. 5b. At such frequencies the proposed quadrature scheme produces same result as the impedance boundary condition formulation, while at low frequencies the two quadrature schemes produce the same result. The proposed quadrature scheme has been used to find the Q-factor of a realistic on-chip spiral inductor in Fig. 6.

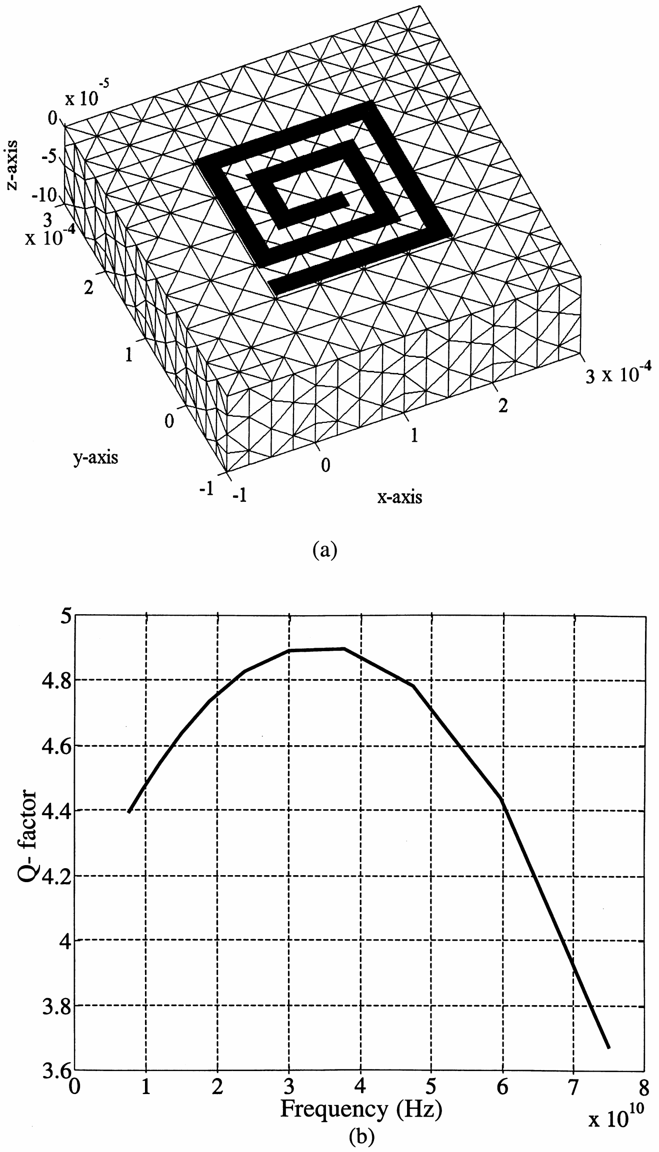

(a)

(b)

Figure 6: Q-factor (b) computation of a spiral copper inductor on a substrate with shown (a) dimensions. Conductivity of the substrate is 1×10^{-5} Sm^{-1}

VII. CONCLUSION

In this paper, a new approach to evaluate the Green's function operators for RWG functions in conducting media is presented. The method works for arbitrarily located sources and observers for any frequency. This technique has been incorporated into a broadband two-region surface formulation for accurate computation of frequency-dependent parameters, and shows the potential to obviate the need to switch to volumetric formulations at frequencies where volumetric current flow is dominant.

ACKNOWLEDGMENT

The authors would like to thank the anonymous reviewers for their comments. The authors also thank Dipanjan Gope, Yong Wang, and Todd West for their help with numerical simulations.

REFERENCES

[1] H. Heeb and A. E. Ruehli, "Three-dimensional interconnect analysis using partial element equivalent circuits," *IEEE Transactions on Circuits and Systems I: Fundamental Theory and Applications*, vol. 39, no. 11, pp. 974-982, Nov. 1992.

[2] A. Rong and A. C. Cangellaris, "Generalized PEEC models for three-dimensional interconnect structures and integrated passives of arbitrary shapes," *Proceedings Electrical Performance of Electronic Packaging*, pp. 225 –228, Oct. 2001.

[3] V. Jandhyala, W. Yong, D. Gope, and R. Shi, "Coupled electromagnetic-circuit simulation of arbitrarily-shaped conducting structures using triangular meshes," *Proceedings International Symposium on Quality Electronic Design*, pp. 38-42, Mar. 2002.

[4] S. Ponnapalli, A. Deutsch, and R. Bertin, "A package analysis tool based on a method of moments surface formulation," *IEEE Transactions on Components, Hybrids, and Manufacturing Technology*, vol. 16, no. 8, pp. 884-892, Dec. 1993.

[5] J. Wang, J. Tausch, and J. White, "A wide frequency range surface integral formulation for 3-D RLC extraction," *Digest of Technical Papers International Conference on Computer-Aided Design*, pp. 453-457, Nov. 1999.

[6] J. Wang, "A new surface integral formulation of EMQS impedance extraction for 3D structures," Ph.D. dissertation, Dept. EECS MIT, Cambridge, MA, 1999.

[7] S. M. Rao, D. R. Wilton, and A. W. Glisson, "Electromagnetic scattering by surfaces of arbitrary shape," *IEEE Transactions on Antennas Propagation*, vol. 30, no. 3, pp. 409-418, May 1982.

[8] J. S. Zhao and W. C. Chew, "Accurate and efficient simulation of crosstalks," *Proceedings of the Progress in Electromagnetics Research Symposium*, Boston, pp. 396, July 2002.

[9] S. Chen, J. S. Zhao, and W. C. Chew, " Analyzing low-frequency electromagnetic scattering from a composite object," *IEEE Transactions on Geoscience and Remote Sensing*, vol. 40, no. 2, pp. 426-433 , Feb. 2002.

[10] K. Umashankar, A. Taflove, and S. M. Rao, "Electromagnetic scattering by arbitrary shaped three dimensional homogeneous lossy dielectric objects," *IEEE Transactions on Antennas and Propagation*, vol. 34, no. 6, pp. 758-766, June 1986.

[11] R. D. Graglia, "On the numerical integration of the linear shape function times the 3-D Green's function or its gradient on a planar triangle," *IEEE Transactions on Antennas and Propagation*, vol. 41, no. 10, pp. 1448-1455, Oct. 1993.

[12] D. R. Wilton, S. M. Rao, A. W. Glisson, D. H. Schaubert, O. M. Al-Bundak, and C. M. Butler, "Potential integrals for uniform and linear source distributions on polygonal and polyhedral domain," *IEEE Transactions on Antennas and Propagation*, vol. 32, pp. 276-281, March 1984.

[13] M. Abramowitz and I. Stegun, Chapter 25, Handbook of Mathematical Functions, Dover, New York, 1970, pp. 887-894.

[14] R. E. Hodges and Y. R. Samii, "The evaluation of MFIE integrals with the use of vector triangle basis function," *Microwave and Optical Technology Letters*, vol. 14, no. 1, pp. 9-14, Jan.1997.

[15] M. Gimersky, S. Amari, and J. Bornemann, "Numerical evaluation of the two-dimensional generalized exponential integral," *IEEE Transactions on Antennas and Propagation*, vol. 44, pp. 1422-1425, 1996.

[16] J. K. Gamage, “Efficient method of moments for compact large planar scatterers in homogeneous medium,” *Proceedings of 11th International Conference on Antennas and Propagation*, no. 2, pp. 741-744, April 2001.

[17] Z. Zhu, J. Huang, B. Song, and J. White, “Improving the robustness of a surface integral formulation for wideband impedance extraction of 3D structures,” *Proceedings of International Conference on Computer Aided Design*, pp. 592-597, Nov. 2001.

[18] L. Rossi and P. J. Cullen, “On the fully numerical evaluation of the linear-shape function times the 3-D Green’s function on a planar triangle,” *IEEE Transactions on Microwave Theory and Techniques*, vol. 47, pp. 398-402, April 1999.

[19] A. W. Glisson, “Electromagnetic scattering by arbitrarily shaped surfaces with impedance boundary conditions,” *Radio Science*, vol. 27, no. 6, pp. 935-943, Nov. 1992.

Swagato Chakraborty was born in Kolkata, India, on October 3, 1978. He received the B.Tech degree in electronics and electrical communication engineering from the Indian Institute of Technology, Kharagpur, WB India, in the year 2001.He is pursuing his doctoral research in the Applied Computational Electromagnetics (ACE) group in University of Washington, Seattle, WA USA. His research interests include frequency domain integral equation, material models, fast algorithms, coupled circuit-electromagnetic formulations.

Vikram Jandhyala (M’00-SM’03) received the B. Tech degree in electrical engineering from the Indian Institute of Technology, Delhi, in 1993, and the M.S. and Ph.D. degrees from the University of Illinois at Urbana-Champaign, in 1995 and 1998, respectively. As part of his graduate work, he co-developed the steepest-descent fast-multipole method for rapid simulation of a large class of electromagnetic problems. From 1998-2000, he was a research and development engineer at Ansoft Corporation, Pittsburgh, PA. He was involved in the acceleration of Ansoft's integral equation solvers, and co-developed a fast multipole based extraction tool in Ansoft's Spicelink versions released in 1999 and 2000. Since 2000, he has been an assistant professor in the department of electrical engineering at the University of Washington, Seattle.

He directs the applied computational electromagnetics laboratory, with research interests and projects in several areas of computational electromagnetics, including fast solvers and integral equation formulations in frequency and time domains, high-speed circuits and devices, coupled multi-physics simulation, novel materials, and propagation. He has published more than 70 journal and conference articles, has served as a reviewer for several IEEE journals and conferences and national and international proposal panels, and is on the technical program committee of the IEEE Design Automation Conference and the IEEE Antennas and Propagation Symposium.

Dr. Jandhyala is a Senior member of the IEEE, a full elected member of URSI Commission B. He has visiting research status at the Lawrence Livermore National Labs, is a recipient of the NSF CAREER grant (2001), an outstanding graduate research award at the University of Illinois(1998), and an IEEE microwave graduate fellowship (1996-97).

Evaluation of Green's Function Integrals in Conducting Media

Swagato Chakraborty* and Vikram Jandhyala

Department of Electrical Engineering, University of Washington, Seattle WA 98195
Phone: 206-543-2186, Fax: 206-543-3842, Email: jandhyala@ee.washington.edu

1.Introduction

Method of moments (MoM) solvers are useful for simulating coupled circuit-electromagnetic problems [1] involving integrated circuit packages and systems-on-chip, wherein frequency-dependent skin effects can be modeled, and arbitrarily-shaped structures such as on-chip inductors can be analyzed with surface-only formulations. For broadband analog and digital applications, spectral current and field components can arise at sufficiently low frequencies where surface impedance approximations [2] for approximating skin effects are not valid. For seamless surface-based broadband simulation, it is important to explicitly model the interior of conducting materials in order to avoid ad-hoc mixing of surface and volume based formulations. This paper focuses on broadband computation of lossy medium scalar, vector, and gradient Green's function integrals for arbitrarily located sources and observers.

Existing methods for computing Green's function integrals address subsets of the above problem; for instance, singularity extraction [3] in conjunction with 2D Gaussian quadrature [4] can be used for computation of Green's function integrals in lossy media at very low frequencies where exponential spatial decays are weak. Methods suitable for computing Green's function integrals at high frequencies are discussed previously in [5] for lossless media and in [6] for lossy media, for the restricted case of the scalar Green's function. A similar approach is proposed in [7] to evaluate the scalar and the vector cases for self-term integration, with extensions possible in-plane observation. However, the crucial case of near-singular observation points outside the plane, as in the modeling of very thin conductors cannot be handled by the approach in [7]. The computation of gradient Green's function integrals has not been addressed by the methods [5-7].

In this work we propose a polar-coordinate transformation and new mixed analytic and numerical quadrature for accurate evaluation of RWG function [8] based scalar, vector, and gradient Green's function integrals in lossy conducting media in a form more general than other existing methods. The presented technique is broadband and applicable to any distribution of source and testing function locations and orientations and to any lossy material.

2. Formulation and Resultant Integrals

The magnetic and electric potentials due to an RWG basis function in a lossy medium can be described as linear combinations of four two-dimensional integrals $\mathbf{M}_{vect}$ [7], M_{scal} [5-6], $\mathbf{N}_{vect}$ and N_{scal} [9] given as

$$\mathbf{M}_{vect} = \iint_T \boldsymbol{\rho} \frac{e^{-jkR}}{R} ds' \ , \ M_{scal} = \iint_T \frac{e^{-jkR}}{R} ds' \tag{2.1a}$$

$$\mathbf{N}_{vect} = \iint_T \boldsymbol{\rho} \frac{e^{-jkR}(1+jkR)}{R^3} ds' \ , \ N_{scal} = \iint_T \frac{e^{-jkR}(1+jkR)}{R^3} ds' \tag{2.1b}$$

where T denotes a source triangle, $\boldsymbol{\rho}$ is the vector from the projection O of the observation point $\mathbf{r}$ on the plane of T to a source point $\mathbf{r}'$ in T, and $R = |\mathbf{r} - \mathbf{r}'|$ is the

0-7803-7846-6/03/$17.00 ©2003 IEEE

radial distance between the source and the observation point. R can be written as $R = \sqrt{\rho^2 + d^2}$, where d denotes the distance of the observation point $\mathbf{r}$ from the plane of T. The complex wave-number in the interior of the conductor is denoted by k. Equation (2.1a) can be expressed in polar coordinates as

$$\mathbf{M}_{vect} = \hat{\mathbf{x}} \int_{\rho_{\min}}^{\rho_{\max}} \frac{\rho^2 e^{-jk\sqrt{\rho^2+d^2}}}{\sqrt{\rho^2 + d^2}} \left(\int_{\theta_{\min}(\rho)}^{\theta_{\max}(\rho)} \cos\theta \, d\theta \right) d\rho + \hat{\mathbf{y}} \int_{\rho_{\min}}^{\rho_{\max}} \frac{\rho^2 e^{-jk\sqrt{\rho^2+d^2}}}{\sqrt{\rho^2 + d^2}} \left(\int_{\theta_{\min}(\rho)}^{\theta_{\max}(\rho)} \sin\theta \, d\theta \right) d\rho \quad (2.2)$$

where local two-dimensional x-y coordinates have been used in the plane of T and θ is the polar angle of a source point $\mathbf{r}'$ relative to the local coordinate system with origin at O. The limits on ρ are given by its extremals for which a circle with radius ρ centered at O intersects T. The limits on θ for a given ρ are obtained by finding the intersection points of T with the circle of radius ρ. In general, the four integrals in Eqns. (2.1a,b) can be recast into polar coordinates to obtain separable integrals of the form

$$I = \int_{\rho_{\min}}^{\rho_{\max}} f(\rho, k, d) \left(\int_{\theta_{\min}(\rho)}^{\theta_{\max}(\rho)} g(\theta) \, d\theta \right) d\rho \qquad (2.3)$$

The integral in Eqn. (2.3) is separable in its variables ρ and θ, and the integral in θ has a simple closed form expression. Thus the overall integral can finally be expressed as a 1D integral in ρ as, $I = \int_{\rho_{\max}}^{\rho_{\min}} u(\rho) \, d\rho$.

It is important to note the change in order of integration compared to that in [5-7], where the (analytic) integration is done first on ρ. While [5-6] consider only the scalar integral, in [7] the on-plane observer locations ($d = 0$) lead to functions of ρ for the vector integral that are easily integrable, which is not the case for general observation points ($d \neq 0$). To obviate this problem, particularly for the crucial case of near singular off-plane observation points, the change in order of integration is performed in our work. In the proposed method, $g(\theta)$ is always a simple sinusoidal function or a constant, due to the fact that the Green's functions are not dependent on the polar angle θ. Therefore the θ integral can be computed analytically in all cases (arbitrary locations, materials, frequencies, and scalar, vector, and gradient integrals), leading to a final 1D numerical integration in ρ, of the integrand $u(\rho)$, which is a continuous and piece-wise smooth function in the interval $(\rho_{\min}, \rho_{\max})$. Boundaries of the subintervals of ρ over which $u(\rho)$ is smooth, are the radii values for which the circle touches the vertices of T or its edges tangentially. An adaptive 1D integration rule has been developed for the functions above using an approach similar to Matlab's *quad8*.

3. Numerical Results

A relative accuracy comparison between the proposed scheme and fixed-point two-dimensional Gaussian quadrature with singularity extraction is demonstrated in Fig. 1 for the interior of a Copper conductor. At low frequencies, the Green's functions in lossy media exhibit slow decay over distance and hence a 7-point Gaussian quadrature scheme [4] functions adequately. As the frequency is increased, the details of the sharp exponential decay in the Green's functions are not captured by the low-order Gaussian rule. The presented formulation explicitly models the exponential decays and is thus not affected by the added detail. To confirm that the 7-point Gaussian rule has broken down for this case, a higher-order 25-point Gaussian quadrature scheme is also used. This method shows better accuracy than the lower order rule in the range of 100-1000 Hz. However, as is evident, as the frequency is increased further, the 25-point rule also becomes inaccurate. In general, any fixed-order two-dimensional rule will become inaccurate after a certain frequency. While this has not been explicitly verified in this paper, it is expected that a well-designed 1D adaptive quadrature scheme should outperform an adaptive two-dimensional quadrature rule for the reasons that the exponential decay is explicitly extracted in the 1D form, making amenable the use of a specialized quadrature rule (e.g. Gauss-Laguerre [4]), and that the explicit independence of the Green's function on the polar angle is exploited in the 1D form.

Figure 2 demonstrates the ability of the proposed method in conjunction with a coupled two-region circuit-EM MoM formulation [1] to compute the frequency-dependent resistance of a cylinder, with radius 0.5 mm. and length 5 mm, including the low-frequency leveling off behavior to the DC value of 0.109 Ω, using a two-region PMCHW formulation [10]. Also shown is the solution from the surface impedance approximation, which becomes inaccurate at low frequencies (Fig.2, left) but provides the correct answer at higher frequencies (Fig.2, right). A fixed-point two-dimensional Gaussian rule gives correct answers at very low frequencies (Fig.2, left) but is inaccurate above a certain frequency (Fig.2, right).

4. Conclusions

In this paper, a new approach to evaluate the Green's function operators for RWG functions in conducting media is presented. The method works for arbitrarily located sources and observers for any frequency. This technique has been incorporated into a broadband two-region surface formulation for accurate computation of frequency-dependent parameters, and shows the potential to obviate the need to switch to volumetric formulations at low frequencies where skin effect is not well developed.

Acknowledgements

This work was partially supported by DARPA-MTO NeoCAD grant N66001-01-1-8920, NSF-CAREER grant ECS-0093102, NSF-SRC Mixed-Signal Initiative grant CCR-0120371, and by a grant from Ansoft Corporation.

References

[1] V. Jandhyala, W.Yong, D.Gope, and R. Shi, "Coupled electromagnetic-circuit simulation of arbitrarily-shaped conducting structures using triangular meshes," *Proceedings International Symposium on Quality Electronic Design*, pp. 38-42, Mar. 2002.

[2] A.W.Glisson, "Electromagnetic scattering by arbitrarily shaped surfaces with impedance boundary conditions," *Radio Science*, vol. 27(6) , pp. 935-943, Nov. 1992.

[3] R.D. Graglia, "On the numerical integration of the linear shape function times the 3-D Green's function or its gradient on a planar triangle," *IEEE Transactions on Antennas and Propagation*, vol. 41, pp. 1448-1455, 1993.

[4] M. Abramowitz and I. Stegun, Chapter 25, *Handbook of Mathematical Functions*, Dover, New York, 1970.

[5] M. Gimersky, S. Amari, and J. Bornemann, "Numerical evaluation of the two-dimensional generalized exponential integral," *IEEE Transactions on Antennas and Propagation,* vol. 44, pp. 1422-1425, 1996.

[6] Z. Zhu, J. Huang, B. Song, and J. White, "Improving the robustness of a surface integral formulation for wideband impedance extraction of 3D structures," *Proceedings of International Conference on Computer Aided Design*, pp. 592-597, 2001.

[7] L. Rossi and P.J. Cullen, "On the fully numerical evaluation of the linear-shape function times the 3-D Green's function on a planar triangle," *IEEE Transactions on Microwave Theory and Techniques*, vol. 47, pp. 398-402, 1999.

[8] S.M. Rao, D.R.Wilton, and A.W. Glisson, "Electromagnetic scattering by surfaces of arbitrary shape," *IEEE Transactions on Antennas Propagation*, vol. 30, pp. 409-418, 1982.
[9] R.E.Hodges and Y.Rahmat Samii, "The evaluation of MFIE integrals with the use of vector triangle basis function," *Microwave and Optical Technology Letters*, vol. 14 (1), pp. 9-14, Jan.1997.
[10] K.Umashankar, A.Taflove, and S.M.Rao, "Electromagnetic scattering by arbitrary shaped three dimensional homogeneous lossy dielectric objects," *IEEE Transactions on Antennas and Propagation*, Vol 34(6) , pp. 758-766, June 1986.

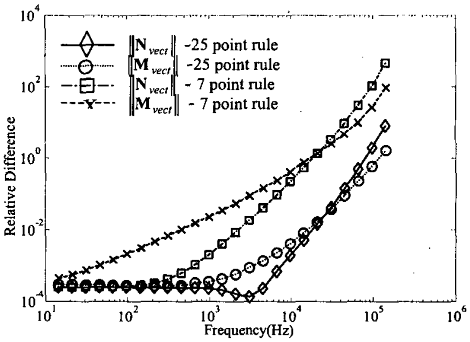

Figure 1: Comparison between 2D Gaussian rules with singularity extraction and proposed method for evaluation of the integrals $\mathbf{M}_{vect}$ and $\mathbf{N}_{vect}$ in Eqns. (2.1a,b) for a non-self-term integral, for a triangle with vertices $(\alpha,-\alpha,0)$,$(\alpha,\alpha/2,0)$,$(-2\alpha,\alpha/2,0)$, and observation point located at $(0,0,\alpha)$,where $\alpha = 1\,\text{mm}$, with $\sigma = 5.8\times10^7$ S/m.

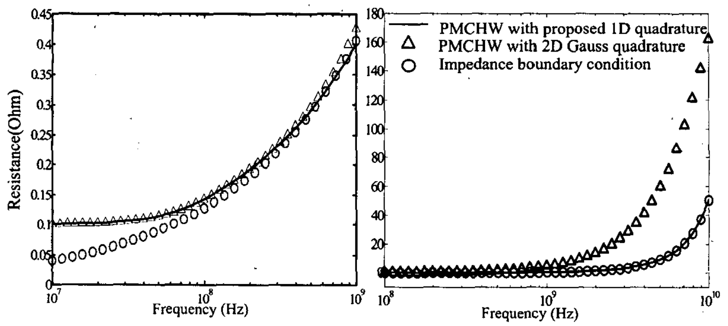

Figure 2: Extracted resistance of a cylinder of radius 0.5mm and length 5 mm with $\sigma = 5.8\times10^4$ S/m using a two region PMCHW formulation with the standard 7-point 2D Gaussian quadrature method and the method proposed in this paper, and an impedance boundary condition formulation, for a low frequency band (left) and higher frequencies (right).

Mixed Electromagnetic and Circuit Simulations using a Higher-Order Hybrid Formulation

Nathan J. Champagne* and John D. Rockway
Defense Sciences Engineering Division
Lawrence Livermore National Laboratory
Livermore, CA 94550

Vikram Jandhyala
Department of Electrical Engineering
University of Washington
Seattle, WA 98195

INTRODUCTION

Standard surface impedance approximations are invalid at lower frequencies approaching DC since the cross sections of conductors are smaller than the skin depth. Hence, a volumetric formulation is typically used at these low frequencies for broadband simulation as necessitated in digital or ultra-wideband systems since the skin effect can be modeled explicitly. This modeling requires fine and frequency dependent volume meshing. However, an approach using higher-order elements and/or bases may alleviate these requirements. The intent of this paper is to present a tightly coupled circuit and hybrid boundary element (or integral equation)/finite element based electromagnetic simulation that has been coded in EIGER [1].

HYBRID FORMULATION

The approach used for the hybrid formulation has been presented in [2]. The body of interest is shown in Fig. 1. The surface of the body is used to create a boundary to separate the problem into interior and exterior regions. Finite elements are used in the interior volume *V*. A boundary element formulation is applied on the body surface *S* to model the exterior. The interior volume of the body is modeled with finite elements using the electric field Helmholtz equation, represented as

$$\nabla \times \left(\bar{\boldsymbol{\mu}}_r^{-1} \cdot \nabla \times \mathbf{E} \right) - k_0^2 \, \bar{\boldsymbol{\varepsilon}}_r \cdot \mathbf{E} = -\, j\omega\mu_0 \mathbf{J} \,, \tag{1}$$

where **E** is the electric field, k_0 is the freespace wave number, ω is the radian frequency, and $\boldsymbol{\varepsilon}_r$ and $\boldsymbol{\mu}_r$ are the relative permittivity and permeability dyads, respectively. The body exterior is modeled using boundary elements on the body surface, in this case using the electric field integral equation (EFIE), which is given by

$$\frac{\mathbf{M}}{2} - \hat{\mathbf{n}} \times \left(j\omega \mathbf{A} + \nabla\Phi + \frac{1}{\varepsilon} \nabla \times \mathbf{F} \right) = -\hat{\mathbf{n}} \times \mathbf{E}^i, \quad \mathbf{r} \uparrow S \,, \tag{2}$$

where $\hat{\mathbf{n}}$ is the normal to the surface at the observation point, $\mathbf{E}^i$ is the impressed electric field, and **A**, Φ, and **F** are the magnetic vector, electric scalar, and the electric vector potentials, respectively. Also, the jump discontinuity of the curl term in (2) has been removed and expressed explicitly in terms of the magnetic current **M**. The fields and currents are expanded using the basis functions described in [3].

CIRCUIT–CONNECTION ALGORITHM

The contact-connection algorithm [4,5] is employed to couple the circuit to the electromagnetic surface. A circuit is attached to a spatially localized surface S_c by enforcing at this contact a modified current-continuity equation, a KCL connection, and a KVL connection from the contact to the circuit node. This is shown in Fig. 2. These three conditions are fundamental to the coupled hybrid-circuit formulation. On a contact surface S_c, the continuity equation is changed to account for injecting branch current from the circuit. This current introduces an additional source term in the continuity equation and thus affects the distribution of both the electromagnetic surface currents and surface charges. Hence, the continuity equation is modified to become

$$\nabla \cdot \mathbf{J} + j\omega\rho = \begin{cases} I_c, & r \in S_c, \\ 0, & \text{otherwise}, \end{cases} \tag{3}$$

where I_c is the contact current. This contact current provides a virtual extension from the distributive electromagnetic surface to the circuit node. The coupling between the electromagnetic formulation and the circuit is done by enforcing (2) at the boundary and coupling them to the circuit by including the contact current from (3). The localized circuit source attached to the contact produces an additional source or sink of charge that alters the scalar potential and the resulting electric field. Because of this additional current, the scalar potentials must be tied to the circuit node voltage V_n. A KVL expression sets the scalar potentials at the equipotent circuit voltage V_n. Finally, the contact current is connected to the circuit by including an addition term I_c to the KCL based circuit equation associated at circuit node *n*.

The hybrid-circuit formulation, including the connecting KCL and equipotential KVL equations, may be summarized as the following block-matrix equation:

$$\begin{bmatrix} FEM & C_A & 0 \\ C_B & BEM & X \\ 0 & -X^T & MNA \end{bmatrix} \begin{bmatrix} V_{EM} \\ I_{EM} \\ I_{ckt} \end{bmatrix} = 0, \tag{4}$$

where the *FEM* block matrix represents the finite elements, *BEM* represents the boundary elements and contacts, and the *C* blocks represent the cross-coupling between the finite elements and boundary elements. The X and X_T block matrices are the connection matrices between circuit nodes and contacts, and the *MNA* block matrix represents the modified nodal circuit analysis.

RESULTS

A rectangular connector (1 mm × 1 mm × 4 mm) is modeled to determine the convergence of the resistance curve around the first resonance of the structure. The results shown in Fig. 3 include the hybrid formulation (164 triangles and 216 tetrahedrons) and the boundary element method formulation (48 rectangles) from [5]. The complete basis order is denoted by p. The various results agree well except when p=0 for the boundary element method since convergence had not been obtained.

SUMMARY

A hybrid boundary element/finite element formulation is coupled with a technique for representing circuit-to-EM connections. Higher-order bases functions and elements may be used in the analysis. Results were presented to validate the hybrid formulation compared to the boundary element formulation.

ACKNOWLEDGMENTS

This work was partially supported by DARPA-MTO NeoCAD grant N66001-01-1-8920.

This work was performed under the auspices of the U.S. Department of Energy by University of California, Lawrence Livermore National Laboratory under Contract W-7405-Eng-48.

REFERENCES

[1] R.M. Sharpe, J.B. Grant, N.J. Champagne, W.A. Johnson, R.E. Jorgenson, D.R. Wilton, W.J. Brown, and J.W. Rockway, "EIGER: Electromagnetic Interactions GEneRalized," *1997 IEEE AP-S International Symposium and North American URSI Radio Science Meeting*, Montreal, Canada, July 1997, pp. 2366–2369.

[2] P.W. Fink and D.R. Wilton, "Higher order modeling in the BEM and hybrid BEM/FEM formulations," Ph.D. dissertation, Univ. Houston, Houston, TX, 2002.

[3] R.D. Graglia, D.R. Wilton and A.F. Peterson, "Higher order interpolatory vector bases for computational electromagnetics," *IEEE Trans. Antennas and Propagation*, vol. 45, No.3, pp. 329–342, Mar. 1997.

[4] V. Jandhyala and C. Yang, "A time domain surface integral technique for mixed electromagnetic and circuit simulation," *Proc. IEEE meeting on Electric. Perf. of Electron. Packaging*, San Jose, October 2002, pp. 41–44.

[5] N.J. Champagne, J.D. Rockway, and V. Jandhyala, "Mixed electromagnetic and circuit simulations using higher-order elements and bases," *2003 International Conference on Electromagnetics in Advanced Applications*, Torino, Italy, September 2003, pp. 103–106.

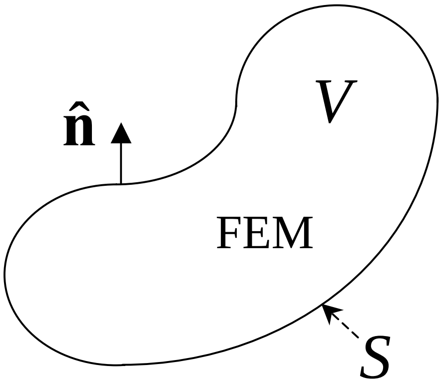

Figure 1. A body is in space where the volume *V* is surrounded by the surface *S*.

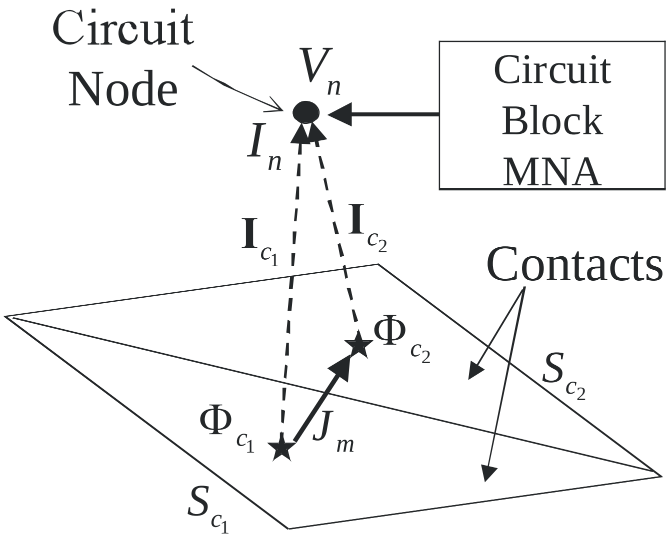

Figure 2. This schematic shows the approach for creating the contact-circuit connection.

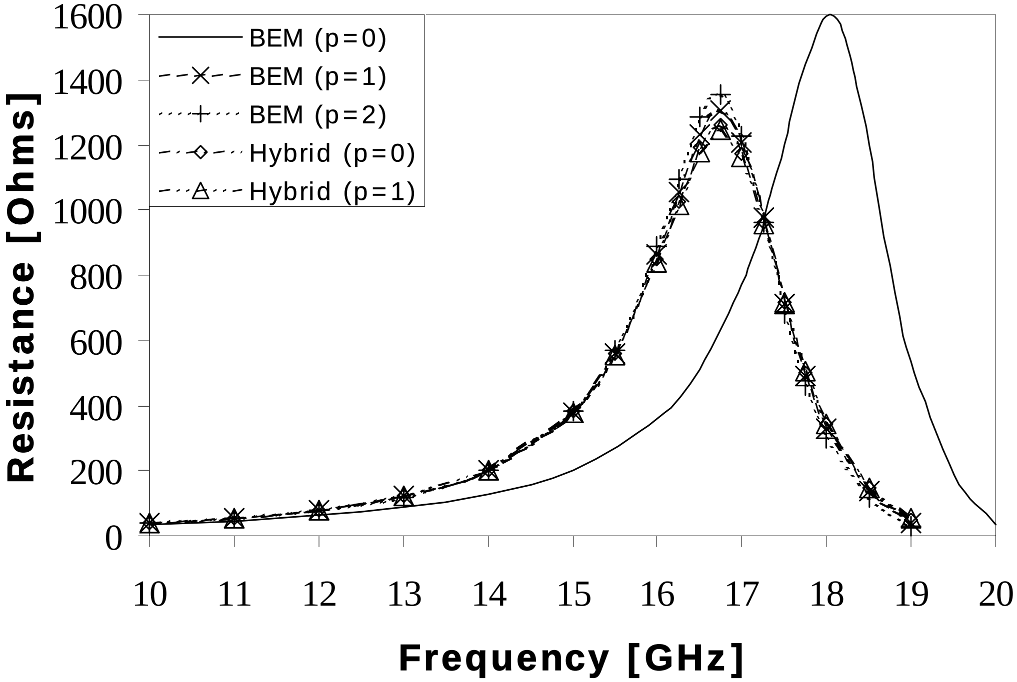

Figure 3. This is a plot of the resistance versus frequency for a rectangular connector. The connector was modeled using a boundary element method (BEM) and hybrid BEM/FEM formulation (FEM). The complete basis order *p* for each case is shown in the legend.

and inverted, compared to the radiating-basis triangular element, is introduced on this antenna (Fig. 5). The goal here is to combine the matching frequencies of the two created antennas (one with h_1 = 7.5 mm, and the other h_2 = 15 mm) and thus to widen the resultant bandwidth of the structure.

This results in a VSWR of about 1.5 (Fig. 6) and a much better adaptation from 3 to 7 GHz (Fig. 7). By comparing these results with those obtained experimentally, a widening of the bandwidth after 7 GHz (which was not observed in the simulation, can be noted. This variation is certainly due to the phenomenon of loss adaptation related to the poor performances of epoxy at high frequencies. The fact that this antenna is fed by a broader CPW line than that of the preceding one (the wave only propagates in the substrate under the feeding line) may explain why this phenomenon was not perceived in the first antenna.

The addition of the slot does not disturb the radiation pattern, in comparison with the first structure, while the efficiency is better and fluctuates around 80% over the entire bandwidth (Fig. 8).

6. CONCLUSION

Two new omnidirectional antennas for short-range UWB communications have been presented; the first one amply covers the WPAN standard, and the other one presents a very good adaptation and good radiation efficiency on a very broad frequency band. Both antennas are approximately the same size as a standard business card, have low manufacturing cost, and are matched to 50Ω. Optimizations of radiation pattern and tests on better quality substrate should increase the high-frequency performances of these two antennas.

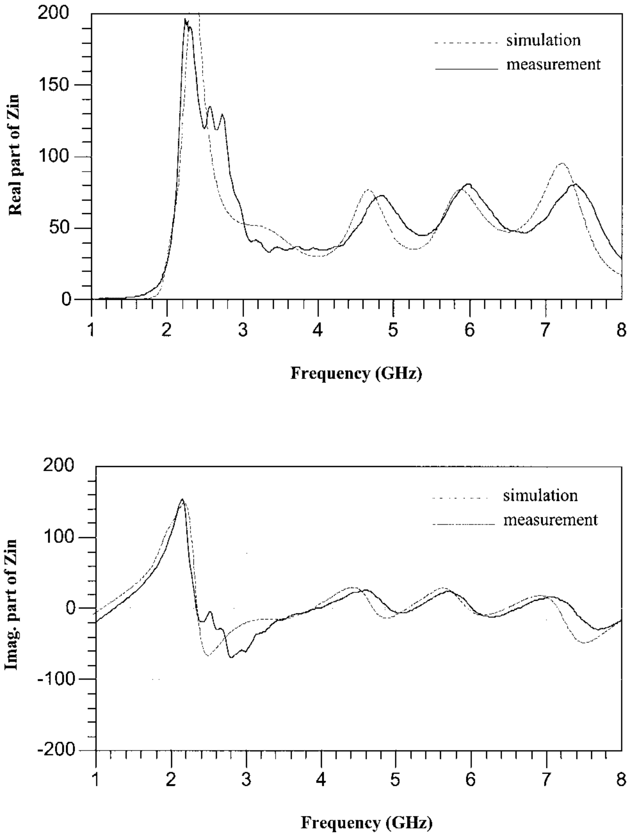

Figure 7 Real and imaginary parts of the input impedance

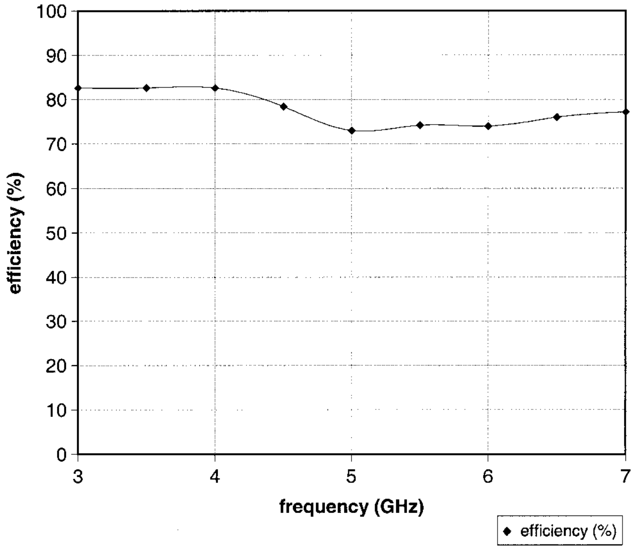

Figure 8 Radiation efficiency

REFERENCES

1. D.J. Daniels, Surface-penetrating radar, IEE Radar Sonar Navigation Avionics Series 6 (1996), 72–93.
2. J.R. Foerster, The effect of multipath interference on the performance of UWB systems in an indoor wireless channel, IEEE Semiannual Vehic Technol Conf, Rhodos, Greece 2001.
3. S.L. March, C.M. Panasik, UWB: Next generation WPAN, Int Microwave Symp UWB Wkshp, Amsterdam, Netherlands 2003.
4. R.C. Johnson, Antenna engineering handbook, 3rd ed. 1993, pp. 42-8–42-13.
5. G.H. Brown, and O.M. Woodward, Experimentally determined radiation characteristics of conical and triangular antennas, RCA Rev 13 (1952), 425–452.
6. Z.N. Chen, Experiments on input impedance of tilted planar monopole antenna, MOTL 26 (2000), 202–204.

PILOT: A FAST ALGORITHM FOR ENHANCED 3D PARASITIC CAPACITANCE EXTRACTION EFFICIENCY

Dipanjan Gope and Vikram Jandhyala
Dept. of Electrical Engineering
University of Washington
Seattle, WA 98195

Received 13 October 2003

ABSTRACT: *Integral-equation methodologies applied to extract parasitics for board, package, and on-chip structures involve solving a dense system of equations. In this paper, we present an improved matrix-compression technique for fast iterative solution of such dense systems, which applies QR decomposition on multilevel oct-tree-based interaction sub-matrices. The regular-tree structure of the fast-multipole method and the rank-revealing QR-based matrix-compression scheme are combined in order to achieve superior time and memory efficiency. As is demonstrated by the numerical-simulation results presented herein, the new algorithm is found to be faster and more memory efficient than both existing QR-based methods and FastCap.* © 2004 Wiley Periodicals,

Inc. Microwave Opt Technol Lett 41: 169–173, 2004; Published online in Wiley InterScience (www.interscience.wiley.com). DOI 10.1002/mop.20083

Key words: *method of moments; fast multipole method; low-rank compression; capacitance; integral equation*

1. INTRODUCTION

Due to the increasing complexity of design structures on boards, packages, and chips, numerical techniques that utilize field solutions for parasitic extraction are preferred when high accuracy is necessary. Among the existing numerical tools, a surface-based integral-equation methodology such as the method of moments (MoM) [1] is ideally suited to address the problem. It leads to a well-conditioned system with reduced size, as compared to volumetric methods [2], but the system of equations generated is inherently dense, thereby creating a time and memory bottleneck. Several fast iterative techniques have been developed to efficiently sore and solve a MoM system with linear time and memory complexity. All these methods, including QR-based approaches [3, 4], fast-multipole methods (FMMs) [5], and FFT-based techniques [6] accelerate matrix-vector products and therefore expedite the Krylov-subspace iterative solution [7].

The QR-based fast iterative solver (IES^3) [3, 4] adopts a binary-tree multilevel decomposition of the geometry and consequent low-rank compression of the MoM sub-matrices which represent the interaction between well-separated geometrical regions. This scheme is particularly attractive for circuit problems, since it can be directly applied with multilayered dielectric Green's functions. Even in terms of free-space capacitance extraction, IES^3 has been demonstrated as being more efficient in terms of memory and solve time. However, this method suffers from a higher setup-time cost, due to the irregular nature of the adopted binary-tree structure for the geometry subdivisions and the unpredictable nature of the optimal matrix structure.

In this work, we have developed a predetermined interaction list oct-tree (PILOT) QR algorithm that greatly reduces the setup time while maintaining the memory and solve-time efficiency of the rank-map-based binary tree QR (RMBT-QR), which is based on the same principles as IES^3. PILOT exploits the properties of a multilevel oct-tree implementation (common to multilevel fast multipole method (FMM) approaches), to create a predetermined tree structure, thereby considerably reducing the setup time.

2. INTEGRAL EQUATION

Capacitance problems formulated using the MoM are solved via Poisson's equation $\nabla^2\phi(\mathbf{r}) = -\rho(\mathbf{r})/\varepsilon$, relating potential ϕ and charge-density ρ. The discretization of the integral form of this equation results in a matrix system of the form $\bar{\mathbf{Z}}\mathbf{I} = \mathbf{V}$ where the $N \times N$ MoM matrix $\bar{\mathbf{Z}}$ is a dense Green's function matrix, $\mathbf{I}$ represents the unknown coefficients of known charge density basis functions, and $\mathbf{V}$ is the known potential excitation. Each element of the MoM matrix denotes the interaction between a testing and a basis function and is written as follows:

$$\bar{\mathbf{Z}}(j, i) = \int_{S_j} ds t_j(\mathbf{r}) \int_{S_i} ds' g(\mathbf{r}, \mathbf{r}') f_i(\mathbf{r}'), \tag{1}$$

where t and f are the testing and basis functions, S is their domain, and $g(\mathbf{r}, \mathbf{r}')$ is the relevant Green's function.

3. EXISTING MULTILEVEL QR ALGORITHM

The IES^3 fast iterative solver reduces the cost of performing the matrix vector product $\bar{\mathbf{Z}}\mathbf{I}$ to $O(N \log N)$ from quadratic time. It is based on using the modified Gram–Schmidt (MGS) method [8] for QR decomposition of a low-ranked interaction sub-matrix $\bar{\mathbf{A}}$ of the MoM matrix $\bar{\mathbf{Z}}$:

$$\bar{\mathbf{A}}_{\mathrm{mxn}} = \bar{\mathbf{Q}}_{\mathrm{mxr}}\bar{\mathbf{R}}_{\mathrm{rxn}}, \tag{2}$$

where $\bar{\mathbf{R}}$ is upper triangle, $\bar{\mathbf{Q}}$ is unitary, that is, $\bar{\mathbf{Q}}^{\mathrm{T}}\bar{\mathbf{Q}} = \bar{\mathbf{I}}$ and $r \ll (m, n)$. At the same time, it is possible to construct the compressed representations without forming the entire submatrix from sampled rows and columns, thereby reducing the setup time to $O(N \log N)$.

In RMBT-QR, which is based on the same principle as IES^3, the algorithm has the following three main steps.

1. Geometry subdivisions into cells. binary decompositions with density balancing and tight bounds, technically known as tightly bound *k-d* trees [9], are employed in a manner similar to those used in IES^3.
2. Rank-map predicted QR formations. a rank-map is a statically-determined lookup table that identifies large and low-ranked submatrices for QR formation so as to ensure maximum compression with minimum setup time. Each entry of the tale outlines the expected rank of a cell-to-cell interaction, which is a function of various parameters pertaining to the source and observer cells and the kernel involved.
3. Fine-tuning through splits and merges. the rank-map only predicts the starting tree structure for a MoM matrix, and the rank estimation is often inaccurate and may result in underestimation of rank or missing larger low-rank blocks. These problems are addressed by splits and merges, respectively [3].

The setup cost of the algorithm is largely controlled by the accuracy of the rank-map predictions. An accurate and exhaustive rank map would preclude the necessity for merges and unnecessary splits, and the optimum tree structure would be achieved without any backtracking or fine-tuning. However, a foolproof rank-map cannot be unfeasibly constructed, due to the fact that the algorithm can lead to cells of any shape and size. This leads to a high constant being associated with the setup-time cost of the algorithm.

4. NEW MULTILEVEL QR ALGORITHM

The proposed PILOT-QR algorithm develops a predetermined multilevel matrix structure for the geometry under consideration, which guarantees maximum compression. The algorithm has three main steps as follows.

1. Oct-tree spatial decomposition in 3D. each cube is recursively decomposed by loosely bounded, spatially balanced spits along orthants [9], which leads to a maximum of eight child cubes in 3D. The cell data structure is in the form of an oct-tree, identical to that in multilevel FMMs [6].
2. Basic multilevel interaction list. every cube c_i has a nearest neighbor list [Fig. 1(a)] and an interaction list [Fig. 1(b)]. The nearest neighbor list is defined as

$$K_{c_i} = \{c_j | c_j \text{ is in the same level as } c_i \text{ and has at least one common vertex with } c_i\} \tag{3}$$

and the interaction list is denoted by

$$I_{c_i} = \{c_j | P_{c_j} \in K_{P_{c_i}};\ c_j \notin K_{c_i}\}, \tag{4}$$

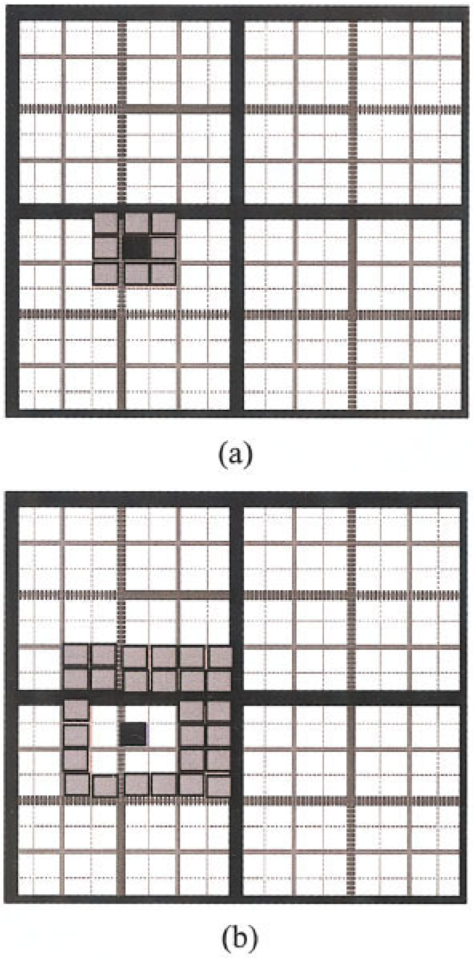

Figure 1 (a) Neighbor list and (b) interaction list for the given cube in FMM at level 4. [Color figure can be viewed in the online issue, which is available at www.interscience.wiley.com]

where P_{c_i} denotes parent of c_i. In FMM, multipole expansions are used to construct $T(c_j, c_i)\ \forall j | c_j \in I_{c_i}$, where $T(c_j, c_i)$ denotes the interaction between testing functions of c_j and basis functions of c_i. Since PILOT does not explicitly require cubical regions, but simply deals with interaction matrices, there is scope for further compression by combining cubes in I_{c_i} in an a priori manner into a new interaction list called the merged interaction list (MIL).

3. Merged interaction list. it is observed that the interaction lists of siblings share many cubes in common, as illustrated in Figure 2 (a 2D version is shown here for ease of illustration). It is possible to group source and observer cubes of different interaction lists in order to compress larger low-rank matrices, and thereby gain, in terms of overall compressibility. The common interaction list is carefully decomposed into disjointed parts such that the overall compression is optimized. Each such disjointed part is an interaction between grouped source cubes and observer cubes and forms an entry of the MIL denoted by μ, which can be expressed as a combination of cube-to-cube interactions as follows:

$$\mu_k = \{T_p(c_j, c_i)\}\ \ \forall\, p | 1 \le p \le n_g, \tag{5}$$

where n_g is the number of regular interactions grouped.

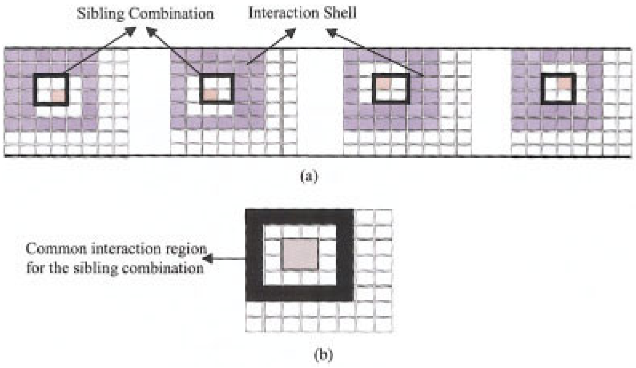

Figure 2 (a) Individual interaction shells of each cube belonging to the sibling combination; (b) common interaction shell for the sibling combination formed by the intersection of individual interaction regions of cubes belonging to the sibling combination (for visualization purposes, 2D shells are illustrated). Similar common interaction regions exist for 3D geometries. [Color figure can be viewed in the online issue, which is available at www.interscience.wiley.com.]

Higher compression is achieved, since a larger matrix is compressed to low rank, given by

$$(m_{\mu_k} + n_{\mu_k}) r_{\mu_k} < \sum_{i=1}^{n_g} (m_i + n_i) r_i, \tag{6}$$

where m, n, and r denote the number of rows, number of columns, and the rank of a submatrix, respectively. The subscript i denotes a regular multilevel interaction list entry that is now a constituent of the MIL. Figure 3 demonstrates the decomposition of the common interaction list of Figure 2 into merged interactions.

In PILOT there are a total of 16 MIL entries in 2D and 40 in 3D. The same MIL pattern is valid for all sibling pairs across the levels. The MIL thus leads to a predetermined tree structure. MoM submatrices pertaining to interactions of the MIL are compressed by forming QRs from samples. At the finest level, dense blocks are retained for interactions of the smallest cube with its neighbors.

5. SIMULATION RESULTS

In this section, simulation results are presented to demonstrate the accuracy and time and memory efficiency of PILOT. For a comparative analysis, results obtained from RMBT-QR and FastCap [5] are presented side-by-side. A QR decomposition tolerance of 1e-3 is used for both PILOT and RMBT-QR, whereas for FastCap the adaptive algorithm with a multipole order of 2 is employed. An

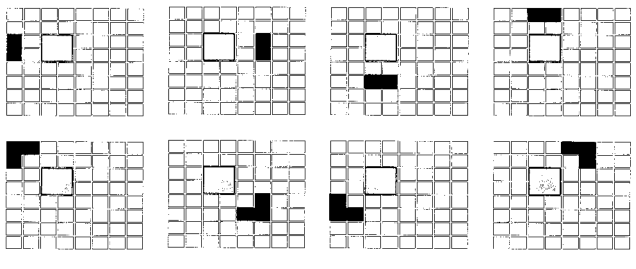

Figure 3 Merged interaction list entries corresponding to the common interaction region of Fig. 2(b). Each entry gives rise to a low-rank matrix block

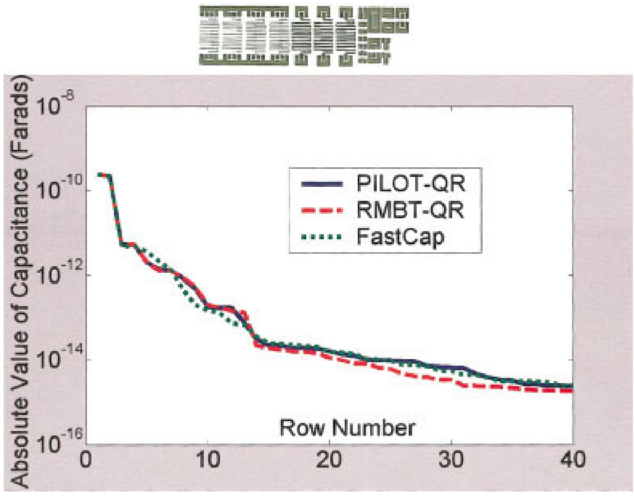

Figure 4 Absolute values of the first column of the capacitance matrix for the structure shown are plotted for all three algorithms (relative error in the capacitance matrix for all algorithms is on the order of 1e-3). [Color figure can be viewed in the online issue, which is available at www.interscience.wiley.com.]

absolute residual of 1e-3 is used for the Krylov subspace iterative solution. All tests were run on a processor with 4-GB RAM and 1.6-GHz CPU speed. The tolerances are chosen such that the results are of comparable accuracies for all the algorithms.

In the first example, the capacitance matrix of the multinet structure [Fig. 2(a)] is simulated for validation. The surface of the structure is meshed with 0.113 million patches. The absolute values of the first column of the matrix are plotted in Figure 4.

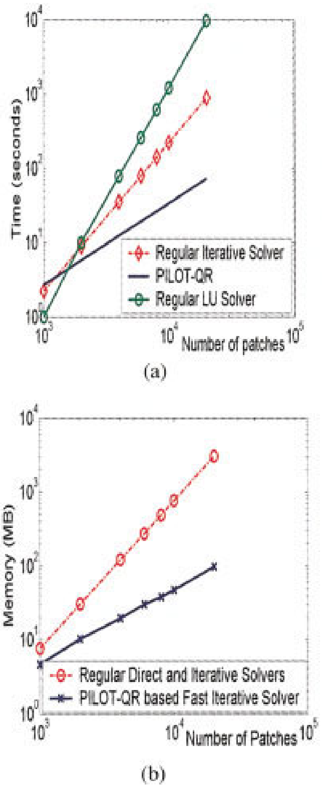

(a)

(b)

Figure 5 (a) Time and (b) memory of PILOT compared to those of the regular iterative and direct solvers. It can be observed from these logarithmic plots that PILOT requires linear time and memory, unlike the regular methods. [Color figure can be viewed in the online issue, which is available at www.interscience.wiley.com.]

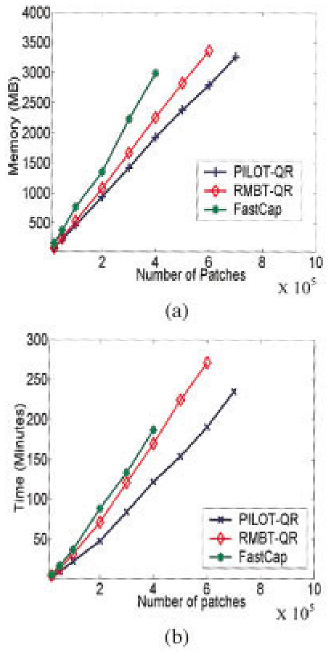

(a)

(b)

Figure 6 (a) Time and (b) memory of PILOT compared to those of the other fast solvers. It can be observed from these linear plots that PILOT has lower constants associated with its linear time and memory growths. [Color figure can be viewed in the online issue, which is available at www.interscience.wiley.com.]

In the next example, a 5 × 5 bus structure is considered. The number of triangular patches is varied from 1000 to 0.7 million. The memory efficiency of PILOT is demonstrated first by a comparison with regular direct and iterative solvers, as shown in Figure 5, and then to RMBT-QR and FastCap, as shown in Figure 6. The relative errors (Euclidean norms) in the capacitance matrices obtained by all the algorithms are on the order of 1e-3.

The next example demonstrates the relative advantage of QR methods for a higher number of nets. A package structure with 14 leads is considered. The surface is meshed with 0.101-million patches and then solved for an increasing number of right-hand sides (1 to 14). The time requirements are plotted in Figure .7 The constant offset between the plots of PILOT and RMBT-QR is due to the superior one-time setup cost. The memory required for the process by PILOT is 441 MB, by RMBT-QR is 445 MB, and by FastCap is 700 MB.

The largest problem solved by using our method thus far is a 10 × 3 array of the structure in example 1. The entire geometry is discretized with 0.913-million patches. The problem took 3.3 Gb and 48 min to set up and 90 min to solve for three specific excited nets. Both the other methods could not fit the problem in the 4-Gb available.

6. CONCLUSIONS

A new oct-tree-based QR technique for fast-parasitic extraction, PILOT, has been presented. The best features of FMM and IES^3 are exploited; along with the generation of new merged-interaction lists in order to yield superior run times and reduced memory consumption. In the battle of reducing constants in the era of mature linear-complexity algorithms, PILOT can potentially emerge as an optimal paradigm for parasitic extraction. While this paper is related to parasitic extraction, the PILOT paradigm can

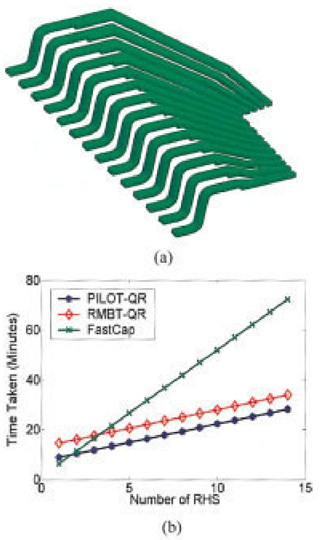

Figure 7 Performance comparison showing the efficiency of QR-based algorithms for increasing number of RHS: (a) multipin structure considered for simulation consisting of 14 pins; (b) setup and solve times for an increasing number of RHS. [Color figure can be viewed in the online issue, which is available at www.interscience.wiley.com.]

also be applied to full-save applications for small electrical structures in multilayered micro-electronic environments.

REFERENCES

1. R.F. Harrington, Field computation by moment methods, IEEE Press, New York, 1991.
2. T.-Y. Chou and Z.J. Cendes, Capacitance calculation of IC packages using the finite element method and planes of symmetry, IEEE Trans CAD Integrated Circ Syst 13 (1994), 1159–1166.
3. S. Kapur and D.E. Long, IES^3: Efficient electrostatic and electromagnetic solution, IEEE Computer Sci Engg 5 (1998), 60–67.
4. S. Kapur and D. Long, IES^3: A fast integral equation solver for efficient 3-dimensional extraction, IEEE/ACM Int Conf CAD, 1997, pp 448–455.
5. K. Nabors and J. White, FastCap: A multipole accelerated 3-D capacitance extraction program, IEEE Trans CAD Integrated Circ Syst 10 (1901), 1447–1459.
6. J.R. Phillips and J. White, A precorrected-FFT method for electrostatic analysis of complicated 3-D structures, IEEE Trans CAD Integrated Circ Syst 16 (1997), 1059–1072.
7. H.A. van der Vorst, Krylov subspace iteration, Computing Sci & Engg 2 (2000), 32–37.
8. G.H. Golub and C.F. Van Loan, Matrix computations, 2nd ed., Johns Hopkins University Press, Baltimore, MD, 1989.
9. R.J. Anderson, Tree data-structures for N-body simulation, SIAM J Computing 28 (1998), 1923–1940.

ANALYSIS OF PHOTONIC BAND-GAP (PBG) STRUCTURES USING THE FDTD METHOD

Ming-Sze Tong,[1] Min Cheng,[1] Yilong Lu,[1] Yinchao Chen,[2] Viktor Krozer,[3] and Rüdiger Vahldieck[4]
[1] School of Electrical and Electronic Engineering
Nanyang Technological University
Nanyang Avenue
Singapore 639798
[2] Department of Electrical Engineering
University of South Carolina
Swearingen Engineering Center
Columbia, SC 29208
[3] EMI/Ørsted
Technical University Denmark
Ørstedplads, Build, 328
DK-2800 Kgs. Lyngby, Denmark
[4] Institute of Field Theory and High Frequency Engineering
Swiss Federal Institute of Technology
CH-8092 Zurich, Switzerland

Received 6 October 2003

ABSTRACT: *In this paper, a number of photonic band-gap (PBG) structures, which are formed by periodic circuit elements printed on transmission-line circuits, are studied by using a well-known numerical method, the finite-difference time-domain (FDTD) method. The results validate the band-stop filter behavior of these structures, and the computed results generally match well with ones published in the literature. It is also found that the FDTD method is a robust, versatile, and powerful numerical technique to perform such numerical studies. The proposed PBG filter structures may be applied in microwave and communication systems.* © 2004 Wiley Periodicals, Inc. Microwave Opt Technol Lett 41: 173–177, 2004; Published online in Wiley InterScience (www.interscience.wiley.com). DOI 10.1002/mop.20084

Key words: *PBG; FDTD; microstrip*

1. INTRODUCTION

Recently, there have been a number of studies on photonic band-gap (PBG) structures in the area of electromagnetism and communications systems. PBGs are structures typically formed by periodic circuit elements, in which a band-gap filter behavior is exhibited in a certain frequency range. They were first proposed in the area of optics, as given in [1], but were then applied in the microwave area [2, 3] by downscaling the operating frequencies.

In this paper, a number of PBG planar structures printed on transmission-line circuits, such as microstrip lines, coplanar waveguides, and striplines, are studied using a well-known numerical method called the finite-difference time-domain (FDTD) method [4]. These PBG circuits can be diversely applied into microwave and communications systems, such as the printed circuit boards (PCB) in computer motherboards or mobile antennas. The circuit characteristics, particularly their band-gap filtering nature, are validated through the analysis of the S parameters. Results also show that the FDTD method is robust, versatile, and reliable for such numerical calculations.

2. FDTD METHOD AND COMPUTATIONAL SETUP

The main idea of the FDTD lies on solving the Maxwell's curl equation pair:

$$\nabla \times \vec{H} = \frac{\partial \vec{D}}{\partial t} + \vec{J} \quad \text{and} \quad \nabla \times \vec{E} = -\frac{\partial \vec{B}}{\partial t} - \vec{M}. \tag{1}$$

Integral Equation Based Time Domain Coupled EM-Circuit Simulation For Packaged Conductors and Dielectrics

Chuanyi Yang, **Gong Ouyang** and **Vikram Jandhyala**
Department of Electrical Engineering, Box-352500, University of Washington, Seattle, WA-98195, Telephone: 206-543-2186 Fax: 206-543-3842, jandhyala@ee.washington.edu

ABSTRACT

A full-wave time domain integral equation formulation for the simulation of finite conductors and dielectrics, linked to linear and non-linear lumped elements, is presented. The method permits coupled rigorous simulation including accounting for EMI and non-linearities in the presence of material effects. In addition, a new quadrature scheme is incorporated for exactly computing temporal delays between every section of finite basis functions defined over triangular patches. This enables finer time step resolution for non-uniform meshes than is permissible with standard Gaussian quadrature and singularity extraction.

I. Introduction

Time domain electromagnetic solvers are useful for simulating coupled circuit-electromagnetic problems involving IC packages and systems-on-chip, wherein effects of nonlinearities[1] of circuit elements can be modeled accurately. Furthermore, broadband simulation for digital and multi-frequency systems can be rendered efficient by time domain simulation. The surface-based time domain integral equation (TDIE) approach has been gaining in popularity due to its flexibility in modeling arbitrary-shaped structures and recent advance in associated fast algorithms [2].

Existing methods to couple TDIE to circuits have been based on port models, convolution methods, and the partial element equivalent circuit approach [3,4]. In this work, a generalized rigorous coupling scheme, to simultaneously simulate circuits with SPICE-like time domain simulation, and EM interactions with a TDIE method, is presented, for both conductors and dielectric materials.

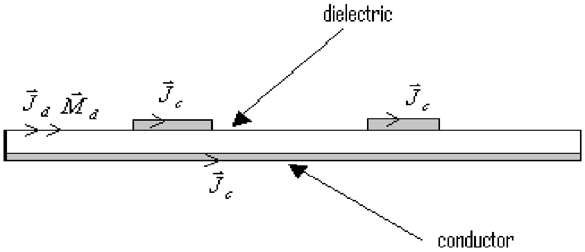

Fig. 1 Dielectric and Conductor Composite Structure

II. Formulation

The modeling of dielectrics in the circuit is facilitated by utilizing the equivalence principle [5,6]. The dielectric body is replaced by a equivalent surface S_d on which there are electric current $\mathbf{J}_d$ and magnetic current $\mathbf{M}_d$ flowing. The scattering field outside and inside of the dielectric body can be written in terms of the equivalent current $\mathbf{J}_d$ and $\mathbf{M}_d$. On the conductor surface S_c there is only electric current $\mathbf{J}_c$ flowing. Here S_d^- (S_d^+) indicates approaching S_d from outside (inside), respectively.

$$\begin{aligned}
&\mathbf{E}_e^s(\mathbf{J}_c, \mathbf{J}_d, \mathbf{M}_d) + \mathbf{E}^{inc} = 0 \quad \mathbf{r} \in S_d^- \\
&\mathbf{E}_e^s(\mathbf{J}_c, \mathbf{J}_d, \mathbf{M}_d) = 0 \quad \mathbf{r} \in S_d^+ \\
&\mathbf{E}_e^s(\mathbf{J}_c, \mathbf{J}_d, \mathbf{M}_d) + \mathbf{E}^{inc} = 0 \quad \mathbf{r} \in S_c
\end{aligned} \tag{1}$$

The conductor surface S_c comprises of two disjoint surfaces S_{EM} and S_{CK}, and such that on S_{EM} the standard continuity equation relating the surface current and charge holds, which is also the case on the dielectric surface S_d .

$$\nabla_s \cdot \mathbf{J}(\mathbf{r},t) + \frac{\partial \rho(\mathbf{r},t)}{\partial t} = 0 \quad \forall \mathbf{r} \in (S_{EM} \ \& \ S_d) \tag{2}$$

where ∇_s denotes the surface divergence. However, on S_{CK}, which we call *terminal* surfaces or *connecting* surfaces, the circuit current flowing onto S_{CK} from a corresponding circuit node introduces an additional source term that alters the surface current and charge on S_c. This permits connection of two disparate domains, the topology-based circuit domain, and the geometry-based EM domain.

Let S_{CK} itself be comprised of disjoint surfaces $S_{CK}^m \quad m=1,.....,M$. Each such unique sub-surface S_{CK}^m is termed one of *M terminals*. On S_{CK}^m the modified continuity equation has the following form

$$\nabla_s \cdot \mathbf{J}(\mathbf{r},t) + \frac{\partial \rho(\mathbf{r},t)}{\partial t} = I_c^m(\mathbf{r},t) \quad \forall \mathbf{r} \in S_{CK}^m \quad m=1,.....,M \tag{3}$$

where $I_c^m(\mathbf{r},t)$ denotes the scalar volumetric current density produced on S_{CK}^m via a circuit interconnect.

The current density introduced by the circuit interconnection produces an additional source or sink of charge that alters the time dependent scalar potential and the resulting the scattering electric field from S_c and S_d^-.

$$\mathbf{E}^s(\mathbf{r},t) = -\frac{\partial \mathbf{A}(\mathbf{J}_c,\mathbf{J}_d,\mathbf{r},t)}{\partial t} - \nabla\Phi_{EM}(\mathbf{J}_c,\mathbf{J}_d,\mathbf{r},t) - \nabla\Phi_{CK}(I_c,\mathbf{r},t) - \frac{1}{\varepsilon_e}\nabla\times\mathbf{F}(\mathbf{M}_d,\mathbf{r},t) \;\; \forall \mathbf{r} \in (S_{EM} \,\&\, S_d^-) \tag{4}$$

The scattering field from S_c and S_d^- can be written in term of magnetic vector potential, **A,** electric scalar potential, Φ, and electric vector potential **F** **w**here $\nabla\Phi_{EM}(\mathbf{J}_c,\mathbf{J}_d,\mathbf{r},t)$ is the contribution from the EM current, $\nabla\Phi_{CK}(I_c,\mathbf{r},t)$ is the contribution from the circuit current, and ε_e is the permitivity of the medium exterior to the dielectric body.

The scattering field from $S_d{}^+$ can be written as following

$$\mathbf{E}^s(\mathbf{r},t) = -\frac{\partial \mathbf{A}(\mathbf{J}_d,\mathbf{r},t)}{\partial t} - \nabla\Phi(\mathbf{J}_d,\mathbf{r},t) - \frac{1}{\varepsilon_d}\nabla\times\mathbf{F}(\mathbf{M}_d,\mathbf{r},t) \;\; \forall \mathbf{r} \in S_d^+ \tag{5}$$

where ε_d is the permitivity of the medium interior to the dielectric body. In addition to the scattering field, two more conditions are required for the circuit interconnection: electrically small terminals are assumed to be equipotential, leading to

$$\Phi_{EM}(\mathbf{J}_c,\mathbf{J}_d,\mathbf{r},t) + \Phi_{CK}(I_c,\mathbf{r},t) = V_m(t) \tag{6}$$

for $m = 1,.....,M$ where $V_m(t)$ is the circuit potential at the circuit node connected to the terminal *m*, and the final set of self-consistency equations relates to the application of Kirchoff's Current Law at the *M* nodes connected to the terminals.

$$\sum_{j=1}^{adj(m)} i_j^m(t) = \int_{S_{CK}^m} I_c^m(t)\,ds \tag{7}$$

The system of equations can be combined to yield the time-domain circuit-EM coupled system. The linear and non-linear circuits connected to the terminals are modeled by Modified Nodal Analysis (MNA). The coupled system has the form, (8)

$$\begin{bmatrix} \overline{\mathbf{Z}_{JJ0}^{cc}} & \overline{\mathbf{Z}_{JJ0}^{cd}} & \overline{\mathbf{Z}_{JM0}^{cd}} & \overline{\mathbf{Q}_{JI0}^{cc}} & \bar{\mathbf{0}} \\ \overline{\mathbf{Z}_{JJ0}^{dc}} & \overline{\mathbf{Z}_{JJ0}^{dd}} & \overline{\mathbf{Z}_{JM0}^{dd}} & \overline{\mathbf{Q}_{JI0}^{dc}} & \bar{\mathbf{0}} \\ \bar{\mathbf{0}} & \overline{\mathbf{Z}_{MJ0}^{dd}} & \overline{\mathbf{Z}_{MM0}^{dd}} & \bar{\mathbf{0}} & \bar{\mathbf{0}} \\ \overline{\mathbf{Z}_{IJ0}^{cc}} & \overline{\mathbf{Z}_{IJ0}^{dd}} & \bar{\mathbf{0}} & \overline{\mathbf{Q}_{II0}^{cc}} & \overline{\mathbf{C}} \\ \bar{\mathbf{0}} & \bar{\mathbf{0}} & \bar{\mathbf{0}} & \overline{\mathbf{C}^{\mathbf{T}}} & \overline{\mathbf{MNA}_0} \end{bmatrix} \begin{bmatrix} \mathbf{J_c}(t_j) \\ \mathbf{J_d}(t_j) \\ \mathbf{M_d}(t_j) \\ \mathbf{I_c}(t_j) \\ \mathbf{CKT}(t_j) \end{bmatrix} = \sum_{i=1}^{j} \begin{bmatrix} \overline{\mathbf{Z}_{JJi}^{cc}} & \overline{\mathbf{Z}_{JJi}^{cd}} & \overline{\mathbf{Z}_{JMi}^{cd}} & \overline{\mathbf{Q}_{JIi}^{cc}} & \bar{\mathbf{0}} \\ \overline{\mathbf{Z}_{JJi}^{dc}} & \overline{\mathbf{Z}_{JJi}^{dd}} & \overline{\mathbf{Z}_{JMi}^{dd}} & \overline{\mathbf{Q}_{JIi}^{dc}} & \bar{\mathbf{0}} \\ \bar{\mathbf{0}} & \overline{\mathbf{Z}_{MJi}^{dd}} & \overline{\mathbf{Z}_{MMi}^{dd}} & \bar{\mathbf{0}} & \bar{\mathbf{0}} \\ \overline{\mathbf{Z}_{IJi}^{cc}} & \overline{\mathbf{Z}_{IJi}^{dd}} & \bar{\mathbf{0}} & \overline{\mathbf{Q}_{IIi}^{cc}} & \bar{\mathbf{0}} \\ \bar{\mathbf{0}} & \bar{\mathbf{0}} & \bar{\mathbf{0}} & \bar{\mathbf{0}} & \overline{\mathbf{MNA}_i} \end{bmatrix} \begin{bmatrix} \mathbf{J_c}(t_{j-i}) \\ \mathbf{J_d}(t_{j-i}) \\ \mathbf{M_d}(t_{j-i}) \\ \mathbf{I_c}(t_{j-i}) \\ \mathbf{CKT}(t_{j-i}) \end{bmatrix} + \begin{bmatrix} \mathbf{SRC_{EM}^c}(t_j) \\ \mathbf{SRC_{EM}^d}(t_j) \\ \bar{\mathbf{0}} \\ \bar{\mathbf{0}} \\ \mathbf{SRC_{CK}}(t_j) \end{bmatrix} \tag{8}$$

The vector $\mathbf{SRC_{EM}^c}(t_j)$ represents the tested incident field, and the $\mathbf{SRC_{CK}}(t_j)$ denotes the values of circuit sources. The matrix $\overline{\mathbf{C}}$ is a sparse bipolar adjacency matrix that is used for enforcing Kirchoff's Voltage and Current Laws at the circuit nodes connected to the terminals. This approach enables both linear and non-linear (through local Newton-Raphson on the MNA sub-matrix) circuit simulation in conjunction with EM simulation.

III. Stability and Accuracy Enhancement

A new integration scheme in polar coordinates which significantly improves the late time stability associated with TDIE and accuracy as well is implemented, for realistic non-uniform meshes. The new formulation takes the exact delay difference into account between every section of two interacting basis functions and uses the polar coordinate integration scheme for each patch-patch interaction calculation. And this method is exact in the sense that all source points are modeld with exact retarded time. The advantage of this technique is the ability to reduce the smallest time step in an implicit scheme beyond what is possible by standard Gaussian quadrature and singularity extraction methods. Figure 2 demonstrates the smallest time step possible with the standard method (old) and the proposed polar coordinate quadrature (new). The proposed approach has been incorporated into a TDIE scheme and is particularly useful for non-uniform mesh examples.

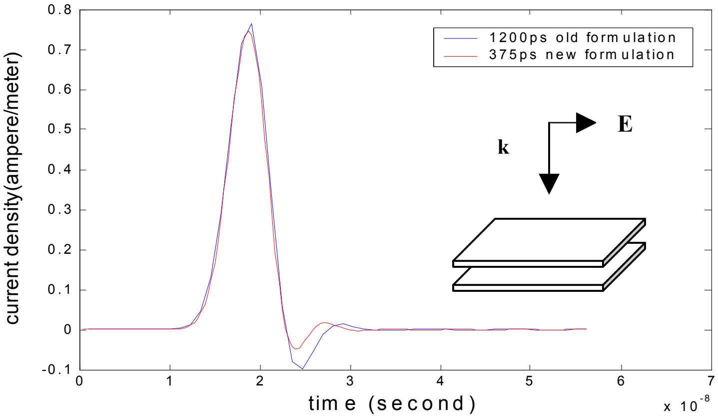

Fig.2 Stability Comparison Between New and Old Formulation

IV. Simulation Result

The ACES IEEE/EMC Society TC9 Challenging Problems have been designed to challenge various modeling techniques. One of the 2001 Challenging Problems "Differential Pair Over Split Ground"(Fig. 3) is used to test the coupled solver. In this example, a ground plane with or without split is located on the left hand side. A driver consisting of two trapezoidal voltage sources with rising and falling time of 200ps, roof time of 1000ps and zero internal impedance, delivers a differential mode signal to two symmetric lines. For the split ground plane case, a decoupling capacitor may be placed across the split. The decoupling capacitor is equivalent to a series connection of a 10nf capacitor, 10nh inductor and 0.03ohm resistor. The pair of wires extends for 1 meter and the ends of the differential lines are terminated by a 100ohm resistor. The task is the find the voltage between Line+ and CM ground point in three case, (1) no split in plane, (2) split in plane and no decoupling capacitor, (3) split in plane with decoupling capacitor. Fig. 4 and Fig. 5 are the simulation result with or without the dielectric substrate that match well with results in the available literature.

References

[1] L.Erdin, M. S. Nakhla, F. Achar, "Circuit Analysisi of electromagnetic radiation and field coupling effects for networks with embedded full-wave modules," *IEEE TRANS. Electromagnetic Compatibility*, vol 42,pp. 449-460, Nov. 2000.

[2] A. E. Yilmaz, D. S. Weile, H.M. Jin, E. Michielssen, "A hierarchical FFT algorithm (HIL-FFT) for the fast analysis of transient electromagnetic scattering phenomena," *IEEE Trans. Antennas Propagat,*vol 50, pp. 971-982, July. 2002.

[3] A. E. Ruehli, "Equivalent circuit models for three dimensional multiconductor systems," *IEEE Trans. Microwave Theory Tech.*, vol. 22, pp. 216–221, Mar. 1974.

[4] W. Pinello, A. C. Cangellaris, A. Ruehli, "Hybrid electromagtic modeling of noise interactions in packaged electronics based on the partial-element equivalent-circuit formulation," *IEEE Trans. Microwave Theory and Techniques*, vol. 45, pp. 1889-1896, Oct. 1997.

[5] S. M. Rao, T, K, Sarkar, "Numerical Solution of Time Domain Integral Equations for Arbitrarily Shaped Conductor/Dielectric Composit Bodies," *IEEE Trans. Antennas Propagat,* vol. 50, pp,1831-1837, Dec. 2002.

[6] R. F. Harrington, "Time-Harmonic Electromagnetic Fields," New York: McGraw-Hill, 1961.

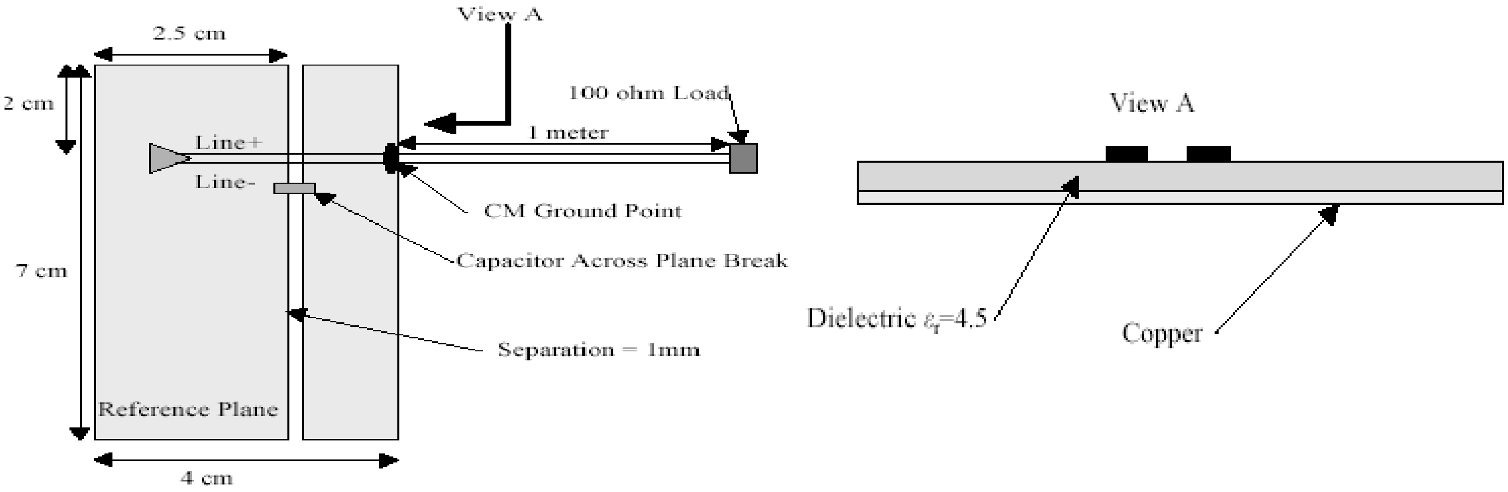

Fig. 3 Differential Pair Over Split ground plane

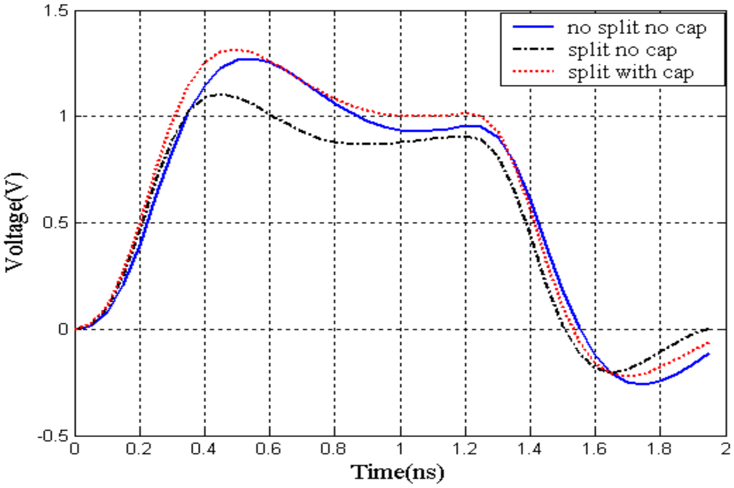

Fig. 4 Line+ to CM voltage(with dielectric)

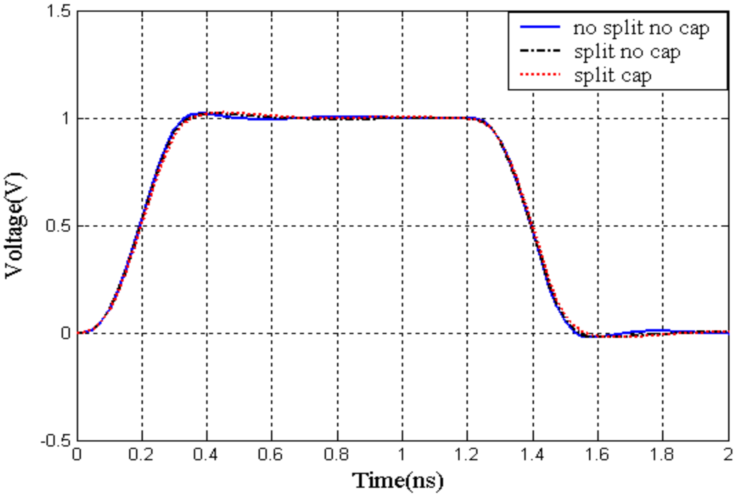

Fig. 5 Line+ to CM voltage(without dielectric)

Modeling and simulation of circuit-electromagnetic effects in electronic design flow

Pavel V. Nikitin[1], Vikram Jandhyala[1], Daniel White[2], Nathan Champagne[2], John D. Rockway[2],
C.-J. Richard Shi[1], Chuanyi Yang[1], Yong Wang[1], Gong Ouyang[1],
Rob Sharpe[2], and John W. Rockway[3]

[1]University of Washington, Department of Electrical Engineering, Seattle, WA 98195
Email: {nikitin, jandhyala, cjshi, cyang1, oyg, yongw}@ee.washington.edu

[2]Lawrence Livermore National Laboratory, 7000 East Ave, Livermore, CA 94550
Email: {dwhite, champagne, rockway2, rsharpe} @llnl.gov

[3]Space and Naval Warfare Systems Command, 4301 Pacific Highway San Diego, CA 92110
Email: rockway@spawar.navy.mil

Abstract

The goal of this paper is to describe a methodology for modeling and simulation of circuit-electromagnetic (EM) effects that fits into a current electronic design flow. Our methodology is based on using time-domain macromodels implemented in a hardware description language (HDL). Simulation of the entire coupled circuit-EM system can be carried out either entirely in HDL simulator or in SPICE-type circuit simulator (using model compiler for macromodel import). We also describe in detail a circuit-EM contact interface and a neutral mesh format necessary to allow for flexibility in choice of EM simulators. At each step of our methodology, we provide an overview of current problems and solutions with reference to existing publications.

As a demonstration example, we consider a simple coupled system (MEMS resonator connected to a lumped circuit) and show that simulations using VHDL-AMS macromodel match full-wave EM results but easily fit in the design flow and take significantly less time. Our methodology is straightforward and permits the use of various EM simulators and macromodel identification algorithms[1].

1. Introduction

Electromagnetic effects have always been important in microwave circuits but now they have become an increasingly significant factor that affects the performance of modern integrated circuit (IC) systems, especially at multi-gigahertz frequencies [18]. Such systems include very large scale integrated (VLSI) chips as well systems-on-chips (SoC), and the examples of objects exhibiting EM behavior are interconnects, spiral inductors, traces, etc. This leads to a necessity of using accurate computer-automated design (CAD) tools for EM modeling and efficient use of those models in circuit simulation [6].

A variety of numerical electromagnetic field solving tools have been developed in the past, all of which have different limitations, capabilities, input and output formats, and computational costs. Choosing the best tool for a particular task and successfully employing and integrating it into an IC CAD design flow are challenging tasks.

Both circuit and EM simulations can be carried out either in time domain or frequency domain but mixed-signal circuit simulations are mostly performed in time domain (due to nonlinearity of analog circuits and sharp rise and fall times of digital signals) whereas EM simulations are mostly performed in frequency domain (due to well developed frequency domain EM methods).

There are three main approaches to incorporate EM simulation results in SPICE-type time-domain circuit simulators. First approach is to extract an equivalent RLC cir-

---

[1] This research was supported by DARPA NeoCAD Program

cuit [1], which can be very large (i.e. for substrate coupling) and cumbersome to deal with (model order reduction is often needed). Second approach is to concurrently couple a circuit and EM simulator. While adding lumped passives to a full-wave EM simulation is straightforward, coupling a full-wave EM solver with a non-linear circuit solver is not a routine procedure (e.g. FDTD-SPICE coupling has been done but on case-by-case basis [15]). Third approach, which we describe in this paper, is to develop compact linear EM macromodels [10].

The last approach is very convenient because macromodels can be implemented in high-level hardware description languages used for design (such as VHDL-AMS [3] or Verilog-A [12]), easily interfaced to non-linear circuits, and re-used. Macromodeling permits significant speed-up of simulations and thus gains more and more attention in CAD community (e.g., for MEMS [17]). We should note that propositions to extend HDL's to directly support PDE's and hence EM modeling have also appeared in the literature [13] but this work is still in the research stage.

In this paper, we describe a methodology for modeling and simulation of circuit-EM effects on system performance by using compact linear EM macromodels implemented in a hardware description language. We provide an example – a simple circuit-driven MEMS system analyzed using VHDL-AMS macromodel extracted from time-domain EM simulation. We also describe specifics of circuit-EM contact interface and EM mesh format in a way that can be used by different circuit and EM simulators.

2. Methodology

Modern electronic design flow includes such steps as schematic capture and simulation, system layout, parasitic extraction, post-layout simulation, etc. At each stage, different tools and file formats, standard and proprietary, are used [9].

Analog and digital circuitry is typically described using SPICE- or VHDL-type netlists, which specify how lumped components or digital logic blocks are connected together. Layout is typically described using CIF or GDS II format files. These files contain 2D data about structures located at different chip layers and together with technology files (which contain information about thickness, material properties, and stacking of different layers) give a complete 3D description of a chip.

Having an ability to do an accurate post-layout simulation is critical for verification of functionality and performance of the complete system. Fully coupled circuit-electromagnetic simulations are very computationally intensive and are not commonly used. A typical approach used in the design process today is to perform parasitic extraction and include equivalent RLC circuits into a circuit simulator.

The process of RLC extraction from EM simulations is difficult, but works well in many cases, especially for capacitances of interconnects. Complex coupled problems result in large RLC networks and require a subsequent application of model order reduction methods, which are not well integrated into design flow. Thus there is a clear need for new approaches in coupled circuit-EM simulation.

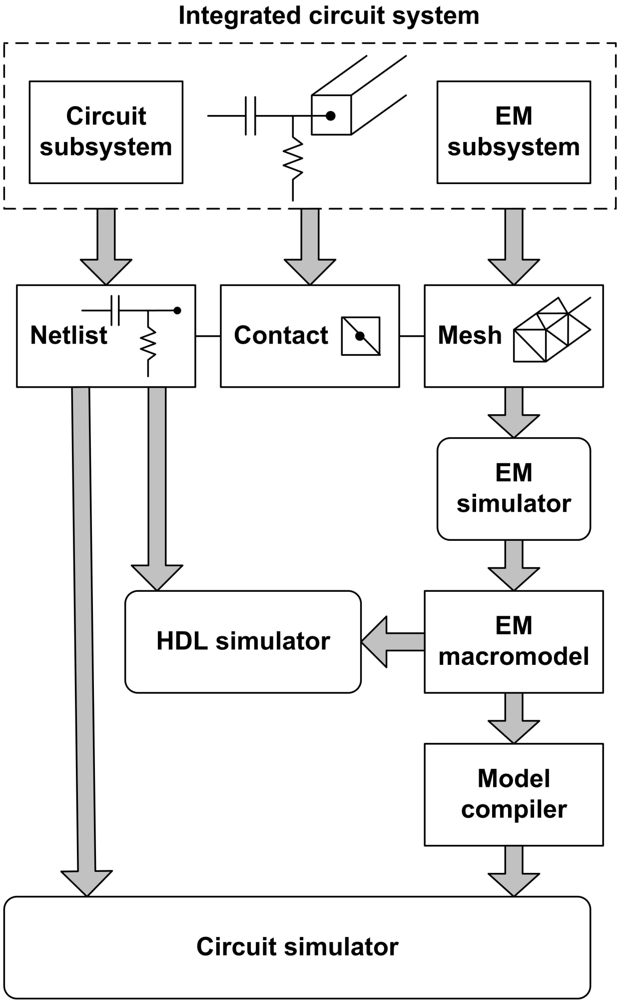

Figure 1. Methodology.

The methodology that we propose is illustrated in Figure 1. An IC system of interest contains lumped circuits connected at certain contact points to geometrical structures that exhibit EM behavior and need to be meshed and accurately modeled. Volumetric or surface mesh is stored in neutral mesh format reusable by various electromagnetic simulators. From frequency- or time-domain simulation data (depending on application and frequency range of interest), time-domain macromodel can be identified and extracted [20]. Such model can easily be implemented in a hardware description language (such as VHDL-AMS) and used either in HDL simulation of the whole system (circuit netlist needs to be converted from SPICE to HDL format) or, with recent advances in model compilers [7, 23], compiled for direct use in a SPICE-type circuit simulator.

2.1. EM simulation, contact interface, mesh format

In circuit simulation, the most popular method is node-based modified nodal analysis (MNA) [16]. In electromagnetic simulation, the variety of methods is richer and includes differential methods (FDTD – finite difference time domain, FEM – finite element method, etc.), integral equation methods (MoM – method of moments, BEM – boundary element method, etc.), hybrid methods [21], etc. Many of these methods can be utilized both in frequency or time domain but traditionally only FDTD has been used for time-domain modeling, and FEM and MoM have been used in frequency domain. Recently, new time-domain methods (TD-FEM [24], TD-MoM [26]) have been developed and successfully applied to a variety of problems. An excellent survey of existing EM methods can be found in [11].

Each method listed above has many variations and deserves a separate overview but most EM commercial tools are based on three major methods and their flavors – method of moments (e.g., *Sonnet* by Sonnet Technologies), finite element method (e.g., *HFSS* by Ansoft Corporation), and finite-difference time domain method (e.g., *XFDTD* by Remcom, Inc.). All electromagnetic solvers require creation of some sort of grid or mesh: either volumetric one that includes all problem space (FEM and FDTD) or surface mesh that covers only certain surfaces (MoM).

An electromagnetic solver applied to coupled circuit-EM problem must recognize the existence of ports or terminals that connect circuit and EM subsystems and through which the interaction happens [22]. Exact definition is different for different EM solving techniques [2]. Examples of specifying such interaction for FDTD can be found in [15] and for MoM in [26, 5]. Circuit world understands currents and voltages, and thus latter serve as common shared quantities at the points of circuit-EM interaction.

Assume that we have identified EM objects and lumped circuit elements connected to them (identification of IC package parts that must be modeled as EM objects is a separate challenging problems that we do not address here). Then circuit-EM contact interface can be defined as an area of the EM object surface to which a circuit element is attached. This concept is shown in Figure 2 (two contacts may form a microwave port).

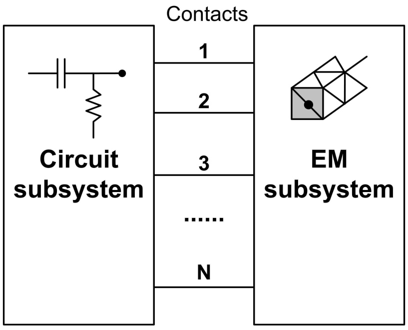

Figure 2. Circuit-EM contact interface.

The contact interface area can be specified in two ways: *mesh-dependent* and *mesh-independent*. *Mesh-dependent* method can be defined as specifying mesh elements that belong to the contact interface. *Mesh-independent* method can be defined as specifying 3D coordinates of contact points (using either x, y, z coordinates in the integrated chip reference frame or text labels in layout/technology files). After the mesh is created, mesh faces in the vicinity of that point (e.g, a spherical region of a certain radius) are recognized as part of contact interface.

Both ways described above have advantages and disadvantages. Mesh-dependent method is less portable as it requires the existence of prior mesh but is better for accurate coupled simulations. Mesh-independent method does not require prior mesh existence and has better portability but may suffer from potential problems related to mesh refinement in the process of EM solution.

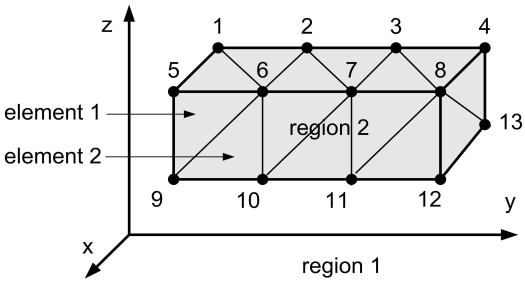

Figure 3. Mesh format.

Mesh itself can also be stored in a variety of ways. Currently, many different mesh formats for EM simulation exist. Unfortunately, there is no standard analogous to netlist standard for circuits. We propose to use the following neutral mesh format, simple and intuitive. To completely define a mesh, three files are needed: *node file*, *element file*, and *material file*. The format of those files can be illustrated with the example shown in Figure 3, where a surface of a perfectly conducting object positioned in free-space is meshed with triangles.

Node file lists coordinates of all nodes (in units selected by user) in the cartesian coordinate system. The node file for the example shown in Figure 3 is:

```
Node x  y  z
1    x1 y1 z1
2    x2 y2 z2
...
```

Element file lists all surface and volume elements (triangles, tetrahedra, etc.) formed by nodes which serve as element vertices. If an element belongs to a surface dividing two regions with different properties, those regions must be specified by their numbers. In the example shown in Figure 3 the elements are triangles on the surface dividing region 1 and region 2, and the node file is:

```
Element n1 n2 n3 region1 region2
1       5  6  9  1       2
2       6  9  10 1       2
...
```

Material file lists all regions (by number), their type (volume, surface, layer), and their properties (permittivity, permeability, and conductivity). Infinite conductivity for perfect electric conductors can be denoted as PEC. The example shown in Figure 3 contains free-space (region 1) and a PEC object (region 2). The material file for this example is:

```
Region eps mu sigma type
1      1   1  0     volume
2      1   1  PEC   volume
...
```

The mesh format, described above, can be used for different EM simulators and translated into mesh formats understood by any of the commercial tools. Once an EM simulation of the multi-port structure is completed, a macromodel needs to be extracted. This process is described in the next subsection.

2.2. Macromodeling

Macromodeling is extremely important for speeding up simulations of complex systems, such as coupled circuit-electromagnetic systems. In order to be easily implementable in a hardware description language, a macromodel must be casted into a time-domain differential equation form. Such model can be obtained from either frequency- or time-domain EM simulation.

A number of different algorithms for extracting macromodels and reduced order models from data are available [14, 8]. An advantage of using time-domain data is that in most cases passivity and stability of obtained macromodel are easier to guarantee than when working with frequency-domain data. Thus, for illustration of our methodology, we choose an approach where a linear compact macromodel is identified from a time-domain electromagnetic response as described in [25].

All possible information about system dynamics is theoretically contained in an impulse response – a system response to a delta-function excitation. System response to any input can be found as a convolution of the impulse response with the input signal. This process is very computationally expensive, especially for highly-resonant devices with long impulse responses. In addition, delta-function causes numerical problems in time-domain EM solvers, and more commonly used excitation is Gaussian pulse:

$$u(t) = u_o \, e^{-\frac{(t-\tau)^2}{2T^2}} \tag{1}$$

with -3dB bandwidth of 0.13/T.

System response to a Gaussian pulse can allow one to identify a continuous time-domain macromodel in its classical state-space form:

$$\begin{aligned} \dot{\vec{x}} &= \hat{A}\,\vec{x} + \hat{B}\,\vec{u} + \hat{K}\,\vec{e}, \\ \vec{y} &= \hat{C}\,\vec{x} + \hat{D}\,\vec{u} + \vec{e}, \end{aligned} \tag{2}$$

where $\vec{x}(t)$ is the vector of state variables, $\vec{u}(t)$ is the excitation, $\vec{y}(t)$ is the output, and $\vec{e}(t)$ is the noise signal. The process of identification can be described as finding $\hat{A}$, $\hat{B}$, $\hat{C}$, $\hat{D}$, and $\hat{K}$ from given $\vec{u}(t)$ and $\vec{y}(t)$.

There exists a large number of different methods and tools for system identification (see, e.g., *MATLAB*[2] system identification toolbox). The order of the model (dimension of the $\hat{A}$ matrix) can be determined from the data. The accuracy and other issues associated with macromodel identification, such as passivity and stability, are not discussed here since they are well covered in the literature (see, e.g., [4, 19]) and lie outside the scope of this paper.

The time-domain state-space model (2) is essentially a set of ordinary differential equations that can easily be implemented in a hardware description language for later use in circuit simulation, as it is shown in the next section.

3. Example

For demonstration of modeling flow methodology described above, consider a simple example: MEMS resonator (micromachined comb structure, approximately 1.5 mm × 0.5 mm in size, and positioned in free-space) driven by an external voltage source as shown in Figure 4. This MEMS structure represents an electromagnetic subsystem and can be thought of as part of a larger integrated package. The voltage source and the resistor represent a lumped circuit subsystem (which can be any transistor circuit).

---

[2] Trademark of *Mathworks, Inc.*

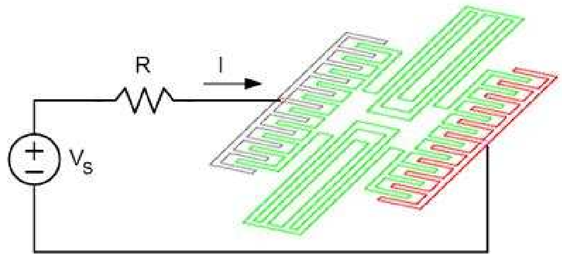

Figure 4. Circuit-driven MEMS resonator.

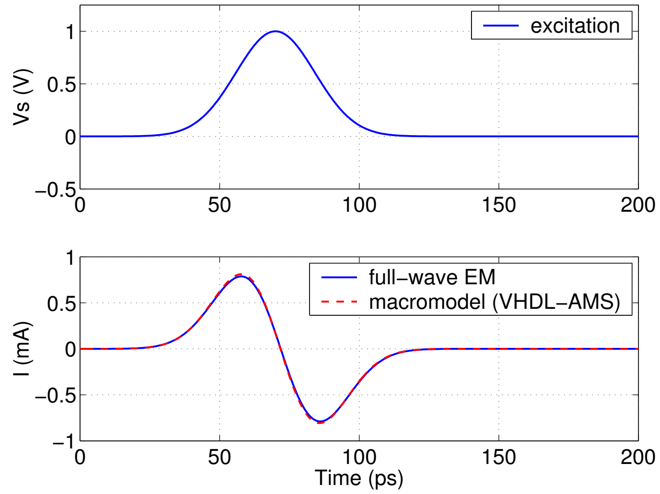

Figure 5. Results of the simulations for the system shown in Figure 4.

The voltage source generates a Gaussian pulse of the form (1) with $u_o = 1$ V, $\tau = 70$ ps, and $T = 14$ ps (bandwidth $\approx$ 10 GHz). The resistor is $R = 100$ Ohm. The mesh for MEMS structure was generated and stored in the neutral format described in the previous section. The problem was solved using a full-wave time-domain integral-equation method [26]. It contained about 1000 triangles (approximately 1500 unknowns) and took approximately 1 minute of runtime on a 1 GHz PC.

Consider a macromodel of the system that includes MEMS resonator in series with 100 Ohm resistor. The input $u(t)$ to this system is the excitation voltage from the source V_s and the output $y(t)$ is the current I through the system. For identifying the continuous state-space system model of the form (2), we used `’pem’` and `’d2c’` functions in *MATLAB* system identification toolbox. The response $y(t)$ was well approximated with the 3rd order model, where noise component was set to zero. The model was implemented in VHDL-AMS as shown below and simulated using VHDL-AMS simulator *Hamster*[3]. The runtime was 0.2 s on 2.5 GHz PC. As one can see from Figure 5, macromodel simulation results match the results of full-wave EM simulation very well.

```
----- Macromodel of MEMS resonator ---
-------- in series with resistor -----
ENTITY macromodel IS
 PORT (TERMINAL a, b : ELECTRICAL);
END;
 ARCHITECTURE behav OF macromodel IS
 QUANTITY u ACROSS i THROUGH a TO b;
 QUANTITY x1,x2,x3: real;
 CONSTANT A11 : real := -4.929E11;
 .....
 CONSTANT C3 : real := -2.04e-8;
 CONSTANT D : real := 0.00518;
BEGIN
x1’dot == A11*x1+A12*x2+A13*x3+B1*u;
x2’dot == A21*x1+A22*x2+A23*x3+B2*u;
x3’dot == A31*x1+A32*x2+A33*x3+B3*u;
-i == C1*x1+C2*x2+C3*x3+D*u;
END ARCHITECTURE;

------ System description ----------
ENTITY system IS END;
ARCHITECTURE behav OF system IS
    TERMINAL n1: ELECTRICAL;
BEGIN
Vs: ENTITY gaussian_source (behav)
    GENERIC MAP (1.0,70.0E-12,14.0E-12)
    PORT MAP (n1,electrical_ground);
Mm: ENTITY macromodel (behav)
    PORT MAP (n1,electrical_ground);
END behav;
```

This example demonstrates that macromodels are an accurate and efficient way of simulating coupled circuit-electromagnetic systems in time-domain. Macromodels in general contain much fewer internal variables than full EM problems (in our example, 3 vs. 1500) and thus provide a significant simulation speedup. They are easy to implement in HDL and can be used in today’s design flow.

4. Conclusions

In this paper, we described in detail the methodology of modeling and simulation of coupled circuit-electromagnetic effects using time-domain EM macromodels implemented in a hardware description language. This methodology fits well into electronic design flow existing today. Simulation of complete integrated circuit system can be carried out either entirely in HDL or in SPICE-type circuit simulator

---

[3] Now part of *Simplorer*, trademark of *Ansoft Corp.*

(using HDL-to-SPICE model compiler). We have also defined a circuit-EM contact interface and a neutral geometry meshing format that can be used by various electromagnetic solvers used in the design process.

For demonstration, we considered a simple coupled system (MEMS resonator connected to a lumped circuit) and showed that VHDL-AMS macromodel simulation results match full-wave EM results but take significantly less time to obtain. This shows that EM macromodeling is a very effective way to include circuit-electromagnetic effects into simulation. Implementing macromodels in a hardware description language allows one to use them in the current IC design flow.

References

[1] R. Achar and M. S. Nakhla. Simulation of high-speed interconnects. *Proceedings of IEEE*, 89(5):693–728, May 2001.

[2] N. J. Champagne. On attaching a wire to a triangulated surface. *IEEE Antennas and Propagation Symposium Digest*, 1:54–57, June 2002.

[3] E. Christen and K. Bakalar. VHDL-AMS – a hardware description language for analog and mixed-signal applications. *IEEE Transactions on Circuits and Systems*, 46(10):1263–1272, October 1999.

[4] S. Grivet-Talocia, I. S. Stievano, I. A. Maio, and F. Canavero. Time-domain and frequency-domain macromodeling: application to package structures. *IEEE International Symposium on Electromagnetic Compatibility*, 2:570–574, August 2003.

[5] V. Jandhyala, Y. Wang, D. Gope, and C.-J. Shi. A surface-based integral-equation formulation for coupled electromagnetic and circuit simulation. *IEEE Microwave and Optical Technology Letters*, 34(2):103–106, July 2002.

[6] K. Kundert, H. Chang, D. Jefferies, G. Lamant, E. Malavasi, and F. Sendig. Design of mixed-signal systems-on-a-chip. *IEEE Transactions on CAD of Integrated Circuits and Systems*, 19(12):1561 –1571, December 2000.

[7] L. Lemaitre, C. McAndrew, and S. Hamm. ADMS – automatic device model synthesizer. *Proceedings of the IEEE Custom Integrated Circuits Conference*, pages 27–30, 2002.

[8] Y. Liu, L. T. Pileggi, and A. J. Strojwas. Ftd: frequency to time domain conversion for reduced-order interconnect simulation. *IEEE Transactions on Circuits and Systems*, 48(4):500–506, April 2001.

[9] D. MacMillen, R. Camposano, D. Hill, and T. W. Williams. An industrial view of electronic design automation. *IEEE Transactions on CAD of Integrated Circuits and Systems*, 19(12):1428–1448, December 2000.

[10] G. Marrocco and F. Bardati. Time-domain macromodel of planar microwave devices by FDTD and moment expansion. *IEEE Transactions on Microwave Theory and Techniques*, 49(7):1321–1328, July 2001.

[11] E. K. Miller. A selective survey of computational electromagnetics. *IEEE Transactions on Antennas and Propagation*, 36(9):1281–1305, September 1988.

[12] I. Miller and T. Cassagnes. Verilog-A and Verilog-AMS provide a new dimension in modeling and simulation. *Proceedings of the 2000 Third IEEE International Caracas Conference on Devices, Circuits and Systems*, pages C49/1–c49/6, March 2000.

[13] P. V. Nikitin, C. J.-R. Shi, and B. Wan. Modeling partial differential equations in VHDL-AMS. *IEEE System-on-Chip Conference*, pages 345–348, September 2003.

[14] A. Odabasioglu, M. Celik, and L. T. Pileggi. PRIMA: passive reduced-order interconnect macromodeling algorithm. *IEEE Transactions on CAD of Integrated Circuits and Systems*, 17(8):645–654, August 1998.

[15] N. Orhanovic and N. Matsui. FDTD-SPICE analysis of high-speed cells in silicon integrated circuits. *Proceedings of Electronic Components and Technology Conference*, pages 347–352, 2002.

[16] D. Pederson. A historical review of circuit simulation. *IEEE Transactions on Circuits and Systems*, 31(1):103–111, January 1984.

[17] B. F. Romanowicz. Methodology for the modeling and simulation of microsystems. *Kluwer Academic Publishers*, 1998.

[18] A. E. Ruehli and A. Cangellaris. Progress in the methodologies for the electrical modeling of interconnects and electronic packages. *Proceedings of IEEE*, 89(5):740–771, May 2001.

[19] J. J. Sanchez-Gasca, K. Clark, N. W. Miller, H. Okamoto, A. Kurita, and J. Chow. Identifying linear models from time domain simulations. *IEEE Computer Applications in Power*, 10(2):26–30, April 1997.

[20] K. Seok-Yoon, N. Gopal, and L. T. Pillage. Time-domain macromodels for VLSI interconnect analysis. *IEEE Transactions on CAD of Integrated Circuits and Systems*, 13(10):1257–1270, October 1994.

[21] R. Sharpe, J. B. Grant, N. J. Champagne, W. A. Johnson, R. E. Jorgenson, D. R. Wilton, W. J. Brown, and J. W. Rockway. EIGER: Electromagnetic Interactions GEneRalized. *IEEE Antennas and Propagation Symposium Digest*, 4(12):2366–2369, July 1997.

[22] I. A. Tsukerman, A. Konrad, G. Meunier, and J. C. Sabonnadiere. Coupled field-circuit problems: trends and accomplishments. *IEEE Transactions on Magnetics*, 29(2):1701–1704, August 1992.

[23] B. Wan, B. Hu, L. Zhou, and C.-J. R. Shi. MCAST: an abstract-syntax-tree based model compiler for circuit simulation. *Proceedings of IEEE Custom Integrated Circuits Conference*, 2003.

[24] D. A. White. Orthogonal vector basis functions for time domain finite element solution of the vector wave equation. *IEEE Transactions on Magnetics*, 35(3):1458–1461, May 1999.

[25] D. A. White and M. Stowell. Full wave simulation of electromagnetic coupling effects in RF and mixed-signal IC's using time domain finite element method. *IEEE Transactions on Microwave Theory and Techniques*, submitted.

[26] C. Yang and V. Jandhyala. A time domain surface integral technique for mixed electromagnetic and circuit simulation. *Electrical Performance of Electronic Packaging Conference*, pages 41–44, 2002.

A Fast Parasitic Extractor Based on Low-Rank Multilevel Matrix Compression for Conductor and Dielectric Modeling in Microelectronics and MEMS

Dipanjan Gope
dips@u.washington.edu

Swagato Chakraborty
swagato@u.washington.edu

Vikram Jandhyala
jandhyala@ee.washington.edu

Department of Electrical Engineering,
Box 352500, University of Washington,
Seattle, WA-98195.
Telephone: 206-543-2186.

ABSTRACT

Parasitic parameter extraction is a crucial issue in Integrated Circuit design. Integral equation based solvers, which guarantee high accuracy, suffer from a time and memory bottleneck arising from the dense matrices generated.

In this paper we present a hybrid FMM-QR algorithm that combines the best features of the Fast Multipole Method and the QR based matrix compression method to achieve faster setup and solve time and lower memory requirements. The method is applied to extract parasitic capacitances from the layout of arbitrarily shaped conductors and dielectrics. Examples demonstrating the accuracy and the superior time and memory performances as compared to existing solvers are also presented.

Categories and Subject Descriptors

J.6 [**Computer-Aided Engineering**]: Computer-Aided Design

General Terms

Algorithms, Performance, Design.

Keywords

Parasitics, Multilevel, Low-rank, conductors and dielectrics

1. INTRODUCTION

In deep-submicron technology diminishing wire spacing and higher aspect ratio structures lead to increased parasitic effects [1]. As a consequence, the interconnect delay may significantly increase and eventually dominate over the gate delay causing erroneous clock-timing that leads to a malfunctioning circuit. Hence proper modeling of interconnects is key for meeting timing requirements in a circuit level simulation of VLSI packages. Also in rapidly growing MEMS application electrostatic analysis of large MEMS array has become extremely important.

Analytic models like charge-based capacitance measurement method [2] often suffer from oversimplification of the geometry of interconnects. Stochastic models like the floating random walk method [2] suffer from problems of convergence and the effects of multilayered dielectrics. Therefore to achieve a guaranteed high degree of accuracy a numerical 3D electromagnetic solver is necessitated. The direct application of integral equation solvers leads to the generation of a dense matrix with large number of unknowns, the solution of which presents a time and memory bottleneck.

Existing fast solver algorithms aimed at solving the dense system of integral equations through fast matrix-vector product based iterative solutions include the Fast Multipole Method (FMM) [3], the QR-based method (IES^3) [4] and the Pre-corrected Fast Fourier Transform (FFT) method [5]. The pre-corrected FFT method degrades in efficiency for non-uniform distribution of basis-functions, which is often encountered in circuit problems, due to the inherent necessity of a uniform global grid. The FMM and the IES^3 algorithms on the other hand are ideally suited for application to arbitrarily shaped circuit structures. However they suffer from discrepancies in the setup and solve times and the memory requirements. The FMM method has a faster setup time but a higher memory requirement and a slower solve time. On the other hand the IES^3 method leads to higher compression and consequently a faster solve time at the cost of a slow setup time. Due to these discrepancies, the applicability of the algorithms become problem specific: QR-based methods are ideally suited for large number of nets which involve a single setup but multiple solution phases, and the FMM method is better applicable for a single or small number of excitations.

In the new algorithm presented here, the multilevel oct-tree structure (common to FMM approaches) and the QR compression technique in IES^3 are combined. Further optimizations in the form of a merged interaction list developed here ensure significantly better all-round performance of the hybrid algorithms. The reasons behind the superior performance of this algorithm as compared to FMM and IES^3 are discussed. The method is then applied to extract parasitic capacitance from the layout of conductors and dielectric structures. Accuracy, memory and timing results are compared with FastCap [3], which is an FMM-based open source code and RMBT-QR (Rank-Map based Binary Tree), which is our prototype implementation of IES^3. In the last example it is demonstrated that the algorithm can also be applied for the fast computation of electrostatic forces on MEMS structures.

DAC 2004, June 7–11, 2004, San Diego, California, USA

2. INTEGRAL EQUATION

The conductor and dielectric interfaces are discretized into panels. Basis functions are defined on the discretized panels and appropriate boundary conditions are enforced on the conductor-to-dielectric and dielectric-to-dielectric interfaces [6]. Let S_C and S_D represent the set of discretized panels on the conductor-to-dielectric and dielectric-to-dielectric interfaces. The application of the method of moments formulation leads to the following matrix equation:

$$\begin{pmatrix} \bar{\mathbf{Z}}_{CC} & \bar{\mathbf{Z}}_{CD} \\ \bar{\mathbf{Z}}'_{DC} & \bar{\mathbf{Z}}'_{DD} \end{pmatrix} \begin{pmatrix} \boldsymbol{\sigma}_C \\ \boldsymbol{\sigma}_D \end{pmatrix} = \begin{pmatrix} \mathbf{V} \\ \mathbf{0} \end{pmatrix} \tag{2.1}$$

where, σ_C represents the set of total-charge on S_C, σ_D represents the set of total-charge on S_D and $\mathbf{V}$ represents the set of potentials on S_C. The first set of equations ensures equipotentiality on conductor surfaces.

$$\bar{\mathbf{Z}}_{CC/CD}(j,i) = \left\{ \int_{t_j} ds\, h_j(\mathbf{r}) \int_{t_i} ds' g(\mathbf{r},\mathbf{r}') f_i(\mathbf{r}') \right\} \mid t_i \in S_{C/D}; t_j \in S_C \tag{2.2}$$

where h and f are the testing and basis functions respectively, g represents the Greens function and t is the domain of definition of each basis function. The second set of equations enforces the continuity of the normal component of the electric displacement vector $\mathbf{D}$, across the dielectric-to-dielectric interfaces:

$$\bar{\mathbf{Z}}'_{CD/DD}(j,i) = \left\{ \begin{matrix} \left[-\int_{t_j} ds\, h_j(\mathbf{r}) \int_{t_i} \hat{\mathbf{n}} \cdot ds' \nabla g(\mathbf{r},\mathbf{r}') f_i(\mathbf{r}') \right] \\ + \left[\dfrac{\varepsilon_r^+ + \varepsilon_r^-}{2\varepsilon_0 \left(\varepsilon_r^+ + \varepsilon_r^- \right)} \right] \delta_{ij} \end{matrix} \right\} \mid t_i \in S_{C/D}; t_j \in S_D \tag{2.3}$$

where δ_{ij} is the Kronecker delta function, $\hat{\mathbf{n}}$ is the outward-pointing unit vector, ε_r^+ and ε_r^- are the dielectric constants for the 2 sides of the dielectric-to-dielectric interface.

The entries of the capacitance matrix for p conductors ($Y_i \mid i = 1,2,3,.....p$) can be evaluated thereafter by the well-known formulation:

$$\bar{\mathbf{C}}_{ij} = \left\{ \int_{Y_i} \sigma_F(r') dr' \right\} \tag{2.4}$$

when $\mathbf{V}_j = 1;\ \mathbf{V}_{m;\, m \neq j} = 0 \mid m = 1,2,3....,p$

(2.5)

where σ_F represents the free-charge density on the conductor- dielectric interface and is obtained as:

$$\sigma_F(r) = \varepsilon_r(r)\sigma_C(r) \tag{2.6}$$

where ε_r is the dielectric constant of the dielectric at the conductor-to-dielectric interface.

3. MULTILEVEL OCT-TREE BASED QR ALGORITHM

The pre-determined interaction list oct-tree (PILOT) QR algorithm efficiently compresses the method of moments matrix in a multilevel scheme. The algorithm has 4 main constituents:

3.1 Oct-tree spatial decomposition in 3D

The basis functions are grouped together by a regular geometric pattern of cells. The best combination, which yields a regular cell pattern, is *loosely bounded*, *spatially balanced* decomposition into *orthants* (quadrants in 2D and octants in 3D).The starting cell c_0^0 is the smallest cube that encloses the entire geometry. The superscript indicates the level of decomposition to which the cube is associated and the subscript denotes the cube number in that level. Each cell is then recursively decomposed into a maximum of 8 cubes in 3-D, depending on the distribution of basis functions. Thus each cube c_i^l, which is the i^{th} cube at level l is decomposed by spatially balanced splits along each coordinate, *x*, *y* and *z*. Each cube c_j^{l+1} resulting from this decomposition is called a child of c_i^l and the latter is denoted as the parent of c_j^{l+1}:

$$P_{c_j^{l+1}} = c_i^l \tag{3.1}$$

All the child cubes of c_i^l are siblings of each other, where a sibling set is defined as:

$$S_{c_j^{l+1}} = \{ c_k^{l+1}\ \forall k \mid P_{c_k^{l+1}} = P_{c_j^{l+1}} \} \tag{3.2}$$

The geometric decomposition is hence exactly similar to that of multilevel FMM and therefore its interaction scheme can be leveraged in the presented algorithm.

3.2 Basic multilevel interaction list

Every cube $c_i^l\ \forall i,l \mid\ 0 \le l \le l_c\ ; 0 \le i < n_c^l$, where l_c is the total number of levels and n_c^l is the total number of cubes at level *l*, has a nearest neighbor list $K_{c_i^l}$ and an interaction list $I_{c_i^l}$. The nearest neighbor list, is defined as:

$$K_{c_i^l} = \{ c_j^l \mid c_j^l \text{ is in the same level as } c_i^l \text{ and has atleast one contact point with } c_i^l \} \tag{3.3}$$

Consequently the interaction list is defined as:

$$I_{c_i^l} = \{ c_j^l \mid P_{c_j^l} \in K_{P_{c_i^l}}\ ; c_j^l \notin K_{c_i^l} \} \tag{3.4}$$

The neighbor and the interaction list of a typical cube in level 4 is shown in figure 1:

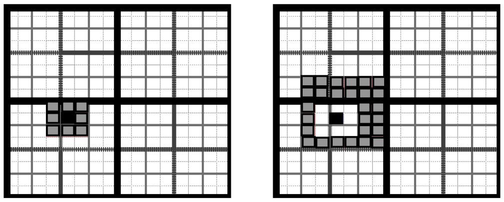

Figure 1: (a) Neighbor list and (b) Interaction list for the given cube at level 4.

3.3 Merged interaction list

It is observed that the interaction lists of siblings share many common cubes:

$$I_S = \bigcap I_{c_i^l} \neq \phi \qquad \forall i \,|\, c_i^l \in S_{c_j^l} \tag{3.5}$$

The common cubes in the interaction lists of the siblings are denoted by I_s. For visualization purposes, parts of the 2D common interaction shell is illustrated in figure 2, though our algorithm is designed for 3D geometries.

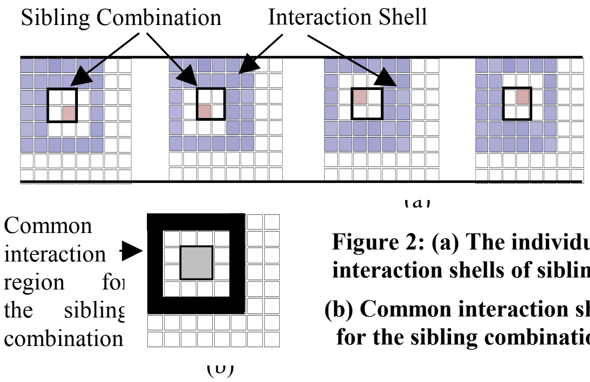

Figure 2: (a) The individual interaction shells of siblings

(b) Common interaction shell for the sibling combination

It is possible to merge overlapping interaction lists belonging to siblings in order to compress larger matrices to low epsilon-ranks (numerical rank under a user-defined tolerance) and thereby gain in terms of overall compression. It must be noted that the common interaction list does not directly translate into a low-ranked merged interaction. The common interaction list is decomposed into disjoint parts such that the overall compression is optimized. Each such part denoted by μ is an interaction between grouped source cubes and observer cubes and forms an entry of the Merged Interaction List (MIL). A μ can be expressed as a combination of multilevel oct-tree cube-to-cube interactions:

$$\mu_k = \{T_p(c_j^l, c_i^l)\} \;\forall p \,|\, 1 \leq p \leq n_g \tag{3.6}$$

where $T_p(c_j^l, c_i^l)$ denotes the interaction between the source basis functions in cube c_i^l and testing functions in cube c_j^l and n_g is the number of multilevel oct-tree interactions grouped. Higher compression is achieved since a larger matrix is compressed to a low epsilon-rank under the same tolerance:

$$\left(m_{\mu_k} + n_{\mu_k}\right) r_{\mu_k} < \sum_{i=1}^{n_g} \left(m_i + n_i\right) r_i \tag{3.7}$$

where *m*, *n* and *r* denote the number of rows, number of columns and the epsilon-rank of a sub-matrix. The subscript *i* denotes a regular multilevel interaction list entry that is now a constituent of the MIL. Figure 3 demonstrates the decomposition of the common interaction list of figure 2 into merged interactions.

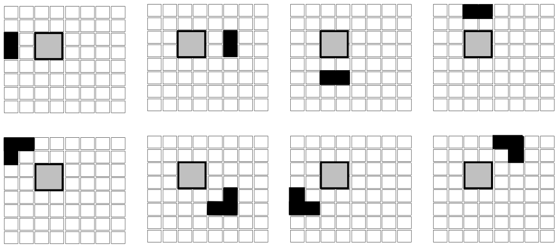

Figure 3: Merged interaction list entries corresponding to the common interaction region of figure 2. Each such entry gives rise to a low-rank matrix block.

Thus the regular interaction list is replaced by the merged interaction list, which has fewer interactions to consider and larger low epsilon-ranked matrices to compress with the same tolerance. In PILOT, the interaction lists of 4 siblings in 2D are replaced by 16 merged interaction entries. Each MIL entry constitutes of the grouping information for source cubes and observer cubes and the corresponding expected epsilon-rank. The expected epsilon-rank is the maximum rank observed for sources and observers randomly placed in an MIL setup. The MIL entries along with the expected ranks are setup as a one-time process for a given kernel. Though there are 16 entries in the MIL, there are only 3 different types of interactions to be evaluated and the rest could be derived from symmetry considerations. The same MIL pattern is valid for all sibling pairs across levels. Although for visualization purposes the 2D MIL construction is illustrated in detail, PILOT supports MIL for both 3D and 2D geometries. A similar MIL is derived for 3D geometries with 40 entries, with only 5 unique entries owing to symmetry.

3.4 QR compression of MIL entries

MoM sub-matrices pertaining to interactions of the MIL are compressed separately for testing functions belonging to S_C and S_D by forming QRs from samples [4]. Consider *n* source basis functions f_i for *i* = 1, 2, …, n belonging to μ_{k_S}, which is the k^{th} MIL source group. Similarly, consider *m* testing functions belonging to S_C inside μ_{k_O}, which is the observer group of the same MIL. Let the sub-matrix $\overline{\mathbf{Z}}_{m\times n}^{sub}$ of the full MoM matrix $\overline{\mathbf{Z}}$ represent the interactions between the basis and the testing functions through the designated Green's function $g(\mathbf{r},\mathbf{r}')$. The column of $\overline{\mathbf{Z}}^{sub}$ pertaining to the interaction of f_i with all testing functions is closely related to other columns.

Using the Modified Gram-Schmidt (MGS) process [6] and a user-specified tolerance ε, $\overline{\mathbf{Z}}^{sub}$ can be decomposed into a unitary matrix $\overline{\mathbf{Q}}_{m\times r}$ and an upper triangular matrix $\overline{\mathbf{R}}_{r\times n}$ such that:

$$\frac{\left\| \overline{\mathbf{Z}}^{sub} - \overline{\mathbf{Q}}\overline{\mathbf{R}} \right\|}{\left\| \overline{\mathbf{Z}}^{sub} \right\|} < \varepsilon \qquad (3.8)$$

where, $$\overline{\mathbf{Q}}^{H}\overline{\mathbf{Q}} = \overline{\mathbf{I}} \qquad (3.9)$$

and the matrix norm $\left\|\overline{\mathbf{X}}\right\|$ is defined as the maximum singular value of the matrix $\overline{\mathbf{X}}$. Similarly the interactions corresponding to testing functions belonging to S_D can be compressed for the same MIL.

4. ADVANTAGES OF PILOT

The main idea behind PILOT is to maintain the superior compression efficiency inherent to QR-based methods compared to FMM based methods, while expediting the process of matrix compression. In other words the setup time is reduced while preserving the solve time and memory efficiency.

The absolute setup time for RMBT-QR (our prototype implementation of IES^3) is largely controlled by the accuracy of rank map predictions. An accurate and exhaustive rank map would preclude the necessity for unnecessary merges and splits and the optimum tree structure would be achieved without any backtracking or refinement within the tree structure. However, a foolproof rank-map is difficult if not impossible to construct owing to the fact that the algorithm can lead to cells with any shape and size as can be seen in figure 4.

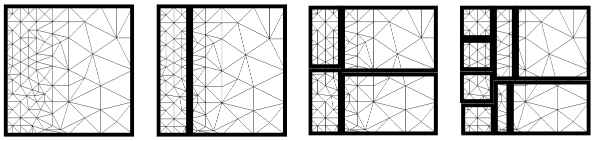

Figure 4: Multilevel tight bound *k*-d tree used in RMBT-QR (IES^3)

It is infeasible to cover the infinite combinations of parameters, thus introducing a scope of error in the rank map. A conservative rank map will require more merges, whereas a liberal rank map will induce wastage of time by constructing unacceptable QR factorizations which are then discarded. Thus the setup time is considerably influenced by the variability of the tree structure and the resulting backtracking and refinement. In PILOT, the setup time is significantly reduced without compromising on memory or solve-time compression. The new algorithm exploits the regularity of cell size, shape and location of a spatially balanced oct-tree as in a multilevel FMM algorithm. By recourse to the FMM interaction list and by adding a few additional features to maximize compression, a regular and compressed interaction pattern is generated. The number of different interactions to be evaluated is finite and small and therefore exhaustive and accurate *a priori* epsilon-rank estimation is possible. PILOT therefore incorporates the best features of the regular tree structure of multilevel FMM and the kernel-independent low-epsilon-rank compression of IES^3.

5. RESULTS

In this section we present simulation results to demonstrate the accuracy and time and memory efficiency of the PILOT-QR algorithm as compared to other existing solvers. All experiments are performed on a 1.6GHz processor with 4GB available RAM space. For PILOT and RMBT-QR analytic integrations are used for the near field terms in conjunction with the collocation scheme. For off-diagonal blocks, a QR decomposition tolerance of 1e-3 is used for both PILOT and RMBT-QR whereas for FastCap, the adaptive algorithm with multipole order of 2 is employed. A relative residual of 1e-3 is used for the GMRES iterative solution. The number of iterations required is observed to be similar for all the methods.

In the first example we consider a 3 level interconnect structure in a 10mm x 4mm x 1mm space. Each interconnect is 0.1mm x 0.1mm in cross-section. The separations between the levels are 0.4mm and the minimum separation between traces on the same level is 0.15mm.

The problem is solved with 10 interconnects as active nets and the rest as floating conductors. The norm$_2$ errors observed for all the algorithms in the capacitance matrix so extracted are around 1e-3.

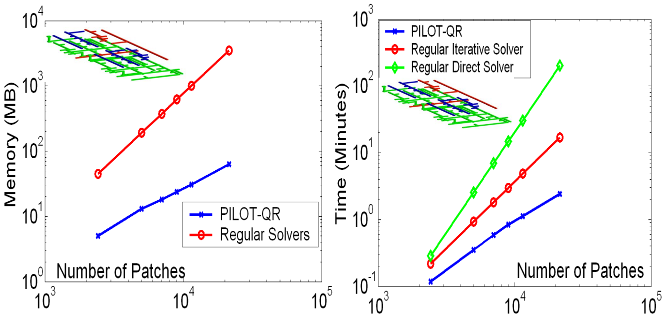

(a) (b)

Figure 5: Performance comparison of PILOT with regular direct (dense-LU) and iterative solvers

In figures 5a and 5b the performance of PILOT is compared with that of regular direct (LU) and iterative solvers for the 3 level VLSI interconnect structure as discussed above. It can be observed that both the time and memory requirement scales linearly for PILOT as compared to the quadratic memory and time scaling for the regular iterative solver and the quadratic memory and cubic time scaling for the regular direct solver. It must be mentioned that for very small number of unknowns the regular approaches (direct/iterative) could be more profitable owing to the computational overhead of the fast solvers.

In figures 6a and 6b, the linear scaling coefficients of PILOT are compared with those of other existing fast solvers, FastCap and RMBT-QR. It is observed that PILOT maintains the compression efficiency of RMBT-QR while improving on the time requirements owing to a faster set-up time, thereby achieving an all-round superior performance over the existing fast solvers.

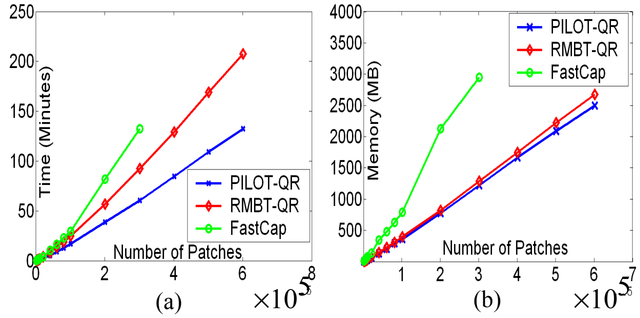

Figure 6: Performance comparison of PILOT with existing fast solvers, FastCap (FMM based) and IES^3 (QR-based)

In the next example we consider a package structure with 56 conducting leads as shown in figure 7:

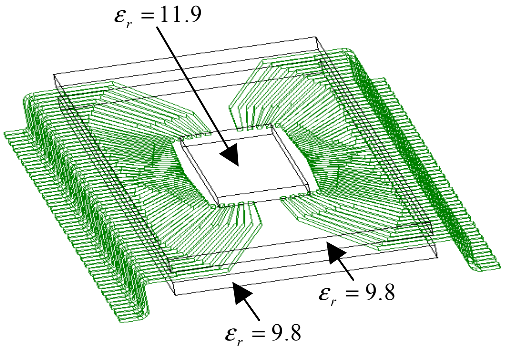

Figure 7: Package structure 280μm×680μm×56μm with 56 leads. The package is sandwiched by a top and a bottom Al_2O_3 ceramic layer (ε_r=9.8) of thickness 20μm. A dielectric slab of ε_r=11.9 and thickness of 10μm is placed in the space between the leads (96μm×220μm).

The first row of the capacitance matrix obtained for the 2 cases, with and without dielectrics, are plotted in figure 8 using PILOT-QR and FastCap. It can be observed that the results demonstrate excellent match between the values obtained from the 2 different algorithms. It can also be noted that due to the presence of the dielectrics the coupling-capacitances between the leads increase.

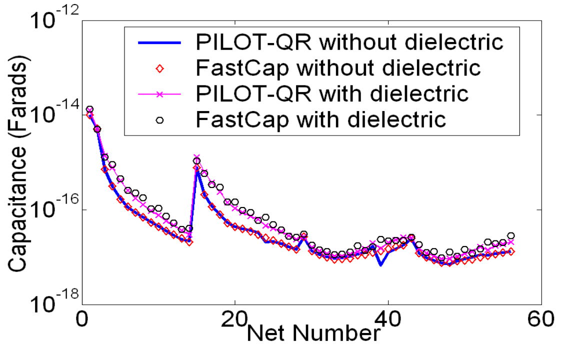

Figure 8: Comparison of results of PILOT with FastCap with or without dielectrics compared with/without dielectrics for the package structure in figure 8.

The required memory is compared with FastCap in figure 9a. In figure 9b, the advantage of PILOT is demonstrated over RMBT-QR for multiple nets for the package structure shown in Fig. 7, without the dielectrics. Time taken by RMBT-QR is always more compared to the time taken by PILOT, by an offset amount, though they demonstrate to have the same slope. This observation supports an improved set-up time performance of PILOT compared to RMBT-QR which is emphasized for a multiple net problem.

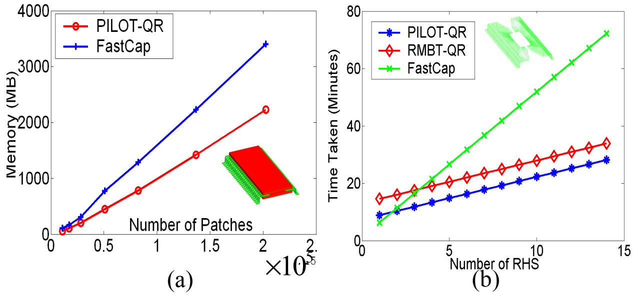

Figure 9: a) Memory comparison of PILOT with FastCap in the presence of dielectrics b) The total time required by the different algorithms for multiple right hand side solutions for the package structure in figure 8.

In the last example we demonstrate the applicability of PILOT in the electrostatic force analysis for MEMS array structures where large number of unknowns necessitates fast solution. The structure under consideration is a prototype of an array of micro-mirrors, which are used as electro-statically controlled optical switches. One array element is shown in figure 10.

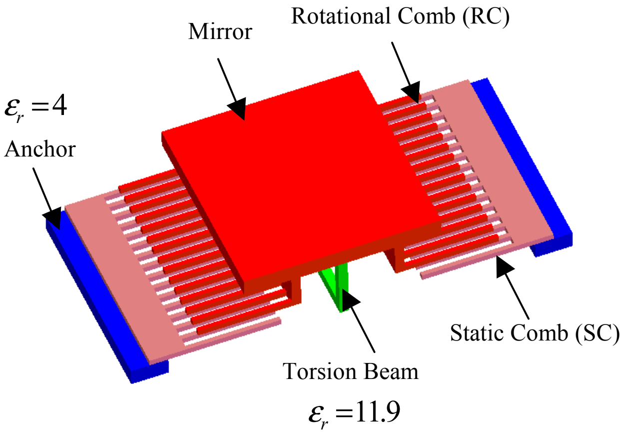

Figure 10: Micro-mirror array element. Two static combs are anchored to the base by 3 μm thick SiO_2 slabs. Each static comb has 16 teeth each with dimensions of 20μm×1μm teeth, separated by 3 μm. Each mirror is 45μm×32μm×2μm and can be tilted about the axis of the supporting torsion beam. Two comb structures are attached one on each side of the mirror, each containing 15 teeth each with dimensions of 20μm×1μm teeth.

Application of voltage on any of the static combs (SC) can rotate the micro-mirror about its supporting torsion beam. The PILOT-QR algorithm is applied to compute the electrostatic fields and forces on the structures at various mirror angles. Since in an array of micro-mirrors the combs are placed close to each other there is electrostatic cross-coupling between the elements. This necessitates the simulation of the entire array for accurate prediction of the pull-down voltage of every mirror.

In this example the pressure distribution on a 10×10 array of micro-mirrors due to electrostatic actuation is simulated. The results are demonstrated in figure 11 on a part of the array.

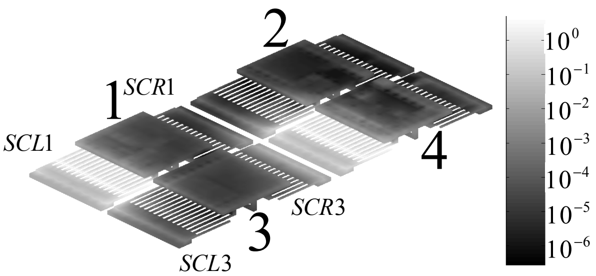

Figure 11: Electrostatic pressure (N/m2) distribution obtained on a 4 element part of a 10 × 10 array of MEMS micro-mirror structure, by placing 1Volt on SCL1 and SCL4

In figure 12, the cross-coupling effects between the elements of the micro-mirror array structure are demonstrated. The static right comb of element 1 (SCR1) is excited by applying 1Volt. The electrostatic pressures on points at the edge of the rotational comb to the left of element 1 (RCL1) are plotted. Maintaining the excitation on the SCR1, additional excitations are applied in succession on static combs intended to rotate other elements. However, due to cross coupling, the electrostatic pressure on the RCL1 change and the effects are demonstrated in figure 9. It is observed that as we move the second excitation closer to the RCL1 (observation comb), the coupling effect becomes pronounced. The simulation results confirm that the excitation of neighboring elements could change the electrostatic torque on a mirror, which in turn affects its rotational angle.The number of patches used for the simulation of the entire array is 0.342 million. The PILOT solved the problem with 3.5GB memory, 54 minutes of one-time setup and 16 minutes of solve-time per right hand side. FastCap could not fit the problem in the given RAM resources.

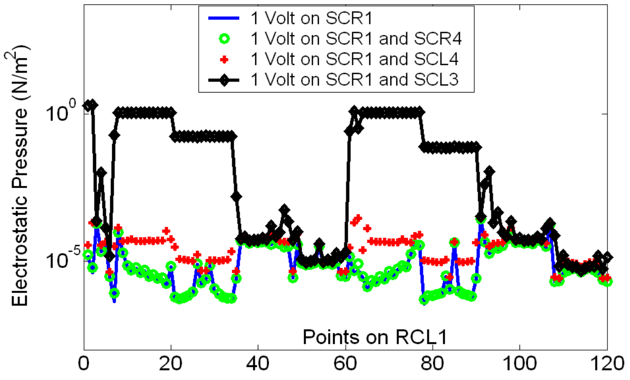

Figure 12: The cross-coupling effects in a micro-mirror array are demonstrated by plotting the electrostatic pressure distribution at points on rotational-comb-1left due to excitations at various static-combs.

6. CONCLUSIONS

In this paper an improved multilevel scheme for QR-based matrix compression and subsequent fast iterative solution is presented. The method is based on exploiting the regular geometry structure of oct-tree decomposition along with merged-interaction optimizations to achieve a pre-determined block-matrix structure and consequently a faster setup time for QR-based compression. The memory and solve-time efficiency common to QR based approaches is preserved and hence overall superior performance is achieved.

The method is applied to parasitic capacitance extraction for structures on boards, packages and chips. The superior time and memory performance of the algorithm is demonstrated as compared to existing fast solvers. The method is also applied to predict the electrostatic pressure distribution on a MEMS array structure.

The algorithm is kernel independent and hence can be applied to solve multi-layered dielectric problems. It is also amenable to fast solution of full-wave kernels for electrically small structures.

7. REFERENCES

[1] M. Kamon, S. McCormick and K. Shepard, “Interconnect parasitic extraction in the digital IC design methodology” IEEE/ACM International Conference on Computer-Aided Design, pp. 223 -230 Nov. 1999.

[2] A. Brambilla, P. Maffezzoni, L. Bortesi and L. Vendrame, “Measurements and extractions of parasitic capacitances in ulsi layouts”**,** *IEEE Transactions on Electron Devices*, vol. 50, Issue: 11, Nov. 2003, pp. 2236 -2247.

[3] K. Nabors and J. White, “FastCap: a multipole accelerated 3-D capacitance extraction program”*, IEEE Transactions on Computer-Aided Design of Integrated Circuits and Systems*, vol. 10 issue 11 pp.1447-1459, Nov. 1991.

[4] S. Kapur and D. Long, “IES^3: A fast integral equation solver for efficient 3-dimensional extraction”, *IEEE/ACM International Conference on Computer-Aided Design*, 1997, pp. 448 –455, Nov. 1997.

[5] J.R. Phillips and J. White, “A precorrected-FFT method for electrostatic analysis of complicated 3-D structures”, *IEEE Transactions on Computer-Aided Design of Integrated Circuits and Systems*, vol. 16 issue 10 pp.1059-1072, Oct. 1997.

[6] S. Rao, T.K. Sarkar and R.F. Harrington, “The Electrostatic Field of Conducting Bodies in Multiple Dielectric Media”, *IEEE Transaction on Microwave Theory and Techniques*, vol. 32, issue 11, Nov 1984 pp. 1441-1448.

[7] G.H. Golub and C.F. Van Loan, *Matrix computations* 2nd Ed. The Johns Hopkins University Press, Baltimore, 1989.

A Padé via AWE Fast Frequency Sweep for Quasi-static Coupled Electromagnetic and Circuit Simulation

Todd West and Vikram Jandhyala
Department of Electrical Engineering, University of Washington, Seattle, WA 98195
Phone: (206) 543-2186, Fax: (206) 543-3842, Email: {twest,jandhyala}@ee.washington.edu

1 Introduction

Padé via AWE (Asymptotic Waveform Expansion) [1] and other model order reduction techniques such as PVL (Padé via Lanczos) [2] and PRIMA [3] have been used for efficient solution of a wide variety of problems. PVL and PRIMA use Lanczos and Arnoldi processes, respectively, to extract the dominant eigenvalues of system matrices of the form $\overline{\mathbf{G}} + s\overline{\mathbf{C}}$. Extending PVL or PRIMA to handle system matrices with other functional forms is difficult for a number of reasons [4]. AWE based methods do not suffer from some of these limitations, so EM (electromagnetic) MOR (model order reduction) has focused on applying AWE to various types of problems. Of particular interest is treatment of the system matrix as the superposition of several other matrices that form a polynomial in frequency [5].

This work considers a coupled EM-circuit system [6] where the EM portion of the system is expressed using boundary element integral equations represented by the method of moments (MoM), and the circuit portion is described using modified nodal analysis (MNA). The system therefore contains two different kinds of physics. The advantage of the coupled approach is the ability to observe circuit effects on EM quantities, and to design EM-aware microelectronic circuits. Here we show that Padé via AWE can be used successfully to implement fast frequency sweeps for coupled EM-circuit systems.

2 Single Point AWE Expansion and Padé Approximation

As described in [6], coupled EM-circuit simulation can be performed by forming the system

$$\begin{bmatrix} \overline{\mathbf{Z}}_{11} & \overline{\mathbf{Z}}_{12} & \overline{\mathbf{0}} \\ \overline{\mathbf{Z}}_{21} & \overline{\mathbf{Z}}_{22} & \overline{\mathbf{C}} \\ \overline{\mathbf{0}} & \overline{\mathbf{C}}^{T} & \overline{\mathbf{MNA}} \end{bmatrix} \mathbf{x} = \mathbf{z},\ \mathbf{x} = \begin{bmatrix} \mathbf{J} \\ \mathbf{I}_c \\ \mathbf{ckt} \end{bmatrix},\ \mathbf{z} = \begin{bmatrix} \mathbf{ex}_{em} \\ \mathbf{0} \\ \mathbf{ex}_{ckt} \end{bmatrix} \tag{1}$$

where $\overline{\mathbf{Z}}_{11}$ is the pure electromagnetic part of the system and $\overline{\mathbf{Z}}_{12}$, $\overline{\mathbf{Z}}_{21}$, and $\overline{\mathbf{Z}}_{22}$ extend the electromagnetic system to provide terminals where the circuit part of the system, $\overline{\mathbf{MNA}}$, can be coupled to the electromagnetic part. $\overline{\mathbf{C}}_{12}$ expresses the coupling between the electromagnetic and circuit systems. $\mathbf{J}$ is a vector of electromagnetic unknowns and $\mathbf{ckt}$ is the voltage and current unknowns in the circuit part of the system. $\mathbf{I}_c$ is the unknowns for the EM connection points. $\mathbf{ex}_{em}$ is the electromagnetic excitation of the system and $\mathbf{ex}_{\mathrm{ckt}}$ is a circuit excitation vector containing independent voltage and current sources. Such a system enables fully-coupled simulation as well as terminal-based EM models for use in circuit simulation.

For the EM portion of the system, we use the electric field integral equation (EFIE) with surface impedance. The EFIE enforces tangential continuity of electromagnetic fields through

$$-\left\langle j\omega\mathbf{A}(\mathbf{J}_{\mathbf{s}},\mathbf{r})\right\rangle - \left\langle \nabla\phi\left(\frac{-\nabla\cdot\mathbf{J}_{\mathbf{s}}}{j\omega},\mathbf{r}\right)\right\rangle - \left\langle Z_s\left(\sqrt{\omega}\right)\mathbf{J}_{\mathbf{s}}(\mathbf{r})\right\rangle = -\left\langle \mathbf{E}_{incident}(\mathbf{r})\right\rangle \tag{2}$$

where **r** is some position on the surface of a conductor**,** **A** is the magnetic vector potential in the Lorentz gauge, ϕ the electric scalar potential, Z_s the surface impedance, $\mathbf{J}_s$ the surface current, and $\mathbf{E}_{\text{incident}}$ the incident electric field strength. For electrically small systems, such as mixed-signal systems-on-chip, the quasi-static Green's function applies. **A** is therefore frequency independent, $\nabla\phi$ is inversely proportional to frequency, and Z_s is proportional to the square root of frequency. Similarly, the circuit part of the system is

$$\overline{\mathbf{MNA}} = \frac{\overline{\mathbf{Y}}_L}{f} + \overline{\mathbf{Y}}_R + f\overline{\mathbf{Y}}_C \tag{3}$$

where $\overline{\mathbf{Y}}_L$, $\overline{\mathbf{Y}}_R$, and $\overline{\mathbf{Y}}_C$ are the admittances associated with inductive, resistive, and capacitive elements in the circuit portion of the system, respectively. In turn, the coupled system matrix is expressed as the sum of frequency dependent matrices

$$\begin{bmatrix} \overline{\mathbf{Z}}_{11} & \overline{\mathbf{Z}}_{12} & \overline{\mathbf{0}} \\ \overline{\mathbf{Z}}_{21} & \overline{\mathbf{Z}}_{22} & \overline{\mathbf{C}} \\ \overline{\mathbf{0}} & \overline{\mathbf{C}}^T & \overline{\mathbf{MNA}} \end{bmatrix} = \frac{\overline{\mathbf{C}}_f}{f} + \overline{\mathbf{R}} + \sqrt{f}\,\overline{\mathbf{Z}}_s + f\overline{\mathbf{L}} \tag{4}$$

Rewriting in terms of $g = \sqrt{f}$ yields the system equation

$$\left(\overline{\mathbf{C}}_f + g^2\overline{\mathbf{R}} + g^3\overline{\mathbf{Z}}_{Z_s} + g^4\overline{\mathbf{L}}\right)\mathbf{x} = g^2\mathbf{z} \tag{5}$$

We then expand $\mathbf{x}$ in a Taylor series of k terms about $g_0 = \sqrt{f_0}$ with $g = g_0 + \gamma$, using a conditioning factor ξ as in [2], and derive the AWE recursion relationships as in [6] to find the AWE moments $\mathbf{x}_0 \ldots \mathbf{x}_k$. A vector Padé approximation $\hat{\mathbf{x}}_{Padé}$ is then computed for $\mathbf{x}$ by forming and solving the Padé Hankel matrix for denominator coefficients of each element in $\mathbf{x}$ and using the direct formula for numerator coefficients ([7], Chapter 1, equations 1.6 and 1.7).

3 Multipoint Expansion and Numerical Conditioning

Typically, the frequency range of interest is known *a priori*, and it is desired to find an approximation or set of approximations which is accurate over the entire range. We use a binary search which places the Padé expansion point in the middle of the frequency range. The resulting expansion is evaluated at the interval's endpoints and compared to the exact solution at the endpoints. If the approximation's error is larger than some specified tolerance, the interval is divided into two sub intervals of equal size, new expansions performed, and checked against exact solutions at their intervals' endpoints. If necessary, additional subdivision is performed recursively until the desired accuracy is obtained.

Calculation of Padé approximants directly from AWE moments is notoriously poorly conditioned [7]. The scaling factor ξ used in (7) has great impact on the Padé Hankel matrix's conditioning. A variety of possible choices for ξ have been proposed [1]; our current method is to compute an initial $\mathbf{x}_1$ with ξ=1 and then update ξ as

$$\xi = \text{mean}\left(\mathbf{x}_1 ./\, \mathbf{x}_0\right) \tag{6}$$

where ./ denotes element by element division and near zero elements in $\mathbf{x}_0$ are ignored. $\mathbf{x}_1 \ldots \mathbf{x}_k$ are then computed with the new value of ξ. Such single step adaptation of ξ is not, in principle, optimum. However, effective values of ξ have reliably been produced using this method. The authors have also implemented the WCAWE method of [5] and found WCAWE and Padé via AWE with adaptive ξ produce near identical results on a variety of test cases.

Each node present in $\overline{\mathbf{MNA}}$ whose voltage is invariant in frequency results in an exact AWE expansion with $x_{i,0} = V_i$ and $x_{i,1} \ldots x_{i,k} = 0$, where V_i is the node's voltage. The Hankel matrix is thus singular for all Padé approximants of order higher than zero. A similar situation arises where any unknown in the system is almost exactly a polynomial in frequency. Adaptive Padé order reduction is needed to handle such cases.

4 Numerical Results

As an example, we consider the low noise amplifier (LNA) shown in figure 1. The operating frequency of inductively decoupled LNAs, such as this design, is determined by the resonance of the output inductor with the output and device capacitances. This is a difficult case for Padé via AWE, as effectiveness of AWE decreases near resonance. For both amplifiers, the inductors are modeled using an EM MoM approach and the rest of the amplifier is represented with a circuit system. The operating points of the amplifiers are found in Spice using the inductors' DC resistances and then small signal models are evaluated for the MOSFETs and used with the Padé fast frequency sweep. Table 1 compares the time needed for Padé solution relative to that of a conventional frequency sweep which solves the system at some number of frequency points. Both Padé and the conventional sweep use only LU factorization to solve the systems. In principle, fast matrix-vector methods can further accelerate the frequency sweep, provided appropriate pre-conditioners for improving the condition number (on the order of 10^9) can be developed.

solve time for conventional frequency sweep	Padé setup time	Padé solve time for frequency sweep	reduction in solve time by using Padé with $\varepsilon<0.01$
100 points: 4.32 hours 250 points: 10.8 hours	6 expansions 53.5 minutes	100 points: 340ms 250 points: 850ms	100 points: 79.4% 250 points: 91.7%

Table 1 Padé simulation results

Figure 2 shows the LNA gain and the Padé accuracy as a function of the number of Padé expansions used. As a way of measuring the accuracy of a Padé expansion, we use the error norm

$$\varepsilon(f) = \frac{\left\| \hat{\mathbf{x}}_{\mathbf{Pad\acute{e}}}(f) - \mathbf{x}(f) \right\|_2}{\left\| \mathbf{x}(f) \right\|_2} \tag{7}$$

5 Conclusion

A fast frequency sweep for coupled EM-circuit systems, enabling rapid characterization of circuits with EM components, has been demonstrated using a simple Padé via AWE approach. In future work, a fast direct solver [8] will be used in conjunction with the sweep to obtain rapid solution of poorly conditioned systems for realistic on-chip structures. Extension to nonlinear MOR [9] is also of interest for handling devices outside of the small signal range.

Acknowledgements

The authors thank Dicle Ozis, Sambuddha Bhattacharya, Brian Ward, and Yong Wang for their helpful input. This work was supported by DARPA-MTO NeoCAD grant N66001-01-1-8920.

References

[1] V. Raghavan, R. A. Rohrer, L. T. Pillage, J. Y. Lee, J. E. Bracken, and M. M. Alaybeyi, "AWE-Inspired," *Proceedings of the IEEE Custom Integrated Circuits Conference*, pp. 18.1.1–18.1.8, 1993.

[2] Peter Feldmann and Roland W. Freund, "Efficient Linear Circuit Analysis by Padé Approximation via the Lanczos Process," *IEEE Transactions on Computer-Aided Design of Integrated Circuits and Systems*, vol. 14, no. 5, pp. 639–649, 1995.

[3] Altan Odabasioglu, Mustafa Celik,, and Lawrence T. Pileggi, "PRIMA: Passive Reduced-Order Interconnect Macromodeling Algorithm," *IEEE Transactions on Computer-Aided Design of Integrated Circuits and Systems*, vol. 17, no. 8, pp. 645–654, 1998.

[4] Joel R. Phillips, Luca Daniel, and L. Miguel Silveira, "Guaranteed Passive Balancing Transformations for Model Order Reduction", *IEEE Transactions on Computer-Aided Design of Integrated Circuits and Systems*, vol. 22, no. 8, pp. 1027–1040, 2003.

[5] Rodney D. Slone and Jin Fa Lee, "Well-Conditioned Asymptotic Waveform Evaluation for Finite Elements", *IEEE Transactions on Antennas and Propagation*, vol. 51, no. 9, pp. 2442–2447, 2003.

[6] Y. Wang, D. Gope, V. Jandhyala and C.J. Richard Shi, "Integral Equation-based Coupled Electromagnetic Circuit Simulation In the Frequency Domain," *IEEE Antennas and Propagation International Symposium*, vol. 3, pp. 328-331, June 22-27, 2003

[7] George Baker and Peter Graves-Morris, *Padé Approximants*, 2nd edition. Cambridge University Press, New York, NY, USA, 1996.

[8] Dipanjan Gope and Vikram Jandhyala, "An Iteration Free Fast Multilevel Solver for Dense Method of Moment Systems", *Electrical Performance of Electronic Packaging*, pp.177–180, 2001.

[9] Michał Rewieński and Jacob White, "A Trajectory Piecewise-Linear Approach to Model Order Reduction and Fast Simulation of Nonlinear Circuits and Micromachined Devices", *IEEE Transactions on Computer-Aided Design of Integrated Circuits and Systems*, vol. 22, no. 2, pp. 155–170, 2003.

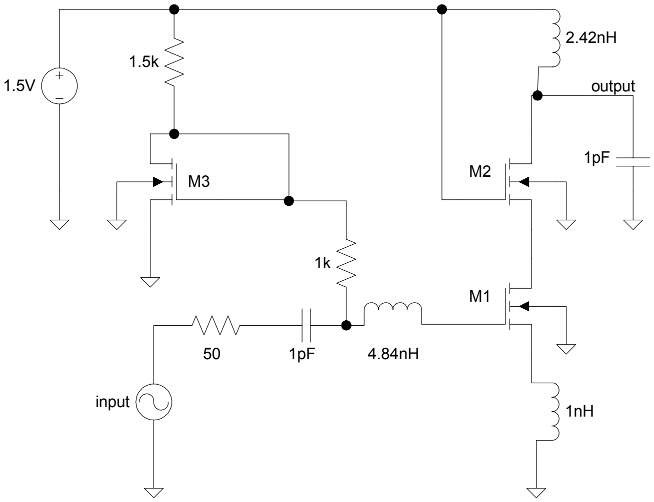

Figure 1 single ended LNA

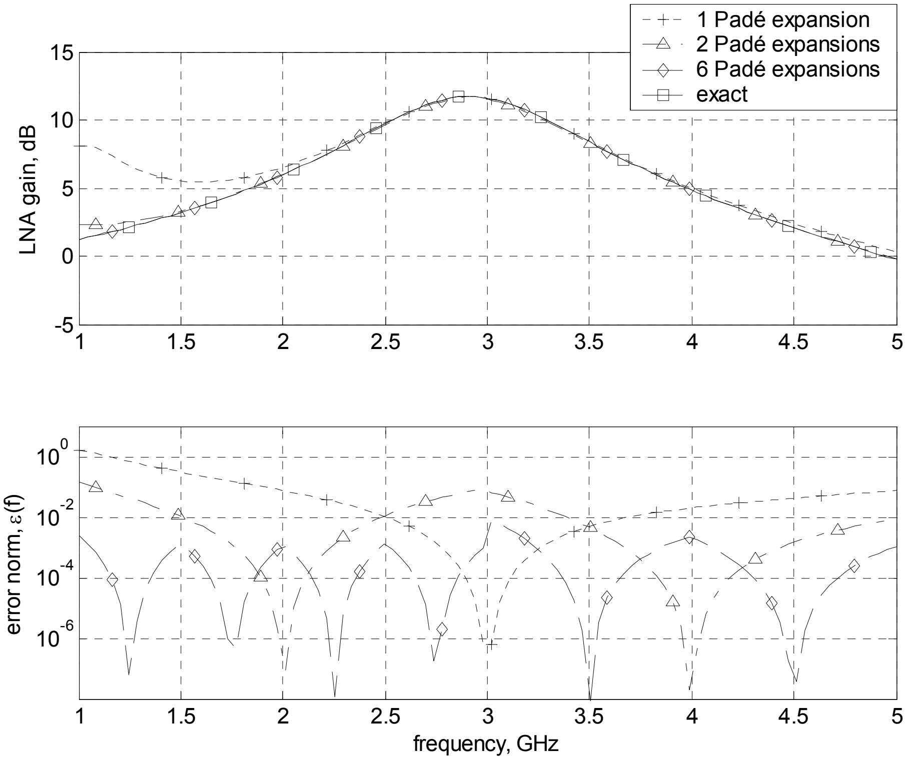

Figure 2 Padé results for single ended LNA

Surface-Based Broadband Electromagnetic-Circuit Simulation of Lossy Conducting Structures in Microelectronic Circuits

Swagato Chakraborty* and Vikram Jandhyala
Department of Electrical Engineering, University of Washington, Seattle WA 98195, Email: jandhyala@ee.washington.edu, Ph: 206-543-2186, Fax: 206-543-3842

Introduction

Rapid growth in the switching speed, and packing density of integrated digital, analog, RF, and microwave circuits has increased the importance of accurate electromagnetic (EM) modeling. While modeling an entire system with full-wave EM simulation is impractical due to the computational complexity, it is important to model the distributed effects in sensitive portions and couple them to the lumped-element models from circuit simulation. This coupled EM-circuit approach is particularly important for field-aware design, such as hot spot prediction, decoupling capacitor placement, and ground bounce, where port models will not suffice.

The volume integral equation (IE) based partial element equivalent circuit (PEEC) approach [1], works well for interconnects at frequencies where volume conduction is the dominant current flow, but requires an explicit modeling of skin depth in the form of a frequency dependent volumetric discretization at higher frequencies. Surface IE based methods are typically well suited for interconnect analysis due to their frequency independent discretization for modeling the skin effect. Such methods, using scalar Green's functions have been implemented for RLC extraction [2]. Fully-coupled circuit-EM solution [3] has been reported for perfect electric conductors and also for lossy conducting material at high frequency where the surface impedance assumption [4] is valid. The surface impedance approach, though very useful for high frequency applications, fails to capture the low frequency effects due to volumetric current flow through the conductor and hence is unsuitable for broadband digital applications. The method presented here is focused towards a frequency domain broadband simulation of arbitrarily shaped lossy objects coupled to circuits using surface integral equations and a unified coupling matrix approach, and presents itself as a smooth and seamless transition from high-frequency surface impedance approximations to low-frequency volumetric methods, in a single formulation.

Formulation

A two-region PMCHWT [5] formulation, formed by decomposition of the problem into an equivalent exterior and interior problem using the background and the conducting medium Green's functions respectively, is used. For an interconnect with finite conductivity, the interior electric field **E** does not completely vanish, hence equivalent magnetic current sources **M** exist on the boundary, along with the equivalent electric current source **J** as,

$$\mathbf{M} = \hat{\mathbf{n}} \times \mathbf{E} \neq 0 \tag{1}$$

where $\hat{\mathbf{n}}$ is the unit normal to the conductor surface. The boundary condition in the tangential components of the electric and magnetic field on the surface of the EM object can be expressed in terms of the potentials as,

$$\begin{aligned}&\left(-j\omega\mathbf{A}_e - \nabla\phi_e - \frac{1}{\varepsilon_e}\nabla\times\mathbf{F}_e + \mathbf{E}_e^{exc}\right)_{\tan} \\ &= \left(-j\omega\mathbf{A}_i - \nabla\phi_i - \frac{1}{\varepsilon_i}\nabla\times\mathbf{F}_i + \mathbf{E}_i^{exc}\right)_{\tan}\end{aligned} \tag{2a}$$

$$\begin{aligned}&\left(-j\omega\mathbf{F}_e - \nabla\psi_e + \frac{1}{\mu_e}\nabla\times\mathbf{A}_e + \mathbf{H}_e^{exc}\right)_{\tan} \\ &= \left(-j\omega\mathbf{F}_i - \nabla\psi_i + \frac{1}{\mu_i}\nabla\times\mathbf{A}_i + \mathbf{H}_i^{exc}\right)_{\tan}\end{aligned} \tag{2b}$$

where the suffix *e*, *i* stand for the exterior and interior medium respectively, **A**, **F** denote the Magnetic and electric vector potential and ϕ , ψ are the electric and magnetic scalar potential. ε_e , ε_i are the permittivities and μ_e , μ_i are the permeabilities of he exterior and the interior media respectively. ω is the angular frequency. E_m^{exc} and H_m^{exc} are the incident electric and magnetic field in the m^{th} (*e* or *i*) medium. The potentials are related to the electric current density $\mathbf{J}_m$, magnetic current density $\mathbf{M}_m$,electric charge density ρ_m , and magnetic charge density ζ_m in the m^{th} medium.

$$\begin{pmatrix} \mathbf{A}_m \\ \phi_m \\ \mathbf{F}_m \\ \psi_m \end{pmatrix} = \begin{pmatrix} \mu_m \\ \dfrac{1}{\varepsilon_m} \\ \varepsilon_m \\ \dfrac{1}{\mu_m} \end{pmatrix} \cdot * \, G_m \otimes \begin{pmatrix} \mathbf{J}_m \\ \rho_m \\ M_m \\ \zeta_m \end{pmatrix} \tag{3}$$

$\otimes$ and $\cdot *$ are the convolution and the element by element product operations respectively. G_m is the Green's function in the m^{th} medium, and is given by

$$G_m(\mathbf{r},\mathbf{r}') = \frac{e^{-jk_m|\mathbf{r}-\mathbf{r}'|}}{4\pi|\mathbf{r}-\mathbf{r}'|} \tag{4}$$

k_m is the wave-number in the m^{th} medium. It is important to note that for highly lossy media, *k* has a strong negative imaginary part, hence the Green's function show a rapid spatial decay and polar-coordinate based quadrature is required to carry out the Green's function convolution [6]. The current densities are related to the corresponding charge densities by the continuity equation as

$$\begin{pmatrix} \nabla \cdot J_m \\ \nabla \cdot K_m \end{pmatrix} = -j\omega \begin{pmatrix} \rho_m \\ \zeta_m \end{pmatrix} \tag{5}$$

The coupling between the EM object and the circuit is achieved through a set of coupling currents (Fig. 1), from the circuit nodes to the EM object, where the circuit node is connected to the corresponding faces of the EM object. The coupling currents are related to the circuit currents by KCL at the connection nodes, and with the equivalent electric current density of the connection patches by a modified continuity equation

$$\nabla_S \cdot \mathbf{J}_m(\mathbf{r}) + j\omega\rho_m(\mathbf{r}) = \frac{I_c}{A}, \tag{6}$$

where ∇_S is the surface divergence, I_c is the coupling current, A is the area of the connection patch on the EM object. The right hand side of Eqn. (6) contributes to the electric field of both the exterior medium and the interior medium as an extra electric charge density by Eqns. (2a and 3). Also the coupling from the EM object to the circuit is obtained by enforcing the exterior medium electric potential on the connection patch to be equal to the voltage of the corresponding circuit node. Thus we obtain a complete set of linear equations that can be solved as a coupled system to obtain the EM currents as well as the circuit variables. Also we can obtain a terminal model for the EM object that can be used directly as a stamp for the MNA matrix to solve for different circuits with the same EM object. The electric field can be found inside the EM object by plugging in the EM unknowns in the interior medium problem

$$\mathbf{E}_i^{tot} = -j\omega\mathbf{A}_i - \nabla\phi_i - \frac{1}{\varepsilon_i}\nabla\times\mathbf{F}_i + \mathbf{E}_i^{exc} \tag{7}$$

The true electric current in the interior of the EM object can be found from the field as

$$\mathbf{J}_i^{True} = \sigma\,\mathbf{E}_i^{tot} \tag{8}$$

This is also important to note that the formulation is sufficiently robust to incorporate the effect of incident field, both interior and exterior to the matrix in addition to the circuit excitation.

Results

Resistance and inductance of a rectangular cross section interconnect is extracted by observing the terminal voltage difference across the object with a given current excitation. Fig. 2(a,b) depicts the frequency behaviour of the inductance and resistance of a Copper trace of dimension $5mm \times 0.5mm \times 0.5mm$. In Fig.2a the inductance curve shows the expected leveling off at low- and high frequencies, and also shows excellent agreement with the DC inductance obtained from a volumetric solver, and the AC inductance obtained from a surface-PEC solver respectively. Fig. 2b show the excellent agreement of the quasi-static resistance obtained using the presented method, with the analytic resistance computed from the skin-depth thickness at a given frequency. Fig. 3 shows the effect of radiation resistance captured through a full-wave simulation. Fig. 4 depicts the volumetric current flow inside the conductor by using Eqns.(7,8). As the skin depth decreases with increase in the conductivity, the current flow becomes dominant near the surface and the corners, and the ratio between the maximum and minimum current density increases. Also, the computed logarithmic slope of the current density is plotted in Fig. 4, against the expected skin-depth based slope along the diameter of a Copper cylinder of diameter 1mm. and length 5 mm.

Conclusions

A seamless broadband method is presented to model the EM behaviour of conducting structures in microelectronic circuits through a unified matrix. The EM modeling as well as the coupling scheme has been explained. Results have been presented to validate the proposed broadband technique against existing commercial solver. Further post-processing is performed in order to determine the volumetric current flow inside the conductor using a surface only formulation, and comparisons to skin effect models is also demonstrated. Continuing work includes low-frequency stabilization and fast multilevel solvers based on QR methods.

Acknowledgements

This work was supported by DARPA-MTO NeoCAD grant N66001-01-1-8920.

References

[1] A.E. Ruehli , "Equivalent Circuit Models for Three-Dimensional Multiconductor Systems", *IEEE Trans. on Microwave Theory and Techniques,*Vol-22(3),Mar 1974, pages-216 –221.

[2] Z.Zhu, J. Huang, B. Song. J. White, "Improving the robustness of a surface integral formulation for wideband impedance extraction of 3D structures", *IEEE ICCAD 2001,*. 4-8Nov. 2001, Pages: 592 –597.

[3] Y.Wang, D.Gope ,V.Jandhyala, "Integral equation-based coupled electromagnetic circuit simulation in the frequency domain", *IEEE AP-S 2003*, 23-26 Jun 2003. Pages 328-331.

[4] A.Glisson, "Electromagnetic scattering by arbitrarily shaped surfaces with impedance boundary conditions," *Radio Science*, Vol. 27(6), Nov. 1992., pages 935-943.

[5] K.Umashankar, A.Taflove, and S.M.Rao, "Electromagnetic scattering by arbitrary shaped three dimensional homogeneous lossy dielectric objects," *IEEE Tran. on Antennas and Propagation,* Vol 34(6) , June 1986. pages 758-766 .

[6] S. Chakraborty,V.Jandhyala, " Evaluation of green's function integrals in conducting media", *IEEE AP-S 2003*, 23-26 Jun. 2003, Pages 320-323.

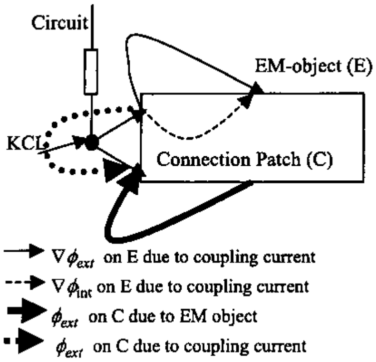

Fig. 1 Circuit coupling

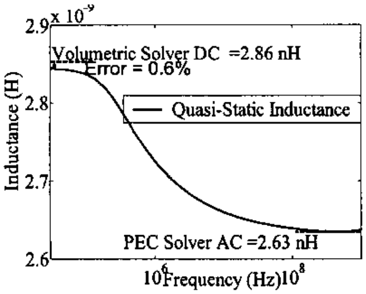

Fig. 2a Frequency dependence of inductance

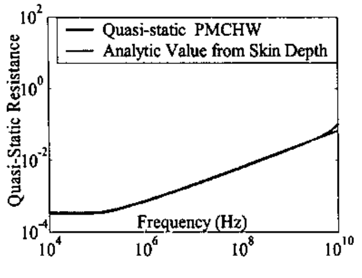

Fig. 2b Frequency dependence of resistance

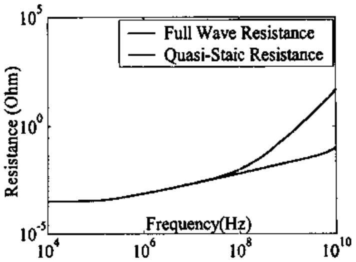

Fig.3 Full-wave radiation resistance

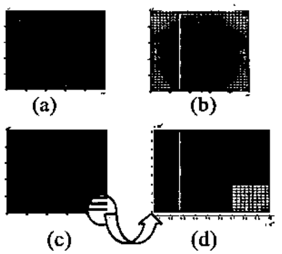

Fig 4. Interior Volume current distribution

(a) $\sigma = 5.8 \times 10^4$, J_{max}/J_{min}=99%

(b) $\sigma = 5.8 \times 10^6$, J_{max}/J_{min}=10.3%

(c) $\sigma = 5.8 \times 10^7$, J_{max}/J_{min}=0.09%

(d) Zoomed view of a corner of (c)

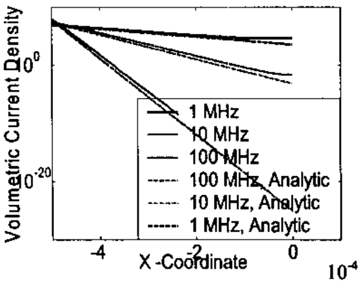

Fig 5. Skin-depth decay of current in volume

Electromagnetic Modeling and Electromagnetic-Circuit Co-Simulation of Mixed-Signal Systems-on-Chip

Vikram Jandhyala*[1], Pavel Nikitin[1], Daniel White[2], John D. Rockway[2], Nathan Champagne[2], C.J. Richard Shi[1], John W. Rockway[3], David Allstot[1], and Robert Sharpe[2]

1 Dept of Electrical Engineering, University of Washington, Seattle WA 98125 {jandhyala,nikitin,cjshi,allstot}@ee.washington.edu; 2 Lawrence Livermore National Lab, 7000 East Ave, Livermore CA 94550 {dwhite, nchampagne, rockway2,rsharpe}@llnl.gov; 3 Space and Naval Warfare Systems Command, 4301 Pacific Hwy, San Diego CA 92110 rockway@spawar.navy.mil

1 Introduction

Electromagnetic (EM) modeling is a critical part of present and future analog and mixed-signal system-on-chip (SoC) simulation and design. This paper presents an overview of selected approaches for large-scale efficient simulation of EM-effects for such microelectronic systems. In particular, coupled formulations, fast solvers, fast frequency sweeps, material models, and time domain approaches are discussed. Further examples and references will be provided at the special session on computational challenges for mixed-signal integrated circuits and radio-frequency packaging.

2.1 Coupled Formulation in Time and Frequency Domains

The mixed-signal simulation environment embodies a complex interaction of digital, analog, and geometry-dependent EM effects and related modeling. Traditionally, different modalities have been modeled separately in an *ad hoc* manner, necessitating heavy user intervention, estimation and even guesswork, and using a myriad different simulation programs and methods to connect between them.

The first step is the development of a combined topology-geometry based description. The circuit description of the mixed-signal system is complemented by a layout-technology description. Selected sections are, either manually or automatically on the basis of previous templated results, chosen as EM-sensitive regions. These might involve interconnects, substrate coupling regions, or sensitive passive components, for example.

The figure below shows an example of the layout and sensitive regions. This separation enables a coupled formulation to be set up; both circuit simulation through modified modal analysis (MNA), and EM simulation, in this case through the method of moments (MoM) integral equation techniques, can be formulated as a coupled system. Such a system can then be hierarchical or *telescoped* to the degree required, depending on the choice of using circuit (or transmission line models) or EM simulation for a specific section of the mixed-signal system.

The coupled matrix represents the formal description of the overall solution; however in many cases, port model representations of the EM structures suffice. In the coupled formulation, this is exactly equivalent to a Schur decomposition of the two-by-two block system, and automatically enables EMI/EMC excitations in addition to circuit sources. The coupled formulation proves to be useful where the internals of the EM simulation results, as dependent on circuit components and sources, is critical. This is particularly useful in applications such as ground bounce prediction, where the location of circuit

0-7803-8302-8/04/$20.00 ©2004 IEEE

sources changes the potential distribution. In addition, in the time domain, a coupled SPICE-time domain integral equation formulation enables non-linear effects to be incorporated into EM models where the need arises, such as in large-signal models. Iteration-based design also benefits from the coupled formulation, where EM matrices can be pre-computed and represented by models. Alternatively, EM-based design can be performed by pre-computing and inverting circuit sub-matrices and using these as excitations into the EM sectionof the coupled formulation.

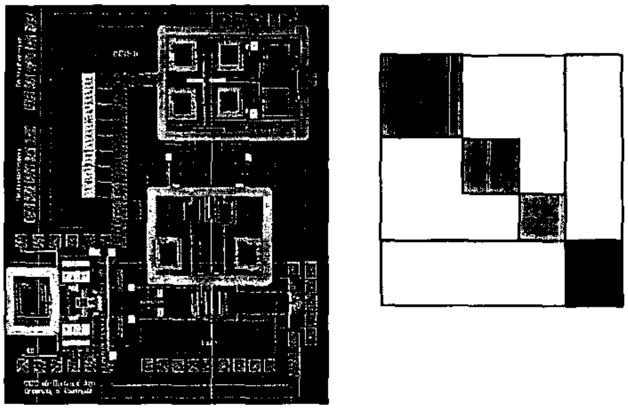

Figure 1: Left: Layout of a mixed-signal circuit, sensitive passives are outlined in red. Right: Associated coupled EM-circuit system. The block diagonal blocks depict EM modeling where interaction between sections has been ignored in this particular simulation instance. The lowest block in the right corner is the MNA; the two rectangular blocks are the sparse coupling matrices.

2.2 Fast Solvers

A necessary requirement in order to be able to model large-scale circuits is a physics-based fast solver for rapid solution of the EM and coupled problems. In particular, established fast methods such as the fast multipole method, and FFT-based techniques, may be exploited. Owing to (i) the multilayered environment and (ii) the presence of electrically small structures, our own solver is based on an alternative technology; the solver exploits a variant of the multilevel QR methodology developed at Lucent by Kapur and Long. An intriguing extension of the fast iterative solver based on this methodology is the promise it has shown as a direct solver, with the potential of solving poorly-conditioned systems and dramatically speeding up massive right hand side number problems.

2.3 Broadband Simulation

Broadband simulation is another key element of mixed-signal simulation. This problem is approached here through two distinct methods. The first is the use of time domain integral equation techniques, wherein broadband simulation is automatically ensured. The second is the use of fast frequency sweep methods or model order reduction in the frequency domain. In the context of coupled simulation, this permits frequency sweeps of impedance, quality factor, and circuit/EM quantities of interest. The distinction between regular frequency sweep approaches and the ones used here is that a unified circuit-EM frequency sweep can be performed on the coupled system.

Complementary to these broadband approaches are formulations and quadrature specializations that are required for broadband integral-equation based simulation. In particular, loop-star and loop-tree methods, as well as new second-kind formulations, have enabled well-conditioned formulations. In addition, the skin effect behavior needs to be captured over a range of frequencies, where surface impedance approximations could be invalid. This is accomplished by a two-region formulation employing an interior medium lossy-Green's function based on polar coordinate quadrature schemes. As shown in Fig. 2, such formulations permits the automatic prediction, with a surface formulation, of all skin effect-related phenomena such as the leveling off of inductance at low and high frequencies (before self-resonance effects become dominant). The low frequency and high frequency values are within 1% of those computed with commercial finite element (for low frequency) and method of moments (for high frequency) solvers.

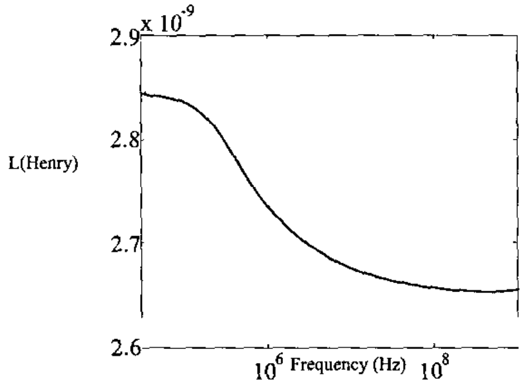

Fig. 2 Broadband frequency dependence of a single layer inductor with a two-region, low-frequency stabilized surface integral formulation

2.4 Hybrid Simulation

The presence of finite non-planar discontinuities, such as passivation, active region modeling, and substrates in general necessitates both surface and volume methods. In addition to surface integral equation methods, we also use a hybrid surface-volume integral equation method in the frequency domain. Also, time- and frequency- domain versions of the finite element method are coupled to integral equations for the hybrid problem, and act as exact boundary conditions for the partial differential equation representations of the inhomogeneous regions.

2.5 Link to VHDL-AMS

High-level behavioral modeling languages have become critical for not only digital modeling but also analog as well as multi-physics and multi-technology simulation. It is not surprising that there is also a trend in directly integrating EM simulation results and methods into these languages and formats. While VHDL-AMS is originally designed for time-domain simulation, there are emerging harmonic-balance based implementations for non-linear small-signal frequency domain modeling as well. In the presented approach, generation of time-domain macromodels is performed through state-space models generated directly from time domain EM simulation, as well as through reduced-order models in the frequency domain. Figure 3 depicts this simulation flow as used in conjunction with a behavioral modeling language. Note that EM sub-systems that include lumped circuits (such as decoupling capacitors in plane sub-sections, or tuning elements for distributed inductors) are modeled as coupled systems which are then converted into behavioral macromodels.

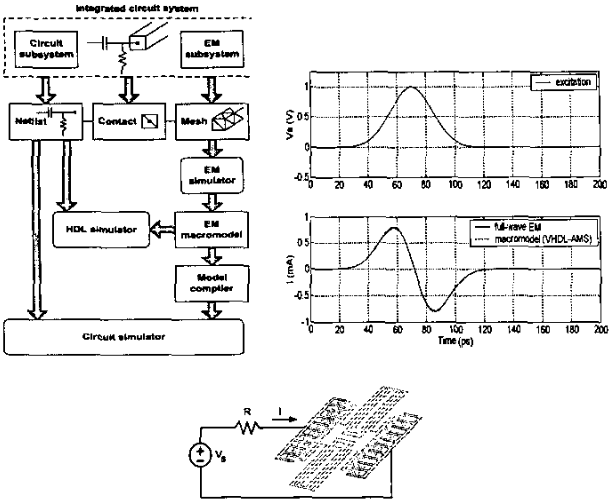

Fig. 3. Top left: Simulation flow into macromodelling language. Top right: EM response, as computed with a TDIE and VHDL-AMS state-space model, for the MEMS structure (bottom).

2.6 Sensitivity and Parametrics

Geometrical sensitivity of EM performance, and design enabling through parametrics is critical in mixed-signal systems. This has been implemented through incorporation of gradient-based methods into coupled formulations. Specifically, this is achieved by analytically computing spatial gradients within the integral equation matrices. These can then be used in gradient-based optimization as well as to estimate sensitivity of components to process (material and geometry) variation.

3 Conclusions

An overview of simulation requirements and methods for addressing the mixed-signal simulation problem are given. At the special session on Computational Electromagnetics Challenges for Mixed-Signal Circuits and RF Packaging, references, details, and further example will be provided that could not be incorporated here. This paper also aims to kickoff the special session where experts in the field will present complementary and competing specific simulation advances.

4 Acknowledgements

The authors would like to thank Swagato Chakraborty, Dipanjan Gope, Gong Ouyang, Yong Wang, Todd West, and Chuanyi Yang. This work was supported by DARPA-MTO NeoCAD grant N66001-01-1-8920.

A Surface Equivalence-Based Method to Enable Rapid Design and Layout Iterations of Coupled Electromagnetic Components in Integrated Packages

Swagato Chakraborty and Vikram Jandhyala
Department of Electrical Engineering, University of Washington, Seattle, WA 98195
Phone: (206) 543-2186, Fax: (206) 543-3842, e-mail: {swagato, jandhyala}@ee.washington.edu

Abstract

A novel methodology is presented that expedites the electromagnetic analysis in the design cycle of individual layout components in close proximity to other radiating and electromagnetic structures. The proposed method retains all the advantages of a surface based moment method technique, but avoids explicit modeling of the interactions between the object under design and the neighboring ones, without compromising on the accuracy of capturing the electromagnetic coupling between them. As a result the simulation time in individual design cycle is greatly reduced.

I. Introduction

“Faster” and “smaller” are two key foci of today’s electronic industry; the operating frequency or switching speeds and the packing density are increasing in modern day packages. As a result, full-wave electromagnetic and proximity effects are playing increasingly more important roles in determining the package performance. Also, low power applications reduce the noise tolerance and therefore demand greater fidelity in modeling the aforementioned effects especially in densely coupled environments. As a result accurate electromagnetic analysis of complex coupled system is of paramount interest in today’s packaging technology.

In a package design process, the final layout is achieved through a number of design iterations where the electrical behavior of the layout is numerically modeled at each iteration step. In a densely packed system, such computation becomes very expensive due to the coupling effects from the interacting objects, such as mutually coupled inductors, located in close proximity to the component under design.

Finite element methods [1] are based on the differential form of Maxwell’s equations and lead to a sparse matrix system of equations. This system also has the advantage that different components are represented independently in a decoupled manner, thereby enabling design. FEM based methods do suffer from some disadvantages that include large system sizes due to volumetric discretization, frequency dependent meshing to capture exact skin effects, and the requirement for accurate absorbing boundary conditions (ABCs) to truncate FEM meshes. As an alternative, surface integral equation based techniques such as the Method of Moments (MoM)[2] have become popular in package-level EM simulation due to smaller system sizes, automatic built in radiation conditions (and hence no ABCs), and frequency independent meshing upto foreseeable frequencies of interest. For design purposes, however, the MoM poses a challenge. The Green’s function-based underlying formulation results in a highly dense and highly coupled system, where every piece of the discretization interacts with every other piece through a mutual coupling term. Circuit-centric variations of the MoM such as the Partial Element Equivalent Circuit (PEEC) [3] method also suffer from the similar problem, as all the circuit elements representing the cross-coupling between the discretized representation of a design-iterated object and the discretized representation of unaltered objects in close proximity need to be recomputed and re-solved at each design iteration step. The reason for the inherent inefficiency is the inability to exploit the unchanging nature of interacting components that have already been designed or are fixed in design.

The proposed method retains the strengths of surface based MoM formulations while removing the bottleneck of explicitly modeling the coupling between the geometry under design and all the neighboring layout components in every design iteration. The paradigm is based on using the surface equivalence principle [4] on an enclosing mathematical surface, followed by storing the Schur complements [5] of the sub-set of the system matrix that do not change with the design iterations. It is important to note that the proposed technique bypasses the cost of modeling all the mutual coupling explicitly without compromising on the accuracy in accounting for the coupling.

II. Formulation

Isolation

The electromagnetic isolation of the object under design is achieved by introducing a smooth mathematical surface around the object. The surface isolates the problem into an exterior equivalent problem (Fig.1b) and an interior equivalent problem (Fig. 1c), where the object under design belongs only to the interior problem and the neighboring layout components belong to the exterior problem.

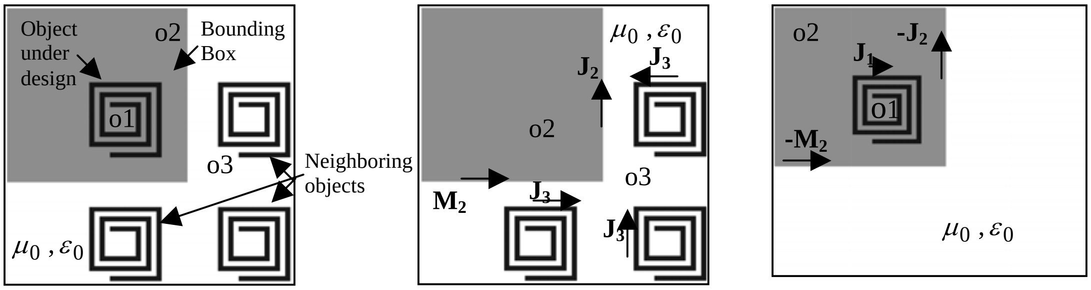

(a) (b) (c)

Fig.1 (a) Original problem (b) Exterior equivalent problem (c) Interior Equivalent problem

It is important to notice that the exterior equivalent problem does not change with a change in the design or location of the object o1 within the mathematical surface. However if the shape and size of the object o1 change drastically, it may require a change in the smooth surface o2, to maintain a desired level of accuracy. As a result of decomposing the actual problem into the equivalent problems the mutual couplings between the object under design (o1) and the other neighboring objects (o3) are captured in two separate problems and are never required to be modeled explicitly.

Figure 1 depicts the equivalent surface currents in both exterior and the interior problems for a simple case where all the physical objects (o1 and o3) are modeled as perfect electric conductors. However the methodology presented here is generally valid for any object where the material property is modeled using surface impedance approximations or more rigorous lossy dielectric models [6]. Here the metal objects o1 and o3 support equivalent electric currents $\mathbf{J_1}$ and $\mathbf{J_3}$ respectively, whereas the mathematical bounding box o2 supports both electric current $\mathbf{J_2}$ and magnetic current $\mathbf{M_2}$. On the metal surface, the electric field integral equation [2] is enforced, whereas on the dielectric surface, the continuity of tangential electric and magnetic fields across dielectric boundary is enforced, as in a PMCHWT formulation [4]. Thus combining all the interactions the overall system of linear equations is written in a matrix form as

$$\begin{bmatrix} \mathbf{E}^{1,int}_{\mathbf{J_1}} & -\mathbf{E}^{1,int}_{\mathbf{J_2}} & -\mathbf{E}^{1,int}_{\mathbf{M_2}} & 0 \\ -\mathbf{E}^{2,int}_{\mathbf{J_1}} & \mathbf{E}^{2,ext}_{\mathbf{J_2}}+\mathbf{E}^{2,int}_{\mathbf{J_2}} & \mathbf{E}^{2,ext}_{\mathbf{M_2}}+\mathbf{E}^{2,int}_{\mathbf{M_2}} & \mathbf{E}^{2,ext}_{\mathbf{J_3}} \\ -\mathbf{H}^{2,int}_{\mathbf{J_1}} & \mathbf{H}^{2,ext}_{\mathbf{J_2}}+\mathbf{H}^{2,int}_{\mathbf{J_2}} & \mathbf{H}^{2,ext}_{\mathbf{M_2}}+\mathbf{H}^{2,int}_{\mathbf{M_2}} & \mathbf{H}^{2,ext}_{\mathbf{J_3}} \\ 0 & \mathbf{E}^{3,ext}_{\mathbf{J_2}} & \mathbf{E}^{3,ext}_{\mathbf{M_2}} & \mathbf{E}^{3,ext}_{\mathbf{J_3}} \end{bmatrix} \begin{bmatrix} J_1 \\ J_2 \\ M_2 \\ J_3 \end{bmatrix} = \begin{bmatrix} -\mathbf{E}^{inc}_1 \\ -\mathbf{E}^{inc}_2 \\ -\mathbf{H}^{inc}_2 \\ -\mathbf{E}^{inc}_3 \end{bmatrix} \tag{1}$$

Where $\mathbf{X}^{\alpha,k}_{\mathbf{Y}_\beta}$ in general represents the tangential electric or magnetic field $\mathbf{X}$ ($\mathbf{E}$ or $\mathbf{H}$) on the surface α (o1,o2 or o3), due to the source current $\mathbf{Y}$ (electric current $\mathbf{J}$ or magnetic current $\mathbf{M}$) on surface β (o1,o2 or o3), radiating in the k (interior or exterior) region. The unknown vector represents the strengths of the electric and magnetic currents, and the right hand side vector (RHS) consists of the incident electric or magnetic field in the corresponding media, tangential to the surface. Typically for an external radiation-free microelectronic environment there is no direct excitation on the surface o2, but circuit excitations (modeled here as simple gap-source excitations) [7] exist for the appropriate basis functions on the surfaces o1 and o3.

At each step of the design iteration for the object o1, only the blocks associated with the surface of o1, i.e. the blocks in the first row and the first column change. However, since there is no direct interaction between the surfaces of o1 and o3, the corresponding blocks are null. Typically, there is a large number of unknowns associated with o3 that represents the union of all the discertizations of surfaces of objects interacting with o1. Thus the isolation prevents the larger size matrices involving basis functions on o3 from changing through the design iterations.

Matrix Decomposition

The linear system in (1) can be represented in a more convenient and compact way by representing the unknowns on o1, o2 and o3 by $\mathbf{Y}_1$, $\mathbf{Y}_2$ and $\mathbf{Y}_3$, and all the tested fields by $\mathbf{X}^1$, $\mathbf{X}^2$ and $\mathbf{X}^3$, as

$$\begin{bmatrix} \mathbf{X}^1_{\mathbf{Y}_1} & \mathbf{X}^1_{\mathbf{Y}_2} & 0 \\ \mathbf{X}^2_{\mathbf{Y}_1} & \mathbf{X}^2_{\mathbf{Y}_2} & \mathbf{X}^2_{\mathbf{Y}_3} \\ 0 & \mathbf{X}^3_{\mathbf{Y}_2} & \mathbf{X}^3_{\mathbf{Y}_3} \end{bmatrix} \begin{bmatrix} \mathbf{Y}_1 \\ \mathbf{Y}_2 \\ \mathbf{Y}_3 \end{bmatrix} = \begin{bmatrix} \mathbf{R}_1 \\ 0 \\ \mathbf{R}_3 \end{bmatrix} \tag{2}$$

where $\mathbf{R}_1$ and $\mathbf{R}_3$ represents the excitation.

Finally using variable substitution, the unknown on the object under design, i.e. o1, can be written as

$$\mathbf{Y}_1 = \left[\mathbf{X}^1_{\mathbf{Y}_1} - \mathbf{X}^1_{\mathbf{Y}_2} \{ \mathbf{X}^2_{\mathbf{Y}_2} - \mathbf{X}^2_{\mathbf{Y}_3} (\mathbf{X}^3_{\mathbf{Y}_3})^{-1} \mathbf{X}^3_{\mathbf{Y}_2} \}^{-1} \mathbf{X}^2_{\mathbf{Y}_1} \right]^{-1} \left[\mathbf{R}_1 + \mathbf{X}^1_{\mathbf{Y}_2} \mathbf{X}^2_{\mathbf{Y}_3} (\mathbf{X}^3_{\mathbf{Y}_3})^{-1} \mathbf{R}_3 \right] \tag{3}$$

Clearly, the terms $\{ \mathbf{X}^2_{\mathbf{Y}_2} - \mathbf{X}^2_{\mathbf{Y}_3} (\mathbf{X}^3_{\mathbf{Y}_3})^{-1} \mathbf{X}^3_{\mathbf{Y}_2} \}^{-1}$, and $\mathbf{X}^2_{\mathbf{Y}_3} (\mathbf{X}^3_{\mathbf{Y}_3})^{-1}$ do not change during the design iterations of object (o1), and can be pre-computed for all the design steps.

If N_1, N_2, N_3 are the number of unknowns on the surface o1, o2, o3, the cost of solving for $\mathbf{Y}_1$ during the stages of the design iterations where the appropriate blocks are pre-computed is given by C_1 , where

$$C_1 = N_1^3 + N_1 N_2 (N_1 + N) + N_1^2 + N_1 N_2 + N_2 N_3 \tag{4a}$$

If the flexibility of changing the excitation on the neighboring geometry is not required the cost can be further reduced to C_1' given by

$$C_1' = N_1^3 + N_1 N_2 (N_1 + N) + N_1^2 + N_1 N_2 \tag{4b}$$

The direct approach without any isolation or decomposition has the cost given by C_2 , where

$$C_2 = (N_1 + N_3)^3 + (N_1 + N_3)^2 \tag{5}$$

Also, it is straightforward to identify the unchanging nature of the neighboring object (o3). Therefore using just decomposition without the isolation the solution $\mathbf{Y}_1$ can be computed as

$$\mathbf{Y}_1 = \left[\mathbf{X}^1_{\mathbf{Y}_1} - \mathbf{X}^1_{\mathbf{Y}_3} (\mathbf{X}^3_{\mathbf{Y}_3})^{-1} \mathbf{X}^3_{\mathbf{Y}_1} \right]^{-1} \left[\mathbf{R}_1 + \mathbf{X}^1_{\mathbf{Y}_3} (\mathbf{X}^3_{\mathbf{Y}_3})^{-1} \mathbf{R}_3 \right] \tag{6}$$

Where the cost is given by C_3 , where

$$C_3 = N_1^3 + N_1 N_3 (N_1 + N_3) + N_1^2 + N_1 N_3 + N_3^2 \tag{7}$$

For accurate analysis of a small component in the layout we need to consider the coupling effects due to all the nearby components, i.e. $N_3 >> \{N_1, N_2\}$. Thus from (4,5 and 7) we conclude for such cases $C_1 << \{C_2, C_3\}$.

III. Numerical Results

The presented method is applied in extracting the scattering (S) parameters of a transmission line structure(Fig. 2a) in the presence of a near-by spiral inductor and a ground plane. The structures are residing in a medium with relative dielectric constant of 4. In the design iteration, where the line width is changed from $3\mu m$ to $5\mu m$, and the gap between the two conductors is reduced from $10\mu m$ to $8\mu m$, the new S-parameters are modeled using the isolation technique presented in the paper. The result is in excellent agreement (Fig. 2b) with that obtained by a fully coupled analysis of the perturbed design including all the neighboring objects. Table 1 demonstrates the ability of the proposed isolation technique in modeling the coupling effects from the nearby objects, for a 4 by 4 spiral inductor array (Fig. 3a). It is important to note that the coupling effects increase as frequency is increased. Also, the S-parameters corresponding to ports 1 and 2s behave asymmetrically due to the uneven nature of coupling from the neighboring inductors, as opposed to the case where the coupling is not modeled where the S- parameters are symmetric.

IV. Conclusion

The proposed methodology develops and utilizes a surface-equivalence based isolation technique to accelerate repeated electromagnetic analysis through the design iterations of a layout component in a densely coupled environment. The accuracy and the relative cost advantage of the proposed method have been demonstrated compared to the existing techniques.

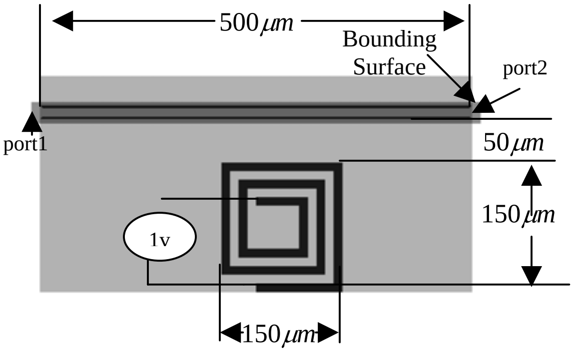

Fig. 2a Transmission line near a 3 turn spiral inductor, 10μm above a ground plane. The inductor turns are 10μm wide with 10μm gaps between the turns. The conductors of the transmission line are 3μm wide with a 10μm gap for DESIGN1, and 5μm wide with a 8μm gap for DESIGN2

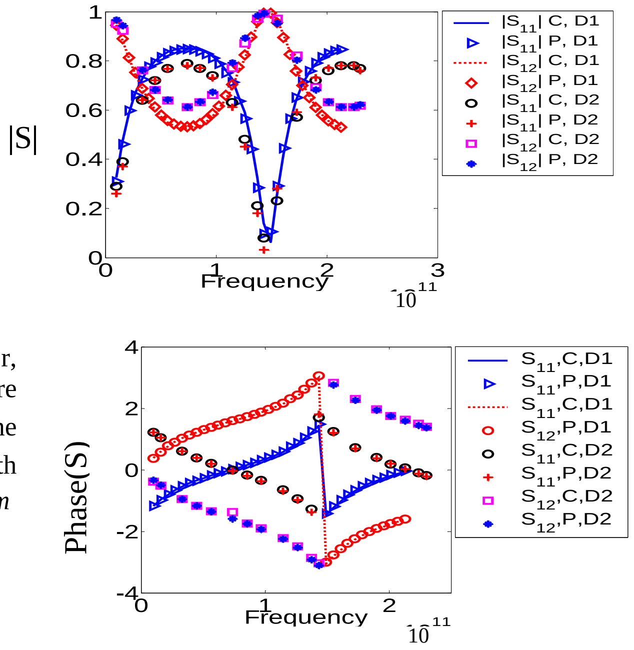

Fig. 2b Scattering parameter for DESIGN1(D1) and DESIGN2(D2), using the fully coupled method (C) and the proposed method (P)

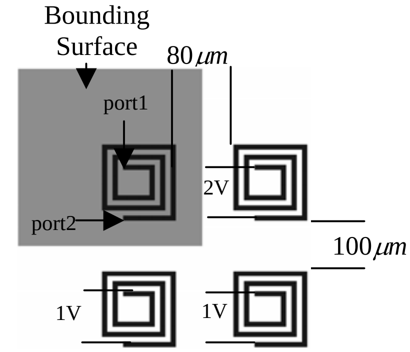

Fig. 3a Four 3 turn 150$\mu m \times$150μm spiral inductors The inductor turn are 10μm wide with 10μm gaps between the turns.

Freq		S_{11}	S_{12}	S_{21}	S_{22}
60 GHz	1	$.98\angle-11^0$	$.16\angle-102^0$	$.16\angle-102^0$	$.98\angle-11^0$
	2	$.98\angle-12^0$	$.15\angle-101^0$	$.17\angle-101^0$	$.98\angle-11^0$
	3	$.98\angle-12^0$	$.15\angle-101^0$	$.17\angle-101^0$	$.98\angle-11^0$
100 GHz	1	$.99\angle-65^0$	$.08\angle-156^0$	$.08\angle-156^0$	$.99\angle-65^0$
	2	$.96\angle-69^0$	$.04\angle-128^0$	$.09\angle-168^0$	$1.0\angle-61^0$
	3	$.96\angle-70^0$	$.04\angle-127^0$	$.09\angle-169^0$	$1.0\angle-61^0$

Table1. Scattering parameters of the top-left inductor in Fig.3 using the fully coupled analysis (2), proposed isolation technique (3) and ignoring the coupling effects (1)

Acknowledgement

The authors acknowledge Dipanjan Gope and Yong Wang for their valuable inputs in designing the examples for the paper. This work is funded by DARPA-MTO NeoCAD grant N66001-01-1-8920.

Reference:

[1] J.Jin, "The Finite Element Method in Electromagnetics", *New York: John Wiley & Sons*, 1993.

[2] S.Rao, D.Wilton, and W.Glisson, "Electromagnetic scattering by surfaces of arbitrary shape", *IEEE Trans. on Antennas and Propag.* Vol -30(3), Pp. 409-418, May 1982.

[3] A.Ruehli, "Equivalent circuit models for three-dimensional multiconductor systems", *IEEE Trans. on Microwave Theory and Techniques*, Vol -22(3), Pp. 216-221, Mar 1974.

[4] K.Umashankar, A.Taflove and S.Rao, "Electromagnetic scattering by arbitrarily shaped three-dimensional homogeneous lossy dielectric objects", *IEEE Trans. on Antennas and Prop*. Vol -34(6), Pp. 758-766, Jun 1986.

[5] I. Imam and L.Lamont, "An algorithm using the Schur complement in inverting large matrices", *IEEE Proc. –Energy and information technologies in the southeast*- Southeastcon '89, Vol-2, Pp. 421-426, 9-12 Apr 1989.

[6] S.Chakraborty and V.Jandhyala, "Evaluation of green's function integrals in conducting media", *IEEE, AP-S 2003*, Pp. 320-323, 23-26 Jun 2003.

[7] R. Harrington, "Field computation by moment methods", *IEEE Pres. New York*, 1981.

A Generalized Fast Frequency Sweep Algorithm for Coupled Circuit-EM Simulations

Benjamin Fasenfest[*]
Department of Electrical and Computer Engineering
University of Houston
Houston, TX 77204-4005

John D. Rockway, Nathan J. Champagne, and Rob M. Sharpe
Lawrence Livermore National Laboratory
Livermore, CA 94550

INTRODUCTION

Frequency domain techniques are popular for analyzing electromagnetics (EM) and coupled circuit-EM problems. These techniques, such as the method of moments (MoM) and the finite element method (FEM), are used to determine the response of the EM portion of the problem at a single frequency. Since only one frequency is solved at a time, it may take a long time to calculate the parameters for wideband devices.

In this paper, a fast frequency sweep based on the Asymptotic Wave Expansion (AWE) method is developed and applied to generalized mixed circuit-EM problems. The AWE method, which was originally developed for lumped-load circuit simulations, has recently been shown to be effective at quasi-static and low frequency full-wave simulations [1]. Here it is applied to a full-wave MoM solver, capable of solving for metals, dielectrics, and coupled circuit-EM problems.

FORMULATION

The AWE formulation consists of solving for the unknowns and their derivatives with respect to frequency at one frequency, then using this information in a Pade rational function approximation to find the result at other frequencies. To approximate the derivatives efficiently, the system matrix is first split into several matrices, each with a known frequency variation. The Electric Field Integral Equation (EFIE) with surface impedance, given by

$$j\omega\mathbf{A} + \nabla\Phi + Z_S\mathbf{J}_S = -\mathbf{E}^i, \tag{1}$$

where $\mathbf{A}$ is the magnetic vector potential, Φ is the electric scalar potential, Z_S is the surface impedance, $\mathbf{J}_S$ is the unknown current, and $\mathbf{E}^i$ the impressed electric field, is separated versus frequency content as

$$\left[\frac{B_0}{g} + B_1 + \sqrt{g}B_2 + gB_3\right][X] = [Y], \tag{2}$$

where $g = j\omega$, X is the unknown vector, and Y is the forcing function. Since the separation does not take into account inter-element phasing from the Green's Function, it works best for electrically small problems where this phasing is at a minimum.

Once the separation is complete, combinations of the B matrices may be used to approximate the derivatives of the system matrix needed for the AWE process, while the forcing function derivatives may be found exactly from the excitation data [1]. The system is then solved recursively to obtain the solution and its derivatives at each unknown, as in the standard AWE method.

If the derivatives are used to form a Pade approximation, the approximate solution may be more likely to converge near resonances than a Taylor series approximation. Since the Pade approximation is a rational function, it may match resonant behavior better than a truncated power series. The Pade rational function is then computed for each unknown at each desired frequency to obtain the approximate solution [2].

The AWE method may be applied to other integral equations where the operators may be separated by frequency content. For the PMCHWT dielectric formulation, the electric and magnetic fields are given by

$$\mathbf{E}(\mathbf{J},\mathbf{M}) = -j\omega\mathbf{A}(\mathbf{J}) - \nabla\Phi(\mathbf{J}) - \frac{1}{\varepsilon}\nabla\times\mathbf{F}(\mathbf{M}) \tag{3}$$

and

$$\mathbf{H}(\mathbf{J},\mathbf{M}) = -j\omega\mathbf{F}(\mathbf{M}) - \nabla\Psi(\mathbf{M}) + \frac{1}{\mu}\nabla\times\mathbf{A}(\mathbf{J}), \tag{4}$$

where F is the electric vector potential, ε is the permittivity, and μ is the permeability. To incorporate this into the AWE method, both vector potentials A and F need to be put into B_3 in (2), while the scalar potentials have an inverse frequency dependence and are placed into B_0. The vector potential curl terms lack an explicit frequency dependence and are put into B_1. The jump potentials on the self term of the electric vector potential are separated and placed into B_1.

For mixed circuit-EM simulation, two options are implemented: a contact-connection model and an N-port representation of the EM system. For the contact-connection model, the current continuity equation is enforced for EM elements that are connected to circuit nodes. In addition, the scalar potential is pinned to the circuit node voltage for connecting elements. This leads to a coupled system matrix equation,

$$\begin{bmatrix} EM & X \\ X^T & MNA \end{bmatrix} \begin{bmatrix} I_{EM} \\ I_{ckt} \end{bmatrix} = \begin{bmatrix} 0 \\ 0 \end{bmatrix}. \tag{5}$$

Here, the matrix *X* expresses the coupling between the electromagnetic (*EM*) and Modified Nodal Analysis circuit (*MNA*) parts of the system. Also, I_{EM} is the electric current, and I_{ckt} is the circuit current. The connectivity portions of the matrix (X and X^T) are frequency independent, while components of the *MNA* are filled according to frequency dependence [3].

The N-port model is used instead of the contact model if the EM system is to remain fixed while the circuit system is varied. The N-port result is a port admittance matrix showing the relation between the voltages and currents at each port for a given frequency. This information can then be incorporated into the circuit model, and used to quickly and accurately evaluate many circuits using the same EM pieces. The N-port representation is given by

$$[N_{port}] = [X^T][EM][X]. \tag{6}$$

In order to solve for the N-port representation using AWE, it is expressed as a linear matrix equation with multiple right hand sides using an intermediate matrix *M* as

$$\begin{aligned} [M] &= [EM]^{-1}[X] \\ [N_{port}] &= [X^T][M] \end{aligned} \tag{7}$$

In (7), the linear system is solved for *M* using the AWE method. Then, the N-port representation is found by multiplying *M* by the connectivity matrix. This increases the cost per approximate frequency by *O(number of ports squared)* over the contact connection model. However, it reduces the total unknowns in the system by the number of circuit nodes.

In many cases a single frequency expansion point cannot be used to accurately calculate the approximations over the entire frequency range of interest, requiring a multipoint expansion. Several frequency expansion points are used, and the AWE method is applied to each one independently. Each expansion point is used to form the approximations for frequencies within a certain range of its center frequency. This multipoint method allows for a tradeoff between accuracy and efficiency [4]. The fewer expansion points used, the quicker the solution and the lower the accuracy. An automated method of choosing expansion frequencies was implemented to ensure that error remained within required tolerances across the band.

RESULTS

A number of test cases were run to test the AWE implementation. To test the basic EFIE implementation, a strip dipole made of triangles was used. There were 23 unknowns on the dipole and it was fed by a delta-gap source at its center. The dipole dimensions were 39 cm × 1 cm, giving a resonant frequency of about 1.3 GHz. The automated AWE frequency sweep was used and the resulting errors are shown in Figure 1. The error norm of the approximation compared to the exact solution is shown by the crosses and each expansion point frequency is shown as a square. It is clear by the clustering of the expansion points near the upper bound that the AWE approximation becomes worse at higher frequencies.

For the frequency sweep up to 300 MHz, the exact solution took 77.11 seconds, while the AWE sweep completed in 12.4 seconds. This gives an improvement ratio of 6.2. If the exact solution was needed at more points, the improvement from the AWE would be even more dramatic, as each frequency point requires a complete fill and solution for the standard method, while it only requires a simple O(N) calculation for the AWE.

A very simple test of the coupled circuit-EM formulation is a resistive interconnect. The interconnect was modeled using the PMCHWT formulation, with a conductivity of 5.7E8 ℧/m on the interior. The dimensions of the interconnect are 1 mm × 1 mm × 4 mm. The interconnect is excited by a circuit voltage source which is connected to contacts on its ends, as shown in Figure 2.

The terminal resistance across the interconnect for both the AWE frequency sweep and the standard method is shown in Figure 3. The AWE required 24 minutes, while the exact method required 168 minutes. This test showed that coupled circuit-EM problems may be solved successfully using the AWE method.

SUMMARY

The Asymptotic Wave Expansion method was developed and applied to a full wave computational electromagnetic code. The AWE method was expanded to include the PMCHWT dielectric formulation, lumped loads, and coupled circuit-EM problems. A simple adaptive sweep was shown to be effective for some problems. Good results were demonstrated for test problems including resistors and printed circuit dipoles.

ACKNOWLEDGEMENTS

This work was performed under the auspices of the U.S. Department of Energy by University of California, Lawrence Livermore National Laboratory under Contract W-7405-Eng-48.

REFERENCES

[1] V. Jandhyala and T. West, "A fast frequency sweep method for mixed electromagnetic and circuit simulation", University of Washington Internal Report.

[2] L. Goins and W.T. Smith, "Reduced order modeling of thin wire scatterers", *1999 IEEE Southeastcon*, Lexington, KY, March 1999, pp. 323 - 328.

[3] Y. Wang, D. Gope, V. Jandhyala, and C.J.R. Shi, "Integral equation-based coupled electromagnetic circuit simulation in the frequency domain ," *2003 IEEE AP-S International Symposium and North American URSI Radio Science Meeting*, Columbus, OH, June 2003, pp. 328-331.

[4] E. Chiprout and M. Nakhla, "Transient waveform estimation of high-speed MCM networks using complex frequency hopping", *1993 IEEE Multi-Chip Module Conference*, Santa Cruz, CA, March 1993, pp. 134 – 139.

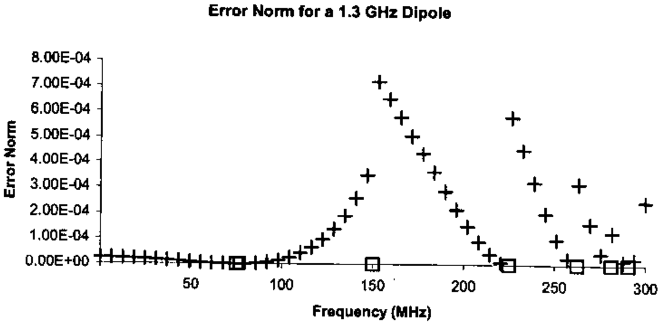

Figure 1. Error norm for a PEC dipole in free space. The + indicates the error of AWE versus exact simulation. The squares show the expansion frequencies.

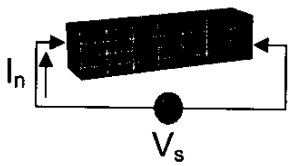

Figure 2. The geometry for the copper interconnect.

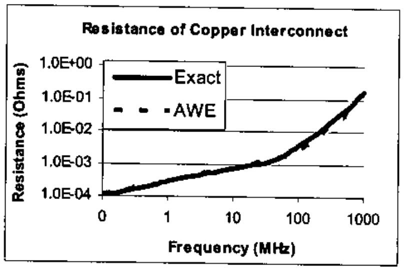

Figure 3. Terminal resistance of the copper interconnect for both the fast and standard method.

Fast Iterative and Direct, QR-based Solvers for Large Scale, Massively Coupled Parasitic Extraction Problems

Dipanjan Gope and Vikram Jandhyala

Department of Electrical Engineering, University of Washington, Seattle, WA 98195

Ph: 206-221-6513 Fax: 206-543-3842, email {dip, jandhyala}@ee.washington.edu

Abstract

Quasi-static parasitic extraction is a crucial design issue in digital circuits and mixed signal IC analysis. A surface-based, integral equation methodology aimed at modeling the problem results in a dense system of equations. Fast iterative algorithms developed to efficiently handle such systems, are limited by the speed of convergence and the number of nets involved. In this paper, we present a faster and improved oct-tree based implementation of the QR iterative solver. We demonstrate the relative efficiency of QR based solvers in fast matrix-vector products, which is critical to multiple RHS problems. Also a fast non-iterative QR/LU algorithm is developed with adaptive fill-in reduction, applicable mainly to medium sized problems with massive number of nets.

I. Introduction

Parasitic capacitance extraction has become more and more significant with increase in circuit performance (high speed) and density (shrinking feature size). A surface – based integral equation methodology like the Method of Moments (MoM) is ideally suited to address the problem. It leads to a well-conditioned system with reduced size, but the system of equations generated is inherently dense, thereby creating a time and memory bottleneck.

Several fast iterative techniques have been developed to efficiently store and solve an MoM system. All these methods (e.g. the fast multipole method (FMM), QR-based method, FFT-based technique) rely on algorithms to accelerate matrix vector products and therefore expediting the iterative solution. The memory requirement and the setup time is reduced from $O(N^2)$ to $O(N)$ or $O(N\log N)$ and the solve time is reduced from $O(N^3)$ (Gaussian Elimination) or $O(N^2)*p*r$ (Regular Iterative Solver) to $O(N)*p*r$ or $O(N\log N)*p*r$, where p is the number of iterations for convergence per RHS and r is the number of RHS vectors.

The QR based fast iterative solver developed by Kapur and Long (IES^3) [1] is particularly attractive for circuit problems. It is independent of the kernel (Green's function), and can be applied directly to multi-dielectric cases without increasing the size of the problem unlike the other competitive methods. Even in terms of free-space capacitance extraction IES^3 has been demonstrated as being more efficient in terms of memory and solve time. This method is based on low rank decomposition of MoM sub-matrices by SVD or Modified Gram Schmidt method. The method however, suffers from a higher setup time cost. For problems with large number of nets, that require many RHS solutions, the higher setup cost is more than offset by faster matrix vector multiplies. However for well-conditioned fewer nets systems where the setup cost dominates, IES^3 is not a good choice.

In this paper, we present DICOT-QR, a Deterministic Interaction Capacitated Oct Tree based QR algorithm, that greatly reduces the setup time while maintaining the memory and solve time efficiency of RMBT-QR, Rank-Map oriented Binary Tree based QR, which is based on the same principles as IES^3. The DICOT-QR algorithm exploits the properties of an oct-tree implementation, to create a predetermined set of interaction list, thereby reducing the setup time considerably. Performance comparison of DICOT-QR, RMBT-QR and Fast-Cap (an FMM based open source code [2]) are presented.

Problems involving a large number of nets (massively coupled interconnects) or large number of excitation points (substrate coupling), entails the solution of many RHS vectors. A fast direct solver, which bypasses the need for an iterative scheme, associated preconditioning and the uncertainty and time of convergence, is a better choice for such problems.

The multilevel schemes developed for fast matrix-vector products do not inherently lend themselves to obtain fast methods for direct decomposition or inversion. To accomplish fast direct solution Canning and Rogovin [3] suggested sparse-LU and Sherman-Morrison-Woodbury schemes based on a multilevel sparse representation of the MoM matrix. But the a priori matrix block structure assumed by their algorithm prevents it from being applicable equally to general 3D structures. In this work, the QR-based low-rank representation and the sparse-LU computation are integrated in order to alleviate the computational overhead associated with fill-ins and thereby generating a dynamically optimized block structure.

II. Theory

a) *MoM formulation*: Capacitance problems formulated using MoM are solved by the integral form of the Poisson's Equation:

$$\nabla^2\phi(\mathbf{r}) = -\rho(\mathbf{r})/\varepsilon$$

relating potential ϕ and charge-density ρ. The discretization of the integral equation results in a matrix system of the form

$\overline{\mathbf{Z}}\mathbf{I} = \mathbf{V}$ where the $N \times N$ MoM matrix $\overline{\mathbf{Z}}$ is a dense Green's function matrix, $\mathbf{I}$ represent the unknown coefficients of known basis functions for charge density, and $\mathbf{V}$ represent the known potential excitations. Each element of the MoM matrix denotes the interaction between a testing and a basis function and is written as follows:

$$\overline{\mathbf{Z}}(\mathrm{j,i}) = \int_{S_j} ds\, t_j(\mathbf{r}) \int_{S_i} ds' g(\mathbf{r},\mathbf{r}') f_i(\mathbf{r}')$$

where $\mathrm{t_j}$ is the testing function defined over $\mathrm{S_j}$, $\mathrm{f_i}$ is the basis function defined over $\mathrm{S_i}$ and $g(\mathbf{r},\mathbf{r}')$ is the relevant Green's function. In the electrostatic case for P disconnected conductors, each column of the required $P \times P$ capacitance matrix is obtained by enforcing a voltage of 1V on the excited conductor, 0V on all other conductors, solving the above system, and integrating the charge density over each conductor. The $N \times N$ system of equations is therefore solved P times to obtain the capacitance matrix.

b) *QR decomposition of MoM sub-matrices:* This method exploits the rank-deficiency of far-field MoM sub-matrices using QR decomposition. A sub-matrix $\overline{\mathbf{A}}$ of the MoM matrix $\overline{\mathbf{Z}}$ can be decomposed as $\overline{\mathbf{A}}_{\mathrm{mxn}} = \overline{\mathbf{Q}}_{\mathrm{mxr}} \overline{\mathbf{R}}_{\mathrm{rxn}}$ where $\overline{\mathbf{R}}$ is upper triangular and $\overline{\mathbf{Q}}$ is orthonormal i.e. $\overline{\mathbf{Q}}^{\mathrm{T}} \overline{\mathbf{Q}} = \overline{\mathbf{I}}$. If $r < \frac{m*n}{m+n}$ the $\overline{\mathbf{Q}}$ and $\overline{\mathbf{R}}$ matrices together require less storage than the matrix $\overline{\mathbf{A}}$ and the latter is said to be compressed into its QR form. Also under the same situation, a matrix vector product involving $\overline{\mathbf{A}}$ will take less operations if done in the correct order with $\overline{\mathbf{Q}}$ and $\overline{\mathbf{R}}$.

c) *RMBT-QR (based on IES^3 principles):* This method is based on recursively dividing the geometry into 2 parts along its largest coordinate, thereby forming a binary tree for the geometric subsections. The primary objective of the algorithm is to identify the low-rank sub-matrices representing interactions between well-separated geometric sections and are therefore low-rank candidates. A conservative estimate of the optimum matrix structure is created and is called the Rank-Map. This map is created only once for a given dielectric environment and is utilized for all extraction cases there-in. A simplified algorithm for the process is given :

Algorithm 1:

Step 1. *Consider the matrix:*

If Rank-Map predicts low rank, then go to Step2.

Else Split (divide the structure into 2 parts, therefore matrix into 4 parts) and for each sub-matrix go to Step 1.

Step 2. *Make the QR of the matrix from samples* [3]*:*

If rank is acceptable then go to Step 3.

Else delete QR, Split and for each sub-matrix go to Step 1.

Step 3. *Check if sibling matrices are low rank:*

If yes then go to Step 4.

Else this sub-matrix has attained its optimal form.

Step 4. *Merge the 4 sibling matrices (develop parent Q and R from children Qs and Rs):*

If merge successful (parent Q and R memory less than combined children memory) send merged matrix to Step 3.

Else this sub-matrix has attained its optimal form.

The RMBT-QR algorithm optimizes the matrix structure for minimum memory. However, since memory and the number of matrix vector products per iteration, have a one-to-one correspondence, solve time is also optimized. As shown in the results the RMBT-QR algorithm performance is significantly better than Fast-Cap for many RHS problems, both in terms of time and memory, even for the free-space environment. However, in problems where the setup time dominates the algorithm cost, RMBT-QR performance is worse. The setup cost of the algorithm is largely controlled by the accuracy of rank map predictions. An accurate and exhaustive rank map is difficult if not impossible to construct. This is because of the fact that the algorithm can lead to boxes with any shape and size, due to the binary nature of the split. It is impossible to cover the infinite combinations of boxes, thus introducing a scope of error in the rank map. A conservative rank map will require more Merges, whereas a liberal rank map will induce wastage of time constructing unacceptable QRs. Thus the setup time is largely increased by the uncertainty of the matrix structure.

DICOT-QR employs an oct-tree to construct the geometric subsections, leading to the formation of same sized cubes at every level, as in static FMM (Fast-Cap). The rank map is replaced by the concept of interaction list or shell similar to multilevel FMM. The matrix block-structure is therefore predetermined and thus setup time is greatly reduced without sacrificing on the memory or the solve time of the RMBT-QR algorithm.

III. Faster Iterative Solver (DICOT-QR)

The DICOT-QR algorithm can be analyzed in 3 parts:

a) *Geometric Subdivisions*: The geometric split employed, follows directly from the FMM box structures. Every cube is split into half in all dimensions through the geometrical center, resulting into 8 children cubes in 3D of equal shape and size (Fig. 1a).

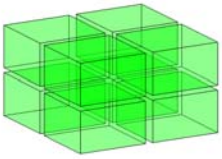

Fig. 1a) Cube Split

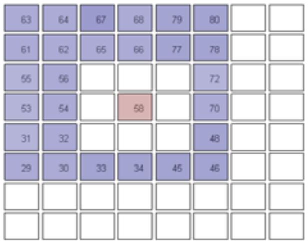

Fig. 1b) FMM shell

b) *Creating Interaction List*: This is the most crucial part of the algorithm and is closely related to that of multilevel FMM. Every cube (e.g. cube A) has a neighbor list and an interaction list. The neighbor list comprises of cubes that are adjacent to cube A. The interaction list of cube A comprises of cubes that do not feature in its neighbor list and also whose parents do not feature in the interaction list of the parent of cube A (Fig. 1b). In FMM, matrices are formed involving interactions of every cube with all cubes in its interaction list and every cube at the lowest level with its neighbors. Also, multipole expansions are formed only once for each cube and is used for all its interactions with other cubes. However, since DICOT-QR does not group sources/observers but simply deals with interaction matrices, there is further scope of combining interactions into a new interaction list called the merged interaction list (MIL). This is possible because siblings share a part of their interaction shell (Fig. 2a). The same pattern for merged interactions is repeated for each interaction shell and at all levels. The MIL is thus the rank map substitute for DICOT-QR. An illustration of a merged interaction entity is shown (Fig 2b), where interactions of siblings are combined.

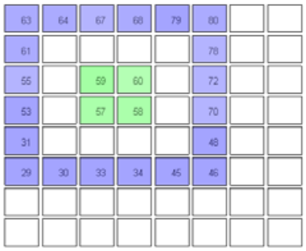

Fig. 2a) Common Interaction space

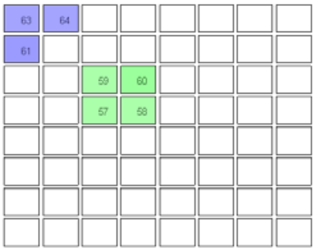

Fig. 2b) A Merged Interaction entity

c) *Performing QR compression of MIL entities*: Row and column samples are created for each merged interaction matrix based on the same principles as IES^3 [1]. The $\overline{\mathbf{Q}}$ and $\overline{\mathbf{R}}$ matrices are computed from samples using the modified Gram-Schmidt Method [4].

III. Fast Direct Solver

The proposed method presented herein relies on a combination of QR-based compression of MoM sub-matrices, followed by a fast method to obtain the LU-decomposition of the compressed matrix. To illustrate the QR-based sparse LU paradigm, consider the low ranked sub matrix $\overline{\mathbf{A}}$ in Fig. 3.

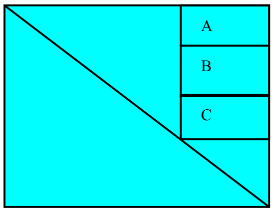

Fig. 3: Upper triangular blocks

For ease of illustration assume $\overline{\mathbf{A}}$ has rank 1 i.e. $\overline{\mathbf{A}}_{mxn} = \overline{\mathbf{Q}}_{A\,mx1} \overline{\mathbf{R}}_{A1xn}$. While performing the LU transformation on this block, the first row will remain unchanged. Notice that all the elements of the second row are transformed by changing the second element of $\overline{\mathbf{Q}}_A$ as follows $\overline{\mathbf{Q}}_A^{lu}(2) = \overline{\mathbf{Q}}_A(2) - \overline{\mathbf{Q}}_A(1)\,L(1)$ where L(1) is the appropriate coefficient from the lower triangular part. Thus the sparse LU transform of block A is $\overline{\mathbf{Q}}_A^{lu} \overline{\mathbf{R}}_A$. For block B, in addition to modifying $\overline{\mathbf{Q}}_B$, contributions from block A in the form of fill-ins are also necessitated. The sparse LU representation for block B will thus be of the form of $\overline{\mathbf{Q}}_B^{lu} \overline{\mathbf{R}}_B - \overline{\mathbf{F}}_{AB} \overline{\mathbf{R}}_A$ where $\overline{\mathbf{F}}_{AB}$ is the fill in contribution to block B from block A. In a similar manner, the sparse representation of block C is of the form $\overline{\mathbf{Q}}_C^{lu} \overline{\mathbf{R}}_C - \overline{\mathbf{F}}_{AC} \overline{\mathbf{R}}_A - \overline{\mathbf{F}}_{BC} \overline{\mathbf{R}}_B$. When the blocks A,B, and C have arbitrary rank, then the relevant LU transforms for each block are of the form $\overline{\mathbf{Q}}^{lu}_{A_{m_A \times r_A}} \overline{\mathbf{R}}_{A_{r_A \times n_A}}$, where $\overline{\mathbf{Q}}_A^{lu}(i,r) = \overline{\mathbf{Q}}_A(i,r) - \sum_{n=1}^{i-1} \overline{\mathbf{Q}}_A^{lu}(n,r) * L(n)$, $\overline{\mathbf{Q}}^{lu}_{B_{m_B \times r_B}} \overline{\mathbf{R}}_{B_{r_B \times n_B}} - \overline{\mathbf{F}}_{AB_{m_B \times r_A}} \overline{\mathbf{R}}_{A_{r_A \times n_A}}$, and $\overline{\mathbf{Q}}^{lu}_{C_{m_C \times r_C}} \overline{\mathbf{R}}_{B_{r_C \times n_C}} - \overline{\mathbf{F}}_{AC_{m_C \times r_A}} \overline{\mathbf{R}}_{A_{r_A \times n_A}} - \overline{\mathbf{F}}_{BC_{m_c \times r_B}} \overline{\mathbf{R}}_{B_{r_B \times n_B}}$, where $\overline{\mathbf{F}}_{AB}(i,r) = \sum_{n=1}^{m_A} \overline{\mathbf{Q}}_A^{lu}(n,r) * L(n)$, and $\overline{\mathbf{F}}_{AC}(i,r) = \sum_{n=1}^{m_A} \overline{\mathbf{Q}}_A^{lu}(n,r) * L(n) + \sum_{n=1}^{m_B} \overline{\mathbf{F}}_{AB}(n,r) * L(n)$. The situation is reversed for lower triangular blocks, where $\overline{\mathbf{Q}}$ factors are unaltered and fill-in factors act as substitutes for $\overline{\mathbf{R}}$ instead of for $\overline{\mathbf{Q}}$.

The crucial component of the algorithm is the manipulation of the matrix block structure in order to reduce fill-ins generated in the sparse LU process.

IV. Results: DICOT-QR

The performance of the DICOT-QR is compared to that of RMBT-QR and FastCap on several complicated structures. The results pertaining to a 5x5 bus crossover is presented below. A tolerance of 1e-3 is chosen for QR compression and a corresponding multipole order of 3 was chosen. The GMRES tolerance was set to 1e-3.

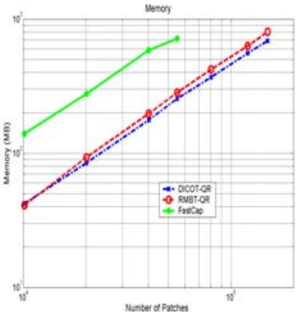

Fig. 4a) Memory

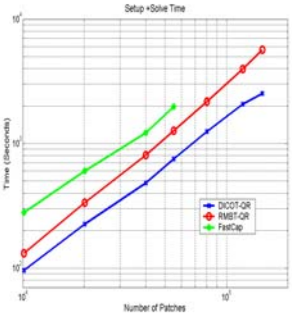

Fig. 4b) Time

The first set of results demonstrates the memory (Fig. 4a) and setup + solve time (Fig. 4b) for the 3 algorithms in computing the 10x10 capacitance matrix (10 RHS solution).

The memory and time were also compared for obtaining 3 columns of the capacitance matrix (solving for only 3 RHS). The results are presented in Fig. 4c and 4d.

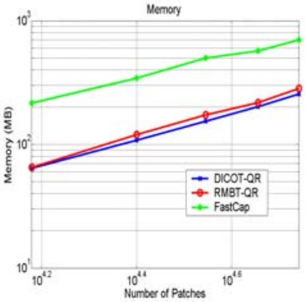

Fig. 4c) Memory

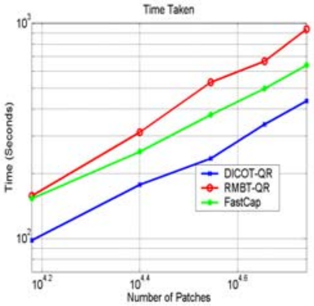

Fig. 4d) Time

From Fig. 4 it is seen that at high number of RHS (solve time dominates) both DICOT and RMBT QR algorithms are superior than its FMM counterpart, DICOT being superior to RMBT. This is more prominent at lower number of RHS where RMBT is worse than FastCap, however, DICOT is still faster.

V. Results: Fast Direct Solver

Timing and memory results for a variety of complex 3D problems were analyzed. The Sparse LU (SLU) setup time (Fig. 5a), solve time (Fig. 5b) and memory (Fig. 5c) scaling as compared to the regular LU method are presented below, for a 14 pin package. The accuracy of a column of the 14 X 14 capacitance matrix as compared to standard solvers is also demonstrated (Fig. 5d).

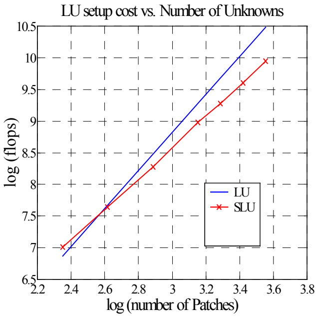

Fig. 5a) Setup time

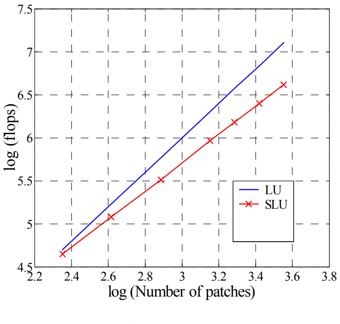

Fig. 5b) Solve time

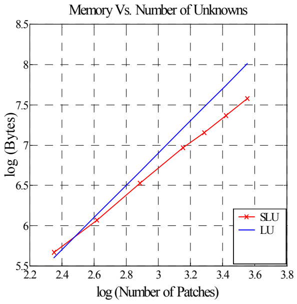

Fig. 5c) Memory

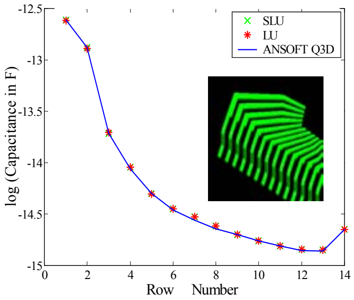

Fig. 5d) Accuracy

Table 1 demonstrates the reduced complexity of the SLU method. The LU setup cost is reduced from N^3 to exponents as low as 2.31 for a true 3D problem. Solution costs and memory are also reduced considerably from the N^2 requirements of the LU method.

Table 1

Structure	N	Setup	Solve	Memory
Thin strip	3500	2.29	1.29	1.29
Plate	3448	2.43	1.65	1.65
Bus cross	3574	2.41	1.667	1.65
Comb drive	3440	2.31	1.68	1.61
14-pin package	3158	2.51	1.667	1.61

VI. Conclusions

QR compression based fast iterative and direct solver algorithms are presented. The performance of the QR based iterative solvers is shown to be superior for many RHS problems compared to its FMM counterpart. A new QR iterative solver with faster setup time is introduced. Also, a fast direct solver for medium sized problems with many nets (RHS) based on QR compression and fill-in controlled LU is implemented. The same algorithms can be applied unchanged to multilayered dielectric problems.

References

[1] *S.Kapur and D.E.Long, "IES^3: Efficient Electrostatic and Electromagnetic Solution"* IEEE Computer Sci. and Engg. *5(4) pp. 60-67 Oct.-Dec 1998.*

[2] *K.Nabors and J.White "FastCap: A multipole accelerated 3-D capacitance extraction program", IEEE Trans. CAD, Vol. 10, No. 11, Nov.1991, 1447-1459.*

[3] *Francis X. Canning and Kevin Rogovin, "Fast Direct Solution of Standard Moment-Method Matrices"* IEEE Antennas and Propagation Magazine *Vol. 40 No. 3 pp. 15 – 26, June 1998.*

[4] *G.H.Golub and C.F.Van Loan Matrix Computations 2nd Ed. The Johns Hopkins University Press Baltimore 1989.*

Tool Name: Fast Quasi-static Frequency Solver for PILOT

Developers: Gong Ouyang, Todd West, Vikram Jandhyala

Related papers:
Todd West, Vikram Jandhyala, "A Pade via AWE fast frequency sweep for quasi-static coupled electromagnetic and circuit simulation," Antennas and Propagation Society Symposium, 2004. IEEE, Volume: 4, June 20-25, 2004

Brief description:
A fast frequency sweep solver based on Pade via quasi-static AWE of coupled circuit and integral equation electromagnetic systems is developed. The Taylor expansion is applied on each matrix to form the reduced order moment matrices over a wide bandwidth. The moments of approximation unknowns are solved through moments matching. Then the Pade approximants of unknown of interest are computed and used to approximate system behavior over a wider frequency range. Binary search method is used to find all expansion points needed.

Funding Sources: DARPA

Coding language: C

Platform: Windows, UNIX

Approximate number of source files: 60

Input description:
1. The code can read in a neutral file format, CFDRC mesh (dtf), ANSOFT mesh and ACE in house geometry input (node_list, patch_list).
2. Excitation (Circuit, Planewave, Delta-Gap, etc.)
3. Material (PEC, Conductivity of metal, permittivity of the dielectrics)

Control parameters:
1. Frequency sweep range, frequency step, convergence criterion, binary search criterion
2. Output request (circuit unknown, S-parameter, EM unknown)

Available output types:
1. Port-parameters (S)
2. Circuit unknowns
3. EM current distribution on surface

Examples:

This example shows the efficiency and accuracy of fast frequency sweep solver. Fig.(a) show the mesh of transmission line. In this example, we used current source at four ports and extract S-parameter over 1-3GHz range. 13 expansion points needed to get accurate results. (b) and (c) show the comparison between brute force method and fast sweep method. The plots shows excellent match and here total frequency sample points number is 121. The speed up ration between fast method and brute force method is 10.2:1.

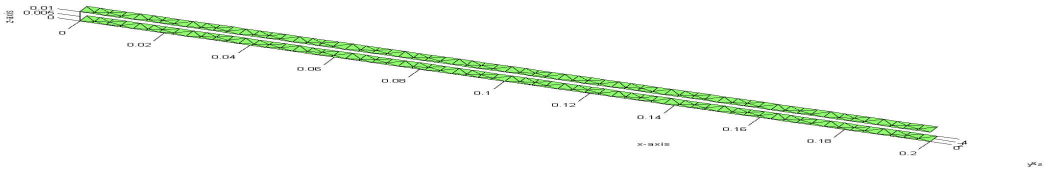

(a) Meshing of transmission line

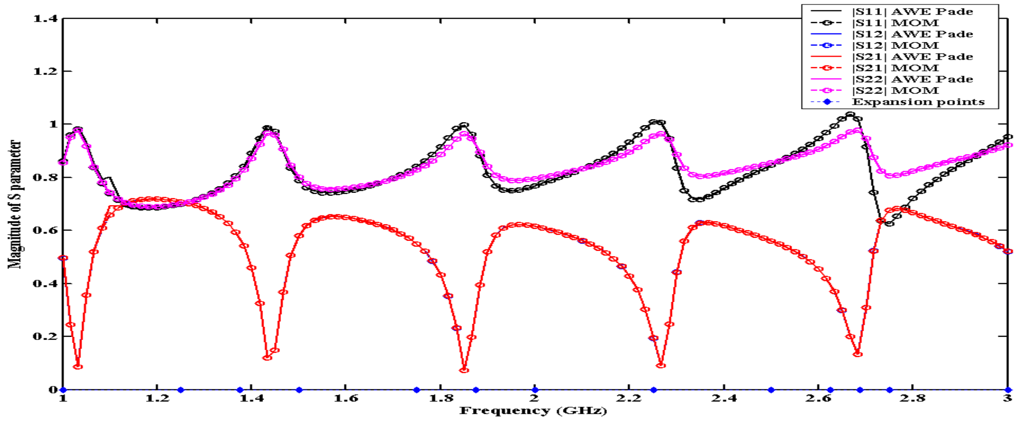

(b)Magnitude of S-parameter

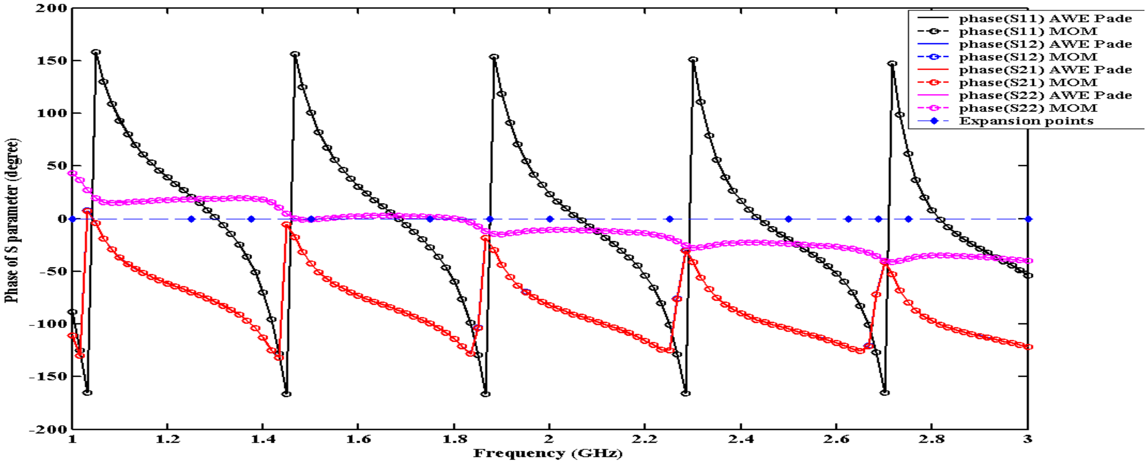

(c)Phase of S-Parameter

Tool Name: Coupled-EM-PILOT

Developers: Yong Wang, Dipanjan Gope, Vikram Jandhyala and Richard Shi

Related papers:

[1] D. Gope and V. Jandhyala, "PILOT: A Fast Algorithm for Enhanced 3D Parasitic Capacitance Extraction Efficiency", *Microwave Optical technology Letters* Vol. 41, Issue 3, pp.169-173 May 2004.

[2] V. Jandhyala, Y. Wang, D.Gope and R. Shi, "A surface based integral equation formulation for coupled electromagnetic and circuit simulation*," Microwave Optical technology Letters*, Vol. 34, No. 2, pp. 102-106, July 2002.

[3] Yong Wang, Dipanjan Gope, Vikram Jandhyala, and C.J. Richard Shi, "Integral Equation-Based Coupled Electromagnetic-Circuit Simulation in the Frequency Domain," *Proc. IEEE APS-URSI Ohio*, vol. 3, pp. 328-331, June 2003.

[4] Y. Wang, D. Gope, V. Jandhyala and C.J. Shi, "Integral equation-based coupled electromagnetic-circuit simulation in the frequency domain," *SRC TechCon Technical Digest*, Dallas, August 2003.
Awarded Best Paper in Session (Mixed Signal Technology).

[5] D.Gope, S. Chakraborty, Y.Wang, Vikram Jandhyala and Richard Shi, "A Surface based 3D coupled circuit electromagnetic simulator with accurate lossy conductor modeling," *Proc. IEEE APS-URSI San Antonio*, June 2002.

[6] V. Jandhyala, Y. Wang, D. Gope and R. Shi, "Coupled electromagnetic-circuit simulation of arbitrarily shaped conducting structures using triangular meshes," *Proc. International Symposium on Quality electronic Design*, San Jose, March 2002.

[7] V. Jandhyala, Yong Wang, D. Gope, S. Chakraborty and R. Shi, "A surface-integral equation based technique for general coupled circuit electromagnetic simulation," (invited) *Proc. Progress in Electromagnetic research Symposium*, Boston, July 2002.

Brief description: The formulation employs full-wave integral equations to model the electromagnetic (EM) behavior of 2D or 3D structures while using modified nodal analysis (MNA) to model circuit interactions. A coupling scheme based on charge and current continuity and potential matching, realized as a generalization of Kirchoff's voltage and current laws, ensures that the EM and circuit interactions can be formulated as a seamless system. While rigorous port models for EM structures can be obtained using the approach discussed herein, it is shown that the coupling paradigm can reveal additional details of the EM-circuit interactions and can provide a path to analysis-based design iteration.

Funding Sources: NSF and SRC

Coding language: C

Platform: Visual Studio (Windows)/ Visual Studio.net (Windows)/ gcc(UNIX)

Approximate number of source files: 40

Input description:

1. EM components: The code can read in neutral file format, CFDRC dtf file format, Ansoft meshes or ACE in-house geometry and material description files (node_list, patch_list, material).
2. Circuit components: SPICE like netlist for circuit elements.
3. Interface information between circuit elements and EM objects.

Control parameters:

1. Kernel: Full-wave / Quasi-static
2. Frequency sweep: Start frequency, end frequency, frequency step (.dec or .lin)

Available output types:

1. The current density distribution on EM objects (visualization)
2. S-Parameters
3. Time and memory profiling
4. Circuit node voltages and branch currents

Example:

One of the typical applications is circuit/layout co-simulation for RF electronics system design where on-chip inductors are often employed. In radio frequency circuit design, accurate characterization of the inductor is the most challenging task. Figure 1 shows the topology of a 5.6GHz differential mode Low Noise Amplifier (LNA), where several on-chip inductors are included either for the frequency selection purpose (L1 L2) or for the impedance matching purpose (L3 L4 L5 L6).

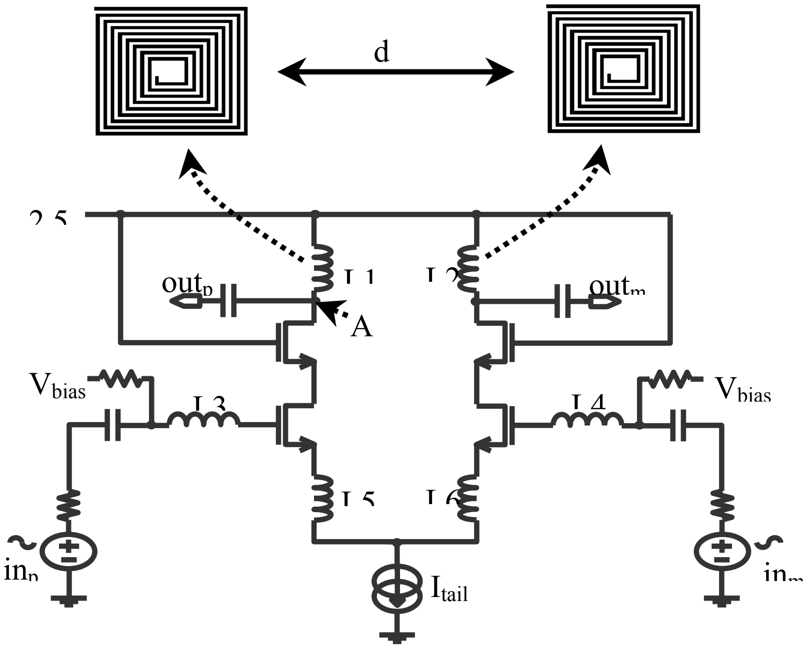

Figure 1: Schematic of a 5.6GHz Low Noise Amplifier.

With 5.6 GHz central working frequency, performance of LNA will be affected by both the distributed effect and the cross talk of on-chip spiral inductors. The precision of two inductors L1 and L2 is most important since it affects the central frequency where the maximum gain can be derived. While the transistor sizes are fixed by the requirement of the optimum noise figure to be 123 µm, the main design task is to adjust the turns and spacing of spiral inductors to tune the resonant frequency of the LC tank to the central frequency 5.6 GHz.

Spiral inductor L1 is first simulated using the coupled solver to decide the number of turns according to the extracted equivalent inductance. With a total parasitic capacitance to be 105fF at node A, the inductor is designed to be 5 turns with an area of 500µm×500µm. Figure 2 shows the extracted equivalent inductance of such a single spiral inductor.

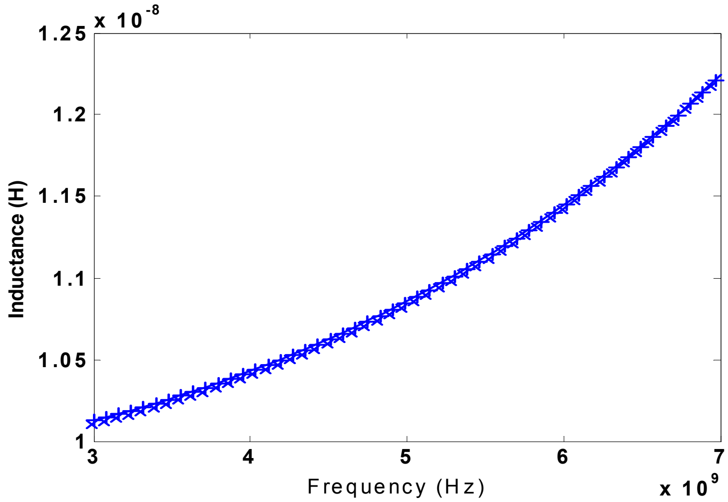

Figure 2: Extracted inductance of a single spiral inductor.

Due to the radiation and inductive coupling effects, the two inductors will mutually couple, and lead to a shift in the central frequency. Figure 3 shows a series of S_{21} curves versus different distances between the two inductors:

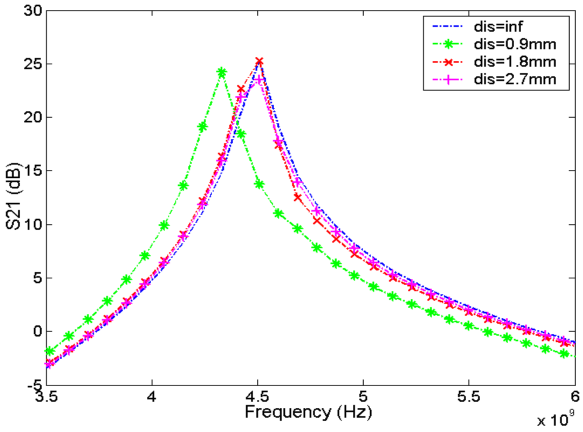

Figure 3: S_{21} curve versus distance between inductors; "inf" or infinite distance corresponds to ignoring all mutual coupling between the inductors.

As the two inductors close in the coupling effect becomes prominent and leads to poorer performance. In actuality, the coupling effect could be used to advantage; due to the differential mode nature of the currents through the two inductors, a larger effective inductance can be realized by tight coupling between the two inductors. In other words the same inductance value could be achieved using less number of turns and thus less chip area. Some multi-level inductor designs are based on this concept.

To simulate the coupled system in frequency domain, an operating point analysis is first performed to linearize the nonlinear BSIM3 transistor model [23]. Then, a frequency sweep is performed for the range of interest. The coupled circuit-EM solver avoids the steps of port model generation, curve fitting, and equivalent passive circuit generation, which are necessary in traditional design methods. Using the presented method, not only is a higher accuracy achieved due to the exclusion of curve fitting and finite filter size errors, but the entire process is also faster since the coupling between the EM and circuit has been automated.

Tool Name: Full-Wave-EFIE-PILOT

Developers: Dipanjan Gope, Swagato Chakraborty and Vikram Jandhyala

Related papers:

[1] Dipanjan Gope and Vikram Jandhyala, "Enhanced Efficiency, Hybrid FMM-QR Fast Parasitic Extractor For Conductors and Dielectrics", Submitted to *IEEE Trans. on Antennas and Propagation..*

Brief description: The Pre-Determined Interaction List Oct-Tree (PILOT) algorithm is applied to the fast iterative solution for Electric Field Integral Equation (EFIE) based formulations. The algorithm is based on predetermining interaction sub-matrices and efficient compression of the scalar and the vector potentials. The solver has been applied to S-parameter extraction and radar cross section estimations.

Funding Sources: NSF, SRC, and DARPA

Coding language: C

Platform: Visual Studio (Windows)/ Visual Studio.net (Windows)/ gcc(UNIX)

Approximate number of source files: 27

Input description: The code can read in neutral file format, CFDRC dtf file format, Ansoft meshes or ACE in-house geometry and material description files (node_list, patch_list, material)

Control parameters:

1. The desired accuracy (choices range between: 1e-2 to 1e-6)
2. Pre-conditioner to be applied (choices are: diagonal, block, near-field)

Available output types:

4. The current density distribution
5. S-Parameters
6. Time and memory profiling
7. Radar cross section/Far field radiation pattern

Example:

1. Chip example: This is a circuit example where a test chip consisting of meander lines, inductors, capacitors and interconnects (Fig. 1a) is simulated at frequency 6GHz. The number of unknowns is increased gradually to demonstrate the time and memory scaling of PILOT as compared to the regular solvers. While the memory and matrix vector product time of regular solvers scale as O(N^2) the same scaling for PILOT is linear as shown in Fig. 1b and 1c respectively. The setup time for PILOT also scales linearly since the compression is achieved without the formation of the entire matrix (Fig. 11d).

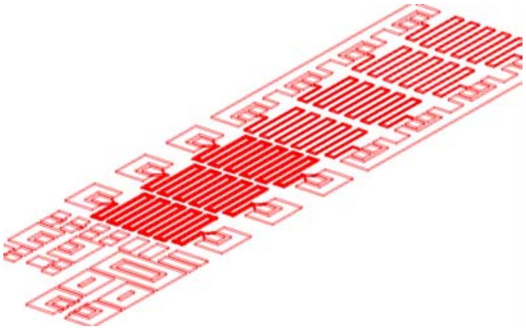

Figure 1a: Hughes Test Chip

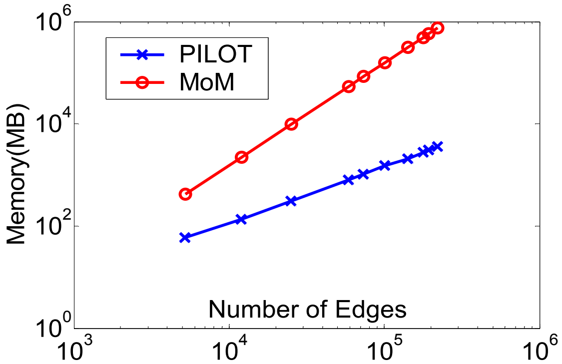

Figure 1b: Memory Scaling

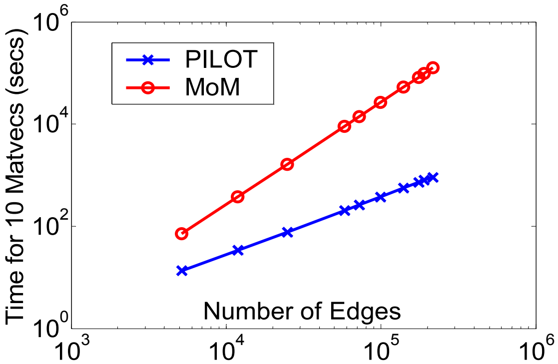

Figure 1c: Matvec Time Scaling

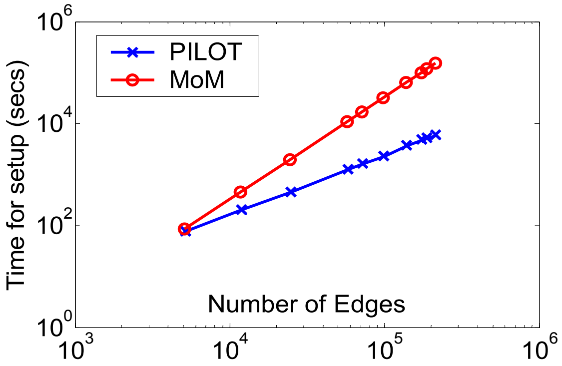

Figure 1b: Setup Time Scaling

2. RCS example: This example deals with the structure of the predator drone (Fig. 2). The surface of the structure is discretized into 2480 patches which leads to 3604 RWG basis functions.

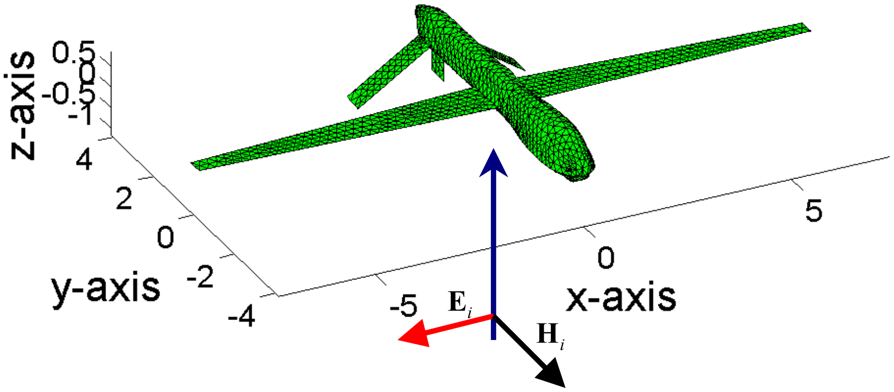

Figure 8: Structure of Predator Drone

The current density on the structure at 30 MHz., obtained using the regular LU solver and PILOT is plotted on a log scale in Fig. 3.

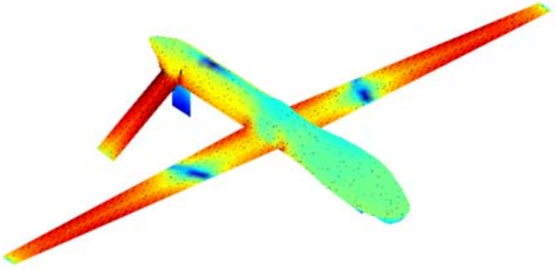

Figure 3a: The current density obtained using LU

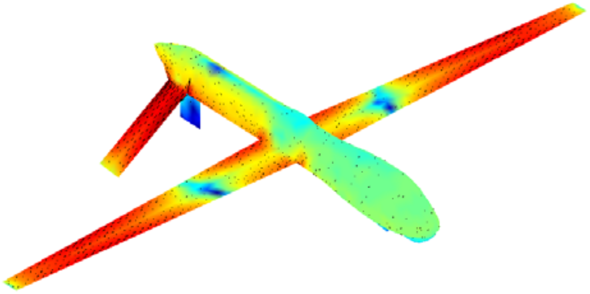

Figure 3b: The current density obtained using PILOT

The RCS of the structures at $\phi = 0^o$ computed using the regular methods and PILOT at $\phi = 0^o$ are plotted in Fig. 4.

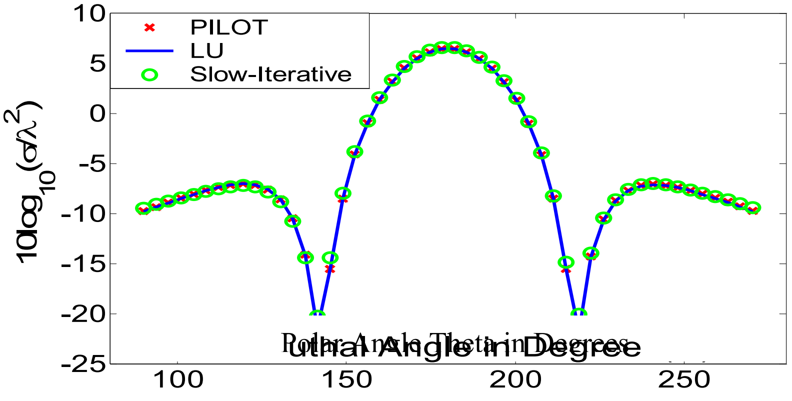

Figure 4: The Bistatic RCS of the predator drone at 30MHz.

The backscattering angle corresponds to ($\theta = 180^o$). As seen in the figure, there is reasonable agreement between the methods. The time and memory requirements for the solution process are demonstrated in Table 1.

	Memory	Setup Time (sec)	Matvec Time (sec)	Solve Time (sec)
Regular LU	207MB	30	X	3306
Regular Iterative	207MB	30	3.62	765
PILOT Iterative	61MB	85	1.43	299

It can be seen that the PILOT has superior time and memory performance for the problem. If the number of basis functions is increased, the setup time of PILOT will better the other algorithms since it has a linear scaling as compared to the quadratic scaling of the other methods.

Tool Name: Fast Fullwave Frequency Sweep Solver

Developers: Gong Ouyang, Swagato Chakraborty, Vikram Jandhyala

Related papers:
Todd West, Vikram Jandhyala, "A Pade via AWE fast frequency sweep for quasi-static coupled electromagnetic and circuit simulation," Antennas and Propagation Society Symposium, 2004. IEEE, Volume: 4 , June 20-25, 2004

Brief description:
A fast frequency sweep solver based on Pade via fullwave AWE of coupled circuit and integral equation electromagnetic systems is developed. This solver incorporate fullwave Green's function kernel of EFIE and fullwave kernel for PMCHW formulation. So it is capable of dealing with multi-region problem. The simple version can do Taylor expansion for PEC or lossy metal with EFIE formulation. The complex version can do Taylor expansion of PMCHW formulation which can handle lossy dielectric. The moments of approximation unknowns are solved through moments matching. Then the Pade approximants of unknown of interest are computed and used to approximate system behavior over a wider frequency range. Binary search method is used to find all expansion points needed.

Funding Sources: DARPA

Coding language: C

Platform: Windows, UNIX

Approximate number of source files: 20

Input description:
1. The code can read in a neutral file format, CFDRC mesh (dtf), ANSOFT mesh and ACE in house geometry input (node_list, patch_list).
4. Excitation (Circuit, Planewave, Delta-Gap, etc.)

5. Material (PEC, Conductivity of metal, lossy material, permittivity of the dielectrics)

Control parameters:

2. Frequency sweep range, frequency step, convergence criterion, binary search criterion
2. Output request (circuit unknown, S-parameter, EM unknown)

Available output types:

3. Port-parameters (S)
4. Circuit unknowns
3. EM current distribution on surface

Examples:

This example shows the efficiency and accuracy of fast frequency sweep solver. Fig(a) show the mesh of two spiral inductors with ground plane. In this example, we used current source at four ports and extract S-parameter over 900-1000GHz range. 9 expansion points needed to get accurate results. (b)(c) show the comparison between brute force method and fast sweep method. The plots shows excellent match and here total frequency sample points number is 61. The speed up ratio between fast method and brute force method is 2.63:1.

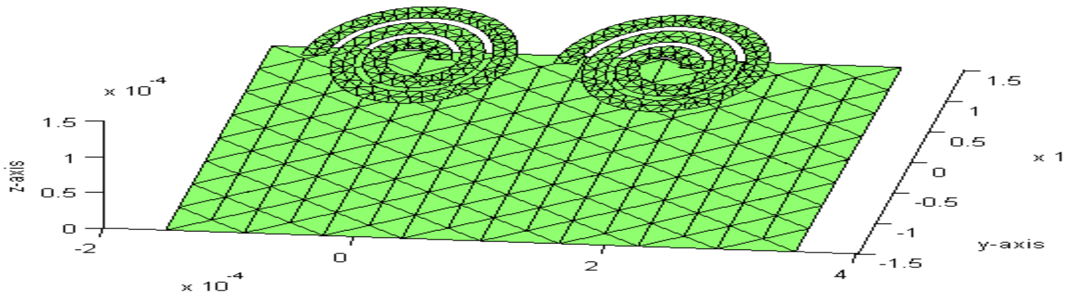

(a) Meshing of two spiral inductors with ground plane

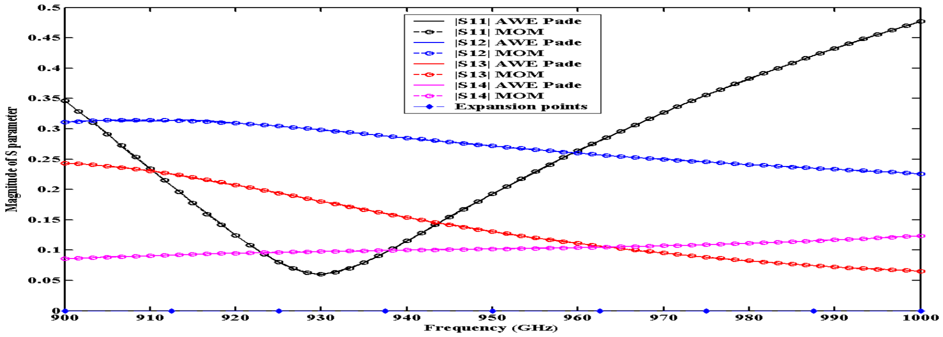

(b)Magnitude of S-parameter

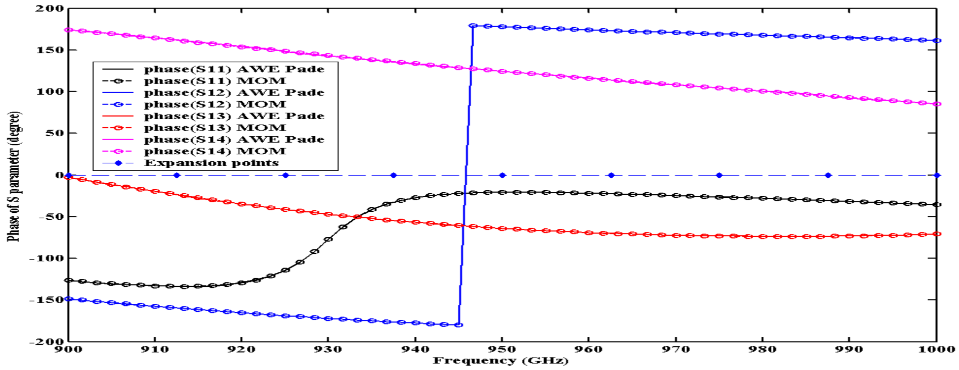

(c) Phase of S-parameter

Tool Name: Static-PILOT

Developers: Dipanjan Gope, Swagato Chakraborty and Vikram Jandhyala

Related papers:

[1] Dipanjan Gope, Swagato Chakraborty and Vikram Jandhyala, "Enhanced Efficiency, Hybrid FMM-QR Fast Parasitic Extractor For Conductors and Dielectrics", *IEEE Design and Automation Conference,* pp. 794-799, 2004.

[2] D.Gope and V.Jandhyala, "PILOT: A Fast Algorithm for Enhanced 3D Parasitic Capacitance Extraction Efficiency", *IEEE meeting on Electric. Perf. of Electron. Packaging*, Princeton, pp. 337-340, Oct. 2003.

[3] Dipanjan Gope and Vikram Jandhyala, "Fast direct solver for massively coupled parasitic extraction problems," *SRC TechCon Technical Digest*, Dallas, August 2003.

[4] D. Gope and V. Jandhyala, "PILOT: A Fast Algorithm for Enhanced 3D Parasitic Capacitance Extraction Efficiency", *Microwave Optical technology Letters* Vol. 41, Issue 3, pp.169-173 May 2004.

[5] Dipanjan Gope and Vikram Jandhyala, "Oct-Tree Based Multilevel Low-Rank Decomposition Algorithm for Rapid 3D Parasitic Extraction", To appear in *IEEE Transactions on Computer-Aided Design of Integrated Circuits and Systems,* Nov. 2004.

Brief description: The Pre-Determined Interaction List Oct-Tree (PILOT) algorithm is applied to aid fast solution of electrostatic formulation for parasitic extraction in circuits and computation of electrical forces in MEMS. The algorithm is based on low-rank compression of sub-matrices on an oct-tree framework with merged interactions for maximum compression.

Funding Sources: NSF, SRC, and DARPA

Coding language: C

Platform: Visual Studio (Windows)/ Visual Studio.net (Windows)/ gcc(UNIX)

Approximate number of source files: 17

Input description: The code can read in neutral file format, CFDRC dtf file format, Ansoft meshes or ACE in-house geometry and material description files (node_list, patch_list, material)

Control parameters:

1. The desired accuracy (choices range between: 1e-2 to 1e-6)
2. Pre-conditioner to be applied (choices are: diagonal, block, near-field)

Available output types:

8. The charge density distribution
9. Capacitance matrix
10. Time and memory Profiling
11. Electrical forces on the structure

Example:

1. Package Structure: In the following example we consider a package structure with 56 conducting leads as shown in figure 1a:

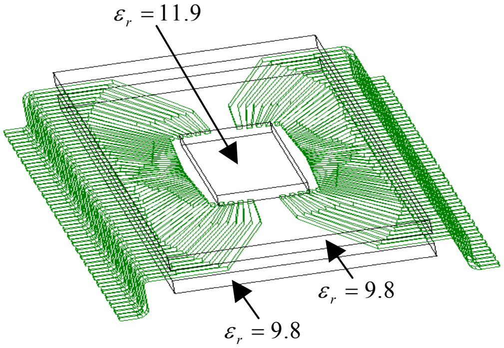

Figure 1a: Package structure 280µm×680µm×56µm with 56 leads. The package is sandwiched by a top and a bottom Al_2O_3 ceramic layer (ε_r=9.8) of thickness 20µm . A dielectric slab of ε_r=11.9 and thickness of 10µm is placed in the space between the leads (96µm×220µm).

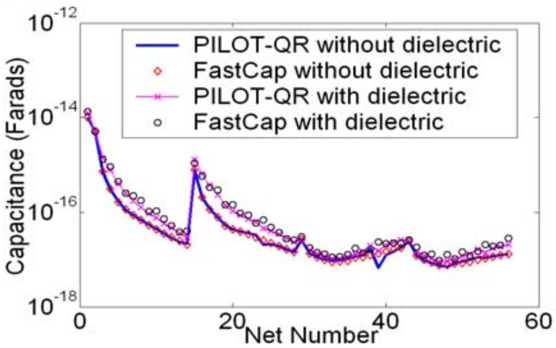

Figure 1b: Comparison of results of PILOT with FastCap with or without dielectrics compared with/without dielectrics for the package structure in figure 8.

The first row of the capacitance matrix obtained for the 2 cases, with and without dielectrics, are plotted in figure 1b using PILOT-QR and FastCap. It can be observed that the results demonstrate excellent match between the values obtained from the 2 different algorithms. It can also be noted that due to the presence of the dielectrics the coupling-capacitances between the leads increase.

The required memory is compared with FastCap in figure 2a. In figure 2b, the advantage of PILOT is demonstrated over RMBT-QR for multiple nets for the package structure shown in Fig. 1a, without the dielectrics. Time taken by RMBT-QR is always more compared to the time taken by PILOT, by an offset amount, though they demonstrate to have the same slope. This observation supports an improved set-up time performance of PILOT compared to RMBT-QR which is emphasized for a multiple net problem.

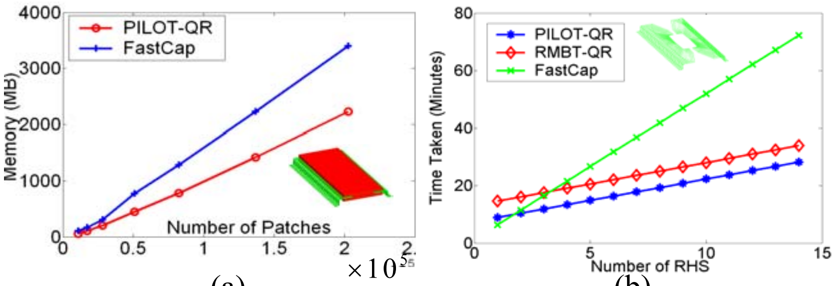

(a) (b)

Figure 2: a) Memory comparison of PILOT with FastCap in the presence of dielectrics b) The total time required by the different algorithms for multiple right hand side solutions for the package structure in figure 7.

2. Chip Structure: The second example demonstrates the computing efficiency of the PILOT algorithm for very large-scale problems. The test-chip structure consisting of meander lines, inductors, capacitors and interconnects is repeated in a 10×3 array, and shown in Fig. 3.

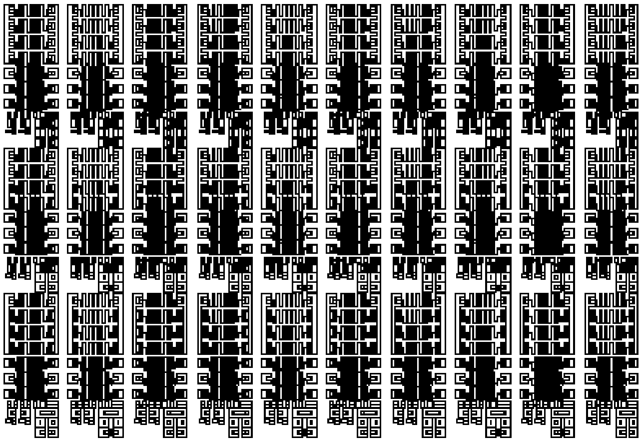

Figure 3: The illustrated structure is generated by placing the geometry of Fig. 9a in a 10×3 array. The surface is meshed with 0.913 triangular patches.

The entire structure is meshed with 0.913 million patches. The problem is setup and solved for 3 different excitations. In the 4 GB of memory available, PILOT was able to fit and run this example, and required 3.3 GB, 48 minutes for setup, and 90 minutes for solution with 3 right hand sides. The other solvers like Fast-Cap and RMBT-QR (prototype implementation of IES^3) could not fit the problem with the given resources.

Tool Name : Surface Integral-Based Material Region Solver for PILOT

Developers : Swagato Chakraborty

Related papers:

[1] S. Chakraborty and V.Jandhyala, "Evaluation of Green's Function Integrals in Conducting Media", Accepted for publication in IEEE.*Trans. on Antennas and Propagations*.

[2] V. Jandhyala, Y. Wang, D. Gope, S. Chakaraborty, and R. Shi, "A surface-integral equation- based technique for general coupled circuit-electromagnetic simulation," (invited) *Proc. Progress in Electromagnetics Research Symposium*, Boston, July 2002.

Brief description :

Surface integral equation based dielectric models uses two region PMCHWT technique[1] . The code can handle 2-D or 3-D metal structures inside or outside the dielectric or on the dielectric-back ground interface. Metal-Metal and Metal-Dielectric junctions edges are handled using additional RWG basis functions. The conducting objects can be directly coupled to circuits [2] or can be excited using delta-gap sources or external wave excitations.

Funding Sources : DARPA

Coding language: C

Platform: Windows, Unix

Approximate number of source files: 50

Input description:

1. The code can read in a neutral file format, CFDRC mesh (dtf), ANSOFT mesh and ACE in house geometry input (node_list,patch_list).
2. Excitation (Circuit,Planewave,Dipole,Delta-Gap, etc.)
3. Material (Conductivity of the metal, permittivity (complex) of the dielectric)

Control parameters :

1. Frequency range (In linear or logarithmic steps)
2. Output request(with corresponding parameters for the output)
3. Debug Options

Available output types:

1. Circuit unknown quantities
2. Port-pramaters (S,Z) , Q -factors

3. EM current distribution on surface
4. Electric and Magnetic field at a given point
5. Far field pattern

Examples:

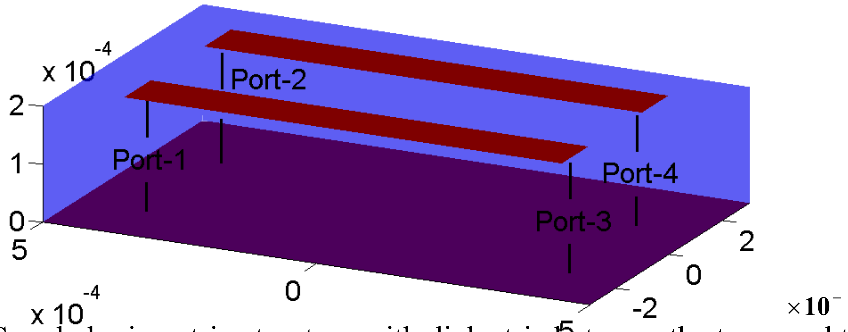

Fig. 1 Coupled microstrip structure with dielectric between the trace and the ground plane

(a)

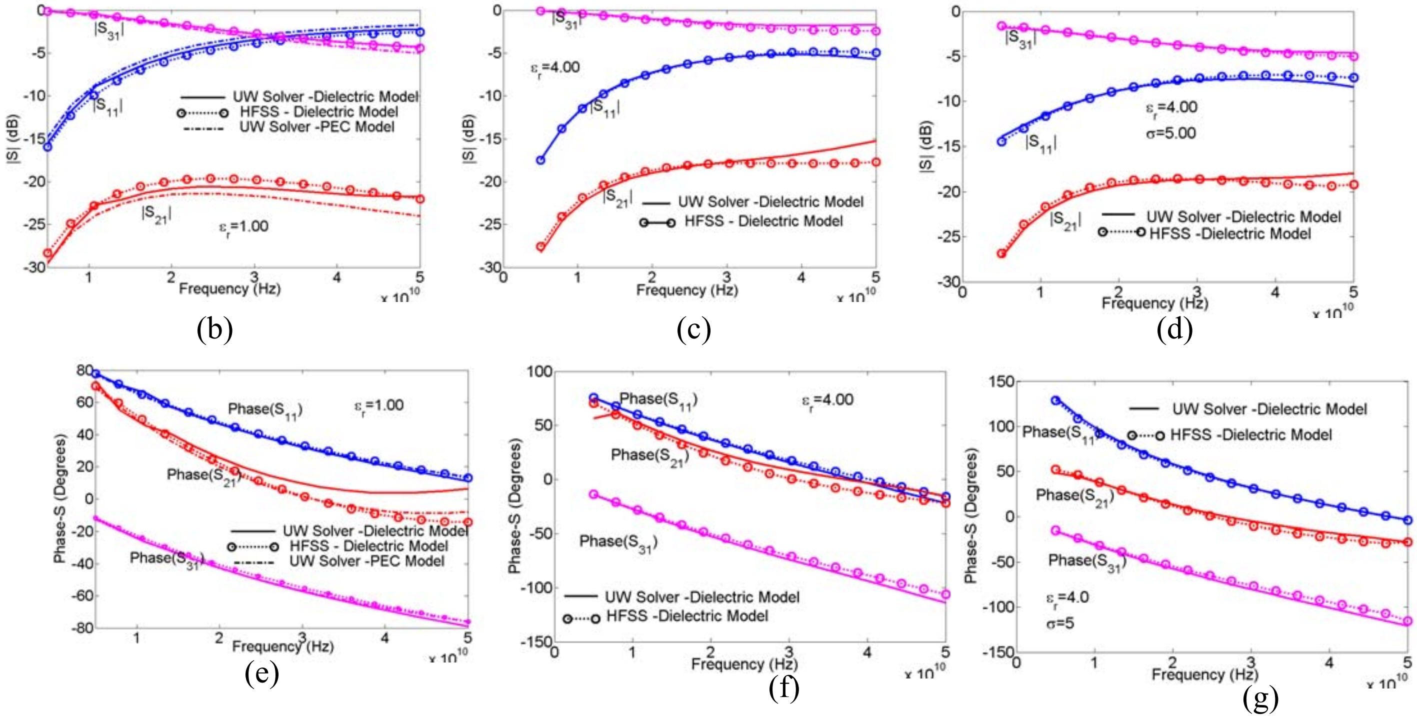

(b) (c) (d)

(e) (f) (g)

Fig. 1 Comparison of the magnitude (b-d) and phase (e-g) behavior of a coupled microstrip(a) structure using UW Solver –Dielectric model and Ansoft HFSS for different properties of the dielectric .

Tool Name: Lossy Conductor Solver for PILOT

Developers : Swagato Chakraborty

Related papers:

[1] S.Chakraborty and V.Jandhyala, “Surface-Based Broadband Electromagnetic-Circuit Simulation of Lossy Conducting Structures in Microelectronic Circuits**”,** Presented in *IEEE APS-URSI* 2004, Monterey CA.

[2].S. Chakraborty and V. Jandhyala, “Accurate computation of vector potentials in lossy media,” *Microwave Optical Technology Letters*, vol. 36, no. 5, pp. 359-363, March 5, 2003.

[3]. S. Chakraborty and V.Jandhyala,"Evaluation of Green's Function Integrals in Conducting Media," *Proc. IEEE Antennas and Propagation Society International Symposium*, 2003, vol. 3, pp. 320-323, 22-27 June 2003.

Brief description :

Surface integral equation based solver for broad-band modeling of lossy conducting structures, coupled to lumped circuit elements is developed. A two region PMCHWT technique is used for modeling the lossy object. The Green’s function integrals are computed using analytic tools [2,3] for highly damped kernels. Coupling methodology is incorporated in the code describing mutual interactions between the circuit and the electromagnetic quantities[1].

Funding Sources : DARPA

Coding language: C

Platform: Windows, Unix

Approximate number of source files: 50

Input description:

1. The code can read in a neutral file format, CFDRC mesh (dtf), ANSOFT mesh and ACE in house geometry input (node_list,patch_list).
2. Excitation (Circuit,Planewave,Dipole,Delta-Gap, etc.)
3. Material (Conductivity of the metal, permittivity (complex) of the dielectric)

Control parameters :

1. Frequency range (In linear or logarithmic steps)
2. Output request (with corresponding parameters for the output)
3. Debug Options

Available output types:

1. Circuit unknown quantities
2. Port-pramaters (S,Z)
3. EM current distribution on surface
4. Volumetric current distribution in the cross section
5. Electric and Magnetic field at a given point
6. Far field pattern

Examples:

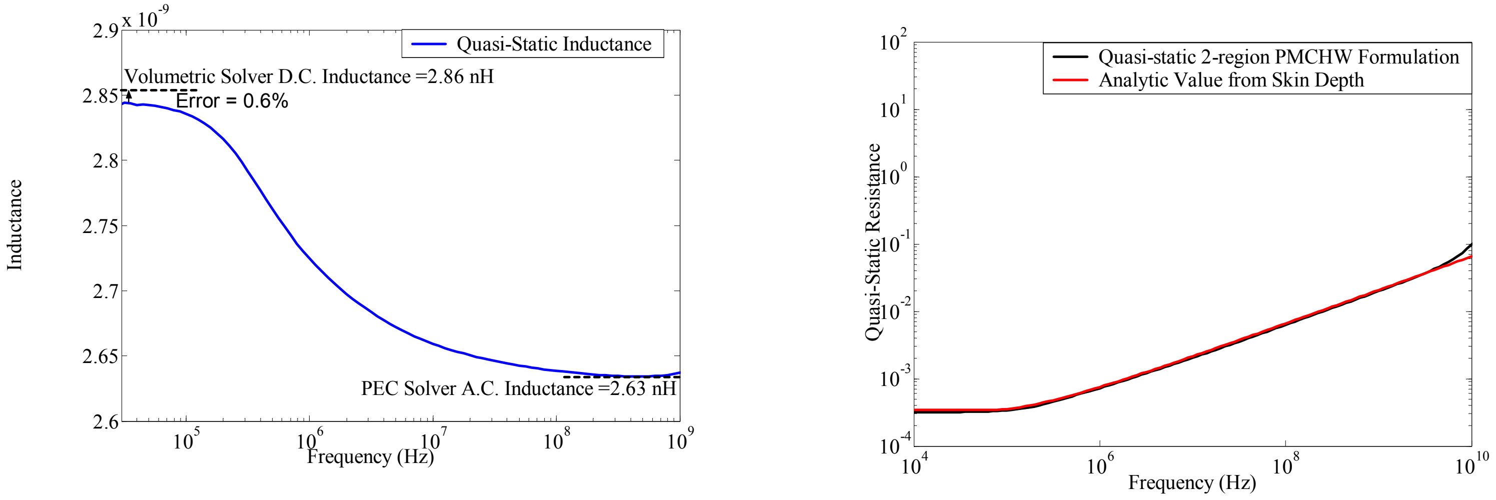

Fig. 2a. Broadband extraction of inductance (Left) and resistance (Right) of a Copper bar of dimension $0.5mm \times 0.5mm \times 5mm$, using the Lossy Conductor Solver

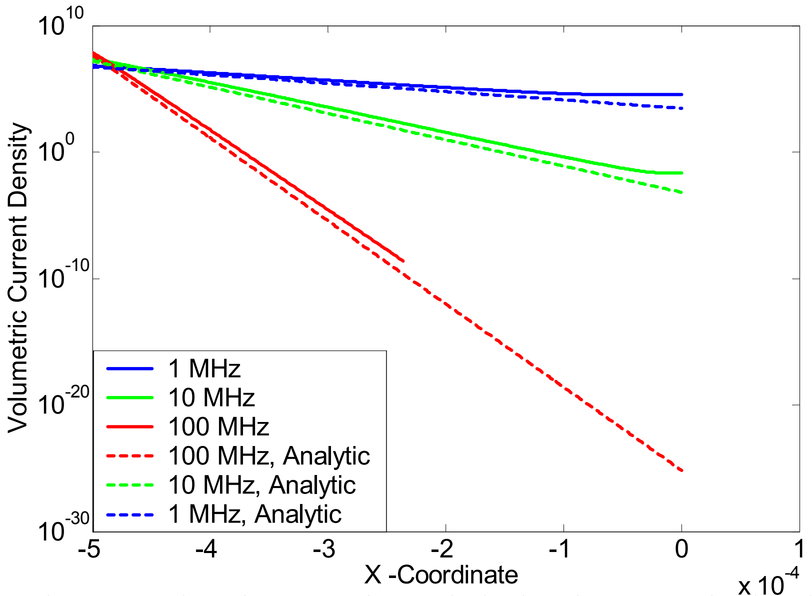

Fig. 2b. Comparison between the analytical and computed skin-effect in the volumetric current density . The surface integral equation based Lossy Conductor Solver can predict the volumetric current inside the cross-section of a conductor.